DEFECT ENGINEERING AND CONVERSION OF METAL-ORGANIC FRAMEWORKS FOR ADSORPTION AND ELECTRICAL ENERGY STORAGE APPLICATIONS

A Dissertation
Presented to
The Academic Faculty

by

Yang Jiao

In Partial Fulfillment
of the Requirements for the Degree
Doctor of Philosophy in the
School of Chemical and Biomolecular Engineering

Georgia Institute of Technology
August 2017

DEFECT ENGINEERING AND CONVERSION OF METAL-ORGANIC FRAMEWORKS FOR ADSORPTION AND ELECTRICAL ENERGY STORAGE APPLICATIONS

Approved by:

Dr. Krista S. Walton, Advisor
School of Chemical & Biomolecular Engineering
Georgia Institute of Technology

Dr. William J. Koros
School of Chemical & Biomolecular Engineering
Georgia Institute of Technology

Dr. Ryan P. Lively
School of Chemical & Biomolecular Engineering
Georgia Institute of Technology

Dr. David S. Sholl
School of Chemical & Biomolecular Engineering
Georgia Institute of Technology

Dr. Meilin Liu
School of Materials Science and Engineering
Georgia Institute of Technology

Date Approved: July 06, 2017

This dissertation is dedicated to my family and my friends.

ACKNOWLEDGEMENTS

First, I would like to express my greatest thanks to my advisor, Professor Krista S. Walton, for your endless support and guidance during my Ph.D. study at Georgia Tech. You encouraged me to think and discover my own research interests, allowed me to collaborate with others in various research fields, provided invaluable advice when I was struggling with my research projects, and helped me become a better independent researcher. I greatly appreciate your mentorship over the past five years.

I am greatly thankful for the valuable mentorship and exceptional feedback provided by my committee members, Dr. David S. Sholl, Dr. William J. Koros, Dr. Ryan P. Lively, and Dr. Meilin Liu. I would like to give a special thanks to Dr. Liu for offering me an opportunity to broaden my research area and allowing me to work closely with his group for the energy storage study.

I would like to thank Walton group members, Dr. Yang Cai, Dr. Katrina Stults, Dr. Bogna Grabicka, Dr. Michael Mangarella, Dr. Greg Cmarik, Dr. Yougui Huang, Dr. Tim Duerinck, Dr. Chris Murdock, Dr. Himanshu Jasuja, Dr. Karen Tulig, Dr. Sudhir Sharma, Ken Onubogu, Erika Garcia-Gutierrez, Lalit Darunte, Jacob Deneff, Yutao Gong, and Eli Carter for their kindness, friendship and support during my daily research life in Bunger-Henry building. I thank all the EFRC Walton subgroup members, Dr. Cody Morelock, Dr. William Mounfield, Dr. Ian Walton, Michael Dutzer, Jay Joshi, Julian Hungerford, Colton Moran for sharing innovative ideas with me during our weekly meeting. Particularly, I want to thank Dr. Nicholas Burtch and Dr. Yi Huang for their tremendous discussions and insightful suggestions to help me overcome obstacles and achieve my research goals.

I would also like to thank Liu group members, Dr. Bote Zhao and Chong Qu for their help in electrochemistry. Their patience and experience helped me out when I first stepped into the field of electrochemistry.

I thank the Center for Understanding and Control of Acid Gas-Induced Evolution of Materials for Energy (UNCAGE-ME), an Energy Frontier Research Center funded by U.S. Department of Energy, Office of Science, Basic Energy Sciences for supporting this work.

Finally, I am grateful to my mother, Huijuan Zhang, my father, Quanyou Jiao, and my girlfriend, Yixuan Shi for their love, encouragement, and support over the years. This Ph.D. work wouldn't have been possible without all of you.

TABLE OF CONTENTS

LIST OF TABLES

LIST OF FIGURES

LIST OF SYMBOLS AND ABBREVIATIONS

A	Ampere
Å	Angstrom
AC	Activated Carbon
ADC	9,10-Anthracenedicarboxylic Acid
AU	Arbitrary Units
BDC	1,4-Benzenedicarboxylic Acid
BET	Brunauer-Emmett-Teller
C	Specific Capacitance
cm^3	Cubic Meter
CUS	Coordinatively Unsaturated Metal Centers
CV	Cyclic Voltammetric
DABCO	1,4-Diazabicyclo[2.2.2]octane
DFT	Density Functional Theory
DMF	N,N'-Dimethylformamide
DOBDC	2,5-Dioxido-1,4-Benzenedicarboxylic Acid
EDLC	Electrical Double-Layer Capacitor
EDS	Energy Dispersive Spectroscopy
EIS	Electrochemical Impedance Spectroscopy
eV	Electron Volt
F/g	Farad per Gram
FTIR	Fourier Transform Infrared Spectroscopy
g	Gram

Gr	Graphene
GCMC	Grand Canonical Monte Carlo
GCD	Galvanostatic Charge-Discharge
h	Hour
HAADF	High-Angle Annular Dark-Field
HCl	Hydrochloric Acid
HR	High-Resolution
H_2SO_4	Sulfuric Acid
I	Current
ICP-OES	Inductively Coupled Plasma Optical Emission Spectroscopy
K	Kelvin
kJ	Kilojoule
kW/kg	Kilowatt per Kilogram
LB	Lorentz-Berthelot
LJ	Lennard-Jones
m	Mass
M	Molarity
mg	Milligram
m^2/g	Square Meter per Gram
MIL	Material of Institute Lavoisier
min	Minute
mL	Milliliter
MM	Mixed-Metal
mmol	Millimole
MOF	Metal-Organic Framework

mol	Mole
MS	Mass Spectrometry
MTV	Multivariate
mV/s	Milliwatt per Second
NDC	1,4-Naphthalenedicarboxylic Acid
NMR	Nuclear Magnetic Resonance
NU	Northwestern University
PCN	Porous Coordination Network
pKa	Basicity of Ligand
P/P_0	Relative Pressure
ppm	Parts per Million
PTFE	Polytetrafluoroethylene
PXRD	Powder X-ray Diffraction
PyC	4-Pyrazolecarboxylate
q	Charge
rGO	Reduced-Graphene Oxide
RH	Relative Humidity
SBU	Second Building Unit
SC	Supercapacitor
SEM	Scanning Electron Microscopy
STEM	Scanning Transmission Electron Microscopy
t	Time
T	Temperature
TEM	Transmission Electron Microscopy
TFA	Trifluoroacetic Acid

TGA	Thermogravimetric Analysis
TM	2,3,5,6-Tetramethyl-1,4-Benzenedicarboxylic Acid
UFF	Universal Force Field
UiO	University of Oslo
USTC	University of Science and Technology of China
V	Volt
VOC	Volatile Organic Compound
W	Pore Width
Wh/kg	Watt-Hour per Kilogram
XPS	X-ray Photoelectron Spectroscopy
ZIF	Zeolitic Imidazolate Framework

SUMMARY

Metal-organic frameworks (MOFs) are hybrid porous materials, constructed by the assembly of inorganic metal ions or clusters and organic ligands. MOFs have attracted considerable research interest in the fields of gas adsorption and separations, owing to their high surface areas, permanent porosity, tailorable pore sizes, and remarkable tunability. Numerous modification strategies have been developed for engineering MOF crystals based on their desired characteristics. MOFs can have intentionally generated crystal imperfections by using defect engineering strategies during their synthesis. Defect engineering is an effective strategy that can be used to tune the physical and chemical features of MOFs such as their chemical stability, textural and adsorption properties. Understanding the impact of defects on the changes in these properties of MOFs is imperative to the development of next-generation defective MOFs. Chapters 3 and 4 provide detailed studies on two typical defect types (e.g. mixed-metal and missing cluster defects) that are commonly found in defective MOFs. In chapter 3, experimental investigations revealing trends related to the effect of mixed-metal centers on CO_2 adsorption and water stability properties are addressed. Chapter 4 provides insight into the impact of missing cluster defects on chemical stability and adsorption properties through experimental and computational methods.

Beyond being used as adsorbents, these hybrid crystals can also be converted to metal oxides, metal hydroxides and carbons via facile chemical treatments. These MOF-derived materials usually possess high surface areas, large pore volumes, diverse functional groups, controllable morphology, and hierarchical-pore architectures. These features make

MOFs-as-templates strategies promising choices for electrical energy storage applications such as supercapacitors. Chapter 5 investigates the relationship between MOF stability and the cycling stability of MOF-derived electrode materials via complimentary experimental techniques. Chapter 6 evaluates the electrochemical performance of both positive and negative electrode materials that are synthesized from a single MOFs-reduced graphene oxide (rGO) precursor. In general, this dissertation explores the possibilities of defect engineering and MOFs-as-templates (MOF conversion) strategies that could be used to design and engineer MOFs or MOF-derived materials for adsorption and electrical energy storage applications.

CHAPTER 1. INTRODUCTION

1.1 Metal-Organic Frameworks

Porous solids have garnered significant attention throughout the past few decades due to their distinct interaction with different atoms, ions, and molecules. According to the current IUPAC notation, porous solids contain three different pore size ranges: micropores ($W \leq 2$ nm), mesopores ($2 \text{ nm} < W \leq 50$ nm), and macropores ($W > 50$ nm).[1] Researchers have made great progress on traditional microporous materials such as zeolites and activated carbons, which are widely used as commercial porous solids throughout the world. The secondary building units (SBUs) of zeolites are made up of AlO_4 or SiO_4 tetrahedra clusters attached via corner-sharing connections. This type of connection gives uniform pore sizes and well-defined microporous crystalline structures which lead to their use in various industry applications such as gas separation, ion exchange, catalysis and water softening.[2-5] Activated carbons are usually produced from carbonaceous materials such as charcoal or biochar and are also used to solve industrial challenges, including water purification, volatile organic compounds (VOC) control and desulfurization.[6-8] However, those porous materials suffer from limited chemical variety, relatively poor control over pore size ranges, and difficulties in tuning surface functionalities.

Metal-organic frameworks (MOFs) are a diverse set of porous crystalline materials, constructed by self-assembly of inorganic metal ions or metal clusters and organic linkers.[9,10] This nanomaterial design methodology affords unlimited possibilities for tuning the pore size, coordinative geometry and ligand functionality by changing the combinations of metal ions or metal clusters and organic ligands.[11, 12] For instance, over 20,000 different

MOFs have been synthesized within the past decade,[13] and the number of synthesized MOFs greatly outnumbers that of traditional porous solids zeolites in the literature.[14] To date, MOFs have been shown to possess extraordinarily high BET surface areas (NU 110 = 7140 m^2/g),[15] surpassing those of traditional porous solids such as zeolites and activated carbons. Isoreticular principles allow for the manipulation of MOF pore sizes and ligand functionalities while preserving topology, which has been used to produce frameworks with relatively large pore apertures and low material densities.[16-18] With those properties, MOFs may play a promising role in many commercial applications such as adsorption, separations, gas storage, ion exchange, drug delivery, luminescence, catalysis, chemical sensing, and electrical energy storage and conversions.[11, 19-26]

1.2 Defective MOFs

The formation of defects in crystalline materials is difficult to eliminate even through the most careful synthesis procedures.[27] Although ideal crystalline structures may form energetically, it is still difficult to avoid the incorporation of defects during crystal synthesis, processing, or use. The "real crystals" often contain considerable amounts of structural imperfections, deviating from the perfect arrangement of ideal crystals. Prospectively, controllable crystal defect incorporation may facilitate enhancements in the tailoring of crystalline material properties. Previous investigations with semiconductors, heterogeneous catalysis, and solid oxide fuel cells have revealed the broad impact of defect engineering in a myriad of industrial applications.[28-30] As a subset of crystalline materials, MOFs have attracted growing attention in this particular field over the past years. Several studies have reported and characterized the internal (point defects) or external defects of some classic MOFs.[31, 32] Defect engineering has emerged as a useful technique to tune the

porosity, enlarge the pore aperture, and manipulate the physical/chemical properties of these unique porous materials.[33-39] In this section, I will briefly focus on two major defective MOFs that are prepared intentionally, which are defective MOFs with mixed-metal centers and defective MOFs with missing linkers and clusters.

1.2.1 Defective MOFs with Mixed-Metal Centers

In the MOF community, chemical engineers and chemists always seek to find an efficient approach to introduce heterogeneous species within preformed MOF structures, in which they can harness the benefits from the incorporation of such heterogeneity.[40] Furukawa further envisaged that these heterogeneous compartments could operate separately, yet function synergistically within these complex arrays.[13] Recently, the idea of multivariate MOFs (MTV-MOFs), in which multiple functional groups of varying ratios are introduced into the well-studied MOF-5 type structure, has received much attention. Deng[41] demonstrated that up to 8 distinct functionalities can be incorporated into a typical MOF framework in a one-pot solvothermal reaction. This idea has been pursued further by Zhang and Yuan to synthesize zinc-based MOF-177 and zirconium-based PCN-700 with multiple functionalities.[42, 43]

Although it is more complicated to apply multivariate strategy to metal centers than organic linkers, some work has revealed the possibility for developing multiple metal centers within one system and then forming defective MOFs with mixed-metal centers or mixed-metal MOFs (MM-MOFs).[44] Mixed-metal center defects, or cation defects, are one of the common defects that exist in MOFs.[31] Heterometal clusters or ions are intentionally introduced into a MOF framework while retaining the structural integrity in the actual long-

range order.[44] There are two synthetic approaches to reach the formation of this type of defects in MOFs. Mixing multiple metal salts in a one-pot reaction[45, 46] is one possible way to develop MM-MOFs. For example, Kozachuk et al. reported that Cu-doped DMOF structures could be synthesized through a one-pot solvothermal reaction, in which up to 95% of Zn^{2+} ions were replaced with Cu^{2+} ions. Interestingly, a distortion of the building units was confirmed using single-crystal X-ray diffraction.[47] Very recently, MM-MOF-74 structures were successfully prepared through the one-pot synthesis. The resulting crystals were found to contain up to 10 different divalent metals (Mg, Ca, Sr, Ba, Mn, Fe, Co, Ni, Zn and Cd).[48] Another strategy for constructing a MM-MOF is to substitute some of the metal centers in an existing MOF by another metal via post-synthetic cation exchange.[49,50] For instance, > 90% of the zirconium based UiO-66 crystals were exchanged with $TiCl_4(THF)_4$ in DMF solution. Zr-Ti-UiO-66 showed good crystallinity and displayed similar porous nature to intact Zr-UiO-66.[51] More recently, Brozek et al. applied this strategy to partially exchange the Zn^{2+} ions in MOF-5 with Ti^{3+}, $V^{2+/3+}$, $Cr^{2+/3+}$, Mn^{2+}, and Fe^{2+} ions. Notably, Cr^{2+} and Fe^{2+} metal centers showed redox reactivity in the MOF-5 framework.[52]

Determination of the spatial arrangements of mixed-metal centers in MM-MOFs has not been greatly pursued in the literature. Howe et al.[53] used a combination of density functional theory (DFT) simulation and paired distribution function analysis on Mg-Ni-MOF-74 and Mg-Cd-MOF-74. They concluded that the mixed-metal arrangement within these systems is dispersive/well-mixed. Similar trend was also observed in mixed-metal

porphyrin-based MOFs by studies of X-ray photoelectron spectroscopy and UV-vis diffuse reflectance spectra.[54]

Interestingly, in some cases, MM-MOFs exhibit improvements in certain textural properties compared to their parent MOFs. Higher surface areas were recorded by Botas et al.[55] during their study on the effect of changing Zn-Co ratio in mixed-metal MOF-74 materials. Kahr et al.[56] also obtained greater surface areas after incorporating Ni into Mg-MOF-74. This was attributed to the surface modification of Ni, which can better maintain the coordinative geometry than Mg during removal of the coordinated solvent. The retained surface crystallinity and permeability can lead to a better accessibility to the internal pore space. Additionally, MM-MOFs display advanced performance in adsorption and separations applications. Through the development of a Cd-Cu based framework, Das et al.[57] not only achieved a highly selective separation of chiral molecules (1-phenylethanol, 2-butanol, and 2-pentanol), but also obtained a highly selective separation of achiral C_2H_2/C_2H_4 molecules. A Zn-Cu-BTC MOF exhibited superior adsorption capacity of dibenzothiophene to that of Cu-BTC.[58] More recently, some studies have addressed the advantages of mixed-metal strategy for developing high-performance materials in some emerging applications such as heterogeneous catalysis, luminescence, and electrical energy storage.[59-65] Although many features of MM-MOFs have been demonstrated, there are still some unsolved issues:

i) What is the incorporating behavior of multiple metal centers from starting solutions into MM-MOF framework?

ii) How might mixed-metal centers differ in how they interact with gas molecules during adsorption processes compared to how they interact in a pure MOF?

iii) What is the effect of mixed-metal centers on the chemical stability of the MM-MOFs, especially water stability?

1.2.2 Defective MOFs with Missing Linkers and Clusters

Missing linker and missing cluster defects, are another important defects that are formed during growth of MOF crystals.[32] Organic ligands can be substituted by negatively charged groups or anions intentionally or naturally, generating missing linker defects. Recent works have also shown that the entire metal clusters can become excluded from the framework as well, leading to the formation of missing cluster defects.[66, 67]

There are two contrasting approaches that can be used to generate missing linker or missing cluster defects in MOF structures intentionally. One approach aims to incorporate such defects into MOFs from starting solutions, containing a mixture of competing ligands (crystallization modulators) and original organic ligands.[68] For instance, Wu et al. reported that acid modulators would associate with metal clusters, resulting in the formation of missing linker defects in UiO-66. In their work, high-resolution neutron power diffraction was collected to provide the first direct structural evidence for the existence of missing linker defects.[69] Furthermore, Shearer et al. conducted a comprehensive investigation into the defect chemistry of UiO-type MOFs using various monocarboxylic acid modulators (acetic acid, formic acid, difluoroacetic acid, and trifluoroacetic acid).[67] They demonstrated that missing cluster defects are the dominant defect when employing acid modulators,

which is in agreement with the observation of Cliffe's work.[66] In addition, several works revealed that the quantity of defects in MOF structures can be manipulated by altering the concentration of modulators in the starting solutions. [69-71]

A second approach, which is called post-synthetic treatment has been employed to introduce missing linkers or missing clusters into preformed MOFs. For example, Vermoortele et al. discovered that the benzenetricarboxylate ligands in MIL-100(Fe) could be re-protonated when being treated with CF_3COOH or $HClO_4$. As evidenced by CO-chemisorption, this acid treatment can introduce a large amount of missing linker defects, as well as the Lewis acid sites into MIL-100(Fe) networks.[72] Using single-crystal X-ray diffraction, Tu et al. demonstrated that the ordered missing cluster defects could be created in a cubic MOF $[Zn_4O(PyC)_3]$ (PyC=4-pyrazolecarboxylate) after immersing into water for 24h.[73] Recent studies have additionally demonstrated that missing linker or missing cluster defects could be introduced in MOF structures through thermal treatment at high temperatures. This unusual behavior was confirmed by a combination of thermogravimetric analysis/mass spectrometry (TGA-MS), X-ray photoelectron spectroscopy (XPS) and surface area analysis.[74, 75]

Missing linker and missing cluster defects have significant effects on the physical/chemical properties of defective MOFs.[33, 76-78] For example, using trifluoroacetic acid (TFA) as the crystallization modulator, Jiang et al. successfully synthesized sulfone-functionalized MOFs (USTC-253-TFA) with missing linker defects. The resulting crystals exhibited an increased CO_2 adsorption capacity (167%) in comparison to their pristine versions.[79] Furthermore, the synthesis of highly stable UiO-66 with missing cluster defects was established through a facile modulator-induced defect-formation approach. The

defective crystals not only efficiently captured the large molecules (metalloporphyrin and phosphotungstic acid), barely capturing by the pristine UiO-66, but also exhibited superior catalytic activity to their pristine analogs.[80] Recently, it was reported that the defective UiO-66-NH_2 with missing linker defects were capable of capturing alkyl phosphonate compounds (nerve agent) in both dry and humid conditions elucidating the great potential of defective UiO-66 type MOFs for next-generation chemical sensors.[81] Through controlling the generation of missing linker defects, Taylor et al. were able to increase the proton mobility of UiO-66, resulting in a pronounced enhancement in the proton conductivity by 3 orders of magnitude. The increased proton mobility was attributed to the increases in the pore volume of defective UiO-66.[39] This remarkable improvement indicates the potential of defective MOFs for fuel-cell applications. In the past years, notable studies have been devoted to manipulating the physical/chemical properties of MOFs by introducing a wide variety of defects in the structures. Among these studies, there still exist some open questions:

i) What are the changes in textural properties (pore size or opening channel) of defective MOFs?

ii) How do defects impact the chemical stability of MOFs?

1.3 MOF Derivatives for Electrical Energy Storage (Supercapacitors)

Supercapacitors (SCs) have become one of the most important energy storage devices with distinguished electrochemical performance such as high power density, rapid charging capability and long cyclelife.[82] Because of these interesting properties, SCs have been considered as promising candidates for a wide range of applications, involving

electric vehicles, portable devices and smart grids. Nowadays, electrical double-layer capacitors (EDLCs) (e.g. activated carbon materials) are widely used in commercial markets. Although EDLCs show excellent cycling stability, their relatively low capacitance limits their pragmatic applicability.[83, 84] Hybrid SCs, which consist of a battery-type electrode (transition metal compounds) and a capacitive electrode (carbon materials), open up a new perspective for developing next-generation SCs. Although sacrificing the cycling stability to some extent, hybrid SCs still exhibit much higher capacitance and wider operating voltage in comparison to EDLCs.[85, 86]

It is well known that the pore structure and morphology of electrode materials have pronounced effects on the electrochemical performance of energy storage devices such as capacitance and rate capability.[87, 88] Therefore, MOFs have been regarded as the promising precursors of electrode materials due to their highly porous frameworks and uniformed morphology. Using MOFs as the template, many studies have been devoted to developing MOF-derived materials with ordered structures (usually porous carbons, metal oxides, and metal hydroxides).[89, 90] By applying the appropriate carbonization temperature on an Al based MOF, Hu et al. successfully fabricated the nanostructured carbon with extremely large pore volume of 4.4 cm^3/g. It was reported that a core-shell structure of nitrogen-doped carbon and graphitic carbon was obtained by pyrolyzing core-shell ZIFs under inert conditions. Compared to conventional carbons, this unique hybrid carbon exhibited a remarkably high specific capacitance of 270 F g^{-1} at a current density of 2 A g^{-1}.[91] Very recently, Pachfule et al. added KOH treatment and thermal activation after carbonization of MOF-74 and produced graphene nanoribbons with excellent electrochemical performance. The obtained graphene nanoribbons showed a distinguished rate capability

with only 16% decrease when increasing current density from 1 to 10 A g^{-1}.[92] A porous reduced graphene oxide (rGO)-MoO_3 electrode material was achieved after a two-step annealing process. Taken rGO-MoO_3 as the electrodes, the assembled SCs performed a high specific capacitance of 404 F g^{-1} at a current density of 0.5 A g^{-1}.[93] Cao et al. fabricated two-dimensional (2-D) nanocomposites of $CoS_{1.097}$ and carbon through a simultaneous sulfidation and carbonization of 2-D Co based MOFs. Assembled into SCs, the resulting nanocomposites exhibited an excellent rate capability with only 43.2% drop, changing from 1.5 to 30 A g^{-1}.[94] Because of their controlled morphology and structure, MOF-derived materials have emerged as attractive candidates for synthesizing high-performance electrode materials. This work aims to extend the study of these MOF-derived materials through two objectives:

i) Is there any relationship between the chemical stability of MOF templates and the electrochemical performance of MOF-derived electrodes, particularly cycling stability?

ii) Can we synthesize both positive and negative electrode materials from a single MOF precursor and improve the electrochemical performance of energy storage devices?

1.4 Dissertation Scope

Overall, two major advances are discussed in this dissertation:

i) Investigate the effects of defects (mixed-metal centers and missing clusters) on MOFs to advance the fundamental understanding of these structural

features and to both engineer and design next-generation defective MOFs for adsorption process.

ii) Develop the knowledge and methods required to unravel the connections between MOFs and MOF-derived materials and drive the future development of MOF-derived materials for electrical energy storage devices.

In this dissertation, I have developed and completed the following studies to address the key questions discussed in this chapter. In chapter 3, MOF-74 was selected as the platform to examine the effects of mixed-metal centers on both CO_2 adsorption and water stability properties. The incorporating behavior of mixed-metal centers was elucidated through systematically designed experiments. In chapter 4, UiO-66 was utilized as the template to explore the impact of missing linker/cluster defects on defective UiO-66. The structural changes (pore size/opening channel) of defective UiO-66 were examined through studies where various adsorbate molecules were used to determine the difference between pristine and defective UiO-66. Altering the concentration and bonding condition of defects, the chemical stability of defective UiO-66 was evaluated. In chapter 5, ligand functionalization strategy was applied to DMOF system in order to probe the correlation between the chemical stability of DMOFs and the cycling stability of MOF-derived electrodes. In chapter 6, a MOF-rGO composite was synthesized solvothermally. Both positive and negative electrode materials were prepared using MOF-rGO composite as the starting material. The structural features and the electrochemical performance of obtained electrodes were comprehensively studied via complimentary experimental approaches.

Chapter 7 presents the summary of this dissertation and proposes the future challenges that can be addressed to advance the understanding in MOFs or MOF-related materials.

1.5 References

1. Rouquerol, J.; Avnir, D.; Fairbridge, C. W.; Everett, D. H.; Haynes, J. H.; Pernicone, N.; Ramsay, J. D. F.; Sing, K. S. W.; Unger, K. K., *Pure Appl. Chem.* **1994**, *66* (8), 1739-1758.

2. Morris, R. E.; Wheatley, P. S., *Angew. Chem. Int. Ed.* **2008**, *47* (27), 4966-4981.

3. Boyd, G. E.; Adamson, A. W.; Myers, L. S., *J. Am. Chem. Soc.* **1947**, *69* (11), 2836-2848.

4. Davis, M. E., *Nature* **2002**, *417* (6891), 813-821.

5. Wang, S. B.; Peng, Y. L., *Chem. Eng. J.* **2010**, *156* (1), 11-24.

6. Crini, G., *Bioresour. Technol.* **2006**, *97* (9), 1061-1085.

7. Dusenbury, J. S.; Cannon, F. S., *Carbon* **1996**, *34* (12), 1577-1589.

8. Seredych, M.; Lison, J.; Jans, U.; Bandosz, T. J., *Carbon* **2009**, *47* (10), 2491-2500.

9. Yaghi, O. M.; O'Keeffe, M.; Ockwig, N. W.; Chae, H. K.; Eddaoudi, M.; Kim, J., *Nature* **2003**, *423* (6941), 705-714.

10. Schoedel, A.; Li, M.; Li, D.; O'Keeffe, M.; Yaghi, O. M., *Chem. Rev.* **2016**, *116* (19), 12466-12535.

11. Li, J. R.; Kuppler, R. J.; Zhou, H. C., *Chem. Soc. Rev.* **2009**, *38* (5), 1477-1504.

12. Stock, N.; Biswas, S., *Chem. Rev.* **2012**, *112* (2), 933-969.

13. Furukawa, H.; Cordova, K. E.; O'Keeffe, M.; Yaghi, O. M., *Science* **2013**, *341* (6149), 974-975.

14. Database of Zeolite Structures. Structure Commission of the International Zeolite Association: 2017.

15. Farha, O. K.; Eryazici, I.; Jeong, N. C.; Hauser, B. G.; Wilmer, C. E.; Sarjeant, A. A.; Snurr, R. Q.; Nguyen, S. T.; Yazaydin, A. O.; Hupp, J. T., *J. Am. Chem. Soc.* **2012**, *134* (36), 15016-15021.

16. Eddaoudi, M.; Kim, J.; Rosi, N.; Vodak, D.; Wachter, J.; O'Keeffe, M.; Yaghi, O. M., *Science* **2002**, *295* (5554), 469-472.

17. Furukawa, H.; Go, Y. B.; Ko, N.; Park, Y. K.; Uribe-Romo, F. J.; Kim, J.; O'Keeffe, M.; Yaghi, O. M., *Inorg. Chem.* **2011**, *50* (18), 9147-9152.

18. Deng, H. X.; Grunder, S.; Cordova, K. E.; Valente, C.; Furukawa, H.; Hmadeh, M.; Gandara, F.; Whalley, A. C.; Liu, Z.; Asahina, S.; Kazumori, H.; O'Keeffe, M.; Terasaki, O.; Stoddart, J. F.; Yaghi, O. M., *Science* **2012**, *336* (6084), 1018-1023.

19. Yu, J.; Xie, L. H.; Li, J. R.; Ma, Y.; Seminario, J. M.; Balbuena, P. B., *Chem. Rev.* **2017**, doi: 10.1021/acs.chemrev.6b00626.

20. Mason, J. A.; Veenstra, M.; Long, J. R., *Chem. Sci.* **2014**, *5* (1), 32-51.

21. Brozek, C. K.; Dinca, M., *Chem. Soc. Rev.* **2014**, *43* (16), 5456-5467.

22. Horcajada, P.; Gref, R.; Baati, T.; Allan, P. K.; Maurin, G.; Couvreur, P.; Ferey, G.; Morris, R. E.; Serre, C., *Chem. Rev.* **2012**, *112* (2), 1232-1268.

23. Hu, Z. C.; Deibert, B. J.; Li, J., *Chem. Soc. Rev.* **2014**, *43* (16), 5815-5840.

24. Liu, J. W.; Chen, L. F.; Cui, H.; Zhang, J. Y.; Zhang, L.; Su, C. Y., *Chem. Soc. Rev.* **2014**, *43* (16), 6011-6061.

25. Kreno, L. E.; Leong, K.; Farha, O. K.; Allendorf, M.; Van Duyne, R. P.; Hupp, J. T., *Chem. Rev.* **2012**, *112* (2), 1105-1125.

26. Li, S. L.; Xu, Q., *Energy Environ. Sci.* **2013**, *6* (6), 1656-1683.

27. Bollmann, W., *Crystal Defects and Crystalline Interfaces*. 1st ed.; Springer-Verlag Berlin Heidelberg: Berlin, 1970.

28. Seker, F.; Meeker, K.; Kuech, T. F.; Ellis, A. B., *Chem. Rev.* **2000**, *100* (7), 2505-2536.

29. Campbell, S. A., *Fabrication Engineering at the Micro - and Nanoscale*. 4th ed.; Oxford University Press: New York, 2013.

30. Paier, J.; Penschke, C.; Sauer, J., *Chem. Rev.* **2013**, *113* (6), 3949-3985.

31. Sholl, D. S.; Lively, R. P., *J. Phys. Chem. Lett.* **2015**, *6* (17), 3437-3444.

32. Cheetham, A. K.; Bennett, T. D.; Coudert, F. X.; Goodwin, A. L., *Dalton Trans.* **2016**, *45* (10), 4113-4126.

33. Fang, Z. L.; Bueken, B.; De Vos, D. E.; Fischer, R. A., *Angew. Chem. Int. Ed.* **2015**, *54* (25), 7234-7254.

34. Thornton, A. W.; Babarao, R.; Jain, A.; Trousselet, F.; Coudert, F. X., *Dalton Trans.* **2016**, *45* (10), 4352-4359.

35. Song, L. F.; Zhang, J.; Sun, L. X.; Xu, F.; Li, F.; Zhang, H. Z.; Si, X. L.; Jiao, C. L.; Li, Z. B.; Liu, S.; Liu, Y. L.; Zhou, H. Y.; Sun, D. L.; Du, Y.; Cao, Z.; Gabelica, Z., *Energy Environ. Sci.* **2012**, *5* (6), 7508-7520.

36. Huang, H. L.; Li, J. R.; Wang, K. K.; Han, T. T.; Tong, M. M.; Li, L. S.; Xie, Y. B.; Yang, Q. Y.; Liu, D. H.; Zhong, C. L., *Nat. Commun.* **2015**, *6*, 8847.

37. Vermoortele, F.; Vandichel, M.; Van de Voorde, B.; Ameloot, R.; Waroquier, M.; Van Speybroeck, V.; De Vos, D. E., *Angew. Chem. Int. Ed.* **2012**, *51* (20), 4887-4890.

38. Katz, M. J.; Klet, R. C.; Moon, S. Y.; Mondloch, J. E.; Hupp, J. T.; Farha, O. K., *ACS Catal.* **2015**, *5* (8), 4637-4642.

39. Taylor, J. M.; Dekura, S.; Ikeda, R.; Kitagawa, H., *Chem. Mater.* **2015**, *27* (7), 2286-2289.

40. Furukawa, H.; Muller, U.; Yaghi, O. M., *Angew. Chem. Int. Ed.* **2015**, *54* (11), 3417-3430.

41. Deng, H. X.; Doonan, C. J.; Furukawa, H.; Ferreira, R. B.; Towne, J.; Knobler, C. B.; Wang, B.; Yaghi, O. M., *Science* **2010**, *327* (5967), 846-850.

42. Jiang, W. C.; Yu, D. S.; Zhang, Q.; Goh, K. L.; Wei, L.; Yong, Y. L.; Jiang, R. R.; Wei, J.; Chen, Y., *Adv. Funct. Mater.* **2015**, *25* (7), 1063-1073.

43. Yuan, S.; Lu, W. G.; Chen, Y. P.; Zhang, Q.; Liu, T. F.; Feng, D. W.; Wang, X.; Qin, J. S.; Zhou, H. C., *J. Am. Chem. Soc.* **2015**, *137* (9), 3177-3180.

44. Burrows, A. D., *Crystengcomm* **2011**, *13* (11), 3623-3642.

45. Chen, B. L.; Fronczek, F. R.; Maverick, A. W., *Inorg. Chem.* **2004**, *43* (26), 8209-8211.

46. Kozachuk, O.; Meilikhov, M.; Yusenko, K.; Schneemann, A.; Jee, B.; Kuttatheyil, A. V.; Bertmer, M.; Sternemann, C.; Poppl, A.; Fischer, R. A., *Eur. J. Inorg. Chem.* **2013**, *2013* (26), 4546-4557.

47. Kozachuk, O.; Khaletskaya, K.; Halbherr, M.; Betard, A.; Meilikhov, M.; Seidel, R. W.; Jee, B.; Poppl, A.; Fischer, R. A., *Eur. J. Inorg. Chem.* **2012**, (10), 1688-1695.

48. Wang, L. J.; Deng, H. X.; Furukawa, H.; Gandara, F.; Cordova, K. E.; Peri, D.; Yaghi, O. M., *Inorg. Chem.* **2014**, *53* (12), 5881-5883.

49. Kahr, J.; Morris, R. E.; Wright, P. A., *Crystengcomm* **2013**, *15* (45), 9779-9786.

50. Evans, J. D.; Sumby, C. J.; Doonan, C. J., *Chem. Soc. Rev.* **2014**, *43* (16), 5933-5951.

51. Kim, M.; Cahill, J. F.; Fei, H. H.; Prather, K. A.; Cohen, S. M., *J. Am. Chem. Soc.* **2012**, *134* (43), 18082-18088.

52. Brozek, C. K.; Dinca, M., *J. Am. Chem. Soc.* **2013**, *135* (34), 12886-12891.

53. Howe, J. D.; Morelock, C. R.; Jiao, Y.; Chapman, K. W.; Walton, K. S.; Sholl, D. S., *J. Phys. Chem. C* **2017**, *121* (1), 627-635.

54. Liu, Q.; Cong, H. J.; Deng, H. X., *J. Am. Chem. Soc.* **2016**, *138* (42), 13822-13825.

55. Botas, J. A.; Calleja, G.; Sanchez-Sanchez, M.; Orcajo, M. G., *Int. J. Hydrogen Energy* **2011**, *36* (17), 10834-10844.

56. Kahr, J.; Morris, R. E.; Wright, P. A., *CrystEngComm* **2013**, *15* (45), 9779.

57. Das, M. C.; Guo, Q. S.; He, Y. B.; Kim, J.; Zhao, C. G.; Hong, K. L.; Xiang, S. C.; Zhang, Z. J.; Thomas, K. M.; Krishna, R.; Chen, B. L., *J. Am. Chem. Soc.* **2012**, *134* (20), 8703-8710.

58. Wang, T. T.; Li, X. X.; Dai, W.; Fang, Y. Y.; Huang, H., *J. Mater. Chem. A* **2015**, *3* (42), 21044-21050.

59. Dhakshinamoorthy, A.; Asiri, A. M.; Garcia, H., *Catal. Sci. Tech.* **2016**, *6* (14), 5238-5261.

60. Sun, D. R.; Sun, F. X.; Deng, X. Y.; Li, Z. H., *Inorg. Chem.* **2015**, *54* (17), 8639-8643.

61. Lee, Y.; Kim, S.; Kang, J. K.; Cohen, S. M., *Chem. Commun.* **2015**, *51* (26), 5735-5738.

62. Cui, Y. J.; Xu, H.; Yue, Y. F.; Guo, Z. Y.; Yu, J. C.; Chen, Z. X.; Gao, J. K.; Yang, Y.; Qian, G. D.; Chen, B. L., *J. Am. Chem. Soc.* **2012**, *134* (9), 3979-3982.

63. Ferey, G.; Millange, F.; Morcrette, M.; Serre, C.; Doublet, M. L.; Greneche, J. M.; Tarascon, J. M., *Angew. Chem. Int. Ed.* **2007**, *46* (18), 3259-3263.

64. Choi, K. M.; Jeong, H. M.; Park, J. H.; Zhang, Y. B.; Kang, J. K.; Yaghi, O. M., *ACS Nano* **2014**, *8* (7), 7451-7457.

65. Yang, J.; Zheng, C.; Xiong, P. X.; Li, Y. F.; Wei, M. D., *J. Mater. Chem. A* **2014**, *2* (44), 19005-19010.

66. Cliffe, M. J.; Wan, W.; Zou, X. D.; Chater, P. A.; Kleppe, A. K.; Tucker, M. G.; Wilhelm, H.; Funnell, N. P.; Coudert, F. X.; Goodwin, A. L., *Nat. Commun.* **2014**, *5*, 4176.

67. Shearer, G. C.; Chavan, S.; Bordiga, S.; Svelle, S.; Olsbye, U.; Lillerud, K. P., *Chem. Mater.* **2016**, *28* (11), 3749-3761.

68. Vermoortele, F.; Bueken, B.; Le Bars, G.; Van de Voorde, B.; Vandichel, M.; Houthoofd, K.; Vimont, A.; Daturi, M.; Waroquier, M.; Van Speybroeck, V.; Kirschhock, C.; De Vos, D. E., *J. Am. Chem. Soc.* **2013**, *135* (31), 11465-11468.

69. Wu, H.; Chua, Y. S.; Krungleviciute, V.; Tyagi, M.; Chen, P.; Yildirim, T.; Zhou, W., *J. Am. Chem. Soc.* **2013**, *135* (28), 10525-10532.

70. Gutov, O. V.; Hevia, M. G.; Escudero-Adan, E. C.; Shafir, A., *Inorg. Chem.* **2015**, *54* (17), 8396-8400.

71. Vandichel, M.; Hajek, J.; Vermoortele, F.; Waroquier, M.; De Vos, D. E.; Van Speybroeck, V., *Crystengcomm* **2015**, *17* (2), 395-406.

72. Vermoortele, F.; Ameloot, R.; Alaerts, L.; Matthessen, R.; Carlier, B.; Fernandez, E. V. R.; Gascon, J.; Kapteijn, F.; De Vos, D. E., *J. Mater. Chem.* **2012**, *22* (20), 10313-10321.

73. Tu, B. B.; Pang, Q. Q.; Wu, D. F.; Song, Y. N.; Weng, L. H.; Li, Q. W., *J. Am. Chem. Soc.* **2014**, *136* (41), 14465-14471.

74. Valvekens, P.; Jonckheere, D.; De Baerdemaeker, T.; Kubarev, A. V.; Vandichel, M.; Hemelsoet, K.; Waroquier, M.; Van Speybroeck, V.; Smolders, E.; Depla, D.; Roeffaers, M. B. J.; De Vos, D., *Chem. Sci.* **2014**, *5* (11), 4517-4524.

75. Gadipelli, S.; Guo, Z. X., *Chem. Mater.* **2014**, *26* (22), 6333-6338.

76. Bennett, T. D.; Cheetham, A. K.; Fuchs, A. H.; Coudert, F. X., *Nat. Chem.* **2017**, *9* (1), 11-16.

77. Canivet, J.; Vandichel, M.; Farrusseng, D., *Dalton Trans.* **2016**, *45* (10), 4090-4099.

78. Ramaswamy, P.; Wong, N. E.; Shimizu, G. K. H., *Chem. Soc. Rev.* **2014**, *43* (16), 5913-5932.

79. Jiang, Z. R.; Wang, H. W.; Hu, Y. L.; Lu, J. L.; Jiang, H. L., *Chemsuschem* **2015**, *8* (5), 878-885.

80. Cai, G. R.; Jiang, H. L., *Angew. Chem. Int. Ed.* **2017**, *56* (2), 563-567.

81. Stassen, I.; Bueken, B.; Reinsch, H.; Oudenhoven, J. F. M.; Wouters, D.; Hajek, J.; Van Speybroeck, V.; Stock, N.; Vereecken, P. M.; Van Schaijk, R.; De Vos, D.; Ameloot, R., *Chem. Sci.* **2016**, *7* (9), 5827-5832.

82. Wang, G. P.; Zhang, L.; Zhang, J. J., *Chem. Soc. Rev.* **2012**, *41* (2), 797-828.

83. El-Kady, M. F.; Strong, V.; Dubin, S.; Kaner, R. B., *Science* **2012**, *335* (6074), 1326-1330.

84. Chmiola, J.; Largeot, C.; Taberna, P. L.; Simon, P.; Gogotsi, Y., *Science* **2010**, *328* (5977), 480-483.

85. Wang, Q.; Wen, Z. H.; Li, J. H., *Adv. Funct. Mater.* **2006**, *16* (16), 2141-2146.

86. Dai, S.; Zhao, B.; Qu, C.; Chen, D. C.; Dang, D.; Song, B.; Deglee, B. M.; Fu, J. W.; Hu, C. G.; Wong, C. P.; Liu, M. L., *Nano Energy* **2017**, *33*, 522-531.

87. Lang, X. Y.; Hirata, A.; Fujita, T.; Chen, M. W., *Nat. Nanotechnol.* **2011**, *6* (4), 232-236.

88. Winter, M.; Brodd, R. J., *Chem. Rev.* **2004**, *104* (10), 4245-4269.

89. Wang, H. L.; Zhu, Q. L.; Zou, R. Q.; Xu, Q., *Chem* **2017**, *2* (1), 52-80.

90. Cao, X.; Tan, C.; Sindoro, M.; Zhang, H., *Chem. Soc. Rev.* **2017,** *46* (10), 2660-2677.

91. Tang, J.; Salunkhe, R. R.; Liu, J.; Torad, N. L.; Imura, M.; Furukawa, S.; Yamauchi, Y., *J. Am. Chem. Soc.* **2015**, *137* (4), 1572-1580.

92. Pachfule, P.; Shinde, D.; Majumder, M.; Xu, Q., *Nat. Chem.* **2016**, *8* (7), 718-724.

93. Cao, X. H.; Zheng, B.; Shi, W. H.; Yang, J.; Fan, Z. X.; Luo, Z. M.; Rui, X. H.; Chen, B.; Yan, Q. Y.; Zhang, H., *Adv. Mater.* **2015**, *27* (32), 4695-4701.

94. Cao, F. F.; Zhao, M. T.; Yu, Y. F.; Chen, B.; Huang, Y.; Yang, J.; Cao, X. H.; Lu, Q. P.; Zhang, X.; Zhang, Z. C.; Tan, C. L.; Zhang, H., *J. Am. Chem. Soc.* **2016**, *138* (22), 6924-6927.

CHAPTER 2. MATERIALS AND METHODS

MOFs studies in this dissertation were synthesized solvothermally, according to reported procedures or with some minor changes. The general background and standard synthesis method of each MOF candidate are presented in this chapter. In general, all the MOFs discussed in this dissertation can be identified as following three well-known and highly porous MOF structures: M-MOF-74/M-CPO-27/M_2(DOBDC), UiO-66, and DMOF-X/Ni-XDC-DABCO. For ease of reference, the detailed synthesis methods and characterization are not included in this chapter, but are provided in the experimental section of each chapter accordingly.

2.1 M-MOF-74/M-CPO-27/M_2(DOBDC)

This is a well-known series of isostructural MOFs, where M = Zn, Mg, Ni, Co, Fe, Mn, or Cu.[1] The MOF-74 structure features one-dimensional metal oxide chains containing divalent metal cations that are interconnected by $DOBDC^{4-}$ ligands ($DOBDC^{4-}$ = 2,5-dioxido-1,4-benzenedicarboxylate), resulting in an array of one-dimensional hexagonal opening channels with width of 11 Å in diameter. The MOF-74 structure is illustrated in Figure 2.1. MOF-74 has been of great interest due to its highly tailorable metal centers/linkers and exceptional gas uptake, particularly in CO_2 capture.[1-6] Containing high density of coordinatively unsaturated (CUS) metal centers,[7] MOF-74 was selected as the initial candidate for studying the effect of metal substitution on gas adsorption and framework stability.

The synthesis was based on a published procedure by Glover.[8] The metal nitrate salts and the H_4DOBDC ligand were dissolved in a solvent mixture of dimethylformamide (DMF), ethanol, and water. The solution was stirred for 3 h. The solution was transferred into a sealed glass vial and heated for various hours. Solvent volume ratios, reaction temperature, and timing vary for distinct analogs. After cooling, the as-synthesized crystals were washed four times with fresh DMF and exchanged four times over four days with fresh methanol. The solvent exchanged crystals were stored under methanol at room temperature for further experiments. In this dissertation, eight distinct MM-MOF-74 were synthesized by incorporating various amounts of Co and Ni into the Mg-MOF-74. The detailed procedures of MM-MOF-74 are described in chapter 3 and Appendix A.

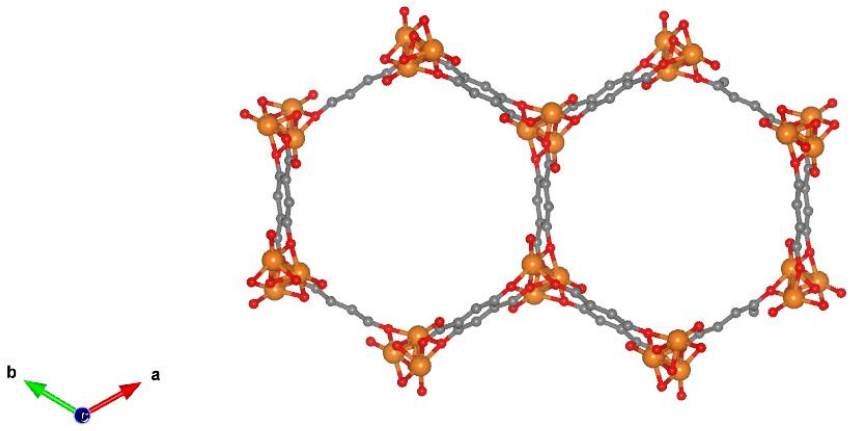

Figure 2.1. Wireframe view of M-MOF-74. Orange: metal centers; Red: oxygen; Grey: carbon and H atoms are omitted for clarity.

2.2 UiO-66

UiO-66 ($Zr_6(OH)_4O_4(BDC)_6$, BDC = 1,4- benzenedicarboxylate), first reported by Cavka et al.[9] in 2008, is a zirconium (IV) based MOF. It has highly stable inorganic metal clusters ($Zr_6(OH)_4O_4$) which are connected by twelve 1,4-benzenedicarboxylic acid (BDC) ligands, resulting in a three-dimensional porous network with 6 Å micropores. The UiO-66 structure is shown in Figure 2.2. Owing to its high coordination numbers, UiO-66 exhibits exceptional thermal, chemical, and mechanical stabilities.[10, 11] Furthermore, 12 coordinated UiO-66 allows the introduction of an unusually high degree of defects without causing structural collapse.[12] Due to its unusual tolerance for defect concentrations, UiO-66 was chosen as the material platform in this dissertation for investigating the impact of defects on the chemical stability and the gas adsorption of defective MOFs.

The synthesis recipe was adapted from a previous study by Cavka.[9] The $ZrCl_4$ and BDC were added into DMF solvent. The solution was continuously sonicated until homogeneous. The solution was placed into a sealed Teflon reactor and transferred to a pre-heated oven at 120 °C. The as-synthesized crystals were obtained after 24 h. The crystals were washed by DMF and methanol abundantly to remove the unreacted species. The crystals were dried at ambient condition before use. In this dissertation, four distinct defective UiO-66 with varying concentrations of defects were obtained, adding different amount of acid modulators (trifluoroacetic acid, TFA)[13] within the starting synthesis solution. The detailed methods of synthesizing defective UiO-66 are provided in chapter 4.

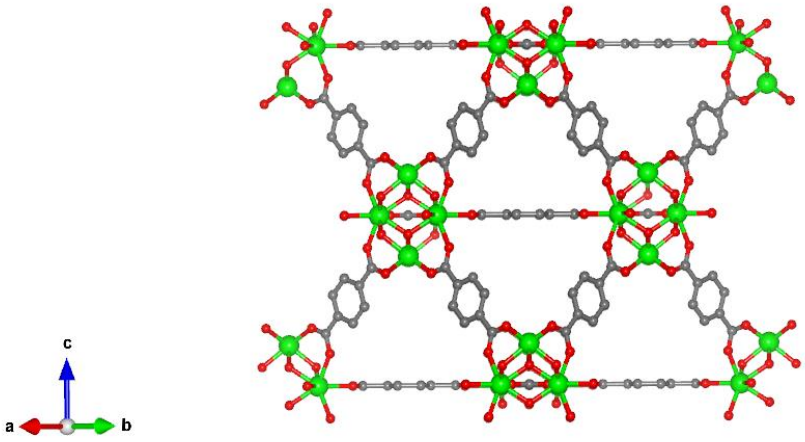

Figure 2.2: Wireframe view of UiO-66. Green: zirconium; Red: oxygen; Grey: carbon and H atoms are omitted for clarity.

2.3 DMOF-X/Ni-XDC-DABCO

Non-catenated pillared MOFs (DMOF-X) consists of paddlewheel Ni clusters that are coordinated by four dicarboxylic ligands (XDC) to generate two-dimensional layers. Each layer is connected to each other by 1,4-diazabicyclo[2.2.2]octane (DABCO) ligand, leading to a three-dimensional framework.[14] The DMOF framework is displayed in Figure 2.3. As a result of its highly tailorable structure,[15] ligand functionalization was applied to this isostructural system for studying the correlation between chemical stability and electrochemical performance.

The synthesis procedure was modified from a published literature.[10] The nickel nitrate salts, XDC, and DABCO were dissolved into DMF solvent. The solution was continuously stirred for 2 h. The mixture was poured into a sealed glass vial and kept in a

preheated oven at 120 °C for 48 h. Once cooled, the resulting crystals were filtered and washed with DMF and methanol repeatedly. The prepared crystals were dried under air at room temperature prior to further experiments. In this dissertation, three dicarboxylic acids 1,4-naphthalenedicarboxylic acid (NDC), 2,3,5,6-tetramethyl-1,4-benzenedicarboxylic acid (TM), and 9,10-anthracenedicarboxylic acid (ADC) were used to synthesize Ni based DMOFs. The detailed synthesis of Ni-DMOF-XDC can be found in chapter 5.

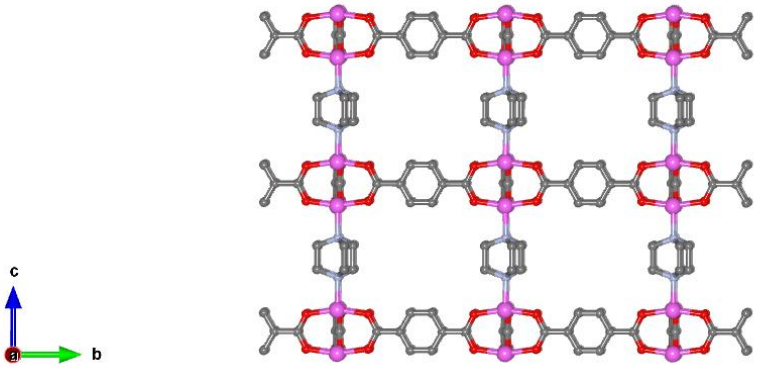

Figure 2.3: Wireframe view of Ni-XDC-DABCO. Pink: nickel; Red: oxygen; Grey: carbon and H atoms are omitted for clarity.

2.4 References

1. Queen, W. L.; Hudson, M. R.; Bloch, E. D.; Mason, J. A.; Gonzalez, M. I.; Lee, J. S.; Gygi, D.; Howe, J. D.; Lee, K.; Darwish, T. A.; James, M.; Peterson, V. K.; Teat, S. J.; Smit, B.; Neaton, J. B.; Long, J. R.; Brown, C. M., *Chem. Sci.* **2014**, *5* (12), 4569-4581.

2. Wang, L. J.; Deng, H. X.; Furukawa, H.; Gandara, F.; Cordova, K. E.; Peri, D.; Yaghi, O. M., *Inorg. Chem.* **2014**, *53* (12), 5881-5883.

3. Deng, H. X.; Grunder, S.; Cordova, K. E.; Valente, C.; Furukawa, H.; Hmadeh, M.; Gandara, F.; Whalley, A. C.; Liu, Z.; Asahina, S.; Kazumori, H.; O'Keeffe, M.; Terasaki, O.; Stoddart, J. F.; Yaghi, O. M., *Science* **2012**, *336* (6084), 1018-1023.

4. Britt, D.; Furukawa, H.; Wang, B.; Glover, T. G.; Yaghi, O. M., *Proc. Natl. Acad. Sci. U.S.A.* **2009**, *106* (49), 20637-20640.

5. Mason, J. A.; Sumida, K.; Herm, Z. R.; Krishna, R.; Long, J. R., *Energy Environ. Sci.* **2011**, *4* (8), 3030-3040.

6. Sumida, K.; Rogow, D. L.; Mason, J. A.; McDonald, T. M.; Bloch, E. D.; Herm, Z. R.; Bae, T. H.; Long, J. R., *Chem. Rev.* **2012**, *112* (2), 724-781.

7. Lin, L. C.; Kim, J.; Kong, X. Q.; Scott, E.; McDonald, T. M.; Long, J. R.; Reimer, J. A.; Smit, B., *Angew. Chem. Int. Ed.* **2013**, *52* (16), 4410-4413.

8. Glover, T. G.; Peterson, G. W.; Schindler, B. J.; Britt, D.; Yaghi, O., *Chem. Eng. Sci.* **2011**, *66* (2), 163-170.

9. Cavka, J. H.; Jakobsen, S.; Olsbye, U.; Guillou, N.; Lamberti, C.; Bordiga, S.; Lillerud, K. P., *J. Am. Chem. Soc.* **2008**, *130* (42), 13850-13851.

10. Jasuja, H.; Jiao, Y.; Burtch, N. C.; Huang, Y. G.; Walton, K. S., *Langmuir* **2014**, *30* (47), 14300-14307.

11. Howarth, A. J.; Liu, Y. Y.; Li, P.; Li, Z. Y.; Wang, T. C.; Hupp, J.; Farha, O. K., *Nat. Rev. Mater.* **2016**, *1* (3), 15018.

12. Wu, H.; Chua, Y. S.; Krungleviciute, V.; Tyagi, M.; Chen, P.; Yildirim, T.; Zhou, W., *J. Am. Chem. Soc.* **2013**, *135* (28), 10525-10532.

13. Shearer, G. C.; Chavan, S.; Bordiga, S.; Svelle, S.; Olsbye, U.; Lillerud, K. P., *Chem. Mater.* **2016**, *28* (11), 3749-3761.

14. Burtch, N. C.; Jasuja, H.; Walton, K. S., *Chem. Rev.* **2014**, *114* (20), 10575-10612.

15. DeCoste, J. B.; Peterson, G. W.; Jasuja, H.; Glover, T. G.; Huang, Y. G.; Walton, K. S., *J. Mater. Chem. A* **2013**, *1* (18), 5642-5650.

CHAPTER 3. TUNING THE WATER STABILITY AND ADSORPTION INTERACTIONS OF MG-MOF-74 BY INCORPORATION OF MIXED-METAL CENTERS

This chapter was reproduced from Jiao, Y.; Morelock, C. R.; Burtch, N. C.; Mounfield, W. P.; Hungerford, J. T.; Walton, K. S., "Tuning the kinetic water stability and adsorption interactions of Mg-MOF-74 by partial substitution with Co or Ni" *Industrial & Engineering Chemistry Research*, 2015, volume 54, pages 12408-12414, Copyright 2015, with permission from American Chemical Society.

3.1 Introduction

Metal-organic frameworks (MOFs) are a relatively novel class of porous crystalline materials, constructed by the self-assembly of inorganic metal ions or clusters and organic ligand linkers.[1] This method of construction offers these porous materials nearly unlimited possibilities in terms of pore size, geometry and functionality by changing the combinations of their metal ions or clusters and organic ligands.[2] MOFs have significant advantages over other porous materials due to their exceptionally high surface areas, extremely large porosities, highly uniform pore sizes and tunable structures. With such properties, MOFs may have a promising role in many industrial applications, such as air purification, air separation, gas storage, ion exchange, drug delivery, luminescence, catalysis and chemical sensing.[2-10]

Functionalization of the organic ligand has been often evaluated as a method for tuning the adsorption and stability properties of MOFs. For example, -NH_2 functional

groups are frequently added to MOF linkers to enhance the adsorption interactions of the material with CO_2.[11] Functionalization with methyl groups has been shown to improve the stability of certain MOFs by preventing the adsorption of water near the metal cluster.[12] These methods typically involve the substitution of the ligand used in the parent material with a ligand already functionalized with the desired group. Thus, these groups will be present throughout the structure. Recently, the strategy of multivariate MOFs (MTV-MOFs),[13-15] in which multiple functionalities are introduced into a single MOF network, has attracted much scientific interest. Yaghi and coworkers[13] showed that up to 8 distinct functionalities could be incorporated into a single MOF framework in a one-pot synthesis. More recently, they extended this approach to synthesize MOF-177 with multiple functionalities on the tritopic ligand.[16] Zhou and coworkers[17] applied this method to construct zirconium-based PCN-700, with linkers of various lengths and functionalities.

While many studies have been devoted to manipulating adsorption properties of MOFs by ligand functionalization,[18-22] studies of gas adsorption in isostructural MOFs with the same organic ligand but varying metal nodes are limited.[23] Mishra and co-workers studied the effect of metal node variation on CO, CO_2, CH_4 and N_2 adsorption properties in the DABCO series of MOFs;[24] no significant changes were observed, likely because the metal centers in DABCO series of MOFs are not coordinatively unsaturated. However, the M/DOBDC family of isostructural MOFs (also known as MOF-74 or CPO-27),[25-30] containing coordinatively unsaturated (CUS) metal centers, is a strong candidate for studying the effect of metal substitution on adsorption energy. The metal nodes in MOF-74 are coordinated to five oxygen atoms of the carboxylate and hydroxyl groups of the 2,5-dioxido-1,4-benzenedicarboxylic acid (DOBDC) ligands. The solvent molecule (DMF or

water), occupying the sixth coordinative position, can be removed via heating under vacuum, thus generating CUS metal centers.

Applying the multivariate approach to metal centers is more complicated than ligand variation, but some previous studies have explored methods for synthesizing mixed-metal MOF-74 (MM-MOF-74). Botas et al.[31] synthesized Zn-Co-MOF-74 by a one-pot synthesis, whereas Mg-Ni-MOF-74 was formed by Kahr et al.[32] using a post-synthetic incorporation method. Very recently, the mixed-metal strategy was further developed in the work of Wang et al.,[33] which reported the successful synthesis of MM-MOF-74 containing as many as 10 different divalent metals (Mg, Ca, Sr, Ba, Mn, Fe, Co, Ni, Zn and Cd) in a single framework. The resulting adsorption properties were not explored, but these studies show that MOF-74 can be synthesized with the expected topology while incorporating a large number of different metals.

MOF-74 is known to display high affinity towards CO_2 at low pressures due to its high density of CUS metal centers.[26, 30, 34, 35] Mg-MOF-74 exhibits the greatest CO_2 capacities at 0.1 atm of all reported MOFs but has demonstrated stability issues under humid conditions.[36] However, despite having lower CO_2 adsorption capacities,[26] other MOF-74 analogues with different metal nodes are reported to have better stability in humid conditions. Liu et al.[37] found that Ni-MOF-74 is more stable than Mg-MOF-74, possibly because Ni^{2+} is a weaker reducing agent than Mg^{2+}. Based on the standard reduction potentials for Ni^{2+} (-0.26 eV), Co^{2+} (-0.28 eV) and Mg^{2+} (-2.37 eV), Ni and Co are relatively weak reductive metal centers. Similarly, the water stability of MOF-5 can be enhanced via doping with Ni^{2+};[38] and, in general, the water stability of many other MOFs has been improved by choosing a more inert metal.[39] Kizzie et al.[40] observed that Co-MOF-

74 retains approximately 85% of its initial CO_2 capacity after regeneration of the hydrated sample; this discovery is further supported by a study of the impact of air exposure on adsorption in M-MOF-74 (M= Mg^{2+}, Ni^{2+}, and Co^{2+}).[41] In mixed-metal structures, even if some bonds between Mg^{2+} centers and organic linkers can be displaced by water molecules,[42] it is possible that the framework can still be partially preserved by the intact bonds between Co^{2+} or Ni^{2+} centers and linkers.

M-MOF-74 (M = Mg, Co, Ni) can be obtained via solvothermal synthesis at temperatures between 100 and 125 °C and in dimethylformamide (DMF)-ethanol-water cosolvent solutions with volume ratios of 15:1:1 or 1:1:1, depending on the metal nodes,[26] making the material an appropriate platform to study the influence of different solvothermal conditions on the composition of the final product. The final metal composition of MM-MOF-74 can be measured using various elemental analysis, and thus, insight can be obtained into the thermodynamics of metal incorporation from solution.

Previous work on MM-MOF-74 focused on the incorporation of up to 10 different metals into the same structure. However, the composition space of these mixed-metal materials has not yet been determined. For example, the conditions for synthesizing MM-MOF-74 with a prescribed mixed-metal composition are not known. In this study, the work of Wang et al.[33] is extended by synthesizing microcrystalline MM-MOF-74 containing two different divalent metal ions (Mg/Ni and Mg/Co) in several concentration levels via a one-pot reaction to explore the composition space. We have prepared MM-MOF-74 using various combinations of synthesis temperatures and cosolvent volume ratios, while using the same reagent concentration levels to determine the impact of temperature and solvent on the final metal composition. The effect of mixed-metal centers on the CO_2 adsorption

and water stability properties of Mg-MOF-74 was also studied. We demonstrate that the water stability of Mg-MOF-74 can be enhanced by incorporating relatively stable metal nodes to maintain the structural integrity of the material without strongly impacting CO_2 adsorption loadings.

3.2 Experimental Section

3.2.1 Materials

Chemicals. All chemicals required in this study were used as received (without any purification) from commercial sources: magnesium nitrate hexahydrate ($Mg(NO_3)_2 \cdot 6H_2O$), nickel (II) nitrate hexahydrate ($Ni(NO_3)_2 \cdot 6H_2O$) and cobalt (II) nitrate hexahydrate ($Co(NO_3)_2 \cdot 6H_2O$) from Sigma-Aldrich; 2,5-dihydroxy-1,4-benzenedicarboxylic acid (DOBDC) from TCI America; N,N-dimethylformamide (DMF) and ethanol (EtOH) from VWR.

Synthesis of MOF-74 (Mg, Ni, and Co). Synthesis and solvent exchange of MOF-74 (Mg, Ni and Co) were done according to a previously reported procedure.[43] Mg- and Ni-MOF-74 were activated by heating the as-synthesized samples at 250 °C for 12 h under dynamic vacuum, whereas Ni-MOF-74 was activated at 170 °C for 12 h under dynamic vacuum.

Synthesis of MM-MOF-74 (Mg/Ni and Mg/Co). MM-MOF-74 (Mg/Ni and Mg/Co) samples were synthesized and activated with the same procedure, varying the combinations of temperature and solvent volume ratios (Group A: 120 °C, 15:1:1 (DMF: EtOH: H_2O, v/v); Group B: 120 °C, 1:1:1; Group C: 110 °C, 1:1:1) and the input molar

ratios of metal salts (Mg^{2+}/Ni^{2+} and Mg^{2+}/Co^{2+}: 90%/10%; 70%/30%; 50%/50%; 25%/75%). For example, 16 mol% (nominally 10%) Mg-Ni-MM-MOF-74 (Group A) was synthesized as follows. Because the total molar amount of metal salts is 1.85 mmol, 0.185 mmol $Ni(NO_3)_2 \cdot 6H_2O$, 1.665 mmol $Mg(NO_3)_2 \cdot 6H_2O$ and 0.6 mmol DOBDC were dissolved in a 51 mL solvent mixture of DMF, ethanol and water (15:1:1, by volume). The mixture was continuously stirred until homogeneous, and 10 mL portions of the resulting mixture were transferred into 20 mL scintillation vials and placed into a sand bath. The solution was heated at 120 °C for 24 h. The as-synthesized MM-MOF-74 samples were washed four times with 20 mL fresh DMF, exchanged 4 times over 4 days with 20 mL fresh methanol, and then stored under methanol at room temperature until subsequent characterization. Before collecting any adsorption isotherms, as-synthesized samples stored in methanol were initially heated in situ at 65 °C for 2 h to remove residual solvent and then at 250 °C for another 12 h to fully evacuate the porous compounds.

3.2.2 Characterization

Attempts to prepare monocrystalline MM-MOF-74 samples for single-crystal X-ray diffraction have been unsuccessful. In addition to powder X-ray diffraction and elemental analysis, more detailed characterization methods, including surface area analysis, inductively coupled plasma optical emission spectroscopy (ICP-OES), thermogravimetric analysis (TGA), scanning electron microscopy and energy dispersive spectroscopy (SEM-EDS) and carbon dioxide and water vapor adsorption isotherms, were also performed on the subset of structures synthesized at 120 °C and a 15:1:1 solvent ratio (Group A).

Powder X-ray diffraction (PXRD). PXRD patterns were collected on a PANalytical X'Pert X-ray diffractometer equipped with an X'Celerator detector module and using Cu Kα (λ = 1.5418 Å) radiation at room temperature, with a step size of 0.02˚ in 2θ. The crystallinity and phase purity of the as-synthesized MM-MOF-74 samples were confirmed by comparing experimental PXRD patterns with simulated patterns of the parent MOF-74 structure. Changes in the crystallinity of MOF structures resulting from exposure to humid air were assessed by comparing the PXRD patterns of the as-synthesized and water-exposed samples.

Inductively coupled plasma optical emission spectroscopy (ICP-OES). Elemental analysis for Mg, Ni and Co in the MM-MOF-74 samples was performed using ICP-OES on a PerkinElmer 7300DV ICP-OES instrument. Prior to analysis, 15-20 mg of as-synthesized MM-MOF-74 was activated at 250 ˚C for 12 h under vacuum.

N_2 physisorption. N_2 physisorption isotherms were measured at 77 K on a Quadrasorb system from Quantachrome Instruments. MM-MOF-74 samples (Group A) were activated on a Quantachrome FloVac Degasser at 250 ˚C for 12 h under dynamic vacuum. Brunauer-Emmett-Teller (BET) surface areas were determined for each activated MOF before and after water exposure by fitting the BET model to the collected isotherms and calculating the BET surface area over the low pressure range ($P/P_o < 0.05$).[44]

Thermogravimetric analysis (TGA). TGA of the as-synthesized MM-MOF-74 samples (Group A) was performed on a NETZSCH STA 449 F1 Jupiter® device under helium in the temperature range of 25-700 ˚C at a heating rate of 2 ˚C/min and flow rate of 20 mL/min.

Scanning electron microscopy (SEM) and energy dispersive spectroscopy (EDS). SEM images of the as-synthesized MM-MOF-74 samples (Group A) were collected on a Zeiss Ultra60 FE-SEM instrument with a high-efficiency In-lens SE detector at a working distance of 7-8 mm and accelerating voltage of 10 kV. Prior to SEM observations, all samples were sonicated for 30 s in methanol and dispersed on a flat Al sample holder with two-sided adhesive conductive carbon tape. The examined samples were coated with carbon using a Cressington 108A Carbon Coater to reduce the risk of the charging effect. EDS measurements were conducted for each sample, followed by SEM observations on the same Zeiss Ultra60 FE-SEM instrument at 10 kV with an Oxford EDS Super-X 50 mm^2 detector, changing the aperture size from 30 µm to 120 µm and switching to high-current conditions. Localized metal compositions within the MM-MOF-74 samples were analyzed at three different regions using point mode to determine metal content homogeneity. Using mapping mode, the metals of interest were mapped to investigate metal distributions.

CO_2 adsorption isotherms. Pure CO_2 adsorption isotherms were measured on an Intelligent Gravimetric Analyzer by Hiden Analytical Ltd (IGA-1) from 0 to 1 bar at 5 ˚C, 25 ˚C and 45 ˚C. Each MM-MOF-74 sample (Group A) was outgassed *in situ* at 250 ˚C under dynamic vacuum for approximately 12 h before isotherm collection. The maximum equilibration time was set to 40 min for each point during the collection of CO_2 isotherms.

Water vapor isotherms. 3Flex Surface Characterization Analyzer from Micromeritics was used to collect water vapor isotherms at 22 ˚C for the as-synthesized MM-MOF-74 samples (Group A). Prior to water adsorption measurements, the samples

were activated *in situ* at 250 ˚C for 12 h under dynamic vacuum. All water vapor isotherms were measured up to $P/P_0 = 0.95$ to avoid water condensation.

3.3 Results and Discussion

3.3.1 MM-MOF-74 Characterization

The phase purity and topology of all as-synthesized MM-MOF-74 samples were confirmed by PXRD. As shown in Appendix A (Figure A.1-A.6), all as-synthesized MM-MOF-74 samples have PXRD patterns that are similar to simulated patterns for the single-crystal parent MOF-74 structures.[27-29] No additional diffraction peaks are observed in the experimental PXRD patterns, indicating that all obtained Mg-Ni- and Mg-Co-MM-MOF-74 samples are isostructural to the parent MOF-74 and that the expected topology is maintained upon employing the mixed-metal strategy.[45]

N_2 physisorption isotherms (Figure A.11 and A.12) were collected at 77 K for activated MM-MOF-74 samples to determine the porosity of the resulting materials. The N_2 isotherms for all evacuated MM-MOF-74 structures are typical type-I isotherms.[46] The BET surface areas of M-MOF-74 (M = Mg, Co, Ni), Mg-Ni- and Mg-Co-MM-MOF-74 samples (Group A) are shown in (Table 3.1). These surface areas trends are consistent with those expected, as heavier transition metal substitution leads to a reduction in surface area,[33] and the values for parent MOF-74 are consistent with previous studies.[26, 47]

To investigate the thermal stability of MM-MOF-74, TGA was carried out under helium flow. As shown in Figure A.16 and A.17, the decomposition temperature of each Mg-Ni- and Mg-Co-MM-MOF-74 sample is lower than that of Mg-MOF-74 (~420 ˚C),[26]

whereas the thermal stability of MM-MOF-74 shows a slight improvement over both Ni-MOF-74 (~270 ˚C)[28] and Co-MOF-74 (~280 ˚C).[47] Furthermore, a gradual increase in decomposition temperature is observed in the examined Mg-Ni- and Mg-Co-MM-MOF-74 samples with increased Mg content.

Table 3.1: BET surface areas and total pore volumes of parent MOF-74 and MM-MOF-74.

Material[a]	BET surface area (m^2/g)	Total pore volume[b] (cm^3/g)
Mg-MOF-74	1607	0.69
Ni-MOF-74	1337	0.54
Co-MOF-74	1372	0.52
16 mol% Ni; 84 mol% Mg	1502	0.59
41 mol% Ni; 59 mol% Mg	1473	0.6
75 mol% Ni; 25 mol% Mg	1387	0.58
89 mol% Ni; 11 mol% Mg	1419	0.6
15 mol% Co; 85 mol% Mg	1394	0.56
44 mol% Co; 56 mol% Mg	1331	0.53
76 mol% Co; 24 mol% Mg	1447	0.58
96 mol% Co; 4 mol% Mg	1294	0.54

[a]Prepared at 120 ˚C and a 15:1:1 cosolvent volume ratio (DMF: EtOH: H_2O, v/v).
[b]Calculated from N_2 adsorption at 77 K at $P/P_0 = 0.8$.

The distribution of divalent metal ions in each MM-MOF-74 sample was analyzed using SEM and EDS. No amorphous phases or multiple morphologies are observed in the SEM images for MM-MOF-74. The expected metals (Mg/Ni or Mg/Co) are distributed throughout the MM-MOF-74 crystals, as shown in the EDS maps for MM-MOF-74 (Figure A.18-A.25). However, careful observation of these maps indicates that the metal distribution within MM-MOF-74 is inhomogeneous. To determine the metal distribution, MM-MOF-74 samples were examined via EDS point mode in multiple regions (Figure

A.18-A.25). The variation in metal content at different points within the sample further suggests an inhomogeneous metal distribution, which is consistent with the work of Wang et al[33] and can be attributed to different crystal growth rates[48] during the synthesis of MM-MOF-74 samples.

3.3.2 Effects of Reaction Temperature and Solvent Composition on Final Metal Content

To understand the effects of temperature and solvent on the incorporation behavior of the different divalent metals during MM-MOF-74 synthesis, we conducted a series of systematic studies at four concentration levels, based on the input molar percentage of secondary metal salts (10%, 30%, 50% and 75%, $M^{2+} = Ni^{2+}$ or Co^{2+}). Mg-Ni- and Mg-Co-MM-MOF-74 samples were synthesized using three different sets of reaction temperatures and cosolvent ratios: Group A 120 °C, 15:1:1 (DMF: ethanol: water, v/v), Group B 120 °C, 1:1:1 and Group C 110 °C, 1:1:1. All attempts at preparing MM-MOF-74 with these temperatures and solvent ratios were successful except the Group C synthesis of MM-MOF-74 at 10% input molar ratio of M^{2+}/Mg^{2}.

The relative metal compositions in MM-MOF-74 were determined by ICP-OES. Figure 3.1 illustrates the relationship between the input molar percentage of Ni^{2+} or Co^{2+} in the starting solution and the output molar percentage of those metal ions in the resulting MM-MOF-74 crystals for the three sets of synthetic conditions. The black solid line represents the scenario in which the resulting mol% M^{2+} is equal to the initial mol% M^{2+} in the starting reaction mixture, and the colored lines represent the three different synthetic condition sets.

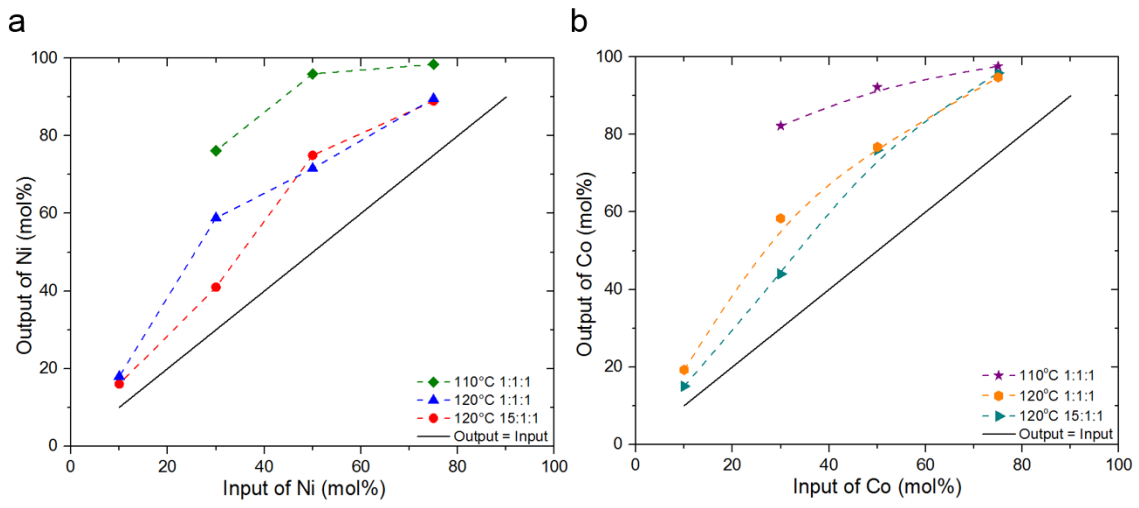

Figure 3.1: Relationship between input and output molar percentages of secondary metal centers in Mg-*M*-MM-MOF-74 (a: M = Ni, b: M = Co) prepared using different combinations of reaction temperature and cosolvent volume ratios (DMF: EtOH: H_2O).

The mol% M^{2+} in the resulting materials clearly increases when a higher amount of the corresponding metal salt is used in the synthesis. From a comparison of the black solid line and colored dotted lines for each sample in Figure 3.1, it is evident that Ni^{2+} and Co^{2+} ions are more favorably incorporated than Mg^{2+} into MM-MOF-74 networks. This preferential incorporation of Ni^{2+} and Co^{2+} relative to Mg^{2+} may be attributed to differences in the formation energy of the metal clusters. Additionally, kinetic effects, including temperature and solvent effects, have some role in this phenomenon. Notably, the resulting mol% M^{2+} for MM-MOF-74 prepared at 120 °C but two different cosolvent ratios, 15:1:1 and 1:1:1, are similar, demonstrating that the solvent has only a slight effect on Ni^{2+}, Co^{2+} and Mg^{2+} incorporation during synthesis. This conclusion is consistent with the calculation of Gee et al.,[49] who demonstrated the minor contribution of the solvent effect during the synthesis of ZIF-8. However, the distinct differences between output mol% M^{2+} for MM-MOF-74 prepared at 110 and 120 °C but at a constant 1:1:1 solvent ratio, for both Mg-Ni

and Mg-Co scenarios, indicate that temperature is a more significant factor in the synthesis process than solvent. This distinct difference is supported by the work of Guasch et al.,[50] who reported the important role of temperature in nucleation and crystal growth rate during Ni-MOF-74 synthesis. In general, composition curves such as those in Figure 3.1 are useful in the development of MM-MOF-74 materials in which a particular concentration of incorporated metals is desired.

3.3.3 CO_2 Adsorption Properties

The temperature of post-combustion flue gas is in the range of 40-60 °C,[34] and the partial pressure of CO_2 in flue gas is approximately 0.1 bar at a total pressure of 1 bar. Figure A.26 displays CO_2 isotherms measured at 45 °C and in the 0-1 bar region for Mg-M^{2+}-MM-MOF-74 (a: Ni^{2+}, b: Co^{2+}) and parent M^{2+}-MOF-74 (Mg^{2+}, Ni^{2+} and Co^{2+}) samples from the Group A synthesis. Rather than the standard units of mmol CO_2/g MOF, these isotherms are present with units of mol CO_2/mol M^{2+} to exclude the effects of weight variations among Mg, Ni and Co and allow for a direct comparison of adsorption loadings.

All MM-MOF-74 samples show the expected strong affinity for CO_2 molecules (Figure A.27) in the low-pressure regime, illustrating that MM-MOF-74 samples still possess a high density of CUS metal centers, which is a feature observed in the parent MOF-74 (Mg, Ni and Co) materials[30, 34] after incorporating mixed CUS metals into the Mg-MOF-74 structure. To further evaluate the effect of mixed-metal centers on CO_2 capacity throughout the MM-MOF-74 series, the relationship between the concentration of mixed CUS metal centers and CO_2 capacity at 45 °C and 0.1 bar is illustrated in Figure 3.2. In each panel of Figure 3.2, a black solid line represents the linear scenarios in which all the

values for MM-MOF-74 at different concentration levels that are calculated from the amount of adsorbed CO_2 for pure Mg-MOF-74 and Ni-MOF-74 or Co-MOF-74, using weighted coefficients based on ICP elemental results. The colored data points indicate the experimental values measured for the eight MM-MOF-74 derivatives and three parent MOF-74 samples. In terms of CO_2 affinity, it is expected that the CO_2 isotherms of Mg-*M*-MM-MOF-74 will decrease in uptake with increasing concentration of low-affinity CUS Ni or Co metal centers.[26, 30] Indeed, the CO_2 capacities at 45 °C and 0.1 bar show the following trend: Mg-MOF-74 > 16 mol% Ni > 41 mol% Ni > 75 mol% Ni > 89 mol% Ni > Ni-MOF-74, as shown in Figure 3.2a. Interestingly, all CO_2 capacities for Mg-Ni-MM-MOF-74 derivatives are slightly greater than the linear scenario (calculated line), indicating that Ni CUS metal centers have a synergistic effect on CO_2 adsorption in MM-MOF-74 materials. Mg-Co-MM-MOF-74 samples follow a similar order in CO_2 capacity, 15 mol% Co > 44 mol% Co > 76 mol% Co > 96 mol% Co (Figure 3.2b). However, Co CUS metal centers display a strong antagonistic effect on CO_2 adsorption in MM-MOF-74, as the adsorbed amount of CO_2 in each Mg-Co-MM-MOF-74 is much less than the expected values based on the linear combination scenario (black solid line).

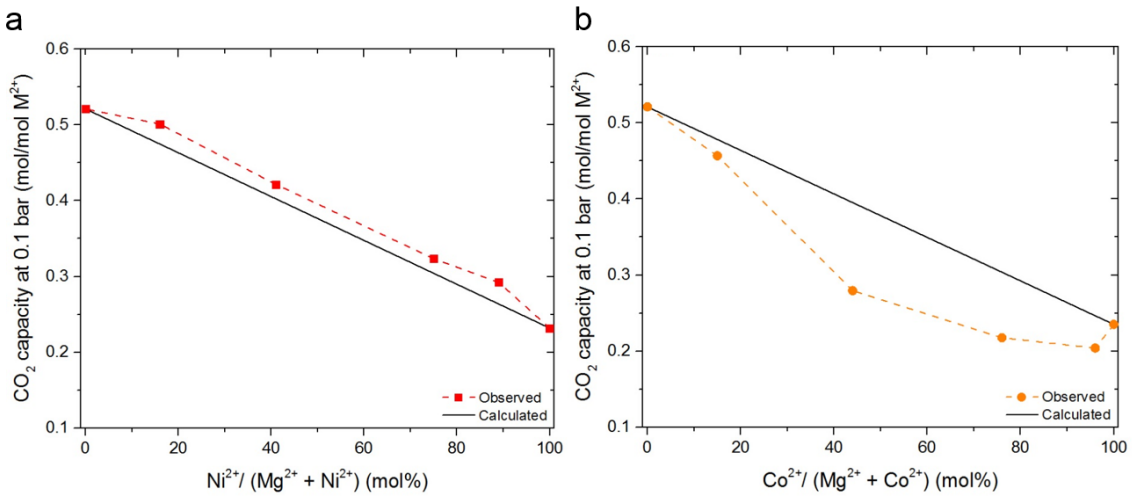

Figure 3.2: CO_2 adsorption loading curves at 45 °C and 0.1 bar for Mg-*M*-MM-MOF-74 (a: M = Ni, b: M = Co) with different concentrations of mixed CUS metal centers, prepared at 120 ˚C and a 15:1:1 cosolvent volume ratio (DMF: EtOH: H_2O, v/v).

In both scenarios, CO_2 adsorption in MM-MOF-74 gradually decreases with an increase in the incorporation of other divalent metals (Co and Ni) with Mg. This adsorption behavior is attributed to the weaker electrostatic interactions of Ni or Co metal centers with CO_2 gas molecules relative to those of Mg. This reasoning is supported by the findings of Caskey et al.[26] and Queen et al.,[30] in which the isosteric heats of CO_2 adsorption at infinite dilution for these three parent frameworks are in the following order: Mg > Ni > Co.

To understand the effect of mixed-metal defects on heats of CO_2 adsorption, single-component CO_2 adsorption isotherms for each MM-MOF-74 sample were collected at 5, 25 and 45 °C. After fitting each isotherm with the Toth model,[26] the isosteric heats of CO_2 adsorption for each sample were calculated using the Clausius-Clapeyron equation, and the results are presented as a function of CO_2 loading (mol CO_2/mol M^{2+}) in Figure A.30. The isosteric heats of CO_2 adsorption for Mg-Ni- and Mg-Co-MM-MOF-74

gradually drop with an increase in CO_2 loading (Figure A.30), which is in agreement with the previously reported trend.[26]

3.3.4 Water Stability Analysis under Humid Conditions

Water adsorption isotherms were recorded at 22 °C for the MM-MOF-74 derivatives (Group A) and parent MOF-74 materials (Figure A.31-A.33). All the examined MM-MOF-74 samples show type-I isotherm profiles with a steep rise in the low pressure ($P/P_0 < 0.1$) regime, indicating a high affinity for water adsorption in these materials. This behavior is due to the presence of a high density of CUS metal centers in the MM-MOF-74 series and has been observed in previous MOF-74 studies.[39, 51] The maximum water adsorption loadings observed for the measured MM-MOF-74 samples at $P/P_0 = 0.9$ range from 31.6 to 41.4 mmol/g, which is comparable to the work of Furukawa et al.[51] Additionally, the water desorption isotherm for each MM-MOF-74 exhibits a non-negligible hysteresis loop,[51-52] illustrating that water molecules are strongly bound to the CUS metal centers in MM-MOF-74.

A combination of PXRD and BET surface area analysis before and after water exposure were employed to evaluate the water stability of the MM-MOF-74 samples.[52-53] The PXRD patterns (Figure A.7-A.9) and surface areas (Table A.1) calculated from BET analysis[44] of N_2 isotherms (Figure A.13-A.15) at 77 K are shown in Appendix A. Figure 3.3 presents the relationship between the retained BET surface area after water exposure (95% RH) and the composition of mixed CUS metal centers in the MOF-74 structure. The black solid lines in Figure 3.3 indicate the correlation that would exist if surface area retention in MM-MOF-74 could be described by a linear combination of the stabilities of

the parent, pure-metal materials. The colored data points exhibit the experimental results collected in this work.

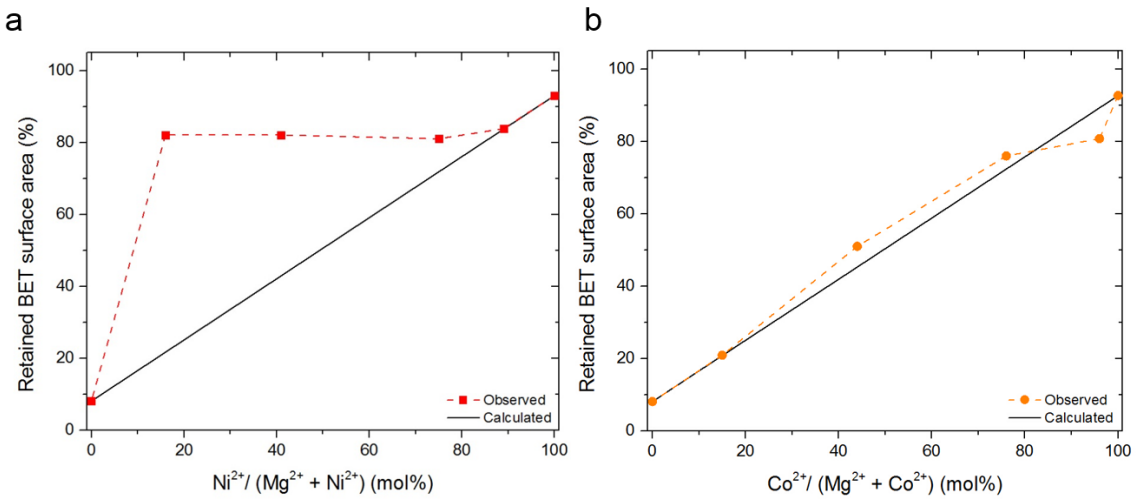

Figure 3.3: Retained BET surface area (%) trends for water exposed Mg-*M*-MM-MOF-74 (a: M = Ni, b: M = Co) with different concentrations of mixed CUS metal centers, prepared at 120 ˚C and a 15:1:1 cosolvent volume ratio (DMF: EtOH: H_2O, v/v).

Contrary to the CO_2 adsorption results, the Mg-Ni-MM-MOF-74 samples show a dramatic departure from the expected stability behavior. As shown by Figure 3.3a, a content of only 16 mol% Ni improves the stability of the sample such that 80% of the starting surface area is maintained after water exposure instead of the expected 20% retention. This stability is held at the same level until the Ni substitution is > 90%. Thus, it appears that the water stability of Mg-Ni-MM-MOF-74 can be adjusted by controlling the concentration of CUS metal centers in the MOF-74 structure. On the other hand, as the fraction of Co metal centers in Mg-Co-MM-MOF-74 structure increases (Figure 3.3b), the retained BET surface area of the framework after water exposure increases in a nearly linear fashion. The experimental results measured for this MM-MOF-74 structure are in excellent agreement with the expected results based on a linear correlation (black solid

line), demonstrating that the water stability of MM-MOF-74 can be tuned continuously by adjusting the composition of CUS Co centers. The unexpected difference between the behaviors of the Mg-Ni- and Mg-Co-MM-MOF-74 systems is not yet understood but may be due to metal configurational differences. For example, the presence of an evenly distributed mixture of metals throughout the framework versus a clustering of metals in distinct regions would explain the observed stability differences.

3.4 Conclusions

We have synthesized and characterized a variety of MM-MOF-74 that are isostructural to Mg-MOF-74 by incorporating mixed CUS metal centers via a one-pot synthesis. Surprisingly, the water stabilities of the modified Mg-MOF-74 structures increase significantly upon addition of a relatively small amount of Ni. For the parent Mg-MOF-74 structure, only 8% of the surface area is retained after exposure to $P/P_0 = 0.95$ water vapor, whereas 82% of the surface area is retained after incorporating just 16 mol% Ni into the CUS metal centers. Furthermore, only a slight (4%) decrease in the low-pressure CO_2 affinity is observed in this structure in comparison to pure Mg-MOF-74. This newly synthesized MM-MOF is therefore attractive for applications based on its greatly increased water stability while maintaining a high CO_2 affinity. On a fundamental level, we have demonstrated that: (i) Ni and Co are more favorably incorporated in the final MM-MOF-74 framework than Mg from solution, (ii) reaction temperature more significantly impacts the final composition in the MM-MOF-74 structure than does reaction solvent composition, (iii) CO_2 capacity and heats of CO_2 adsorption can be tuned by the incorporation of low-affinity CUS metal centers (Ni or Co) into the MOF-74 framework,

and (iv) the water stability of Mg-MOF-74 can be enhanced through the incorporation of more stable CUS metal centers (Ni or Co) within the MOF-74 framework.

3.5 References

1. Yaghi, O. M.; O'Keeffe, M.; Ockwig, N. W.; Chae, H. K.; Eddaoudi, M.; Kim, J., *Nature* **2003**, *423* (6941), 705-714.

2. Li, J. R.; Kuppler, R. J.; Zhou, H. C., *Chem. Soc. Rev.* **2009**, *38* (5), 1477-1504.

3. Murray, L. J.; Dinca, M.; Yano, J.; Chavan, S.; Bordiga, S.; Brown, C. M.; Long, J. R., *J. Am. Chem. Soc.* **2010**, *132* (23), 7856-7857.

4. Bloch, E. D.; Murray, L. J.; Queen, W. L.; Chavan, S.; Maximoff, S. N.; Bigi, J. P.; Krishna, R.; Peterson, V. K.; Grandjean, F.; Long, G. J.; Smit, B.; Bordiga, S.; Brown, C. M.; Long, J. R., *J. Am. Chem. Soc.* **2011**, *133* (37), 14814-14822.

5. Murray, L. J.; Dinca, M.; Long, J. R., *Chem. Soc. Rev.* **2009**, *38* (5), 1294-1314.

6. Brezesinski, T.; Wang, J.; Tolbert, S. H.; Dunn, B., *Nat. Mater.* **2010**, *9* (2), 146-151.

7. Horcajada, P.; Serre, C.; Vallet-Regi, M.; Sebban, M.; Taulelle, F.; Ferey, G., *Angew. Chem. Int. Ed.* **2006**, *45* (36), 5974-5978.

8. Allendorf, M. D.; Bauer, C. A.; Bhakta, R. K.; Houk, R. J. T., *Chem. Soc. Rev.* **2009**, *38* (5), 1330-1352.

9. Lee, J.; Farha, O. K.; Roberts, J.; Scheidt, K. A.; Nguyen, S. T.; Hupp, J. T., *Chem. Soc. Rev.* **2009**, *38* (5), 1450-1459.

10. Kreno, L. E.; Leong, K.; Farha, O. K.; Allendorf, M.; Van Duyne, R. P.; Hupp, J. T., *Chem. Rev.* **2012**, *112* (2), 1105-1125.

11. Lu, W. G.; Wei, Z. W.; Gu, Z. Y.; Liu, T. F.; Park, J.; Park, J.; Tian, J.; Zhang, M. W.; Zhang, Q.; Gentle, T.; Bosch, M.; Zhou, H. C., *Chem. Soc. Rev.* **2014**, *43* (16), 5561-5593.

12. Burtch, N. C.; Jasuja, H.; Walton, K. S., *Chem. Rev.* **2014**, *114* (20), 10575-10612.

13. Deng, H. X.; Doonan, C. J.; Furukawa, H.; Ferreira, R. B.; Towne, J.; Knobler, C. B.; Wang, B.; Yaghi, O. M., *Science* **2010**, *327* (5967), 846-850.

14. Furukawa, H.; Cordova, K. E.; O'Keeffe, M.; Yaghi, O. M., *Science* **2013**, *341* (6149), 974-975.

15. Yuan, S.; Qin, J. S.; Zou, L. F.; Chen, Y. P.; Wang, X.; Zhang, Q.; Zhou, H. C., *J. Am. Chem. Soc.* **2016**, *138* (20), 6636-6642.

16. Zhang, Y. B.; Furukawa, H.; Ko, N.; Nie, W. X.; Park, H. J.; Okajima, S.; Cordova, K. E.; Deng, H. X.; Kim, J.; Yaghi, O. M., *J. Am. Chem. Soc.* **2015**, *137* (7), 2641-2650.

17. Yuan, S.; Lu, W. G.; Chen, Y. P.; Zhang, Q.; Liu, T. F.; Feng, D. W.; Wang, X.; Qin, J. S.; Zhou, H. C., *J. Am. Chem. Soc.* **2015**, *137* (9), 3177-3180.

18. Cmarik, G. E.; Kim, M.; Cohen, S. M.; Walton, K. S., *Langmuir* **2012**, *28* (44), 15606-15613.

19. Lin, X.; Telepeni, I.; Blake, A. J.; Dailly, A.; Brown, C. M.; Simmons, J. M.; Zoppi, M.; Walker, G. S.; Thomas, K. M.; Mays, T. J.; Hubberstey, P.; Champness, N. R.; Schroder, M., *J. Am. Chem. Soc.* **2009**, *131* (6), 2159-2171.

20. Li, B. Y.; Zhang, Z. J.; Li, Y.; Yao, K. X.; Zhu, Y. H.; Deng, Z. Y.; Yang, F.; Zhou, X. J.; Li, G. H.; Wu, H. H.; Nijem, N.; Chabal, Y. J.; Lai, Z. P.; Han, Y.; Shi, Z.; Feng, S. H.; Li, J., *Angew. Chem. Int. Ed.* **2012**, *51* (6), 1412-1415.

21. Deria, P.; Mondloch, J. E.; Tylianakis, E.; Ghosh, P.; Bury, W.; Snurr, R. Q.; Hupp, J. T.; Farha, O. K., *J. Am. Chem. Soc.* **2013**, *135* (45), 16801-16804.

22. Wang, B.; Huang, H. L.; Lv, X. L.; Xie, Y. B.; Li, M.; Li, J. R., *Inorg. Chem.* **2014**, *53* (17), 9254-9259.

23. Zhou, W.; Wu, H.; Yildirim, T., *J. Am. Chem. Soc.* **2008**, *130* (46), 15268-15269.

24. Mishra, P.; Edubilli, S.; Mandal, B.; Gumma, S., *Microporous Mesoporous Mater.* **2013**, *169*, 75-80.

25. Rosi, N. L.; Kim, J.; Eddaoudi, M.; Chen, B. L.; O'Keeffe, M.; Yaghi, O. M., *J. Am. Chem. Soc.* **2005**, *127* (5), 1504-1518.

26. Caskey, S. R.; Wong-Foy, A. G.; Matzger, A. J., *J. Am. Chem. Soc.* **2008**, *130* (33), 10870-10871.

27. Dietzel, P. D. C.; Blom, R.; Fjellvag, H., *Eur. J. Inorg. Chem.* **2008**, *2008* (23), 3624-3632.

28. Dietzel, P. D. C.; Panella, B.; Hirscher, M.; Blom, R.; Fjellvag, H., *Chem. Commun.* **2006**, (9), 959-961.

29. Dietzel, P. D. C.; Morita, Y.; Blom, R.; Fjellvag, H., *Angew. Chem. Int. Ed.* **2005**, *44* (39), 6354-6358.

30. Queen, W. L.; Hudson, M. R.; Bloch, E. D.; Mason, J. A.; Gonzalez, M. I.; Lee, J. S.; Gygi, D.; Howe, J. D.; Lee, K.; Darwish, T. A.; James, M.; Peterson, V. K.; Teat, S. J.; Smit, B.; Neaton, J. B.; Long, J. R.; Brown, C. M., *Chem. Sci.* **2014**, *5* (12), 4569-4581.

31. Botas, J. A.; Calleja, G.; Sanchez-Sanchez, M.; Orcajo, M. G., *Int. J. Hydrogen Energy* **2011**, *36* (17), 10834-10844.

32. Kahr, J.; Morris, R. E.; Wright, P. A., *Crystengcomm* **2013**, *15* (45), 9779-9786.

33. Wang, L. J.; Deng, H. X.; Furukawa, H.; Gandara, F.; Cordova, K. E.; Peri, D.; Yaghi, O. M., *Inorg. Chem.* **2014**, *53* (12), 5881-5883.

34. Mason, J. A.; Sumida, K.; Herm, Z. R.; Krishna, R.; Long, J. R., *Energy Environ. Sci.* **2011**, *4* (8), 3030-3040.

35. Britt, D.; Furukawa, H.; Wang, B.; Glover, T. G.; Yaghi, O. M., *Proc. Natl. Acad. Sci. U.S.A.* **2009**, *106* (49), 20637-20640.

36. Sumida, K.; Rogow, D. L.; Mason, J. A.; McDonald, T. M.; Bloch, E. D.; Herm, Z. R.; Bae, T. H.; Long, J. R., *Chem. Rev.* **2012**, *112* (2), 724-781.

37. Liu, J.; Benin, A. I.; Furtado, A. M. B.; Jakubczak, P.; Willis, R. R.; LeVan, M. D., *Langmuir* **2011**, *27* (18), 11451-11456.

38. Li, H. H.; Shi, W.; Zhao, K. N.; Li, H.; Bing, Y. M.; Cheng, P., *Inorg. Chem.* **2012**, *51* (17), 9200-9207.

39. Jasuja, H.; Jiao, Y.; Burtch, N. C.; Huang, Y. G.; Walton, K. S., *Langmuir* **2014**, *30* (47), 14300-14307.

40. Kizzie, A. C.; Wong-Foy, A. G.; Matzger, A. J., *Langmuir* **2011**, *27* (10), 6368-6373.

41. Stults, K. Metal Organic Framework-Metal Oxide Composites for Toxis Gas Adsorption and Sensing. Georgia Institute of Technology, Atlanta, GA, 2014.

42. Low, J. J.; Benin, A. I.; Jakubczak, P.; Abrahamian, J. F.; Faheem, S. A.; Willis, R. R., *J. Am. Chem. Soc.* **2009**, *131* (43), 15834-15842.

43. Glover, T. G.; Peterson, G. W.; Schindler, B. J.; Britt, D.; Yaghi, O., *Chem. Eng. Sci.* **2011**, *66* (2), 163-170.

44. Walton, K. S.; Snurr, R. Q., *J. Am. Chem. Soc.* **2007**, *129* (27), 8552-8556.

45. Burrows, A. D., *Crystengcomm* **2011**, *13* (11), 3623-3642.

46. Kitagawa, S.; Kitaura, R.; Noro, S., *Angew. Chem. Int. Ed.* **2004**, *43* (18), 2334-2375.

47. Mishra, P.; Edubilli, S.; Mandal, B.; Gumma, S., *J. Phys. Chem. C* **2014**, *118* (13), 6847-6855.

48. Bergmann, J.; Stein, K.; Kobalz, M.; Handke, M.; Lange, M.; Mollmer, J.; Heinke, F.; Oeckler, O.; Glaser, R.; Staudt, R.; Krautscheid, H., *Microporous Mesoporous Mater.* **2015**, *216*, 56-63.

49. Gee, J. A.; Sholl, D. S., *J. Phys. Chem. C* **2013**, *117* (40), 20636-20642.

50. Guasch, J.; Dietzel, P. D. C.; Collier, P.; Acerbi, N., *Microporous Mesoporous Mater.* **2015**, *203*, 238-244.

51. Furukawa, H.; Gandara, F.; Zhang, Y. B.; Jiang, J. C.; Queen, W. L.; Hudson, M. R.; Yaghi, O. M., *J. Am. Chem. Soc.* **2014**, *136* (11), 4369-4381.

52. Schoenecker, P. M.; Carson, C. G.; Jasuja, H.; Flemming, C. J. J.; Walton, K. S., *Ind. Eng. Chem. Res.* **2012**, *51* (18), 6513-6519.

53. DeCoste, J. B.; Peterson, G. W.; Jasuja, H.; Glover, T. G.; Huang, Y. G.; Walton, K. S., *J. Mater. Chem. A* **2013**, *1* (18), 5642-5650.

CHAPTER 4. HEAT-TREATMENT OF DEFECTIVE UIO-66 FROM MODULATED SYNTHESIS: ADSORPTION AND STABILITY STUDIES

In this chapter, Yang (Anny) Liu performed computational simulations and analysis; Guanghui Zhu, Souryadeep Bhattacharyya, and Julian Hungerford aided in SO_2 exposure experiments.

4.1 Introduction

Metal-organic frameworks (MOFs) are a diverse set of crystalline, nanoporous materials connected by the self-assembly of metal ions or clusters and multidentate organic ligand linkers.[1] A wide variety of these nanoporous materials can be prepared with different pore size, geometry, and chemical functionality by changing metal precursors or organic ligands.[2] With exceptionally high surface areas and chemically tunable structures, MOFs often display adsorption properties that are comparable or better than the highest performing zeolites in the fields of gas separations[3-7] and adsorption.[8-11] Because of these interesting properties, these tailorable and ordered MOFs are drawing interest in emerging applications such as sensing,[12] catalysis,[13-15] and electrical energy storage and conversion.[16-18]

It is difficult to avoid defects in crystals even with the most careful synthesis procedures. The "real crystal" always contains some variety of defects, deviating from perfect arrangement of atoms, ions, or molecules.[19] Defects in crystalline materials play an important role in influencing and manipulating the properties of the crystals. For instance,

defects (impurities and dopants) are frequently added into semiconductors to tune their electrical conductivity.[20] Incorporation of defects (e.g., atomic vacancies) has been shown to enhance the catalytic activity of metal oxide catalysts in some situations.[21, 22] Defects in porous crystals (e.g., zeolites) have been shown to affect porosity, thus altering molecular adsorption properties.[23, 24]

MOFs can also contain a considerable amount of defects,[25] and in recent years, defect engineering has become an emerging topic of interest in the MOF community.[26, 27] Although evidence is emerging that extended defects such as stacking faults can exist in MOFs,[28] most works in this area have focused on point defects. Modulated synthesis is a common method to synthesize defective MOFs.[29] For a particular defect site in a MOF framework, the metal ion or cluster can either connect with modulated groups,[30-33] or OH^- and other compensating groups.[34] These defective MOFs exhibit different textural properties and adsorption behavior in comparison to their pristine versions. For example, the defective UiO-66 shows a ~150% increase in pore volume compared to the theoretical value of the defect-free UiO-66 when using acetic acid as the modulator during synthesis. The CO_2 capacity of the resulting defective UiO-66 is increased by ~50% in the high pressure region.[30] Babarao and coworkers found that defective UiO-66 is more hydrophilic than defect-free UiO-66, with a significant water uptake at low humidity levels.[35] Lillerud and coworkers[36] further extended this concept to synthesize a series of defective UiO-66 materials by altering the concentration and the acidity of modulators in the MOF synthesis. While many efforts have been devoted to investigating adsorption properties of defective MOFs, studies of the changes in pore size/opening channel in defective MOFs are limited.

There is a need for systematic adsorption studies utilizing various adsorbate molecules to probe this issue.

Recently, Bennett et al.[37] and Coudert et al.[38] found that the defective UiO-66 derived from modulated synthesis exhibits an increase in mechanical robustness, a factor that needs to be considered when contemplating practical applications with these materials. In addition to mechanical properties, chemical stability is another important factor that needs to be considered when using these porous solids under realistic conditions.[39, 40] A number of contaminants are commonly found in industrial streams of various processes,[8, 41, 42] including CO_2, H_2O, SO_x, NO_x and H_2S. Although there have been many studies on the chemical stability of MOFs,[39, 43-45] the impact of defects on the chemical stability of MOFs still remains an open question. Thus, it is useful to compare the chemical stability of defective MOFs with different compensating groups and concentrations of defects under exposure to water and acidic environments.

In this chapter, we have developed a two-step method (modulated synthesis and post-synthetic heat treatment) to control the concentration of defects and the type of compensating groups incorporated into the structure of UiO-66. Trifluoroacetic acid (TFA), possessing a low boiling point (72.4 °C) and strong acidity (pKa = 0.23),[36] is utilized as the modulator during the synthesis of defective UiO-66. It was found that subjecting the MOF to heat treatment at 320 °C under vacuum can completely remove the TFA compensating groups and generate additional mesopores (5 nm and 9 nm) in the defective UiO-66. However, after heating at 200 °C under vacuum, the defective UiO-66 still possesses TFA compensating groups and only displays additional supermicropores (using the IUPAC definition)[46] without any evidence of mesoporous characteristics. SO_2,

benzene, and cyclohexane are utilized to probe the impact of defects on pore size in the defective UiO-66. When using SO_2 as the probe molecule, the deviation in adsorption capacity between the parent and defective UiO-66 is primarily attributed to the difference in accessible surface areas. However, when using cyclohexane as the probe molecule, we observe that the defective UiO-66 possessing supermicropores displays a 163% increase (mmol/cm^3) in cyclohexane capacity compared to that of the parent UiO-66. The parent and defective UiO-66 are treated separately with aqueous H_2O exposure and SO_2 exposure in dry, humid and aqueous environments to compare and evaluate the chemical stability. Upon removal of TFA compensating groups from the framework, the defective UiO-66 (320 °C) decomposes after exposure to pure water or SO_2-water environments. On the contrary, the parent and defective UiO-66 (200 °C) with TFA compensating groups can better maintain their porosity and crystallinity.

4.2 Experimental Section

4.2.1 Materials

Chemicals. All the chemicals were directly used as obtained from commercial suppliers: $ZrCl_4$ and 1,4-benzenedicarboxylic acid (H_2BDC) from Sigma-Aldrich, trifluoroacetic acid (TFA) from Fisher Chemical, and N, N′-dimethylformamide (DMF) from VWR.

Synthesis of parent UiO-66. Synthesis and solvent exchange of parent UiO-66 were done according to a reported procedure.[47] Activation of parent UiO-66 was done by heating the as-synthesized sample at 200 °C for 18 h under dynamic vacuum.

Synthesis of defective UiO-66. Defective UiO-66 samples were synthesized with the same procedure as parent UiO-66, varying the molar equivalents of TFA with respect to the molar concentration of $ZrCl_4$ in the synthesis solutions (2.5X, 5X, 10X, and 20X, X=equivalent). Typically, 20X defective UiO-66 was synthesized as follows. 0.682 mmol $ZrCl_4$, 0.682 mmol H_2BDC, 13.64 mmol TFA were mixed in 26.5 mL DMF at room temperature. The mixture was homogenized by sonication for 10 min before the solution was placed into a Teflon-lined stainless steel reactor and transferred in a preheated oven at 120 °C for 24.5 h. The as-synthesized defective UiO-66 samples were washed abundantly with fresh DMF, methanol and then dried under air for further use. Defective UiO-66 was heated at 200 °C for 18 h under dynamic vacuum to prepare defective UiO-66 200°C sample (D200). Similarly, defective UiO-66 320 °C (D320) was obtained by heating the as-synthesized sample at 320 °C for 18 h under dynamic vacuum.

4.2.2 Characterization

^{19}F solid-state nuclear magnetic resonance spectroscopy (^{19}F SS-NMR). ^{19}F SS-NMR data were collected with a Bruker (Billerica, MA) Avance 600 spectrometer, using a Bruker 4mm HFX magic-angle spinning (MAS) probe. MAS frequency was actively controlled at ± 2 Hz with cooling and spinning air exit temperature maintained at 0 °C. ^{19}F (564.641 MHz) spectra were collected with a Hahn-echo pulse sequence with a 2.4 μs excitation pulse, a rotor synchronized 4.8 μs refocusing π-pulse and Spinal-64[48] 70 kHz ^{1}H decoupling. EXORCYCLE[49] phase cycling of the excitation and refocusing pulses was used to minimize pulse artifacts from RF inhomogeneity. Recycle delays were set to be at

least 5*T_1 where ^{19}F T_1 was estimated from the null time ($T_1 \sim \tau_{null}/\ln 2$) with an inversion-recovery sequence.

Powder X-ray diffraction (PXRD). PXRD patterns were obtained on a PANalytical X'Pert X-ray diffractometer coupled with an X'Celerator detector and Cu Kα (λ = 1.5418 Å) radiation in ambient conditions, with a step size of 0.02° in 2θ.

N_2 physisorption isotherms. N_2 physisorption isotherms were collected at 77 K on a Quadrasorb system (Quantachrome Instruments). Samples were activated on a Quantachrome FloVac Degasser at 200 ˚C for 18 h under vacuum. The pore size distributions were deduced by using non-local density functional theory (DFT) method that provided in the commercial software (QuadraWin).

Transmission electron microscopy (TEM). TEM images were acquired by a high-resolution TEM FEI Tecnai F30.

Elemental analysis. Elemental analysis for zirconium and fluorine within the defective UiO-66 was performed using inductively coupled plasma-optical emission spectroscopy (ICP-OES) by ALS Global.

Vapor sorption analysis. Vapor isotherms for parent and defective UiO-66 were collected on a 3Flex Surface Characterization Analyzer (Micromeritics) at 25 °C. Prior to sorption measurements, the samples were activated in situ at 200 °C for 18 h under dynamic vacuum.

Aqueous water exposure. Parent and defective UiO-66 (~150 mg) were soaked into DI water in a sealed reactor for 5 days at 25 °C. The reactor was mounted in a rotating

oven to keep homogeneous mixing. The exposed sample was centrifuged and washed with methanol and finally dried under vacuum at 60 °C.

Dry SO_2 analysis. Dry SO_2 isotherms were collected on a lab-built volumetric system. Parent and defective UiO-66 (~30 mg) were activated under vacuum at 200 °C for 18 h. Adsorption isotherms were conducted for pressures ranging from 0 to 2.7 bar at 25 °C. SO_2 loading for each adsorption point was deduced by using the Peng-Robinson equation of state.

Humid SO_2 exposure. Parent and defective UiO-66 (~150 mg) were exposed to humid SO_2 environment at approximately 50 ppm in 85% RH. Details of procedure can be found in a previously reported literature.[50]

Aqueous SO_2 exposure. Parent and defective UiO-66 (~150 mg) were exposed to aqueous SO_2 environment, which was in equilibrium with 50 ppm SO_2 in the vapor phase by Henry's law. Details can be found in a published literature.[51]

4.2.3 Computational Methods

Density functional theory calculations. All UiO-66 related framework structures were optimized by Density Functional Theory calculations with periodic models performed in the Vienna Ab initio Simulation Package (VASP) with a planewave basis set and core electrons represented with projector augmented wave (PAW) potentials.[52, 53] For all DFT calculations, we used Perdew−Burke−Ernzerhof (PBE) functional and semiempirical dispersion corrections via DFT-D3 method to better capture van der Waals dispersion interactions.[54, 55] We used a planewave basis set with a cutoff energy of 600eV, with total

energy and atomic force convergence criteria for energy relaxation of 10^{-6} eV and 0.03 eV/Å. We first optimized the atomic positions and lattice constants of the parent UiO-66 structure using 2×1×1 primitive cell. The optimized lattice constant of corresponding UiO-66 cubic unit cell was 22.66 Å, in good agreement with the experimental value of 20.76 Å. Based on the optimized parent UiO-66 structure, one of the original BDC ligand was substituted by either two trifluoroacetate ligands or two water molecules with two hydroxyl groups incorporating to Zr_6 clusters, both of which were further optimized in calculations where the lattice constants were fixed. Water insertion to metal-ligand bond reaction and water displacement of the protonated ligand reaction occurred on both three optimized framework structures.

Molecular mechanics calculations. N_2 adsorption isotherms on parent UiO-66 and defective UiO-66 were computed using Grand Canonical Monte Carlo (GCMC) simulations in RASPA.[56, 57] The missing cluster UiO-66 model was derived from the **reo** defective UiO-66 structure, where one out of four Zr_6 clusters was missing within every unit cell, causing the ligand connectivity decreased to 8 from 12 in ideal UiO-66.[58] In this study, we used trifluoroacetate ligands to compensate Zr_6 clusters in the **reo** defective UiO-66 structure as shown in Figure B.6 . Lennard-Jones (LJ) and Coulombic potentials were combined to describe the guest molecule - guest molecule and guest molecule - MOF interactions with Lorentz-Berthelot (LB) mixing rules. LJ parameters of frameworks and N_2 were taken from DREIDING force field except for zirconium, which was taken from UFF force field.[59, 60] The framework structures were treated as rigid during GCMC simulations. N_2 was modeled as a three-site model with two sites located at two N atoms and the third one located at its center of mass.[61] 50000 initial cycles were applied for the

system to reach equilibrium, and another 100000 cycles were applied to calculate the average adsorption properties. Four types of guest molecule moves were included during each cycle simulation: translation, rotation, reinsertion, and swap. Good agreement between simulated and experimentally measured N_2 isotherms on parent UiO-66 and defective UiO-66 (D200) supported the validity of the computational models we used (See Figure B.7).

4.3 Results and Discussion

4.3.1 Defective UiO-66 Characterization

As shown in Figure 4.1a, defective UiO-66 was prepared by adding 20 equivalents (20X) of TFA with respect to the molar concentration of the metal salt ($ZrCl_4$) during the solvothermal synthesis. De Vos and co-workers discovered that heat treatment at 320 °C can remove the coordinated TFA groups and then increase the porosity of defective UiO-66, resulting in a catalytically reactive framework.[31] Therefore, two temperatures (200 °C and 320 °C) were selected here to investigate the structural changes in the defective UiO-66 framework upon post-synthetic heat treatment. First, defective UiO-66 was heated at 200 °C (hereafter noted as D200, Figure 4.1b) under vacuum to remove the physically trapped solvent and TFA molecules. The ^{19}F solid-state nuclear magnetic resonance spectroscopy (SS-NMR) spectrum (Figure B.1) shows a single sharp signal at -82 ppm, which indicates the complete removal of physisorbed TFA and solvent molecules, leaving behind the coordinated TFA groups in the resulting framework. On the other hand, post-synthetic heat treatment at 320 °C under vacuum (hereafter noted as D320, Figure 4.1b) leads to the complete removal of coordinated TFA groups from defective UiO-66

framework, as the fluorine signal is completely absent (Figure B.1).[31] The powder X-ray diffraction (PXRD) pattern of D200 is in agreement with those of simulated and parent UiO-66, except for a broad peak ranging around 2° and 7° (Figure B.2). This broad peak is consistent with previous work in the literature and can be assigned to the reflections of the **reo** phase or missing cluster defects.[36] In contrast to D200, the broad reflection between 2° and 7° is not shown in the PXRD pattern of D320 and the intensity of peaks are greatly reduced (Figure B.2). The missing broad peak and reduced crystallinity are possibly due to the partial collapse in the defective framework. This collapse is primarily triggered by the total removal of the coordinated TFA groups from the framework under a post-synthetic heat treatment at 320 °C. Transmission electron microscopy (TEM) images of D200 and D320 were collected to visualize the crystal morphology after post-synthetic heat treatments (Figure 4.1c and 4.1d). D200 shows uniform crystal size and shape in the TEM image (Figure 4.1c). However, mesopores are uniformly distributed in each D320 crystal and each crystal is covered by abundant nanorods (Figure 4.1d). The high-resolution TEM (HR-TEM) image (Figure 4.1d) indicates that these nanorods have a lattice fringe with an interplanar spacing of 0.29 nm, corresponding to the (111) plane of the tetragonal ZrO_2 phase (JCPD 17-0923).[62] However, no PXRD reflections for ZrO_2 are directly observed, as the ZrO_2 nanorods are very small, leading to broad signals that are covered by the background of the pattern. Nevertheless, TEM images provide direct evidence to support our hypothesis that the removal of TFA groups can cause the partial amorphization of defective UiO-66 crystals and will subsequently lead to the formation of ZrO_2 nanorods. This observation of changes in morphology is consistent with ^{19}F SS-NMR and PXRD characterization.

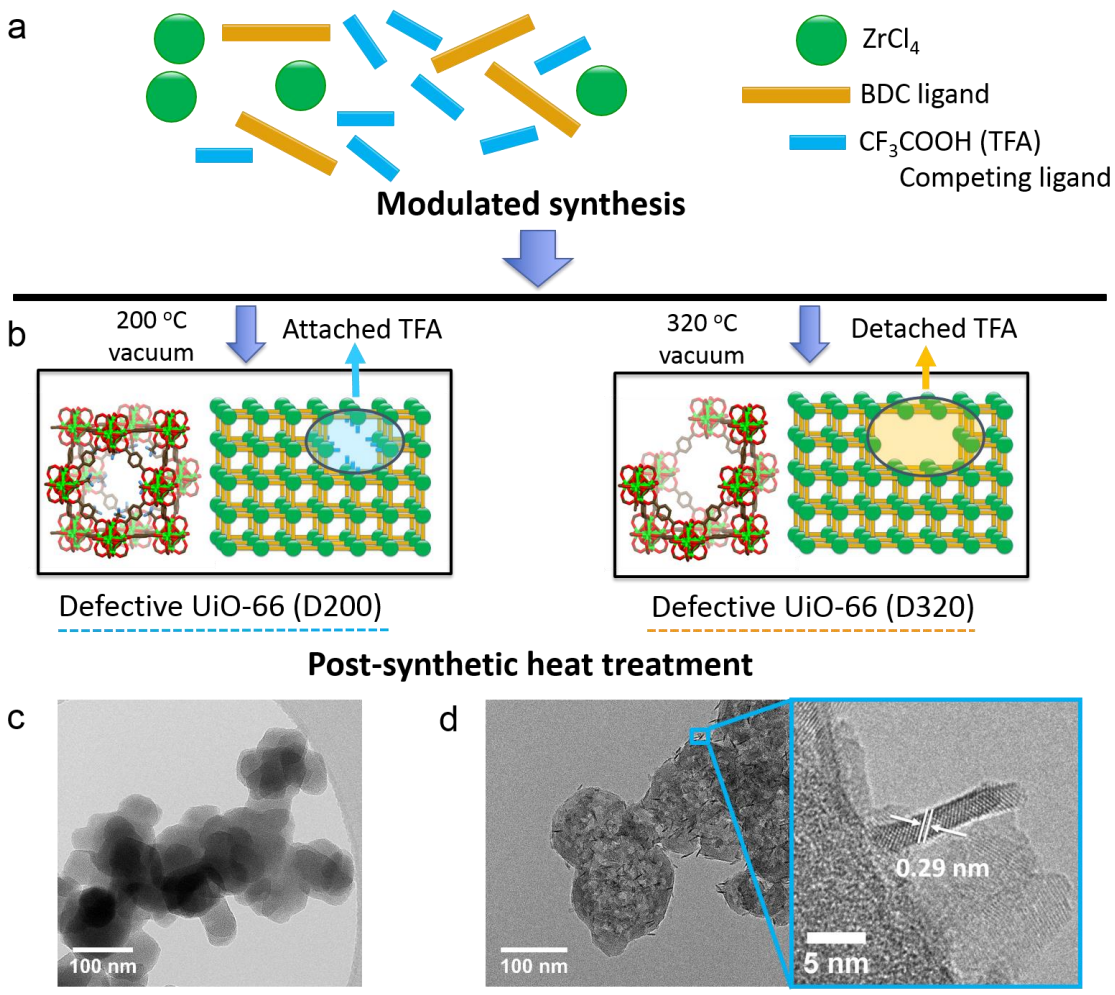

Figure 4.1: (a) Depiction of the modulated synthesis of defective UiO-66 with competing ligands TFA, (b) Proposed structural transformations after post-synthetic heat treatments, (c) TEM image for D200 after post-synthetic heat treatment at 200 °C, (d) D320 after post-synthetic heat treatment at 320 °C and HR-TEM.

N_2 physisorption isotherms at 77 K were measured on parent UiO-66, D200, and D320 (Figure 4.2a). The parent UiO-66 has a Brunauer-Emmett-Teller (BET) surface area of 1179 m^2/g and a total pore volume of 0.56 cm^3/g, which are consistent with values reported in literatures for UiO-66 synthesized without any modulator.[30, 47] The shape of the N_2 adsorption isotherm for D200 exhibits type I behavior but the uptake of N_2 is substantially increased. D200 has a BET surface area of 1808 m^2/g and a total pore volume

of 0.84 cm^3/g, which are significantly higher than those of the parent UiO-66. These higher values can be attributed to the presence of missing cluster defects, which decreases the framework density and increases the porosity. After heating at 320 °C under vacuum, D320 displays a greatly reduced BET surface area of 854 m^2/g with a decreased total pore volume of 0.69 cm^3/g. This is likely a result of partial amorphization of the defective UiO-66 framework, which is consistent with our previous discussion. This partial amorphization behavior is further supported by the shape of the N_2 isotherms of D320. The N_2 isotherms are identified as IUPAC type IV(a) with a hysteresis loop above $P/P_0 = 0.5$, indicating the presence of mesopores in the structure.[46]

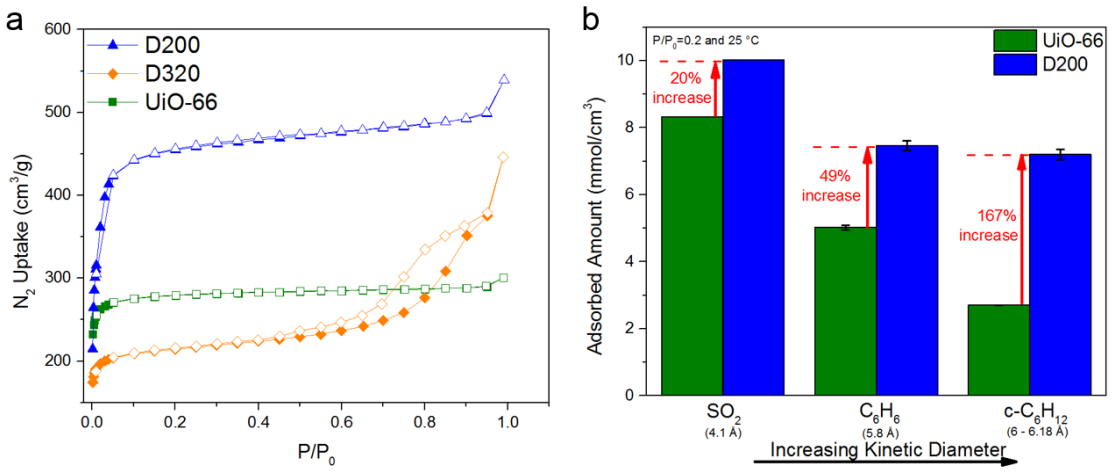

Figure 4.2: (a) N_2 physisorption at 77 K (closed symbols - adsorption; open symbols - desorption), (b) Adsorption capacities (at $P/P_0 = 0.2$ and T = 25 °C) of SO_2, benzene (C_6H_6), and cyclohexane (c-C_6H_{12}) for the parent UiO-66 and D200.

Non-local density functional theory (NL-DFT) was applied to deduce the pore size distributions from the desorption branch of the N_2 isotherms. D320 displays a distribution of pores with widths of 5 nm and 9 nm, demonstrating that mesoporous characteristics are introduced into the framework at 320 °C (Figure B.3). More interestingly, compared with

the parent UiO-66, D200 exhibits a sharp distribution of supermicropores with widths of 1.3 nm, 1.6 nm, and 2 nm (Figure B.3). This observation demonstrates that D200 retains its additional supermicropores after the post-synthetic heat treatment at 200 °C.

4.3.2 Adsorption Properties

Considering the partial amorphization and the relatively low BET surface area in D320, the parent UiO-66 and D200 are chosen as MOF candidates for further adsorption measurements. Given the opening channel in defect-free UiO-66 is ca. 6 Å,[47] SO_2 (4.1 Å), benzene (C_6H_6, 5.8 Å), and cyclohexane (c-C_6H_{12}, 6-6.18 Å)[4] are taken as the probe molecules to determine the impact of defects on the pore size in the defective UiO-66. Based on a reported method,[63] the rate of change in partial pressure of adsorbate molecule in the vapor phase was recorded during the collection of benzene and cyclohexane isotherms. Samples were considered to have reached equilibrium when the observed relative pressure change was less than 0.01% in 5 s. To verify that using an interval of 5 s is reasonable, cyclohexane isotherms with three different interval times (5 s, 30 s, and 300 s) were measured for the parent UiO-66. As shown in Figure B.4, no obvious change was observed among these measurements. With the high concentration of defect sites, the framework density of D200 is not expected to be the same as that of the parent UiO-66. Therefore, it is more appropriate to make a comparison of volumetric capacity between D200 and the parent UiO-66. The volumetric results were obtained by multiplying the gravimetric results (Figure B.5) by the calculated framework density for each material (Parent UiO-66: 1.205 g/cm^3; D200: 0.966 g/cm^3). The framework density for each sample was calculated from the simulated model (Figure B.6) that possesses similar N_2 uptake to the experimental result (Figure B.7). SO_2 adsorption isotherms for the parent UiO-66 and

D200 are shown in Figure B.8. Compared to the parent UiO-66 (8.3 mmol/cm^3 at 25 °C and P/P_0 = 0.2), D200 displays a 20% increase in SO_2 uptake with the capacity of 10 mmol/cm^3 (Figure 4.2b). Since SO_2 (4.1 Å) is small enough to be absorbed in both parent UiO-66 and D200, the dominant factor influencing adsorption behavior is the accessible surface area in each sample. Similarly, multiplying by the corresponding framework density, the gravimetric BET surface areas of parent UiO-66 and D200 were converted to volumetric BET surface areas, resulting in values of 1421 and 1747 m^2/cm^3, respectively. It is worth noting that, compared to the parent UiO-66, D200 shows a 23% increase in volumetric BET surface area that is consistent with the improved SO_2 capacity (20%), confirming that the volumetric capacity is more reasonable to compare the adsorption behavior between D200 and the parent UiO-66.

The benzene and cyclohexane adsorption isotherms for the parent UiO-66 and D200 are present in Figure B.9 and B.10, respectively. When using benzene as the adsorbate molecule, D200 displays a 49% increase in benzene capacity compared to that of the parent UiO-66 (Figure 4.2b). Furthermore, the difference in adsorption capacity between the parent UiO-66 and D200 increases to 163%, using a probe molecule (cyclohexane) with an even larger kinetic diameter (6-6.18 Å), as illustrated in Figure 4.2b. Even though cyclohexane (6-6.18 Å) is slightly larger than the opening size in parent UiO-66, the parent UiO-66 still displays a non-negligible cyclohexane uptake (2.7 mmol/cm^3). Defect-free UiO-66 possesses framework flexibility at some limited levels, but it is not comparable to most flexible MOFs.[64] Therefore, this considerable uptake is more likely due to the opening size being enlarged by the inherent defects in the parent UiO-66.[26, 36] This explanation is supported by the observation that the parent UiO-66 exhibits a small

distribution of supermicropores with widths of 1.3 nm and 1.9 nm in Figure B.3. On the other hand, D200 exhibited a significant cyclohexane capacity of 7.20 mmol/cm^3. This improved cyclohexane adsorption behavior of D200 can be explained by two factors: i) cyclohexane (6-6.18 Å) is much smaller than the supermicropores (1.3 nm, 1.6 nm, and 1.9 nm) in the D200, and ii) D200 possesses a high concentration of supermicropores as shown by the pore size distributions (Figure B.3). Considering the adsorption results for these three molecules, it is clear that missing cluster defects can increase the pore size in the defective UiO-66 and will also enhance the adsorption capacity of large molecules that cannot be effectively captured by the parent UiO-66.

4.3.3 Chemical Stability Analysis under Harsh Conditions

The chemically weak points of most MOF structures are the metal-ligand bonds, where hydrolysis can take place and lead to protonated ligands and dangling metal centers.[39, 65] For a particular defect site of defective UiO-66, a two-sided coordinated ligand is substituted by a one-sided connected modulated group. This fact could make defective UiO-66 less stable than the pristine material, although relevant studies are limited.[25] To evaluate chemical stability, defective UiO-66 variations with various concentrations of defects (2.5X, 5X, 10X, and 20X) were synthesized and exposed to pure liquid water and to SO_2 in dry, humid, and aqueous environments. To make a quantitative comparison, the relationship between the retained BET surface area after exposure and the concentration of defects introduced by TFA modulator in each sample is illustrated in Figure 4.3. The concentration of defects introduced by TFA modulator was determined from inductively coupled plasma optical emission spectrometry (ICP-OES). The obtained results are consistent with the reported values using a thermal gravimetric analysis (TGA) method.[36]

Details of elemental analysis are summarized in Table B.1. The retained BET surface areas (%) were deduced from N_2 physisorption isotherms at 77 K and were summarized in Table B.2. After exposure to liquid water for 120 h (Figure 4.3a, red points), UiO-66 without TFA compensating groups (D320) is unstable at high defect levels, as evidenced by its decrease in retained BET surface area and intensity of PXRD peaks (Figure B.11-B.14). Without the TFA compensating groups in the structure, the extent of degradation in the defective UiO-66 increases as the concentration of defects in the material increases. Similar trends are also observed after exposure to humid SO_2 (6000 ppm-h, 85% relative humidity (85% RH), Figure 4.3c, red points) and aqueous SO_2 (6000 ppm-h, Figure 4.3d, red points). The degradation in D320 results from breakdown of the metal-ligand bonds by the attack of sulfuric and sulfurous acid species.[50, 66] D320 is found to be stable after exposure to dry SO_2 (Figure 4.3b, red points), indicating that SO_2 alone has little impact on the breakage of coordination bonds in D320. In contrast to the relatively low stability of D320, parent UiO-66 and the defective UiO-66 with TFA compensating groups (D200) maintain their porosity and crystallinity (Figure B.15-B.20) after exposure to water and acidic environments. These results indicate that the incorporation of TFA compensating groups can effectively prevent the degradation from the attack of water and acidic sulfur species.

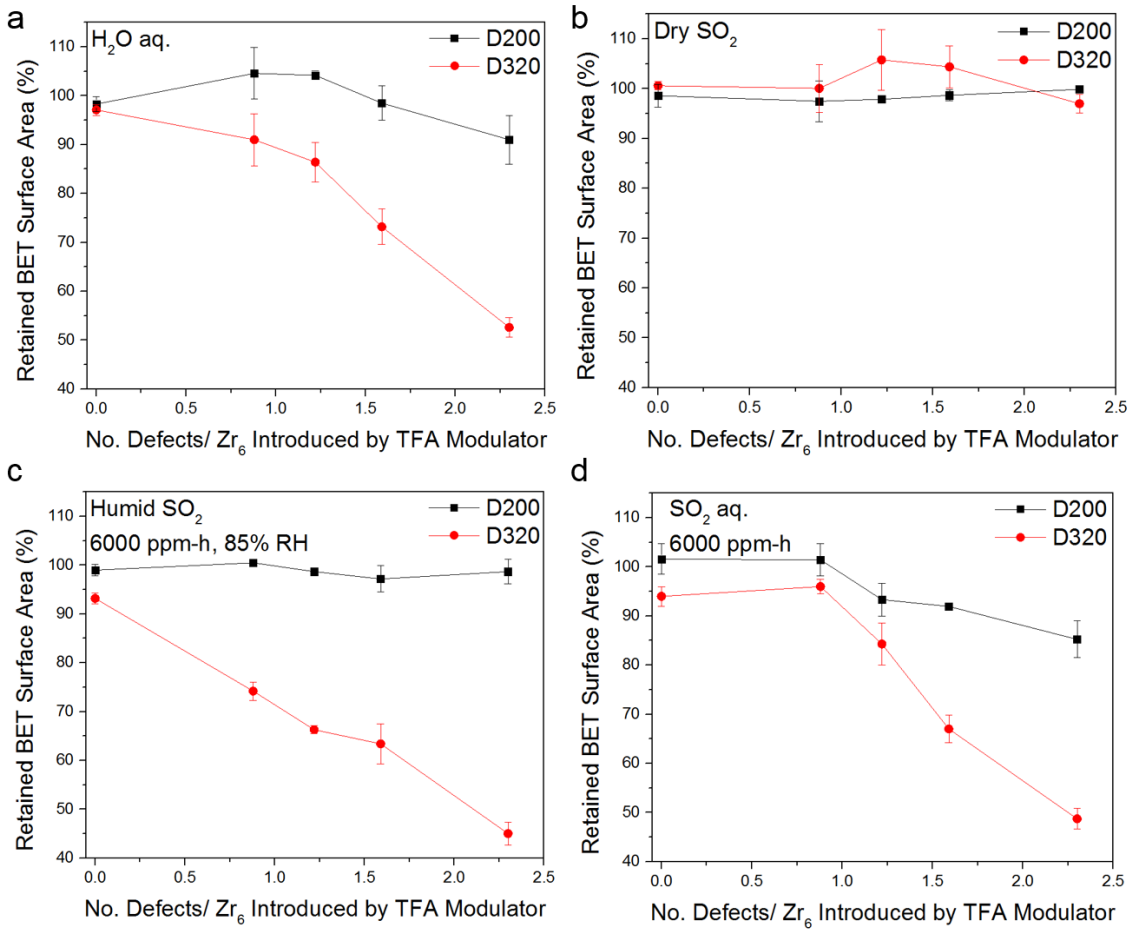

Figure 4.3: Percentages of retained BET surface areas for parent UiO-66 and defective UiO-66 variations (D200 and D320) with different concentration of defects after exposure to (a) aqueous water (120 h), (b) dry SO_2, (c) humid SO_2 (6000 ppm-h, 85% RH), and (d) aqueous SO_2 (6000 ppm-h).

The degradation mechanisms of MOFs upon exposure to water and humid acid gas are currently incompletely understood. Previous studies provide evidence that MOFs undergo degradation, as the reacting molecule attacks the metal-ligand bonds.[43, 50, 66-68] To better understand the extent of degradation observed among these three framework variations upon exposure to water, periodic Density Functional Theory (DFT) calculations were performed to analyze the degradation reaction energetics in the parent and defective UiO-66 structures. Three representative computational models are used in these

calculations: a 2×1×1 unit cell of the UiO-66 primitive unit cell (hydroxylated metal cluster form $Zr_6O_4(OH)_4$) taken from the CoRE MOF database,[69] its derivative unit cell with one BDC ligand substituted by two TFA groups, and its derivative unit cell with one missing BDC ligand capped by a water and hydroxyl group, representing the parent UiO-66, D200, and D320 structures, respectively. In this chapter, we propose a potential degradation pathway for three types of frameworks upon water attack, shown in Figure 4.4.

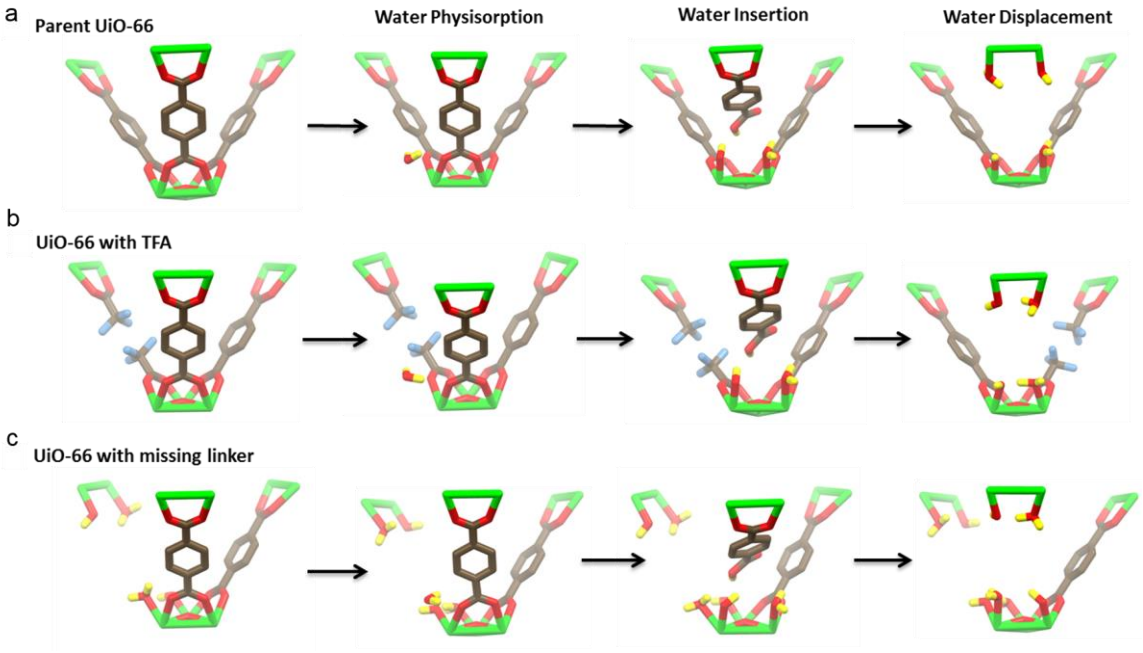

Figure 4.4: Proposed degradation mechanisms for (a) the parent UiO-66, (b) UiO-66 with TFA (D200), and (c) UiO-66 with a missing linker (D320). Only the structural components associated with the degradation reactions are shown, with the rest of the structure omitted for clarity. Zr atoms are shown in green, O atoms are shown in red, C atoms are shown in gray, H atoms are shown in yellow and F atoms are shown in blue.

When a water molecule is physisorbed and dissociates near the Zr metal center, water can donate a proton to the BDC ligand, with the remaining hydroxyl group coordinating to the Zr metal center to maintain charge neutrality. As a result, multiple water insertion reactions can cause the cleavage of the metal-ligand bond and eventually the

removal of neutral, protonated BDC ligand from the frameworks. In the hydrolyzed structures, water molecules are coordinated to the open metal sites and the formation energies along these proposed reaction pathways are calculated as the energy difference between reactants and products, with isolated water molecules and the parent UiO-66 framework serving as the reactants for each product. Water physisorption on the Zr_6 cluster alone is energetically favorable in all three frameworks, as shown in water physisorption step in Table 4.1. This is expected because water isotherms measured experimentally for the parent UiO-66 framework exhibit appreciable water uptake at 30% RH, and the missing linker defects make UiO-66 even more hydrophilic.[70] As the reaction moves forward, water insertion to the metal-ligand bond and the removal of the neutral and protonated BDC ligand by water displacement are only thermodynamically favorable in the UiO-66 with missing linker defective framework, with reaction energies of -84 kJ/mol and -39 kJ/mol, respectively, shown in water insertion step and water displacement step in Table 4.1. For the parent UiO-66 and the defective UiO-66 with the incorporation of TFA compensating groups (D200), the cleavage of the metal-ligand bond and the removal of neutral and protonated BDC ligand are thermodynamically unfavorable, in agreement with the phenomena observed experimentally that the parent UiO-66 and D200 samples retain nearly all their BET surface areas upon water exposure.

Table 4.1: Formation energies of the proposed reaction pathways.

MOF	Water Physisorption (kJ/mol)	Water Insertion (kJ/mol)	Water Displacement (kJ/mol)
Parent UiO-66	-26	20	102
UiO-66 with TFA (D200)	-35	17	29
UiO-66 with missing linker (D320)	-90	-84	-39

4.4 Conclusions

In conclusion, we have taken a combination of modulated synthesis and post-synthetic heat treatment to manipulate the concentration of defects and type of compensating groups in the defective UiO-66. We have conducted SO_2, benzene and cyclohexane adsorption measurements to elucidate the impact of defects on the pore size in the defective UiO-66 (D200). With the presence of supermicropores, D200 can effectively capture larger molecules in comparison to parent UiO-66. Of particular note, the defective UiO-66 with TFA compensating groups exhibits excellent chemical stability towards water and acidic species, as no obvious decrease in surface area was observed after exposure experiments. Additionally, using DFT calculations, we have shown that the steps of water insertion and water displacement are thermodynamically unfavorable for the defective UiO-66 with TFA, which is consistent with our experimental observation. This work not only advances the understanding of textural properties and chemical stability of defect-engineered MOFs but also provides a novel idea of preparing defective MOFs in a chemically stable structure.

4.5 References

1. Zhou, H. C.; Long, J. R.; Yaghi, O. M., *Chem. Rev.* **2012**, *112* (2), 673-674.

2. Schoedel, A.; Li, M.; Li, D.; O'Keeffe, M.; Yaghi, O. M., *Chem. Rev.* **2016**, *116* (19), 12466-12535.

3. Li, J. R.; Sculley, J.; Zhou, H. C., *Chem. Rev.* **2012**, *112* (2), 869-932.

4. Li, J. R.; Kuppler, R. J.; Zhou, H. C., *Chem. Soc. Rev.* **2009**, *38* (5), 1477-1504.

5. Li, J. R.; Ma, Y. G.; McCarthy, M. C.; Sculley, J.; Yu, J. M.; Jeong, H. K.; Balbuena, P. B.; Zhou, H. C., *Coord. Chem. Rev.* **2011**, *255* (15-16), 1791-1823.

6. Britt, D.; Furukawa, H.; Wang, B.; Glover, T. G.; Yaghi, O. M., *Proc. Natl. Acad. Sci. U.S.A.* **2009**, *106* (49), 20637-20640.

7. Bloch, E. D.; Queen, W. L.; Krishna, R.; Zadrozny, J. M.; Brown, C. M.; Long, J. R., *Science* **2012**, *335* (6076), 1606-1610.

8. Liu, J.; Thallapally, P. K.; McGrail, B. P.; Brown, D. R.; Liu, J., *Chem. Soc. Rev.* **2012**, *41* (6), 2308-2322.

9. Wu, H. H.; Gong, Q. H.; Olson, D. H.; Li, J., *Chem. Rev.* **2012**, *112* (2), 836-868.

10. Furukawa, H.; Gandara, F.; Zhang, Y. B.; Jiang, J. C.; Queen, W. L.; Hudson, M. R.; Yaghi, O. M., *J. Am. Chem. Soc.* **2014**, *136* (11), 4369-4381.

11. Jiao, Y.; Morelock, C. R.; Burtch, N. C.; Mounfield, W. P.; Hungerford, J. T.; Walton, K. S., *Ind. Eng. Chem. Res.* **2015**, *54* (49), 12408-12414.

12. Hu, Z. C.; Deibert, B. J.; Li, J., *Chem. Soc. Rev.* **2014**, *43* (16), 5815-5840.

13. Farrusseng, D.; Aguado, S.; Pinel, C., *Angew. Chem. Int. Ed.* **2009**, *48* (41), 7502-7513.

14. Corma, A.; Garcia, H.; Xamena, F., *Chem. Rev.* **2010**, *110* (8), 4606-4655.

15. Liu, J. W.; Chen, L. F.; Cui, H.; Zhang, J. Y.; Zhang, L.; Su, C. Y., *Chem. Soc. Rev.* **2014**, *43* (16), 6011-6061.

16. Qu, C.; Jiao, Y.; Zhao, B.; Chen, D.; Zou, R.; Walton, K. S.; Liu, M., *Nano Energy* **2016**, *26*, 66-73.

17. Choi, K. M.; Jeong, H. M.; Park, J. H.; Zhang, Y. B.; Kang, J. K.; Yaghi, O. M., *ACS Nano* **2014**, *8* (7), 7451-7457.

18. Xia, W.; Qu, C.; Liang, Z.; Zhao, B.; Dai, S.; Qiu, B.; Jiao, Y.; Zhang, Q.; Huang, X.; Guo, W.; Dang, D.; Zou, R.; Xia, D.; Xu, Q.; Liu, M., *Nano Lett.* **2017**, *17* (5), 2788-2795.

19. Bollmann, W., *Crystal Defects and Crystalline Interfaces*. 1st ed.; Springer-Verlag Berlin Heidelberg: Berlin, 1970.

20. Campbell, S. A., *Fabrication Engineering at the Micro - and Nanoscale*. 4th ed.; Oxford University Press: New York, 2013.

21. Polarz, S.; Strunk, J.; Ischenko, V.; van den Berg, M. W. E.; Hinrichsen, O.; Muhler, M.; Driess, M., *Angew. Chem. Int. Ed.* **2006**, *45* (18), 2965-2969.

22. Lawrence, N. J.; Brewer, J. R.; Wang, L.; Wu, T. S.; Wells-Kingsbury, J.; Ihrig, M. M.; Wang, G. H.; Soo, Y. L.; Mei, W. N.; Cheung, C. L., *Nano Lett.* **2011**, *11* (7), 2666-2671.

23. Kortunov, P.; Vasenkov, S.; Chmelik, C.; Karger, J.; Ruthven, D. M.; Wloch, J., *Chem. Mater.* **2004**, *16* (18), 3552-3558.

24. Trzpit, M.; Soulard, M.; Patarin, J.; Desbiens, N.; Cailliez, F.; Boutin, A.; Demachy, I.; Fuchs, A. H., *Langmuir* **2007**, *23* (20), 10131-10139.

25. Sholl, D. S.; Lively, R. P., *J. Phys. Chem. Lett.* **2015**, *6* (17), 3437-3444.

26. Fang, Z. L.; Bueken, B.; De Vos, D. E.; Fischer, R. A., *Angew. Chem. Int. Ed.* **2015**, *54* (25), 7234-7254.

27. Cheetham, A. K.; Bennett, T. D.; Coudert, F. X.; Goodwin, A. L., *Dalton Trans.* **2016**, *45* (10), 4113-4126.

28. Han, R.; Sholl, D. S., *J. Phys. Chem. C* **2016**, *120* (48), 27380-27388.

29. Schaate, A.; Roy, P.; Godt, A.; Lippke, J.; Waltz, F.; Wiebcke, M.; Behrens, P., *Chem. Eur. J.* **2011**, *17* (24), 6643-6651.

30. Wu, H.; Chua, Y. S.; Krungleviciute, V.; Tyagi, M.; Chen, P.; Yildirim, T.; Zhou, W., *J. Am. Chem. Soc.* **2013**, *135* (28), 10525-10532.

31. Vermoortele, F.; Bueken, B.; Le Bars, G.; Van de Voorde, B.; Vandichel, M.; Houthoofd, K.; Vimont, A.; Daturi, M.; Waroquier, M.; Van Speybroeck, V.; Kirschhock, C.; De Vos, D. E., *J. Am. Chem. Soc.* **2013**, *135* (31), 11465-11468.

32. Yuan, S. A.; Zou, L. F.; Qin, J. S.; Li, J. L.; Huang, L.; Feng, L. A.; Wang, X. A.; Bosch, M.; Alsalme, A.; Cagin, T.; Zhou, H. C., *Nat. Commun.* **2017**, *8*, 15356.

33. Fang, Z. L.; Durholt, J. P.; Kauer, M.; Zhang, W. H.; Lochenie, C.; Jee, B.; Albada, B.; Metzler-Nolte, N.; Poppl, A.; Weber, B.; Muhler, M.; Wang, Y. M.; Schmid, R.; Fischer, R. A., *J. Am. Chem. Soc.* **2014**, *136* (27), 9627-9636.

34. Trickett, C. A.; Gagnon, K. J.; Lee, S.; Gandara, F.; Burgi, H. B.; Yaghi, O. M., *Angew. Chem. Int. Ed.* **2015**, *54* (38), 11162-11167.

35. Liang, W. B.; Coghlan, C. J.; Ragon, F.; Rubio-Martinez, M.; D'Alessandro, D. M.; Babarao, R., *Dalton Trans.* **2016**, *45* (11), 4496-4500.

36. Shearer, G. C.; Chavan, S.; Bordiga, S.; Svelle, S.; Olsbye, U.; Lillerud, K. P., *Chem. Mater.* **2016**, *28* (11), 3749-3761.

37. Van de Voorde, B.; Stassen, I.; Bueken, B.; Vermoortele, F.; De Vos, D.; Ameloot, R.; Tan, J. C.; Bennett, T. D., *J. Mater. Chem. A* **2015**, *3* (4), 1737-1742.

38. Thornton, A. W.; Babarao, R.; Jain, A.; Trousselet, F.; Coudert, F. X., *Dalton Trans.* **2016**, *45* (10), 4352-4359.

39. Burtch, N. C.; Jasuja, H.; Walton, K. S., *Chem. Rev.* **2014**, *114* (20), 10575-10612.

40. Sholl, D. S.; Lively, R. P., *Nature* **2016**, *532* (7600), 435-437.

41. Rezaei, F.; Rownaghi, A. A.; Monjezi, S.; Lively, R. P.; Jones, C. W., *Energy Fuels* **2015**, *29* (9), 5467-5486.

42. DeCoste, J. B.; Peterson, G. W., *Chem. Rev.* **2014**, *114* (11), 5695-5727.

43. Pang, S. H.; Han, C.; Sholl, D. S.; Jones, C. W.; Lively, R. P., *Chem. Mater.* **2016**, *28* (19), 6960-6967.

44. Mounfield, W. P.; Tumuluri, U.; Jiao, Y.; Li, M. J.; Dai, S.; Wu, Z. L.; Walton, K. S., *Microporous Mesoporous Mater.* **2016**, *227*, 65-75.

45. Joshi, J. N.; Garcia-Gutierrez, E. Y.; Moran, C. M.; Deneff, J. I.; Walton, K. S., *J. Phys. Chem. C* **2017**, *121* (6), 3310-3319.

46. Thommes, M.; Kaneko, K.; Neimark, A. V.; Olivier, J. P.; Rodriguez-Reinoso, F.; Rouquerol, J.; Sing, K. S. W., *Pure Appl. Chem.* **2015**, *87* (9-10), 1051-1069.

47. Cavka, J. H.; Jakobsen, S.; Olsbye, U.; Guillou, N.; Lamberti, C.; Bordiga, S.; Lillerud, K. P., *J. Am. Chem. Soc.* **2008**, *130* (42), 13850-13851.

48. Fung, B. M.; Khitrin, A. K.; Ermolaev, K., *J. Magn. Reson.* **2000**, *142* (1), 97-101.

49. Rance, M.; Byrd, R. A., *J. Magn. Reson.* **1983**, *52* (2), 221-240.

50. Mounfield, W. P.; Han, C.; Pang, S. H.; Tumuluri, U.; Jiao, Y.; Bhattacharyya, S.; Dutzer, M. R.; Nair, S.; Wu, Z.; Lively, R. P.; Sholl, D. S.; Walton, K. S., *J. Phys. Chem. C* **2016**, *120* (48), 27230-27240.

51. Zhu, G. H.; Hoffman, C. D.; Liu, Y.; Bhattacharyya, S.; Tumuluri, U.; Jue, M. L.; Wu, Z. L.; Sholl, D. S.; Nair, S.; Jones, C. W.; Lively, R. P., *Chem. Eur. J.* **2016**, *22* (31), 10743-10747.

52. Kresse, G.; Joubert, D., *Phys. Rev. B: Condens. Matter.* **1999**, *59* (3), 1758-1775.

53. Blochl, P. E., *Phys. Rev. B: Condens. Matter.* **1994**, *50* (24), 17953-17979.

54. Lee, K.; Murray, E. D.; Kong, L. Z.; Lundqvist, B. I.; Langreth, D. C., *Phys. Rev. B: Condens. Matter.* **2010**, *82* (8), 081101.

55. Grimme, S.; Antony, J.; Ehrlich, S.; Krieg, H., *J. Chem. Phys.* **2010**, *132* (15), 154104.

56. Gelb, L. D.; Gubbins, K. E., *Langmuir* **1999**, *15* (2), 305-308.

57. Dubbeldam, D.; Calero, S.; Ellis, D. E.; Snurr, R. Q., *Mol. Simul.* **2016**, *42* (2), 81-101.

58. Cliffe, M. J.; Wan, W.; Zou, X. D.; Chater, P. A.; Kleppe, A. K.; Tucker, M. G.; Wilhelm, H.; Funnell, N. P.; Coudert, F. X.; Goodwin, A. L., *Nat. Commun.* **2014**, *5*, 4176.

59. Mayo, S. L.; Olafson, B. D.; Goddard, W. A., *J. Phys. Chem.* **1990**, *94* (26), 8897-8909.

60. Rappe, A. K.; Casewit, C. J.; Colwell, K. S.; Goddard, W. A.; Skiff, W. M., *J. Am. Chem. Soc.* **1992**, *114* (25), 10024-10035.

61. Potoff, J. J.; Siepmann, J. I., *AlChE J.* **2001**, *47* (7), 1676-1682.

62. Saravanan, K.; Tyagi, B.; Bajaj, H. C., *Appl. Catal., B* **2016**, *192*, 161-170.

63. Savitzky, A.; Golay, M. J. E., *Anal. Chem.* **1964**, *36* (8), 1627-1639.

64. Bennett, T. D.; Cheetham, A. K.; Fuchs, A. H.; Coudert, F. X., *Nat. Chem.* **2017**, *9* (1), 11-16.

65. Howarth, A. J.; Liu, Y. Y.; Li, P.; Li, Z. Y.; Wang, T. C.; Hupp, J.; Farha, O. K., *Nat. Rev. Mater.* **2016**, *1* (3), 15018.

66. Bhattacharyya, S.; Pang, S. H.; Dutzer, M. R.; Lively, R. P.; Walton, K. S.; Sholl, D. S.; Nair, S., *J. Phys. Chem. C* **2016**, *120* (48), 27221-27229.

67. Burtch, N. C.; Walton, K. S., *Acc. Chem. Res.* **2015**, *48* (11), 2850-2857.

68. Zhang, C. Y.; Han, C.; Sholl, D. S.; Schmidt, J. R., *J. Phys. Chem. Lett.* **2016**, *7* (3), 459-464.

69. Chung, Y. G.; Camp, J.; Haranczyk, M.; Sikora, B. J.; Bury, W.; Krungleviciute, V.; Yildirim, T.; Farha, O. K.; Sholl, D. S.; Snurr, R. Q., *Chem. Mater.* **2014**, *26* (21), 6185-6192.

70. Ghosh, P.; Colon, Y. J.; Snurr, R. Q., *Chem. Commun.* **2014**, *50* (77), 11329-11331.

CHAPTER 5. FUNCTIONALIZED NICKEL HYDROXIDE DERIVED FROM PILLARED METAL-ORGANIC FRAMEWORKS FOR HIGH-PERFORMANCE SUPERCAPACITORS

This chapter was reproduced from Qu, C.*; Jiao, Y.*; Zhao, B.; Chen, D.; Zou, R.; Walton, K. S.; Liu, M., "Nickel-based pillared MOFs for high-performance supercapacitors: Design, synthesis and stability study," *Nano Energy*, 2016, volume 26, pages 66-73, Copyright 2016, with permission from Elsevier. *: co-first authors. In this chapter, Qu, C. conducted electrochemistry experiments. Chen, D. collected FTIR and Raman spectra.

5.1 Introduction

Supercapacitors (SCs) have attracted increasing attention as novel energy storage devices due to their higher power densities, faster charge-discharge rates, and longer cycling lives than conventional rechargeable batteries.[1-2] According to the physicochemical processes responsible for energy storage, SCs are generally classified into: i) electrical double layer capacitors (EDLCs) where the energy storage is associated with charge separation within double layers (e.g. porous carbon materials)[3, 4] and, ii) pseudocapacitors which utilize near-surface redox reactions of transition metal oxides and hydroxides materials.[5-7] In general, EDLCs offer a very high charge-discharge rate with a long cycle life but have low capacitance, while pseudocapacitors have high capacitance but slightly inferior rate capability and cycling life.[3-7]

To narrow the performance gap between these two types of capacitors, rational design of advanced electrode materials is necessary. Metal-organic frameworks (MOFs) are drawing much attention as a potential electrode candidate for SCs[8-16] due to their remarkable surface areas, facile tunable pore sizes, and peculiar structures with potential pseudo-capacitive redox centers[16] either utilized as porous metal oxides,[8, 9] porous carbon templates[10-12] or in a direct application as a new type of electrode material.[13-15] However, the instability of most MOFs or MOF-derived electrode material during charge-discharge process is widely considered a major limitation for their application in SCs.[17, 18]

To achieve an improved cycling performance, we tried to synthesize kinetically stable MOFs via ligand functionalization. Our previous work demonstrates that it is possible to adjust the water stability of pillared MOFs both in the positive and negative directions by proper functionalization of the 1,4-benzenedicarboxylate (BDC) ligand.[19, 20] Notably, placing nonpolar groups (e.g., -methyl) on the BDC linker leads to enhanced stability of DMOF, while placing polar groups (e.g., -OH) on the BDC linker has no such effect on the structure compared to the original version. Besides, Tan et al.[21] also found the stability of different metal based isostructural DMOFs follows the order of Cu-DMOF < Ni-DMOF > Zn-DMOF > Co-DMOF which corresponds to the bond dissociation energy of diatomic molecules metal-oxygen and overall formation (stability) constants of metal amine complexes.

In this chapter, we summarized previous results[17, 19-21] and synthesized nickel-based, pillared MOFs of similar topology using 9,10-anthracenedicarboxylic acid (ADC), 2,3,5,6-tetramethyl-1,4-benzenedicarboxylic acid (TM), and 1,4-naphthalenedicarboxylic acid (NDC) as carboxylate ligands and 1,4-diazabicyclo[2.2.2]octane (DABCO) as pillar

ligands and have successfully confirmed the water stability of Ni-DMOF-ADC and Ni-DMOF-TM. When fabricated as electrodes for SCs, the Ni-DMOF-ADC derived highly functionalized nickel hydroxide electrode inherited the high stability of DMOF-ADC and showed excellent cycling performance, the capacitance retention after 16000 cycles at 10 A/g was > 98%, which was much higher than that of the relatively less stable Ni-DMOF-TM and the unstable Ni-DMOF-NDC derived electrodes. These results indicate the impact of DMOFs' chemical stability on long-term cycling stability and show that water stable DMOFs could be a promising electrode precursor for long cycle-life electrochemical capacitors.

5.2 Experimental Section

5.2.1 Materials

Synthesis of Ni-DMOF-ADC, Ni-DMOF-TM, and Ni-DMOF-NDC. The Ni-DMOF-ADC was synthesized by using a simple solvothermal method modified from literature.[22] All the chemicals were commercially available and used as obtained without further purification. Typically, 1 mmol of $Ni(NO_3)_2 \cdot 6H_2O$, 1 mmol of ADC, and 0.5 mmol of DABCO were dissolved in 10 mL of DMF at room temperature in a glass beaker and the resulting slurry was stirred for 2 h . After filtering the solution, the filtrate was poured into a Teflon-lined stainless steel reactor and kept in a preheated oven at 120 °C for 2 days. The resulting materials were filtered and washed with DMF repeatedly after cooling to room temperature in air. Ni-DMOF-TM was synthesized according to the work of Jasuja et al.[20] and Ni-DMOF-1,4-NDC (Ni-DMOF-NDC) was prepared with slight modification from the literature[22] for Zn-DMOF-1,4-NDC; i.e., by dissolving 0.63 mmol of

$Ni(NO_3)_2 \cdot 6H_2O$, 0.63 mmol of 1,4-NDC, and 0.31 mmol of DABCO in 15 mL of DMF in a glass beaker and kept stirring for 2 h at room temperature. The rest of the procedure was the same as that of Ni-DMOF-ADC. All the activated samples were prepared by heating at 110 °C for 12 h under vacuum.

5.2.2 Characterization

The crystallographic structures of the materials were obtained using an X'Pert X-ray PANalytical diffractometer with an X'celerator and Cu Kα (λ = 1.5418 Å) radiation at ambient condition, with a step size of 0.02° in 2θ. The N_2 isotherms of the materials were measured at 77K using a Quadrasorb system (Quantachrome Instruments). Applying the Brunauer-Emmett-Teller (BET) model[23] to the collected isotherms, specific surface areas were determined for each material. Raman spectroscopy was used for the structural analysis on both fresh and cycled electrode materials. FTIR was used to determine different functional groups in electrode materials. The microstructure and morphology were examined by using a scanning electron microscope (Zeiss Ultra60 FE-SEM). Water vapor adsorption isotherms were collected at 22 °C and 1 bar using a 3Flex Surface Characterization Analyzer (Micromeritics). The samples (~30-40 mg) were activated in situ (110 °C, under dynamic vacuum) to evacuate any guest molecules from the framework prior to the measurements of water vapor isotherms. Experiments were tested only up to $P/P_0 = 0.90$ to avoid the water condensation. After dosing, each adsorption and desorption point was checked every 5 s until pressure change was less than 0.01%.

5.2.3 Electrochemical Measurements

The electrochemical experiments were performed on a Solartron SI 1286 electrochemical workstation. Cyclic voltammograms and galvanostatic charge-discharge (GCD) tests were carried out using a three-electrode configuration. For the working electrode, a mixture consisting of 70 wt% active material, 20 wt% Super P, and 10 wt% PTFE binder was well mixed and then rolled with ethanol solvent to form a uniform thin film with a typical areal mass of ~1.9 mg/cm^2. The film electrode was compressed by two nickel foams and dried overnight under vacuum at 80 ˚C. A Pt mesh electrode was used as the counter electrodes, while an Ag-AgCl electrode filled with AgCl saturated 4 M KCl solution was used as the reference electrode. The cyclic voltammetric (CV) curves were carried out with a potential window from 0 to 0.5 V at different scan rates. The charge-discharge tests were achieved by cycling the potential between 0 and 0.45 V at various current densities with a 2 M KOH electrolyte. To avoid the contributed capacitance from Ni foam during the cycling experiments,[24] we fabricated an asymmetric capacitor with a Ni-DMOF-based anode and an activated carbon (AC)-based cathode. The cyclic stability was evaluated by GCD measurements at a current density of 10 A/g.

5.3 Results and Discussion

5.3.1 Characteristics of Ni-DMOFs

The crystallinity and purity of the prepared DMOF samples was confirmed by comparing with simulated patterns from single crystal X-ray diffraction (Figure C.1). Similarities among all the patterns were evident; these frameworks are isostructural to the simulated pattern, suggesting that all the MOFs probably had a layered topology (CCDC no. 992483) which can be described as metal paddle-wheel clusters connected by

functionalized BDC ligands to form 2-D layers that are further pillared together by DABCO ligands to 3-D structure (Figure 5.1).[22] N_2 physisorption isotherms (Figure C.2) at 77 K on the activated MOF samples showed typical type I behavior according to the IUPAC classification.[25]

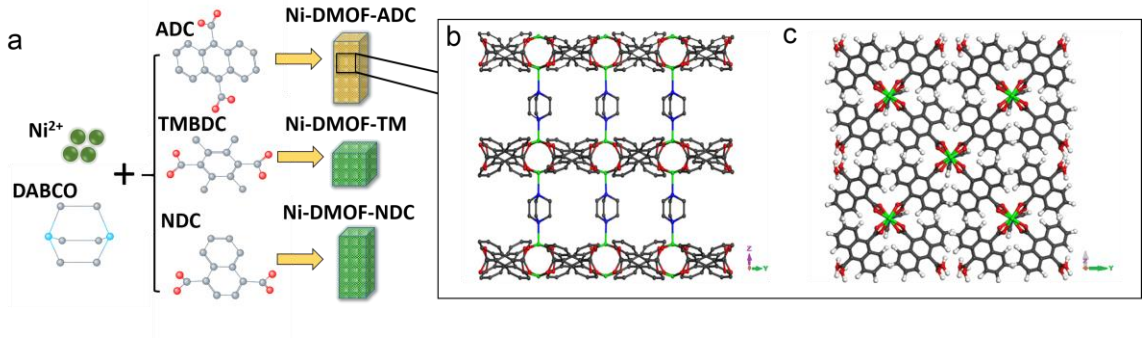

Figure 5.1: (a) Schematic of the synthesis procedure of DMOFs and wireframe view of 3-D Ni-DMOF-ADC along (b) the (1, 0, 0) surface and (c) the (0, 0, 1) surface. N atoms are blue, Ni atoms are green, C atoms are grey, and H atoms are omitted for clarity.

5.3.2 Chemical Stability under Exposure to Water

To investigate the water stability of examined structures, several characterization methods were performed on each nickel-based DMOF variation, including water vapor isotherms, PXRD, SEM, and surface area analysis from BET modeling[23] of N_2 adsorption isotherms before and after water exposure. Figure 5.2d shows the water vapor isotherms at 22 °C for Ni-DMOF-ADC, Ni-DMOF-TM, and Ni-DMOF-NDC. The water vapor adsorption capacities observed at $P/P_0 = 0.9$ are 16.78 mmol/g for Ni-DMOF-ADC, 25.10 mmol/g for Ni-DMOF-TM, and 15.34 mmol/g for Ni-DMOF-NDC. The type V isotherm profiles of the examined samples is likely an attribute of the presence of nonpolar groups (-methyl, -naphthalene, and -anthracene) within the porous structure.[20] In agreement with the trend reported in literature,[19] Ni-DMOF-ADC and Ni-DMOF-TM show non-negligible

hysteresis loops, indicating some amount of water is retained in the pores and cannot be fully desorbed, even exposing to dry air (0% relative humidity (RH) point in the desorption isotherm). This unexpected behavior could be attributed to the various levels of flexibility[26] or defects.[27] Ni-DMOF-NDC retains 42% of maximum uptake which is much higher than 18% for Ni-DMOF-ADC and 9% for Ni-DMOF-TM, indicating that Ni-DMOF-NDC is degraded upon water exposure. Indeed, Ni-DMOF-NDC sample was significantly degraded upon water vapor exposure, as shown in SEM images before and after water exposure (Figure 5.3c and 5.3f). In addition, Ni-DMOF-NDC displayed significant change in crystallinity (Figure 5.2c) and loss of surface area Table 5.1 after water exposure. This result is consistent with the work reported by Jasuja et al.,[17] demonstrating that Zn-based DMOF-1,4 NDC was not stable upon water exposure.

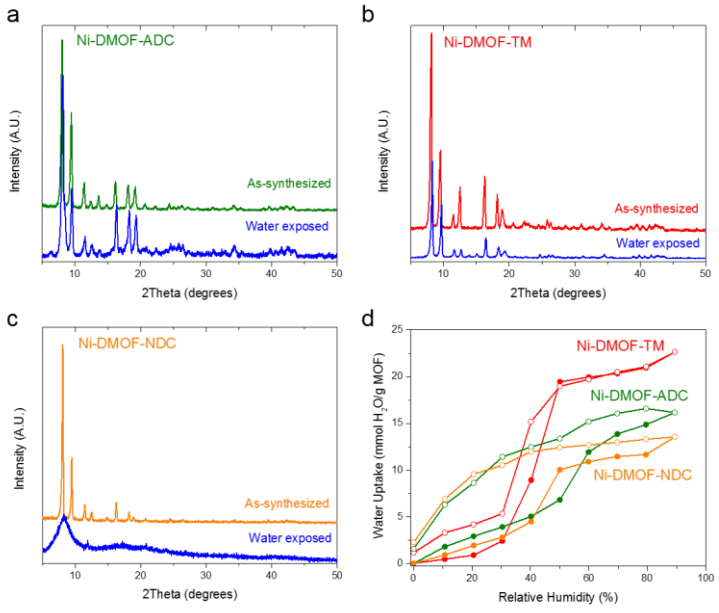

Figure 5.2: PXRD patterns of as-synthesized and water exposed (after 90% RH) (a) Ni-DMOF-ADC, (b) Ni-DMOF-TM and (c) Ni-DMOF-NDC. (d) Water vapor isotherms at 22 ˚C for Ni-DMOFs (closed symbols – adsorption, open symbols – desorption).

On the other hand, no obvious change in PXRD patterns (Figure 5.2a and 5.2b) or loss of surface area (Table 5.1) was observed in both Ni-DMOF-ADC and Ni-DMOF-TM samples after water exposure, illustrating Ni-DMOF-ADC and Ni-DMOF-TM retain their porous structures after adsorbing large amounts of water (> 15 mmol/g at 90% RH). In addition, almost no change in either crystal size or morphology was observed from SEM images of Ni-DMOF-ADC (Figure 5.3a and 5.3d) and Ni-DMOF-TM (Figure 5.3b and 5.3e) before and after water exposure. The stability of Ni-DMOF-ADC and Ni-DMOF-TM could be attributed to the presence of nonpolar groups on the BDC ligand.

Table 5.1: Comparison of properties of Ni-DMOFs synthesized in this chapter.

Material	Activation methods (vacuum)	Total pore volume[a] (cm^3/g)	BET surface areas (m^2/g)	BET surface area (after 90% RH)	Stability
Ni-DMOF-NDC	110 ˚C (12 h)	0.428	943	0.78	Unstable
Ni-DMOF-TM	110 ˚C (12 h)	0.453	1036	960	Stable
Ni-DMOF-ADC	110 ˚C (12 h)	0.365	783	760	Stable

[a]Calculated from N_2 adsorption at 77 K at $P/P_0 = 0.8$.

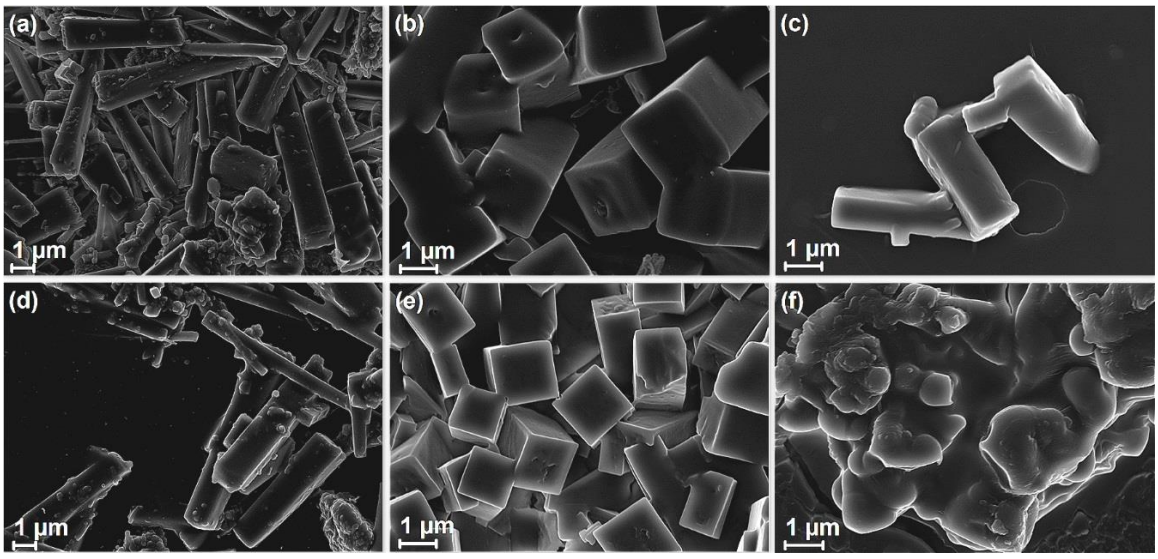

Figure 5.3: SEM images of (a) Ni-DMOF-ADC, (b) Ni-DMOF-TM, (c) Ni-DMOF-NDC before water vapor exposure, and (d) Ni-DMOF-ADC, (e) Ni-DMOF-TM, (e) Ni-DMOF-NDC after water vapor exposure.

5.3.3 Electrochemical Properties

The chemical stability analysis revealed that Ni-DMOF-ADC and Ni-DMOF-TM had a large surface area which can be fully preserved under 90% RH, making them an ideal choice for materials applied in positive electrodes of supercapacitors. Ni-DMOFs were investigated as a three-electrode configuration and the results are shown in Figure 5.4a-5.4d.

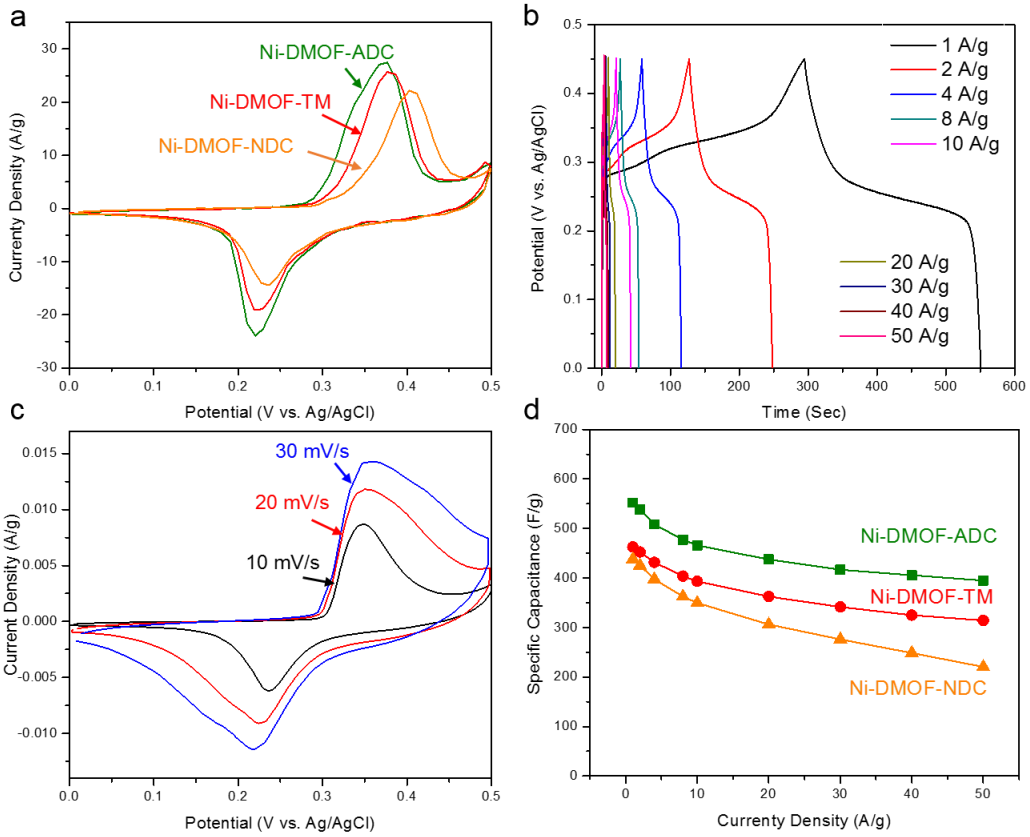

Figure 5.4: Electrochemical performance of the Ni-DMOF electrode. (a) CV curves for Ni-DMOF-ADC, Ni-DMOF-TM and Ni-DMOF-NDC at a scan rate of 10 mV/s in 2 M KOH. (b) GCD curves of Ni-DMOF-ADC at different current densities. (c) CV curves of Ni-DMOF-ADC at scan rates of 10, 30, and 50 mV/s. (d) Specific capacitance of Ni-DMOF-ADC as a function of current densities calculated from the corresponding discharge curves.

CV curves of Ni-DMOF-TM, Ni-DMOF-ADC and Ni-DMOF-NDC electrodes at a scan rate 10 mV/s were shown for comparison in Figure 5.4a. For all the DMOFs, a pair of well-defined redox peaks within 0.15-0.45 V was observable, indicating typical pesudocapacitive behavior. The specific capacitances are correlated to the average area of a CV curve which follow the order of Ni-DMOF-ADC > Ni-DMOF-TM > Ni-DMOF-NDC. Figure 5.4c shows the CV response of Ni-DMOF-ADC at different scan rates ranging from 10 to 30 mV/s. With increasing scan rate, the current response increased

accordingly, indicating the good rate capability. Charge-discharge curves of Ni-DMOF-ADC (Figure 5.4b), Ni-DMOF-TM, and Ni-DMOF-NDC (Figure C.3) at various current densities in a potential range of 0-0.45 V were collected which further confirmed the CV analysis. The discharge curves of the samples at the current density of 1 A/g show a significant deviation from a straight and flat line, indicating the capacitance results are primarily from pseudocapacitive behavior. The specific capacitance can be calculated from the galvanostatic charge-discharge measurements using the following equation:[28]

$$C = \frac{2i_m \int V dt}{V^2 \Big|_{V_i}^{V_f}} \tag{5.1}$$

C represents the galvanostatic charge-discharge (GCD) specific capacitance. $\int V dt$ is the integral current area, where *V* is the potential with initial and final values of V_i and V_f, respectively. i_m =*I/m* is the current density, where *I* is the current and *m* is the active mass of the electrode. The calculated specific capacitance as a function of the discharge current density was plotted in Figure 5.4d. The specific capacitances were in the order of Ni-DMOF-ADC > Ni-DMOF-TM > Ni-DMOF-NDC. The specific capacitances of Ni-DMOF-ADC negatively correlated with current density and were calculated to be 552 F/g and 395 F/g at 1 and 50 A/g, which are very close to theoretical estimation, implying efficient utilization of the MOF structure during charge-discharge measurement. With an increase of current density to 50 A/g, the specific capacitance retained 71.6%, 68.1% and 50.4% compared to their initial values of 1 A/g for Ni-DMOF-ADC, Ni-DMOF-TM and Ni-DMOF-NDC, respectively, indicating better ion diffusion and electron transportability for more stable DMOFs at high current density.

The cycling stability is the most important factor for electrochemical capacitors in practical applications. It has been reported that with increasing cycle number, nickel foam as the current collector for three electrode system in alkaline electrolyte will contribute to the capacitance during the charge-discharge process which leads to non-ignorable error to the results.[29] So we fabricated an asymmetric capacitor with a Ni-DMOF-based anode and an AC-based cathode to evaluate cyclic stability, in which nickel foam was no longer used. The CV curves obtained for the AC electrode are shown in the (Figure C.4) and the calculated specific capacitance was 206 F/g at a scan rate of 10 mV/s. As for asymmetric supercapacitors, the charge balance between the two electrodes needs to follow the relationship $q^+ = q^-$, where the charge stored by each electrode usually depends on the specific capacitance (C), the potential range for the charge-discharge process (ΔE), and the mass of the electrode (m) following equation:[30]

$$q = C \times \Delta E \times m \tag{5.2}$$

In order to obtain $q^+ = q^-$, the mass balancing will be expressed as follows:[30]

$$\frac{m_+}{m_-} = \frac{C_- \times \Delta E_-}{C_+ \times \Delta E_+} \tag{5.3}$$

According to Equation 5.2 and 5.3 and above analysis of the specific capacitance values and potential ranges for DMOF and AC, the mass ratio between the negative and positive electrodes (Ni-DMOF-ADC, -TM, and -NDC) of the asymmetric capacitor is 3.75, 3.16 and 1.95, respectively.

Electrochemical characterizations of the Ni-DMOF-based asymmetric supercapacitor demonstrated in Figure C.5. Figure 5.5 shows the cycling stability of the asymmetric supercapacitors for Ni-DMOF-ADC, Ni-DMOF-TM and Ni-DMOF-NDC in a potential range of 0-1.5 V at a current density of 10 A/g. After 16000 cycles, only 2% of the capacitance of Ni-DMOF-ADC-AC-based asymmetric supercapacitor was lost at this high current density. The less stable Ni-DMOF-TM descended to 60% of its initial value after 9000 cycles, while the unstable Ni-DMOF-NDC asymmetric supercapacitor took only 2200 cycles to drop to 50%. These results of cycling performance indicate the significant impact of DMOFs' chemical stability on the long-term cycling stability of related supercapacitors.

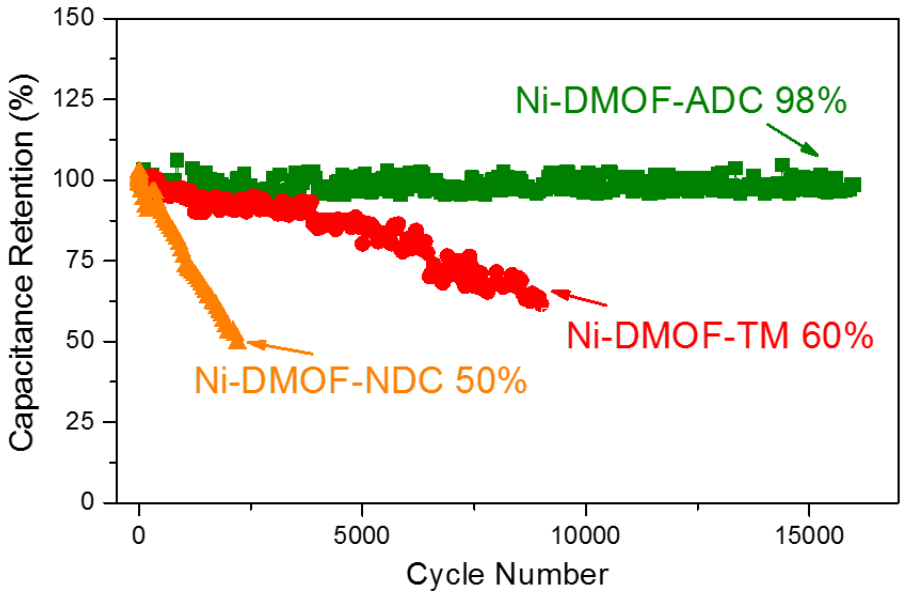

Figure 5.5: Cycle performance for all Ni-DMOFs based asymmetric supercapacitor at a current density of 10 A/g.

In order to investigate the active material that contributed to the pseudocapacitive charge storage of the Ni-DMOF-ADC based capacitor, we performed experiments and analysis including SEM, Raman, FTIR and PXRD analysis to study the Ni-DMOF-ADC derived material. From PXRD pattern (Figure 5.6a), all of the diffractions are basically consistent with the pattern reported for nickel hydroxides,[30] which matches well with the standard pattern (JCPDS 22-752). Raman spectroscopy was used for the structural analysis on both fresh (Figure C.6) and cycled Ni-DMOF-ADC electrode material (Figure 5.6b). After the Ni-DMOF-ADC electrode material cycled in 2 M KOH electrolyte, all the Raman bands of the as-prepared Ni-DMOF-ADC disappeared. Instead, the cycled Ni-DMOF-ADC present same Raman band characteristics with much reduced intensity, which includes a broad hump band within 400-650 cm^{-1}, which is the overlap of Ni-O stretching vibrations due to the complicated structure and a sharp band at 1055 cm^{-1} which correspond to CO_3^{2-} species. These band features suggest the Ni-DMOF-ADC derived material is not simple nickel hydroxides as reported by other works but turbostratic nickel hydroxide highly functionalized with carbonate ions most likely stored in the interlayer spacing. The significant difference between the fresh Ni-DMOF-ADC and cycled Ni-DMOF-ADC indicates the rather weak Ni-ligand coordination bond will be broken during electrochemical charge storage and will be replaced by stronger Ni-OH ionic/covalent bond. Also the carboxyl group bonded on anthracene ring will be oxidized, forming carbonate ions incorporated between the turbostratic $Ni(OH)_2$ layers. Furthermore, the FTIR spectrum (Figure 5.6c) suggested the highly functionalized nature of Ni-DMOF-ADC, the broad absorption band at around 3640 cm^{-1} could be assigned to the O-H stretching vibrations, which is the characteristic of $Ni(OH)_2$.[31] The peak around 1600-1640

cm^{-1} indicates the presence of C=O asymmetric stretching and δH_2O vibration of the water molecule, and the band at 1380 cm^{-1} contributed by CO_3^{2-} anions further corroborate the fact that the presence of carbonate ions within the converted $Ni(OH)_2$ structure.[31, 32] From SEM image (Figure 5.6d and 5.6e), the microstructure of Ni-DMOF-ADC showed a micron-sized rod-like morphology, while the Ni-DMOF-ADC derived material inherited the external morphology from the MOF but with an obvious volume shrinkage of the nanorod. This can be attributed to the substitution effect of the ADC and DABCO ligands to OH^- ions at the presence of KOH.

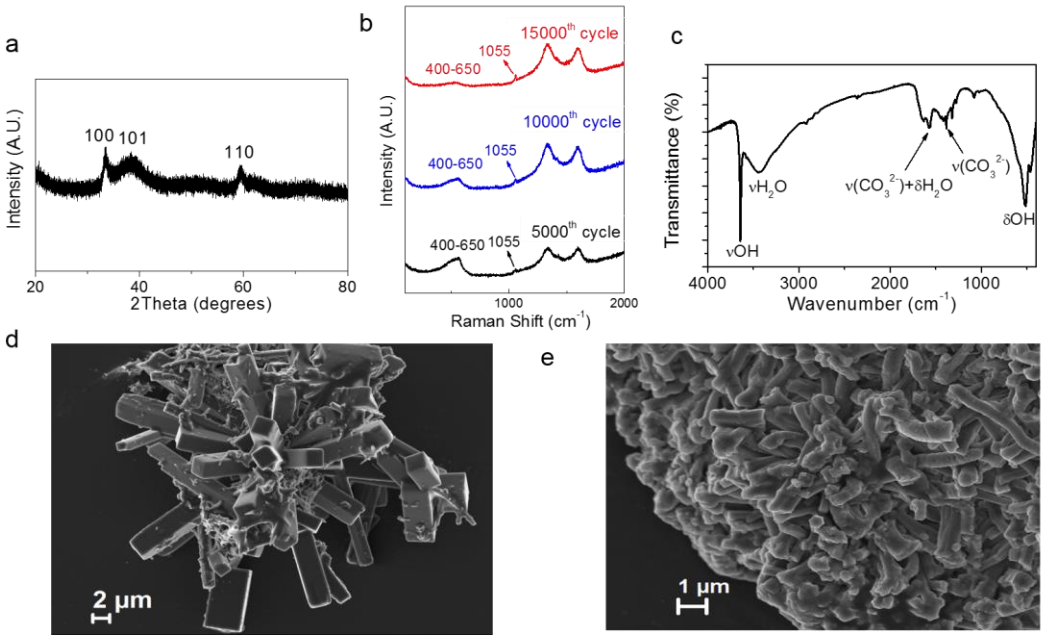

Figure 5.6: (a) PXRD pattern of Ni-DMOF-ADC converted material. (b) Raman spectra of DMOF-ADC electrode from 5000th, 10000th, and 15000th cycle. (c) FTIR spectrum of Ni-DMOF-ADC converted material. SEM images of (d) as-synthesized Ni-DMOF-ADC and (e) Ni-DMOF-ADC converted material.

The water stable DMOF-ADC derived structure converted to nickel hydroxide with incorporation of carbonate ions within its interlayer spacing in alkali, which remained

stable during charge-discharge processes. The reason for the higher cycling stability of DMOF-ADC converted $Ni(OH)_2$ based material were analyzed. First, the layered structure has a three-dimensional nanostructure inherited from MOFs, which has larger surface areas (Figure C.7) compared to other nickel hydroxides, thus increasing the electrode-electrolyte contact area and decreasing the polarization of the electrode in charge-discharge cycles. Secondly, the low-crystalline nature of the structure is another factor for the high stability. According to the work by Li et al.,[33] amorphous-phase or low-crystalline materials always have the potential to exhibit higher electrochemical performance and a longer cycle numbers than the materials with higher crystallinity because of its high structural disorder.

The strong Faradaic redox peaks may come from intercalation and deintercalation of OH^- during electrochemical reaction, which leads to reversible valence state changes between Ni^{2+} and Ni^{3+}. Overall, the detailed mechanism of the structural change and the final structure of MOFs after the charge-discharge processes are still not very clear yet, and further characterization techniques are required.

MOFs were indicated to be very promising as electrode materials for supercapacitor applications due to their large surface areas. However, one of the key problems remain to be solved before extensive application is how to keep original morphology and porous structure after calcination.[34] In order to overcome the structural collapse for most MOFs or MOF-derived materials, we synthesized water-stable pillared Ni-DMOF-ADC with good stability heritage and directly applied it as a supercapacitor electrode without morphology modification. Although Ni-DMOF-ADC converted to highly functionalized nickel hydroxide at the presence of alkali, the DMOF-ADC-derived supercapacitor's capacitance loss was only 2% after 16000 cycles. The excellent cycling stability of DMOF-ADC

derived highly functionalized nickel hydroxide based capacitor is attributed to the good structural stability of the converted material inherited from Ni-DMOF-ADC structure. The cycling performance reported in this chapter is superior to those of Ni-based electrode materials in other literatures[33, 35-39] (Table C.1). The stability of functionalized active material during charge-discharge process was also proved by PXRD (Figure C.8) and Raman data (Figure 5.6b).

5.4 Conclusions

In this chapter, we have synthesized novel isostructural nickel-based, pillared MOFs with different kinetic water stability and directly applied them to supercapacitor electrode. Our study shows that the MOF-derived electrode assembled from the most stable Ni-DMOF-ADC had better electrochemical results in terms of specific capacitance and rate performance than Ni-DMOF-TM and Ni-DMOF-NDC, and exceptional cyclic stability (98% retention after 16000 cycles) compared to other electrochemical studies based on MOFs or MOFs-derived materials. The excellent cycling stability of Ni-DMOF-ADC derived electrode material is attributed to the good structural stability of the converted functionalized nickel hydroxide, which is inherited from Ni-DMOF-ADC. After all, we shed light on the important positive correlation between Ni-DMOFs chemical stability and the electrochemical performance especially the cycling stability when directly used as electrode material of pseudocapacitors. This work opens new channel for the application of water stable MOFs in electrical energy storage.

5.5 References

1. Wang, G. P.; Zhang, L.; Zhang, J. J., *Chem. Soc. Rev.* **2012**, *41* (2), 797-828.

2. Miller, J. R.; Simon, P., *Science* **2008**, *321* (5889), 651-652.

3. El-Kady, M. F.; Strong, V.; Dubin, S.; Kaner, R. B., *Science* **2012**, *335* (6074), 1326-1330.

4. Chmiola, J.; Largeot, C.; Taberna, P. L.; Simon, P.; Gogotsi, Y., *Science* **2010**, *328* (5977), 480-483.

5. Brezesinski, T.; Wang, J.; Tolbert, S. H.; Dunn, B., *Nat. Mater.* **2010**, *9* (2), 146-151.

6. Yu, G. H.; Hu, L. B.; Vosgueritchian, M.; Wang, H. L.; Xie, X.; McDonough, J. R.; Cui, X.; Cui, Y.; Bao, Z. N., *Nano Lett.* **2011**, *11* (7), 2905-2911.

7. Wang, H. L.; Casalongue, H. S.; Liang, Y. Y.; Dai, H. J., *J. Am. Chem. Soc.* **2010**, *132* (21), 7472-7477.

8. Meng, F. L.; Fang, Z. G.; Li, Z. X.; Xu, W. W.; Wang, M. J.; Liu, Y. P.; Zhang, J.; Wang, W. R.; Zhao, D. Y.; Guo, X. H., *J. Mater. Chem. A* **2013**, *1* (24), 7235-7241.

9. Su, C. Y.; Goforth, A. M.; Smith, M. D.; Pellechia, P. J.; zur Loye, H. C., *J. Am. Chem. Soc.* **2004**, *126* (11), 3576-3586.

10. Liu, B.; Shioyama, H.; Akita, T.; Xu, Q., *J. Am. Chem. Soc.* **2008**, *130* (16), 5390-5391.

11. Liu, B.; Shioyama, H.; Jiang, H. L.; Zhang, X. B.; Xu, Q., *Carbon* **2010**, *48* (2), 456-463.

12. Amali, A. J.; Sun, J. K.; Xu, Q., *Chem. Commun.* **2014**, *50* (13), 1519-1522.

13. Yang, J.; Zheng, C.; Xiong, P. X.; Li, Y. F.; Wei, M. D., *J. Mater. Chem. A* **2014**, *2* (44), 19005-19010.

14. Maiti, S.; Pramanik, A.; Mahanty, S., *Chem. Commun.* **2014**, *50* (79), 11717-11720.

15. Jiang, Z.; Li, Z. P.; Qin, Z. H.; Sun, H. Y.; Jiao, X. L.; Chen, D. R., *Nanoscale* **2013**, *5* (23), 11770-11775.

16. James, S. L., *Chem. Soc. Rev.* **2003**, *32* (5), 276-288.

17. Jasuja, H.; Huang, Y. G.; Walton, K. S., *Langmuir* **2012**, *28* (49), 16874-16880.

18. DeCoste, J. B.; Peterson, G. W.; Jasuja, H.; Glover, T. G.; Huang, Y. G.; Walton, K. S., *J. Mater. Chem. A* **2013**, *1* (18), 5642-5650.

19. Jasuja, H.; Jiao, Y.; Burtch, N. C.; Huang, Y. G.; Walton, K. S., *Langmuir* **2014**, *30* (47), 14300-14307.

20. Burtch, N. C.; Jasuja, H.; Walton, K. S., *Chem. Rev.* **2014**, *114* (20), 10575-10612.

21. Tan, K.; Nijem, N.; Canepa, P.; Gong, Q.; Li, J.; Thonhauser, T.; Chabal, Y. J., *Chem. Mater.* **2012**, *24* (16), 3153-3167.

22. Chun, H.; Dybtsev, D. N.; Kim, H.; Kim, K., *Chem. Eur. J.* **2005**, *11* (12), 3521-3529.

23. Walton, K. S.; Snurr, R. Q., *J. Am. Chem. Soc.* **2007**, *129* (27), 8552-8556.

24. Canivet, J.; Bonnefoy, J.; Daniel, C.; Legrand, A.; Coasne, B.; Farrusseng, D., *New J. Chem.* **2014**, *38* (7), 3102-3111.

25. Thommes, M.; Kaneko, K.; Neimark, A. V.; Olivier, J. P.; Rodriguez-Reinoso, F.; Rouquerol, J.; Sing, K. S. W., *Pure Appl. Chem.* **2015**, *87* (9-10), 1051-1069.

26. Bennett, T. D.; Cheetham, A. K.; Fuchs, A. H.; Coudert, F. X., *Nat. Chem.* **2017**, *9* (1), 11-16.

27. Fang, Z. L.; Bueken, B.; De Vos, D. E.; Fischer, R. A., *Angew. Chem. Int. Ed.* **2015**, *54* (25), 7234-7254.

28. Mai, L. Q.; Minhas-Khan, A.; Tian, X. C.; Hercule, K. M.; Zhao, Y. L.; Lin, X.; Xu, X., *Nat. Commun.* **2013**, *4*, 2923.

29. Xing, W.; Qiao, S. Z.; Wu, X. Z.; Gao, X. L.; Zhou, J.; Zhuo, S. P.; Hartono, S. B.; Hulicova-Jurcakova, D., *J. Power Sources* **2011**, *196* (8), 4123-4127.

30. Jiang, H.; Zhao, T.; Li, C. Z.; Ma, J., *J. Mater. Chem.* **2011**, *21* (11), 3818-3823.

31. Adekunle, A. S.; Oyekunle, J. A. O.; Oluwafemi, O. S.; Joshua, A. O.; Makinde, W. O.; Ogunfowokan, A. O.; Eleruja, M. A.; Ebenso, E. E., *Int. J. Electrochem. Sci.* **2014**, *9* (6), 3008-3021.

32. Taibi, M.; Ammar, S.; Jouini, N.; Fievet, F.; Molinie, P.; Drillon, M., *J. Mater. Chem.* **2002**, *12* (11), 3238-3244.

33. Li, H. B.; Yu, M. H.; Wang, F. X.; Liu, P.; Liang, Y.; Xiao, J.; Wang, C. X.; Tong, Y. X.; Yang, G. W., *Nat. Commun.* **2013**, *4*, 1894.

34. Ke, F. S.; Wu, Y. S.; Deng, H. X., *J. Solid State Chem.* **2015**, *223*, 109-121.

35. Wang, R. H.; Xu, C. H.; Lee, J. M., *Nano Energy* **2016**, *19*, 210-221.

36. Yan, J.; Fan, Z. J.; Sun, W.; Ning, G. Q.; Wei, T.; Zhang, Q.; Zhang, R. F.; Zhi, L. J.; Wei, F., *Adv. Funct. Mater.* **2012**, *22* (12), 2632-2641.

37. Jiang, W. C.; Yu, D. S.; Zhang, Q.; Goh, K. L.; Wei, L.; Yong, Y. L.; Jiang, R. R.; Wei, J.; Chen, Y., *Adv. Funct. Mater.* **2015**, *25* (7), 1063-1073.

38. Ji, J. Y.; Zhang, L. L.; Ji, H. X.; Li, Y.; Zhao, X.; Bai, X.; Fan, X. B.; Zhang, F. B.; Ruoff, R. S., *ACS Nano* **2013**, *7* (7), 6237-6243.

39. Wen, P.; Gong, P. W.; Sun, J. F.; Wang, J. Q.; Yang, S. R., *J. Mater. Chem. A* **2015**, *3* (26), 13874-13883.

CHAPTER 6. A HIGH PERFORMANCE HYBRID SUPERCAPACITOR DERIVED FROM A SINGLE METAL-ORGANIC FRAMEWORKS-REDUCED GRAPHENE OXIDE COMPOSITE

In this chapter, Chong Qu evaluated electrochemical properties. Huibin Chang collected FTIR and Raman spectra.

6.1 Introduction

Development of advanced materials with excellent electrochemical properties is critical to meet the growing demand of efficient and clean energy sources. Supercapacitors serve as the advanced power sources for portable devices and electric vehicles[1-6] due to their high power density, rapid charging process, long cycling life and safe operation.[7-9] Because of these advantages, traditional electrical double-layer capacitors (EDLCs) (e.g. porous carbon) have been widely used in the industrial operations and systems. However, the relatively low energy density of EDLCs restricts their broad applicability.[10, 11] Hybrid supercapacitors, assembly by a battery-type electrode (transition metal oxide or hydroxide, Ni,[12, 13] Mn,[14, 15] Fe,[16] Co,[17] Mo,[18] etc.) and a capacitive electrode (porous carbon),[19] have exhibited strong potential for delivering higher energy density because of their broader range of operating voltages and higher capacitance relative to EDLCs.[20, 21]

Among various transition metal-based candidates for battery-type electrode in supercapacitors, $Ni(OH)_2$ has received much attention due to its exceptional theoretical capacitance.[22-24] Extensive works have been done on the optimization of morphology and

porous structure of $Ni(OH)_2$.[25-27] Although $Ni(OH)_2$ shows attractive specific capacitance, its relatively low cycling stability still limits its widespread use. For example, poor cycling performance which mainly results from structural collapse and loss of intercalated crystal water during the charge-discharge procedure is usually reported in α-$Ni(OH)_2$.[22, 23] Many studies have been devoted to improving the structural stability of $Ni(OH)_2$ by employing the strategy of foreign species incorporation. For instance, Jing et al.[28] developed an electrochemical altering voltage approach to synthesizing mixed-metal Ni-Co hydroxide. With the incorporation of Co ions, the capacitance of the resulting electrode only dropped 8.8% after 10,000 cycles at the power density of 2.25 kW/kg. Additionally, a ternary transition mixed-metal hydroxide (Ni-Co-Fe) with a homogeneous distribution was prepared through an idiographic electrochemical method. The obtained Ni-Co-Fe hydroxide possessed a significantly enhanced cycling stability (4% loss after 20,000 cycles at a current density of 34.7 A/g) in comparison to binary Ni-Co hydroxide (19% decrease after 20,000 cycles).[29] Similarly, Chen et al. reported that the cycling stability of Ni-Co hydroxide was greatly enhanced by its interlayered metaborate groups, which served as pillars to support the layered structures and thus increased the structural stability.[30] The strategy of foreign species incorporation shows the broad capability for developing advanced electrodes with excellent cycling stability. However, these as-prepared hydroxides usually exhibit low surface areas and the experimental procedures are not always energy efficient. It is crucially necessary to develop a facile approach to the synthesis of highly porous and stable nickel hydroxide.

Metal-organic frameworks (MOFs) are an important subset of crystalline, nanoporous materials, consisting of metal-containing centers and organic linkers.

Compared to traditional porous materials, these nanomaterials exhibit exceptional porosity, ordered porous structure, and diverse functional groups.[31] Because of these interesting features, MOFs have been considered as promising precursors for preparing high-performance electrodes in supercapacitors.[32, 33] He et al. reported a facile synthesis of porous Ni-Co hydroxide with high specific capacitance from a MOF template, which was developed based on the mixed-metal strategy.[34, 35] However, the as-prepared hydroxide only retained 73% of its initial capacitance after 10,000 cycles.[36] This poor cycling stability is mainly due to the rapid loss of the low surface areas and the unstable layered structures during electrochemical charge-discharge. Using mixed-metal MOF-74 as the template, Qu et al.[37] successfully synthesized functionalized Ni-Co hydroxide electrode with enhanced cycling performance (9.9% loss after 5,000 cycles at a current density of 20 A/g) by a simple hydrothermal procedure. This improved cycling stability was ascribed to the synergistic effect of high surface area (299 m^2/g) with hierarchical porous nature and interlayered functional groups (hydroxyl and carboxyl), which were inherited from the MOF template.

Some previous works have already shown the potential of MOF-derived materials for developing positive electrodes with remarkable electrochemical performance.[38] However, studies investigating the preparation of both positive and negative electrodes from a single MOF precursor are quite limited. Salunkhe et al. successfully synthesized both positive and negative electrodes from ZIF-67 by altering the thermal treatment conditions.[39] However, because of the low surface area and poor electronic conductivity, the observed electrochemical performance of these positive (Co_3O_4) and negative (nanoporous carbon) electrodes were not comparable to other derivatives from MOFs.[33] It

is well known that the electronic conductivity can be significantly enhanced when electrode materials are incorporated with conductive materials, such as reduced graphene oxide (graphene) and carbon fiber paper.[20, 40-42] Therefore, a MOF incorporated with conductive additives composite may represent a promising precursor for high performance positive and negative electrodes.

In this chapter, we present the synthesis of a nickel-based pillared MOF (denoted as DMOF-ADC)[43]-reduced graphene oxide (rGO) composite (denoted as ADC-rGO) through a facile solvothermal reaction. We further synthesize both positive electrode (ADC-rGO-derived $Ni(OH)_2$, denoted as ADC-rGO-OH) and negative electrode (ADC-rGO-derived carbon, denoted as ADC-rGO-C) materials from a single ADC-rGO composite by choosing appropriate treatments (Figure 6.1). The unique morphologies of microrod with and without inner cavity were observed in ADC-rGO-OH and ADC-rGO-C by scanning electron microscopy (SEM) and transmission electron microscopy (TEM). The presence of functional species within electrodes was confirmed by X-ray photoelectron spectroscopy (XPS), Raman spectroscopy, and Fourier transform infrared spectroscopy (FTIR) studies. These features were found to foster high specific capacitance and cycling stability in both positive and negative electrodes. Additionally, the introduction of rGO has also been proved beneficial to improve the rate capability (1594 and 1113 F/g at current densities of 1 and 20 A/g) of the positive electrode ADC-rGO-OH in a three-electrode configuration. Furthermore, a hybrid device was also fabricated by using ADC-rGO-OH as the positive electrode and ADC-rGO-C as the negative electrode. Because of the presence of rGO and functional groups in the aforementioned active materials, the assembled hybrid supercapacitor exhibited superior rate capability (81% capacitance

retention varying from 1 to 20 A/g) and excellent cycling stability (5% loss after 10,000 cycles at a current density of 20 A/g). This study also provides a new MOFs-rGO-as-template strategy for developing high performance energy storage devices.

6.2 Experimental Section

6.2.1 Materials

Chemicals. The chemicals used in this chapter were directly taken from commercial suppliers without further purification: $Ni(NO_3)_2 \cdot 6H_2O$, 9,10-anthracenedicarboxylic acid (H_2ADC), $NaNO_3$, $KMnO_4$, KOH, H_2O_2 from Sigma-Aldrich, 1,4-diazabicyclo[2.2.2]octane (DABCO) from Acros Organics, N,N′-dimethylformamide (DMF), sulfuric acid (H_2SO_4), hydrochloric acid (HCl) from VWR, graphite flake 230U from Asbury.

Synthesis of graphene oxide (GO). The GO was prepared using a modified Hummers method.[44] Typically, graphite flake (1 g, 230U from Asbury) and $NaNO_3$ (1 g) were mixed with concentrated H_2SO_4 (100 mL) in an ice bath. $KMnO_4$ (6 g) was added into the mixture while keeping the temperature below 20 °C. The mixture was first stirred in the ice bath for 2 h and in the water bath at 35 °C for another 0.5 h. 46 mL of water (70 °C) was added into the mixture. To stop the reaction, 140 mL of water (70 °C) was added in the mixture and followed by 20 mL of H_2O_2 (30 wt%). The mixture was filtrated and washed with abundant water to remove the unreacted species. The obtained GO was dried overnight at 55 °C for further use.

Synthesis of positive electrode material (ADC-rGO-OH). First, ADC-rGO composite was synthesized by a one-pot solvothermal reaction modified from the literature.[43] 80 mg of GO was exfoliated in 40 mL of DMF for 6 h under bath sonication. 1 mmol of $Ni(NO_3)_2 \cdot 6H_2O$, 1 mmol of H_2ADC, and 0.5 mmol of DABCO were added in the GO DMF suspension. After sonicating the suspension for 30 min, the solution was divided into four 20 mL glass vials and placed in a preheated oven at 120 °C for 48 h. The obtained materials were washed repeatedly with DMF and methanol and dried in air for subsequent treatments. ADC-rGO-OH was synthesized by soaking ADC-rGO into 2 M KOH solution for 3 h. The resulting ADC-rGO-OH was washed thoroughly with methanol and dried in air.

Synthesis of negative electrode material (ADC-rGO-C). ADC-rGO-C was synthesized by carbonization of ADC-rGO at 600 °C in N_2 atmosphere with an increasing rate of 1 °C/min till 500 °C and then 2 °C/min from 500 to 600 °C. After reaching 600 °C, system was cooled spontaneously to room temperature. The obtained black powder was washed with concentrated HCl at 80 °C for 4 h to remove nickel residues. The powder was collected by filtration, washed with methanol, deionized water and dried in air.

6.2.2 Characterization

Powder X-ray diffraction (PXRD). PXRD patterns were collected using a PANalytical X'Pert X-ray diffractometer combined with an X'Celerator detector and Cu Kα (λ = 1.5418 Å) radiation at room temperature. The step size was set to 0.02° in 2θ.

Scanning electron microscopy and energy dispersive spectroscopy (SEM-EDS). SEM images of samples were recorded by a Zeiss Ultra60 FE-SEM instrument by

using an accelerating voltage of 5 kV. EDS elemental mappings were acquired on the same instrument but with a different accelerating voltage of 10 kV and mapping mode.

Transmission electron microscopy (TEM). TEM, high-resolution TEM (HR-TEM), and high-angle annular dark-field scanning transmission electron microscopy (HAADF-STEM) images of samples were taken from a FEI Tecnai F30 TEM instrument.

N_2 physisorption analysis. N_2 isotherms at 77 K were measured on a Quadrasorb instrument (Quantachrome Instruments). Samples were activated overnight at 110 °C and vacuum condition, using a Quantachrome FloVac degasser. Brunauer-Emmett-Teller (BET) surface areas were determined for the samples by fitting the BET model to the isotherms from 0.05 to 0.3 relative pressure. Using the points from desorption branch, non-local density functional theory (NLDFT) and quenched solid state functional theory (QSDFT) were taken to access the pore size distributions for ADC-OH/rGO and ADC-C/rGO, respectively.

X-ray photoelectron spectroscopy (XPS). XPS measurements were conducted on a Thermo K-Alpha XPS instrument (Thermo Fisher Scientific) with a monochromatic Al-Kα X-ray source. The spectra were acquired with a step size of 0.1 eV, a spot size of 400 μm and dwell time of 40 ms per increment. Survey spectra were average over 3 scans and high-resolution spectra were averaged over at least 15 scans.

Fourier transform infrared spectroscopy (FTIR). FTIR spectra from 3000 to 400 cm^{-1} of samples mixed with dried potassium bromide (KBr) pellets were recorded using an infrared microscope (Spectrum one, Perkin Elmer) with a resolution of 4 cm^{-1}.

Raman spectroscopy. Raman spectra were acquired on samples using a 785 nm laser on a Raman microscope system from HORIBA Scientific.

6.2.3 Electrochemical Measurements

Three-electrode configuration. The electrochemical measurements were performed on a Solartron SI 1286 electrochemical workstation. For the preparation of ADC-rGO-OH working electrode, ADC-rGO-OH, Super P, and PTFE binder were mixed at a weight ratio of 8:1:1 and then were subsequently rolled with ethanol to form a film with a mass of ~3.5 mg/cm^2. The film electrode was compressed between two nickel foams and dried overnight under vacuum at 80 ˚C. The ADC-rGO-C working electrode was prepared in the same procedure using a mixture of 90 wt% ADC-rGO-C and 10 wt% PTFE binder. A Pt mesh electrode was used as the counter electrode, while a 4 M KCl Ag/AgCl electrode was taken as the reference electrode. 2 M KOH aqueous solution was used as the electrolyte. The cyclic voltammograms were conducted with a potential window from 0 to 0.5 V at different scan rates. The galvanostatic charge-discharge (GCD) measurements were performed by varying the potential between 0 and 0.45 V at different current densities. The specific capacitances C (F/g) were calculated using Equation 6.1:

$$\mathrm{C} = \frac{2i_m \int V dt}{V^2 \Big|_{V_i}^{V_f}} \tag{6.1}$$

where $i_m = I/m$ (A/g) is the current density, I is the current, m is the mass of the active material, $\int V dt$ is the integral current area, V is the discharge voltage and V_i and V_f are the

initial and final values of *V*, respectively. The cyclic stability was accessed by long-term GCD measurements using a current density of 20 A/g.

Two-electrode device. The corresponding electrochemical experiments were performed on the same Solartron SI 1286 electrochemical workstation. The two-electrode device was fabricated in a split test cell (MTI Corporation) using ADC-rGO-OH as the positive electrode, ADC-rGO-C as the negative electrode, MPF30AC-100 (Nippon Kodoshi Corporation, Kochi, Japan) as the separator, and 2 M KOH solution as the electrolyte. The positive and negative film electrodes were obtained using the same methods as described in the three-electrode configuration, respectively. The charges of positive and negative electrodes were calculated based on the cyclic voltammograms obtained from three-electrode configuration by using Equation 6.2:

$$q = \int imdV/v \tag{6.2}$$

where q is the charge, m is the mass of the active material, and $\int idV/v$ is the integral area from cyclic voltammograms.

To make the charge balance ($q^+ = q^-$), the mass ratio of positive electrode to negative electrode (R) was determined using Equation 6.3:

$$R = m^+ : m^- = \left(\int \frac{idV}{v}\right)_- : \left(\int \frac{idV}{v}\right)_+ \tag{6.3}$$

The cyclic voltammetric (CV) curves were collected with a voltage from 0 to 1.5 V at different scan rates and the charge-discharge curves were acquired by varying the voltage

between 0 and 1.5 V at different current densities. The cyclic performance was evaluated by long-term GCD experiments at a current density of 20 A/g.

In the Ragone plot of the ADC-rGO-OH//ADC-rGO-C device, the energy density *E* (Wh/kg) and power density *P* (kW/kg) were calculated according to the Equations 6.4 and 6.5:

$$E = \frac{1}{2} \cdot \frac{C \cdot \Delta V^2}{3.6} \tag{6.4}$$

$$P = 3.6 \cdot \frac{E}{\Delta t} \tag{6.5}$$

where *C* is the specific capacitance (F/g), ΔV is the operating potential window (V), and Δt is the discharge time (s).

6.3 Results and Discussion

As illustrated in Figure 6.1, ADC-rGO composite was synthesized according to our previous work[43] with the addition of 9 wt% rGO. ADC-rGO was subsequently soaked into 2 M KOH solution for 3 h to obtain ADC-rGO-OH. On the other hand, ADC-rGO-C was prepared through a thermal and acid (concentrated HCl) treatments. PXRD was used to determine the crystalline phase in ADC-rGO, ADC-rGO-OH and ADC-rGO-C. As shown in Figure D.1, ADC-rGO has a similar PXRD pattern to that of DMOF-ADC, suggesting that the formation of MOF crystal is not prevented upon the incorporation of rGO. In the PXRD pattern of ADC-rGO-OH (Figure D.2), the absence of DMOF-ADC peaks and the emergence of β-$Ni(OH)_2$ (JCPDS No:14-0117) peaks at 19.3°, 33.1°, 38.5°, 39.1°, 59.0°,

and 62.7° illustrate that the transformation from ADC-rGO to ADC-rGO-OH was completed after soaking into 2 M KOH solution for 3 h. Two reflections centered at the 26.2° and 44.0° can be seen in the PXRD pattern of ADC-rGO-C (Figure D.3), which can be assigned to the (002) and (101) planes of graphitic carbon, respectively.[39, 45] This observation confirms that ADC-rGO was converted into sp^2-bonded graphitic carbon upon thermal treatment.

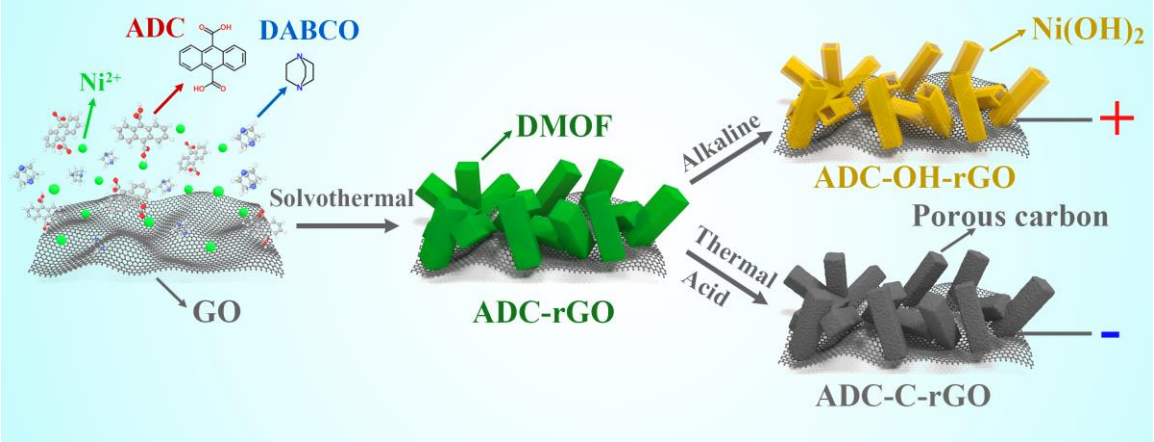

Figure 6.1: Synthesis procedures for ADC-rGO, ADC-rGO-OH, and ADC-rGO-C.

The morphology of both ADC-rGO-OH and ADC-rGO-C were examined using SEM and TEM. Interestingly, when comparing to the morphology of ADC-rGO (Figure D.4), a structural transformation, changing from original microrods into hollow microrods with inner cavity is observed in ADC-rGO-OH (Figure 6.2a) upon alkaline treatment. Under strong alkaline solution (2 M KOH), the metal centers (Ni^{2+}) can dissociate with the organic ligands (Figure 6.1, ADC and DABCO) and will also associate with OH^- ions, leading to the breakdown of the metal-ligand coordination bonds. As reaction proceeds, the OH^- ions continue to diffuse into and react with the inner part of ADC-rGO; meanwhile, newly formed $Ni(OH)_2$ continuously grows on the preformed $Ni(OH)_2$ layers, resulting in

the formation of hollow microrods. Similar hollow structures were also reported previously when treating MOFs with NaOH or KOH.[46] In line with the SEM observation, TEM images of ADC-rGO-OH (Figure 6.2b) also confirm the coexistence of hollow microrods and graphene sheets. Additionally, HAADF-STEM image was acquired on ADC-rGO-OH (Figure 6.2c), confirming its hollow structure and porous characteristics. On the contrary, ADC-rGO-C retains a similar morphology to ADC-rGO, which contains abundant hollow microrods with corrugated graphene sheets. As shown in Figure 6.2d, no obvious inner cavity is observed in these microrods. Porous carbon rod with few layers of graphene sheets is clearly seen in the TEM image of ADC-rGO-C (Figure 6.2e). The highly porous nature of ADC-rGO-C was evidenced by the observation of HAADF-STEM (Figure 6.2f). No bright dots can be seen in ADC-C/rGO, indicating the successful removal of Ni from the structure after reflux with concentrated HCl.

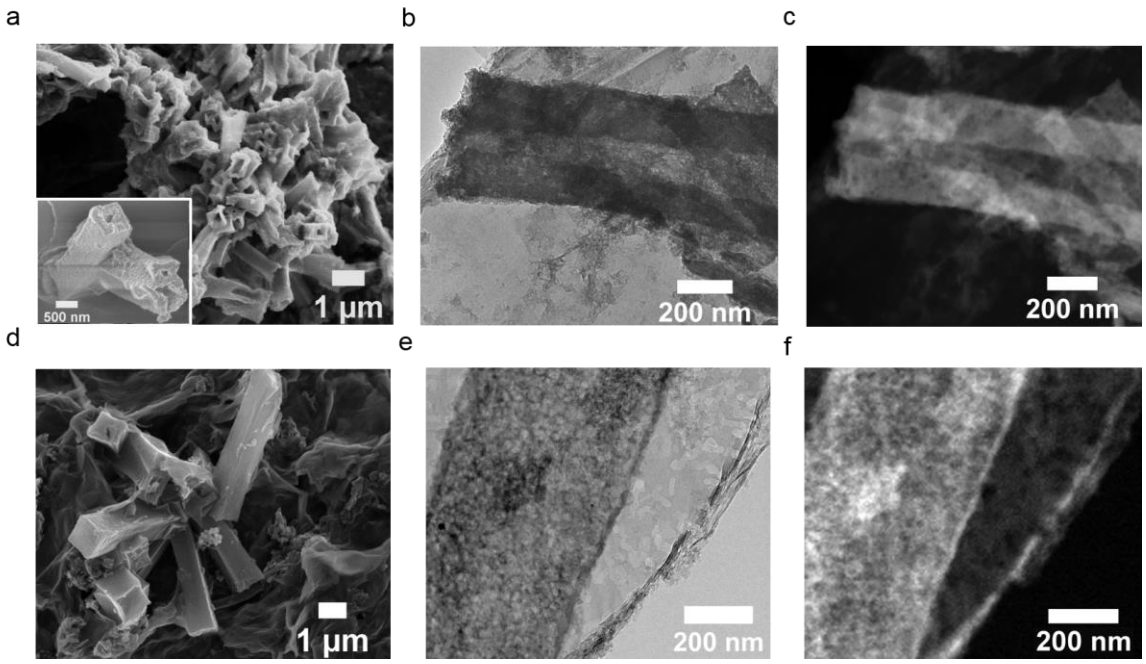

Figure 6.2: (a-c) SEM, TEM, HR-TEM images of ADC-rGO-OH. (d-f) SEM, TEM, and HAADF-STEM images of ADC-rGO-C.

The electrochemical performance is strongly correlated with the surface area, porosity, and pore size distribution of electrode materials. To explore these properties, N_2 physisorption isotherms at 77 K were performed on ADC-rGO-OH and ADC-rGO-C (Figure 6.3a-6.3b). ADC-rGO-OH displays a high Brunauer-Emmett-Teller (BET) surface areas of 309 m^2/g, demonstrating the advantage of MOFs-as-template synthesis over the conventional methods like electrodeposition or hydrothermal synthesis (typically < 100 m^2/g).[47-49] The N_2 isotherms of ADC-rGO-OH are classified as type IV with a hysteresis starting around P/P_0 = 0.4, implying the formation of mesopores. Non-local density functional theory (NLDFT) was used to access the pore size distributions of ADC-rGO-OH (inset of Figure 6.3a). The observation of two sharp peaks at 1.2 nm and 5.3 nm reveals its hierarchical porous structures with the coexistence of micropores and mesopores. On the other hand, the BET surface area of ADC-rGO-C is 472 m^2/g, which is higher than the

nanoporous carbon derived from ZIF-67 (350 m^2/g).[39] The hierarchically porous nature of ADC-rGO-C (inset of Figure 6.3b) was evidenced by the analysis of pore size distributions using QSDFT method.

XPS was utilized to elucidate the surface characteristics and chemical composition of the as-prepared electrodes. C, N, O, and Ni peaks are all present in the survey spectrum of ADC-rGO-OH (Figure D.5a), whereas only C, N, and O peaks are present in the survey spectrum of ADC-rGO-C (Figure D.5b), suggesting that nickel residues were removed by acid reflux. In the Ni 2p spectrum of ADC-rGO-OH (Figure 6.3c), Ni $2p_{3/2}$ (856.2 eV) and $2p_{1/2}$ (873.8 eV) were detected with two corresponding satellite peaks and a spin-orbit coupling energy of 17.6 eV, which are in agreement with the reported values of $Ni(OH)_2$.[50] In the high-resolution N 1s spectrum of ADC-rGO-OH (Figure D.6), a dominant peak at 400.2 eV can be assigned to the tertiary N bonded to carbon ($N\text{-}(C)_3$),[51] indicating that some DABCO functional groups are incorporated into the structure. This is expected as ADC-rGO will degrade under alkaline treatment, resulting in the release of DABCO from the MOF framework and the incorporation of DABCO into the as-synthesized nickel hydroxide. Figure D.7a presents the high-resolution C 1s spectrum for ADC-rGO-OH. Detailed deconvolution analysis over the observed peaks shows four components: C-C (284.6 eV), C-O (286.1 eV), C=O (287.9 eV), and C(O)O (289.1 eV). In the case of ADC-rGO-C, the high-resolution spectrum of C 1s (Figure D.7b) can also be assigned to four types of carbon: C-C (284.6 eV), C-O (286.1 eV), C=O (288.1 eV), and C(O)O (289.1 eV). Moreover, the intensities of C-O, C=O, and C(O)O peaks are lower than that of C-C, indicating the GO was reduced by thermal treatment. Contrary to that of ADC-rGO-OH, the high-resolution N 1s spectrum of ADC-rGO-C (Figure 6.3d) can be deconvoluted into

three species: pyridinic N (398.3 eV), pyrrolic N (400.1 eV), and graphitic N (401.9 eV).[52] The formation of these nitrogen species are possibly attributed to the pyrolysis reaction of ADC-rGO precursor during thermal treatment under N_2. Notably, it has been shown that these pyridinic and pyrrolic N can serve as electrochemically active sites and contribute to increasing the capacitance properties of electrodes in supercapacitors.[53] Elemental mapping was acquired by using Energy Dispersive Spectroscopy (EDS) to reveal the elemental composition and distribution of ADC-rGO-OH and ADC-rGO-C. As shown in Figure D.8, ADC-rGO-OH consists of C, O, N, and Ni with the corresponding atomic percentage of 43.7%, 35.5%, 1.9%, and 18.9%, respectively. On the other hand, ADC-rGO-C (Figure D.9) is only composed of C (94.6%), N (3.0%), and O (2.4%) with the absence of Ni element, which is compatible with XPS results. All the detected elements are uniformly distributed throughout ADC-rGO-OH and ADC-rGO-C.

Using MOF as the precursor, various functional species can be introduced into the MOF-derived electrode materials. This behavior has been shown to increase the electrochemical performance of the MOF-derived electrodes,[33] particularly the cycling stability.[37, 43] Spectroscopic experiments (FTIR and Raman spectroscopy) are useful to detect the functional groups present in the structure. However, the functional groups from graphene sheets, including hydroxyl, carbonyl, and carboxylate groups detected by XPS, may obscure the structural features of ADC-rGO-OH. To avoid this interference from graphene, a similar alkaline treatment was applied on Ni-DMOF-ADC to prepare the MOF-derived nickel hydroxide (hereafter noted as ADC-OH) for subsequent analysis. In the Raman spectrum (Figure 6.3e), the band at 1370 cm^{-1} is attributed to the glass substrate, which agrees with the blank measurement (Figure D.10). A broad band appeared in the

range of 300-685 cm^{-1} can be identified as the overlap of Ni-O stretching vibration, resulting from the complicated $Ni(OH)_2$ structure.[13, 54] Two weak bands with much reduced intensity at 895 cm^{-1} and 1057 cm^{-1} can be assigned to $\upsilon_{25}(\upsilon CC)$ mode of DABCO molecules[55] and δ mode of CO_3^{2-} species,[56] respectively. These band features indicate that the prepared MOF derivatives ADC-OH is a highly functionalized version of nickel hydroxide with the incorporation of DABCO and CO_3^{2-} species. FTIR analysis (Figure 6.3f) was conducted to further elucidate the structural characteristics. Two broad bands observed at 3430 cm^{-1} and 635 cm^{-1} correspond to the stretching and bending vibrations of adsorbed water molecules.[57, 58] The intense peak at 3636 cm^{-1} can be identified as the υO-H stretching vibrations, which is the typical characteristic of $Ni(OH)_2$.[57] The bands at 515 cm^{-1} and 465 cm^{-1} are attributed to Ni-OH bending and Ni-O stretching vibrations, further confirming the formation of $Ni(OH)_2$.[59] Two small bands centered at 1567 cm^{-1} and 1450 cm^{-1} reflect the $C{=}C_{ring}$ stretching vibrations of anthracene,[60] implying that ADC-OH contains some ADC functional groups after the alkaline treatment. This speculation is further supported by the evidence that two bands were observed at 1382 cm^{-1} and 1628 cm^{-1}, which are corresponding to the symmetric and asymmetric stretching vibrations of carboxylate groups, respectively.[61] The band at 1073 cm^{-1} is attributed to the asymmetric stretching vibration of $N\text{-}(C)_3$,[62] suggesting that DABCO ligands are also incorporated into the final structure. Considering the FTIR and Raman spectra, it is clear that ADC-rGO-OH is a highly functionalized nickel hydroxide with incorporation of functional species, including ADC and DABCO groups.

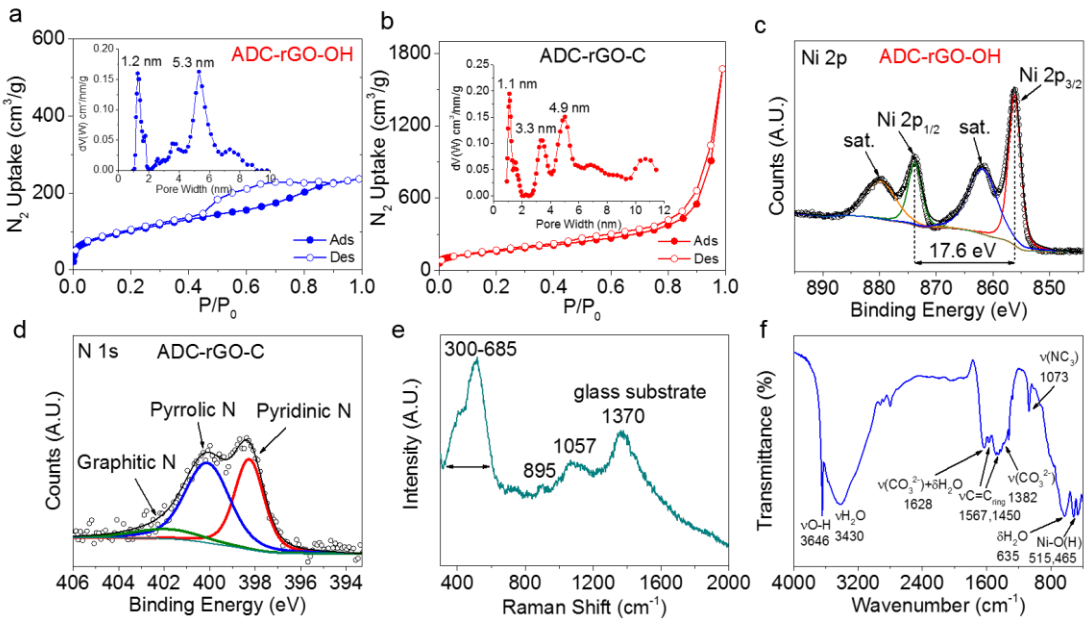

Figure 6.3: N_2 isotherms (at 77K) of (a) ADC-rGO-OH and (b) ADC-rGO-C, with the insets showing the corresponding pore size distributions, respectively (closed symbols, adsorption; open symbols, desorption). High-resolution N 1s XPS spectra of (c) ADC-rGO-OH and (d) ADC-rGO-C. (e) Raman and (f) FTIR spectra of ADC-OH.

The electrochemical properties of ADC-rGO-OH and ADC-rGO-C were first characterized in three-electrode configurations with 2 M KOH aqueous electrolyte. Figure 6.4a presents the typical cyclic voltammetric (CV) curves of ADC-rGO-OH measured at various scan rates (5-50 mV/s) from 0 to 0.5 V (vs Ag/AgCl). All the CV curves display a pair of well-defined redox peaks, which are attributed to the reversible reaction of $Ni(OH)_2 + OH^- \leftrightarrow NiOOH + H_2O + e^-$.[13, 63] Two trends can be observed here: i) as the scan rate increases, the oxidation peak shifts to the positive direction, whereas the reduction peak moves to a more negative position. This is expected because the internal diffusion resistance of the battery-type electrode will increase as the scan rate increases,[63, 64] and ii) the current increases accordingly as scan rate increases, indicating the good rate capability of ADC-rGO-OH. On the other hand, CV curves of ADC-rGO-C (Figure 6.4b) were

acquired in the potential window of -1.0 to 0 V (vs Ag/AgCl), altering scan rates from 10 to 100 mV/s. In the case of ADC-rGO-C, the curves display similar shapes of semirectangular, which is the typical behavior of EDLCs. The current of ADC-rGO-C exhibits a positive correlation with the increase of scan rate, implying a good rate capability of ADC-rGO-C. Figure 6.4c displays the galvanostatic charge-discharge (GCD) curves of ADC-rGO-OH measured at different current densities. The shape of the discharge curves of ADC-rGO-OH indicates an electrochemical redox reaction engaged mechanism which is consistent with the results of CV measurements. The GCD curves (Figure 6.4d) of ADC-rGO-C collected at various current densities show a triangular fashion, which is also corresponding to electrochemical behavior of EDLCs. The specific capacitances of ADC-rGO-C (Figure D.11) were calculated based on the corresponding GCD curves by using Equation 6.1. The specific capacitances are 330, 308, 294, 281, 277, and 269 F/g at the corresponding current densities of 1, 2, 4, 8, 10, and 20 A/g, respectively. When increasing current density from 1 to 20 A/g, the specific capacitance retains nearly 81% of the initial capacitance at 1 A/g. Such excellent rate capability of ADC-rGO-C is attributed to the incorporation of doped N species[53] and conductive graphene sheets.[30] Unlike carbon materials, $Ni(OH)_2$ usually suffers from its limited electronic conductivity, resulting in a relatively poor rate capability.[9] Therefore, it is useful to compare the rate capabilities between ADC-OH and ADC-rGO-OH and understand the effect of graphene sheets on the rate property. To achieve this goal, CV (Figure D.12a) and GCD measurements (Figure D.12b) were also performed on ADC-OH. The specific capacitances of ADC-rGO-OH and ADC-OH were calculated from their corresponding GCD curves according to Equation 6.1. The obtained values are plotted in Figure 6.4e. At the initial current density of 1 A/g,

the specific capacitance of ADC-OH (1273 F/g) is slightly lower than that of ADC-rGO-OH (1594 F/g). However, ADC-OH exhibits a poor rate capability as the charge-discharge current density increases from 1 to 20 A/g. At higher charge-discharge current densities of 8, 10, and 20 A/g, the specific capacitances of ADC-OH retain only 666, 593, and 477 F/g, corresponding to 52%, 47%, and 37% of the capacitance at 1 A/g, respectively. On the contrary, with the addition of graphene sheets, ADC-rGO-OH exhibits a much better rate capability than the ADC-OH. At the current densities of 8, 10, and 20 A/g, the specific capacitances remain at 1235, 1199, and 1113 F/g, which are 77%, 75%, and 70% of the initial capacitance at 1 A/g. This greatly enhanced rate performance clearly shows the good electronic conductivity of ADC-rGO-OH at high current density region, demonstrating the benefits of incorporating graphene sheets into the electrode.[30, 64, 65] This promotion of electronic conductivity is further supported by the electrochemical impedance spectroscopy (EIS) tests. As shown in Nyquist plots (Figure D.13), ADC-rGO-OH has an equivalent series resistance of 0.37 Ω, whereas ADC-OH has a much higher resistance of 1.02 Ω. Notably, these advanced rate capabilities of ADC-rGO-OH and ADC-rGO-C are comparable or even better than most of the reported works.[39,66-68] Cycling stability is another parameter of great importance to evaluate the electrochemical performance of electrode. The cycling curves shown in Figure 6.4f illustrate the change in specific capacitance of ADC-rGO-OH and ADC-rGO-C during the long-term galvanostatic measurement (10,000 cycles) at a high current density of 20 A/g. ADC-rGO-C possesses an excellent cycling stability with a retention of 99% after a 10,000-cycle test. On the other hand, ADC-rGO-OH has an attractive cycling stability, retaining nearly 95% of its original capacitance after 10,000 cycles, which is rarely reported in the studies of nickel hydroxide-

based electrode for supercapacitor. ADC-rGO-OH delivers much more stable capacitance during the long-term run relative to other high-performance $Ni(OH)_2$-graphene or $Ni(OH)_2$-oixde composites.[50, 63, 69]

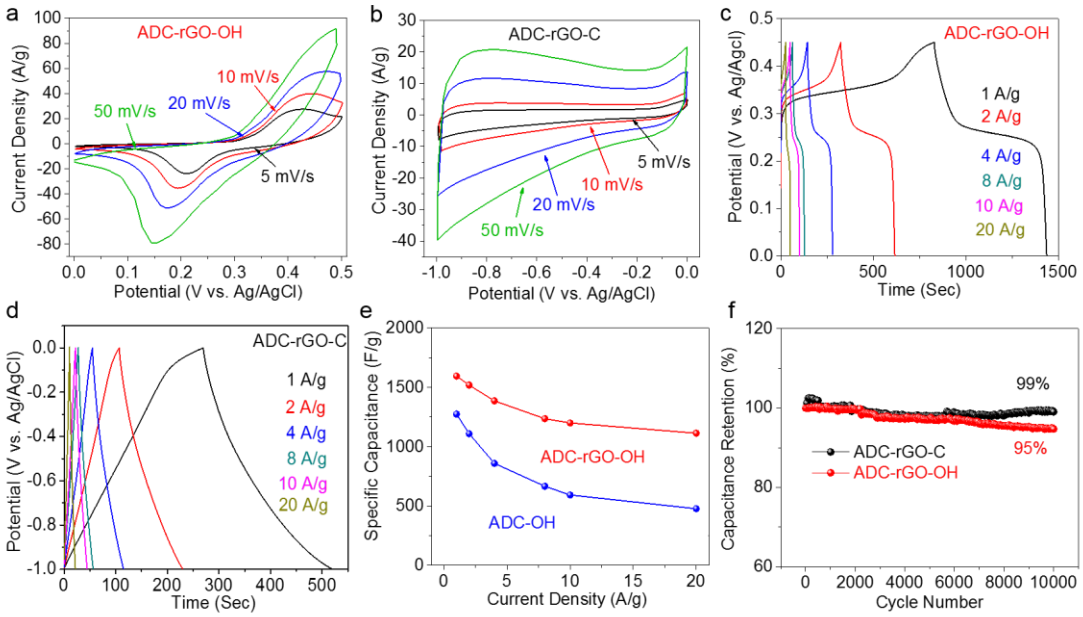

Figure 6.4: CV curves of (a) ADC-rGO-OH and (b) ADC-rGO-C at different scan rates in 2 M KOH. GCD curves of (c) ADC-rGO-OH and (d) ADC-rGO-C at various current densities. (e) Rate performance of ADC-OH and ADC-rGO-OH. (f) Cycling performance of ADC-rGO-OH and ADC-rGO-C at 20 A/g.

To further investigate the performance of the as-prepared electrodes under practical conditions, a hybrid supercapacitor (ADC-rGO-OH//ADC-rGO-C) was assembled using ADC-rGO-OH and ADC-rGO-C as the positive and negative electrodes, respectively. To keep the charge balanced, the mass ratio of negative and positive electrode was set to 2.2 according to the corresponding CV curves of ADC-rGO-C and ADC-rGO-OH (Equations 6.2 and 6.3). As shown in Figure 6.5a-6.5b, the fabricated hybrid supercapacitor can be operated in a broad voltage window of 0-1.5 V. Figure 6.5a presents the CV curves collected at different scan rates, ranging from 10 to 100 mV/s (individual CV curves of

positive and negative electrodes are shown in Figure D.14a). It is clear that the shape of the obtained CV curves indicates the convolution of two different energy storage characteristics, which agrees with the results of CV studies in the three-electrode system. The shape of the CV curves retains in a similar fashion as the scan rate increases, indicating the good rate capability of the device. Figure 6.5b summarizes the corresponding GCD curves of the hybrid supercapacitor acquired at different current densities from 1 to 20 A/g. An inclined plateau from 1.1 to 0.3 V is observed in the discharge curves, which are compatible with the CV trends. Figure D.14b illustrates the relationship between specific capacitances of the hybrid supercapacitor and current densities from 1 to 20 A/g. An outstanding rate performance is achieved such that 81% of the capacitance at 1 A/g is maintained when the current density is increased to 20 A/g. This excellent behavior is attributed to the good rate capabilities of ADC-rGO-OH and ADC-rGO-C electrodes. Figure 6.5c presents the relationship between the gravimetric energy density and power density (Ragone plot) of the ADC-rGO-OH//ADC-rGO-C device. Based on Equations 6.4 and 6.5, this device delivers a high energy density of 59 Wh/kg at a power density of 872 W/kg. Moreover, an energy density of 48 Wh/kg still preserves, as the power density elevates up to 15.5 kW/kg. Notably, ADC-rGO-OH//ADC-rGO-C displays much higher energy and power densities in comparison to those previously reported devices fabricated by high-performance electrode materials (Figure 6.5c), including MOF-derived materials,[39, 70, 71] metal hydroxide or oxide materials,[22, 29, 72] and metal hydroxide or oxide composites embedded with graphene or conductive carbon.[30, 73, 74] The cycling performance of energy storage device at high charge-discharge rates is always the essential requirement for practical processes.[75] As shown in Figure 6.5d, a capacitance retention of

95% is maintained in this hybrid supercapacitor when being tested at a high current density of 20 A/g over 10,000 cycles. Compared to the reported results, ADC-rGO-OH//ADC-rGO-C is one of the most stable hybrid/asymmetric supercapacitor devices (Table D.1).[29, 30, 37, 70, 74, 76-78]

Several features may contribute to the excellent electrochemical performance of ADC-rGO-OH//ADC-rGO-C device: i) the highly porous nature and micro-mesoporous structure inherited from MOF-rGO template not only create more interfaces between electrode and electrolyte for intercalation and deintercalation of OH^- during faradaic reaction, but also shorten ionic diffusion pathways for electrolyte molecules, ii) the functional groups (ADC and DABCO species) derived from MOF-rGO template might serve as pillars, within the structure which can accommodate the large volume expansion during the charge-discharge process, leading to the excellent cycling performance, iii) the doped N species of ADC-rGO-C can function as electrochemically active sites and further increase the capacitance properties, iv) the electronic conductivity of MOF-derived electrodes are significantly enhanced by the presence of rGO, offering efficient electron transportation at fast charge-discharge rates.

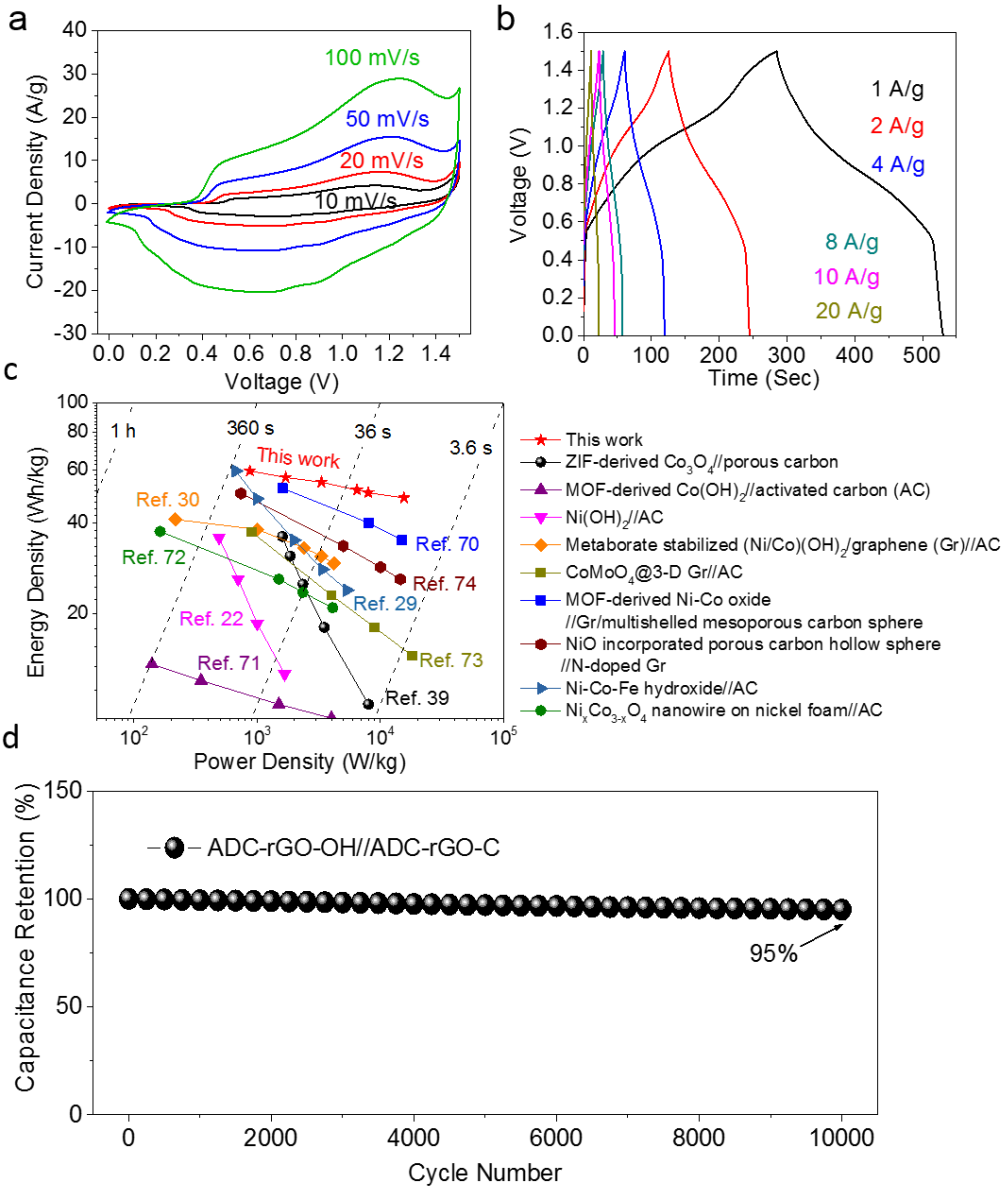

Figure 6.5: (a) CV curves of ADC-rGO-OH//ADC-rGO-C hybrid supercapacitor device at various scan rates. (b) GCD curves of hybrid device at different current densities. (c) Cycling performance of hybrid device at a current density of 20 A/g. (d) Ragone plot of the ADC-rGO-OH//ADC-rGO-C device compared to those of reported electrodes based on mass of active materials.

6.4 Conclusions

In summary, we have synthesized a MOF-rGO composite, containing nickel-based pillared MOFs and reduced graphene oxide using a simple solvothermal procedure. MOF-rGO was used as the precursor and subsequently converted to both positive (ADC-rGO-OH) and negative (ADC-rGO-C) electrodes by different treatments. Supported by the analysis of N_2 physisorption measurements and pore size distributions, the MOF-rGO-derived electrodes ADC-rGO-OH and ADC-rGO-C possess remarkably high surface areas and contain hybrid characteristics of micro and mesopores compared to traditionally synthesized nickel hydroxides. In particular, ADC-rGO-OH is found to be functionalized with multiple functional groups (ADC and DABCO), as demonstrated by XPS, Raman and FTIR studies. When being tested in a three-electrode system, ADC-rGO-OH and ADC-rGO-C exhibited high specific capacitances of 1594 and 330 F/g at a current density of 1 A/g, while maintaining 95% and 99% of its initial capacitance over 10,000 cycles at 20 A/g, respectively. Moreover, ADC-rGO-OH exhibited 70% capacitance retention changing from 1 to 20 A/g, demonstrating the key role of graphene in increasing the conductivity. A hybrid supercapacitor has been further assembled by utilizing ADC-rGO-OH and ADC-rGO-C as the positive and negative electrodes, respectively. With the contributions of both graphene sheets and functional groups, the obtained hybrid supercapacitor exhibits an excellent rate capability (19% loss of capacitance from 1 to 20 A/g) and exceptional cycling stability (95% retention after 10,000 cycles). The present MOF-rGO-as-template strategy provides a new perspective on the development of high performance energy storage materials.

6.5 References

1. Miller, J. R.; Simon, P., *Science* **2008**, *321* (5889), 651-652.

2. Zhang, L. C.; Zhu, P.; Zhou, F. R.; Zeng, W. J.; Su, H. B.; Li, G.; Gao, J.; Sun, R.; Wong, C. P., *ACS Nano* **2016**, *10* (1), 1273-1282.

3. Lu, X. H.; Yu, M. H.; Wang, G. M.; Tong, Y. X.; Li, Y., *Energy Environ. Sci.* **2014**, *7* (7), 2160-2181.

4. Karden, E.; Ploumen, S.; Fricke, B.; Miller, T.; Snyder, K., *J. Power Sources* **2007**, *168* (1), 2-11.

5. Kang, B.; Ceder, G., *Nature* **2009**, *458* (7235), 190-193.

6. Chen, P. C.; Shen, G. Z.; Shi, Y.; Chen, H. T.; Zhou, C. W., *ACS Nano* **2010**, *4* (8), 4403-4411.

7. Miller, J. R.; Simon, P., *Science* **2008**, *321* (5889), 651-652.

8. Simon, P.; Gogotsi, Y.; Dunn, B., *Science* **2014**, *343* (6176), 1210-1211.

9. Wang, G. P.; Zhang, L.; Zhang, J. J., *Chem. Soc. Rev.* **2012**, *41* (2), 797-828.

10. Pandolfo, A. G.; Hollenkamp, A. F., *J. Power Sources* **2006**, *157* (1), 11-27.

11. Zhong, C.; Deng, Y. D.; Hu, W. B.; Qiao, J. L.; Zhang, L.; Zhang, J. J., *Chem. Soc. Rev.* **2015**, *44* (21), 7484-7539.

12. Xia, X. H.; Tu, J. P.; Wang, X. L.; Gu, C. D.; Zhao, X. B., *J. Mater. Chem.* **2011**, *21* (3), 671-679.

13. Xiong, X. H.; Ding, D.; Chen, D. C.; Waller, G.; Bu, Y. F.; Wang, Z. X.; Liu, M. L., *Nano Energy* **2015**, *11*, 154-161.

14. Lang, X. Y.; Hirata, A.; Fujita, T.; Chen, M. W., *Nat. Nanotechnol.* **2011**, *6* (4), 232-236.

15. Chen, W.; Rakhi, R. B.; Hu, L. B.; Xie, X.; Cui, Y.; Alshareef, H. N., *Nano Lett.* **2011**, *11* (12), 5165-5172.

16. Nithya, V. D.; Arul, N. S., *J. Mater. Chem. A* **2016**, *4* (28), 10767-10778.

17. Wang, H. T.; Zhang, L.; Tan, X. H.; Holt, C. M. B.; Zahiri, B.; Olsen, B. C.; Mitlin, D., *J. Phys. Chem. C* **2011**, *115* (35), 17599-17605.

18. Hu, X. L.; Zhang, W.; Liu, X. X.; Mei, Y. N.; Huang, Y., *Chem. Soc. Rev.* **2015**, *44* (8), 2376-2404.

19. Chen, T.; Dai, L. M., *Mater. Today* **2013**, *16* (7-8), 272-280.

20. Zhao, B.; Chen, D.; Xiong, X.; Song, B.; Hu, R.; Zhang, Q.; Rainwater, B. H.; Waller, G. H.; Zhen, D.; Ding, Y.; Chen, Y.; Qu, C.; Dang, D.; Wong, C.-P.; Liu, M., *Energy Storage Mater.* **2017**, *7*, 32-39.

21. Dai, S.; Zhao, B.; Qu, C.; Chen, D. C.; Dang, D.; Song, B.; Deglee, B. M.; Fu, J. W.; Hu, C. G.; Wong, C. P.; Liu, M. L., *Nano Energy* **2017**, *33*, 522-531.

22. Li, H. B.; Yu, M. H.; Wang, F. X.; Liu, P.; Liang, Y.; Xiao, J.; Wang, C. X.; Tong, Y. X.; Yang, G. W., *Nat. Commun.* **2013**, *4*, 1894.

23. Jiang, H.; Zhao, T.; Li, C. Z.; Ma, J., *J. Mater. Chem.* **2011**, *21* (11), 3818-3823.

24. Shi, F.; Li, L.; Wang, X. L.; Gu, C. D.; Tu, J. P., *RSC Adv.* **2014**, *4* (79), 41910-41921.

25. Bastakoti, B. P.; Huang, H. S.; Chen, L. C.; Wu, K. C. W.; Yamauchi, Y., *Chem. Commun.* **2012**, *48* (73), 9150-9152.

26. Cai, F. S.; Zhang, G. Y.; Chen, J.; Gou, X. L.; Liu, H. K.; Dou, S. X., *Angew. Chem. Int. Ed.* **2004**, *43* (32), 4212-4216.

27. Matsui, K.; Kyotani, T.; Tomita, A., *Adv. Mater.* **2002**, *14* (17), 1216-1217.

28. Jing, M. J.; Hou, H. S.; Banks, C. E.; Yang, Y. C.; Zhang, Y.; Ji, X. B., *ACS Appl. Mater. Interfaces* **2015**, *7* (41), 22741-22744.

29. Li, H. B.; Gao, Y. Q.; Wang, C. X.; Yang, G. W., *Adv. Energy Mater.* **2015**, *5* (6), 1401767.

30. Chen, Y. Z.; Pang, W. K.; Bai, H. H.; Zhou, T. F.; Liu, Y. N.; Li, S.; Guo, Z. P., *Nano Lett.* **2017**, *17* (1), 429-436.

31. Furukawa, H.; Cordova, K. E.; O'Keeffe, M.; Yaghi, O. M., *Science* **2013**, *341* (6149), 974-975.

32. Wang, H.; Zhu, Q.-L.; Zou, R.; Xu, Q., *Chem* **2017**, *2* (1), 52-80.

33. Zheng, S.; Li, X.; Yan, B.; Hu, Q.; Xu, Y.; Xiao, X.; Xue, H.; Pang, H., *Adv. Energy Mater.* **2017**, 1602733.

34. Wang, L. J.; Deng, H. X.; Furukawa, H.; Gandara, F.; Cordova, K. E.; Peri, D.; Yaghi, O. M., *Inorg. Chem.* **2014**, *53* (12), 5881-5883.

35. Jiao, Y.; Morelock, C. R.; Burtch, N. C.; Mounfield, W. P.; Hungerford, J. T.; Walton, K. S., *Ind. Eng. Chem. Res.* **2015**, *54* (49), 12408-12414.

36. He, S. H.; Li, Z. P.; Wang, J. Q.; Wen, P.; Gao, J. C.; Ma, L. M.; Yang, Z. G.; Yang, S. R., *RSC Adv.* **2016**, *6* (55), 49478-49486.

37. Qu, C.; Zhao, B.; Jiao, Y.; Chen, D.; Dai, S.; deglee, B. M.; Chen, Y.; Walton, K. S.; Zou, R.; Liu, M., *ACS Energy Lett.* **2017**, *2* (6), 1263-1269.

38. Xie, Z. Q.; Xu, W. W.; Cui, X. D.; Wang, Y., *Chemsuschem* **2017**, *10* (8), 1645-1663.

39. Salunkhe, R. R.; Tang, J.; Kamachi, Y.; Nakato, T.; Kim, J. H.; Yamauchi, Y., *ACS Nano* **2015**, *9* (6), 6288-6296.

40. Fan, Z. J.; Yan, J.; Wei, T.; Zhi, L. J.; Ning, G. Q.; Li, T. Y.; Wei, F., *Adv. Funct. Mater.* **2011**, *21* (12), 2366-2375.

41. Huang, L.; Chen, D. C.; Ding, Y.; Feng, S.; Wang, Z. L.; Liu, M. L., *Nano Lett.* **2013**, *13* (7), 3135-3139.

42. Tao, J. Y.; Liu, N. S.; Ma, W. Z.; Ding, L. W.; Li, L. Y.; Su, J.; Gao, Y. H., *Sci. Rep.* **2013**, *3*, 2286.

43. Qu, C.; Jiao, Y.; Zhao, B.; Chen, D.; Zou, R.; Walton, K. S.; Liu, M., *Nano Energy* **2016**, *26*, 66-73.

44. Lian, G.; Tuan, C. C.; Li, L. Y.; Jiao, S. L.; Wang, Q. L.; Moon, K. S.; Cui, D. L.; Wong, C. P., *Chem. Mater.* **2016**, *28* (17), 6096-6104.

45. Xia, W.; Qu, C.; Liang, Z.; Zhao, B.; Dai, S.; Qiu, B.; Jiao, Y.; Zhang, Q.; Huang, X.; Guo, W.; Dang, D.; Zou, R.; Xia, D.; Xu, Q.; Liu, M., *Nano Lett.* **2017**, *17* (5), 2788-2795.

46. Zhang, L.; Wu, H. B.; Lou, X. W., *J. Am. Chem. Soc.* **2013**, *135* (29), 10664-10672.

47. Gupta, V.; Gupta, S.; Miura, N., *J. Power Sources* **2008**, *175* (1), 680-685.

48. Shao, M. F.; Ning, F. Y.; Zhao, Y. F.; Zhao, J. W.; Wei, M.; Evans, D. G.; Duan, X., *Chem. Mater.* **2012**, *24* (6), 1192-1197.

49. Parveen, N.; Cho, M. H., *Sci. Rep.* **2016**, *6*, 27318.

50. Yan, J.; Fan, Z. J.; Sun, W.; Ning, G. Q.; Wei, T.; Zhang, Q.; Zhang, R. F.; Zhi, L. J.; Wei, F., *Adv. Funct. Mater.* **2012**, *22* (12), 2632-2641.

51. Ong, W. J.; Tan, L. L.; Chai, S. P.; Yong, S. T., *Dalton Trans.* **2015**, *44* (3), 1249-1257.

52. Wang, X. J.; Zhou, J. W.; Fu, H.; Li, W.; Fan, X. X.; Xin, G. B.; Zheng, J.; Li, X. G., *J. Mater. Chem. A* **2014**, *2* (34), 14064-14070.

53. Hulicova-Jurcakova, D.; Seredych, M.; Lu, G. Q.; Bandosz, T. J., *Adv. Funct. Mater.* **2009**, *19* (3), 438-447.

54. Yang, Y.; Li, L.; Ruan, G. D.; Fei, H. L.; Xiang, C. S.; Fan, X. J.; Tour, J. M., *ACS Nano* **2014**, *8* (9), 9622-9628.

55. Guzonas, D. A.; Irish, D. E., *Can. J. Chem.* **1988**, *66* (5), 1249-1257.

56. Lunsford, J. H.; Yang, X. M.; Haller, K.; Laane, J.; Mestl, G.; Knozinger, H., *J. Phys. Chem.* **1993**, *97* (51), 13810-13813.

57. Cha, S. M.; Nagaraju, G.; Yu, J. S., *J. Phys. Chem. C* **2016**, *120* (33), 18411-18420.

58. Yang, S. B.; Wu, X. L.; Chen, C. L.; Dong, H. L.; Hu, W. P.; Wang, X. K., *Chem. Commun.* **2012**, *48* (22), 2773-2775.

59. Xu, P.; Han, X. J.; Zhang, B.; Lv, Z. S.; Liu, X. R., *J. Alloys Compd.* **2007**, *436* (1-2), 369-374.

60. Mary, Y. S.; Jojo, P. J.; Van Alsenoy, C.; Kaur, M.; Siddegowda, M. S.; Yathirajan, H. S.; Nogueira, H. I. S.; Cruz, S. M. A., *Spectrochim. Acta Mol. Biomol. Spectrosc.* **2014**, *120*, 370-380.

61. Taibi, M.; Ammar, S.; Jouini, N.; Fievet, F.; Molinie, P.; Drillon, M., *J. Mater. Chem.* **2002**, *12* (11), 3238-3244.

62. Tan, K.; Nijem, N.; Canepa, P.; Gong, Q.; Li, J.; Thonhauser, T.; Chabal, Y. J., *Chem. Mater.* **2012**, *24* (16), 3153-3167.

63. Ji, J. Y.; Zhang, L. L.; Ji, H. X.; Li, Y.; Zhao, X.; Bai, X.; Fan, X. B.; Zhang, F. B.; Ruoff, R. S., *ACS Nano* **2013**, *7* (7), 6237-6243.

64. Wang, H. L.; Casalongue, H. S.; Liang, Y. Y.; Dai, H. J., *J. Am. Chem. Soc.* **2010**, *132* (21), 7472-7477.

65. Cao, X. H.; Zheng, B.; Shi, W. H.; Yang, J.; Fan, Z. X.; Luo, Z. M.; Rui, X. H.; Chen, B.; Yan, Q. Y.; Zhang, H., *Adv. Mater.* **2015**, *27* (32), 4695-4701.

66. Salunkhe, R. R.; Kamachi, Y.; Torad, N. L.; Hwang, S. M.; Sun, Z. Q.; Dou, S. X.; Kim, J. H.; Yamauchi, Y., *J. Mater. Chem. A* **2014**, *2* (46), 19848-19854.

67. Xiang, Z. H.; Wang, D.; Xue, Y. H.; Dai, L. M.; Chen, J. F.; Cao, D. P., *Sci. Rep.* **2015**, *5*, 8307.

68. Abushrenta, N.; Wu, X. C.; Wang, J. N.; Liu, J. F.; Sun, X. M., *Sci. Rep.* **2015**, *5*, 13082.

69. Chen, H.; Hu, L. F.; Yan, Y.; Che, R. C.; Chen, M.; Wu, L. M., *Adv. Energy Mater.* **2013**, *3* (12), 1636-1646.

70. Guan, B. Y.; Kushima, A.; Yu, L.; Li, S.; Li, J.; Lou, X. W., *Adv. Mater.* **2017**, *29* (17), 1605902.

71. Wang, Z. F.; Liu, Y. S.; Gao, C. W.; Jiang, H.; Zhang, J. M., *J. Mater. Chem. A* **2015**, *3* (41), 20658-20663.

72. Wang, X.; Yan, C. Y.; Sumboja, A.; Lee, P. S., *Nano Energy* **2014**, *3*, 119-126.

73. Yu, X. Z.; Lu, B. A.; Xu, Z., *Adv. Mater.* **2014**, *26* (7), 1044-1051.

74. Kim, S. Y.; Jeong, H. M.; Kwon, J. H.; Ock, I. W.; Suh, W. H.; Stucky, G. D.; Kang, J. K., *Energy Environ. Sci.* **2015**, *8* (1), 188-194.

75. Wang, Y. G.; Song, Y. F.; Xia, Y. Y., *Chem. Soc. Rev.* **2016**, *45* (21), 5925-5950.

76. Li, B.; Dai, F.; Xiao, Q. F.; Yang, L.; Shen, J. M.; Zhang, C. M.; Cai, M., *Energy Environ. Sci.* **2016**, *9* (1), 102-106.

77. Zhao, Y.; Hu, L. F.; Zhao, S. Y.; Wu, L. M., *Adv. Funct. Mater.* **2016**, *26* (23), 4085-4093.

78. Qin, K. Q.; Liu, E. Z.; Li, J. J.; Kang, J. L.; Shi, C. S.; He, C. N.; He, F.; Zhao, N. Q., *Adv. Energy Mater.* **2016**, *6* (18), 1600755.

CHAPTER 7. CONCLUSIONS AND RECOMMENDATIONS

7.1 Conclusions

The main goal of this dissertation is to develop the knowledge and methods that are needed to engineer and optimize MOFs or MOF-derived materials for practical applications such as gas adsorption and electrical energy storage. To improve the performance of MOFs or MOF-derived materials, two promising strategies were developed and studied in this dissertation: i) defect engineering (mixed-metal and missing cluster defects) was utilized for preparing chemically stable MOFs for gas adsorption applications, and ii) MOFs-as-templates (MOF conversion) was employed for synthesizing stable electrode materials for electrical energy storage.

The studies presented in chapter 3 examined the effects of mixed-metal centers on the CO_2 interactions and water stability of Mg-MOF-74. Varying amounts of Co and Ni metal centers were substituted into Mg-MOF-74 via a one-pot solvothermal reaction. Based on elemental analyses, Co and Ni are more favorably incorporated into the MOF-74 framework from solution than Mg. In addition, reaction temperature more strongly impacts the final metal composition in these mixed-metal MOF-74 structures than does the reaction solvent composition. Single-component CO_2 adsorption isotherms were measured for the MM-MOF-74 systems at 5, 25 and 45 °C and isosteric heats of adsorption were calculated. These results suggest that CO_2 sorption properties can be adjusted by mixed-metal defects. Water adsorption isotherms were also measured for the MM-MOF-74 samples, with powder X-ray diffraction patterns and Brunauer-Emmett-Teller surface areas measured both before and after water exposure. Results show that Mg-MOF-74 can gain partial

kinetic water stability by the incorporation of Ni^{2+} or Co^{2+} metal centers that are less vulnerable to hydrolysis than Mg^{2+}. Of particular note, Mg-Ni-MM-MOF-74 showed a significant increase in water stability when incorporating as little as 16 mol% Ni into the mg-MOF-74 structure. These findings demonstrate that mixed-metal synthesis is an effective approach to increasing the chemical stability of Mg-MOF-74 that are known to degrade under humid environments.

Chapter 4 investigated the impact of missing clusters on the adsorption behavior and chemical stability of UiO-66. UiO-66 with different types and numbers of defects were synthesized through a two-step method: modulated synthesis and post-synthetic heat treatment. Systematic adsorption measurements with three adsorbate molecules (SO_2, benzene, and cyclohexane) were used to investigate the changes in the pore size of defective UiO-66. Compared to the parent UiO-66, the defective UiO-66 showed significant changes in adsorption capacities among the selected adsorbate molecules, demonstrating that the pore size is significantly enlarged by the missing cluster defects. A combination of BET surface area analysis and DFT calculations were also performed to interrogate the chemical stability of the defective MOFs after exposure to water and acidic environments. This study demonstrates that the structural incorporation of trifluroacetate groups in the defective UiO-66 leads to an increase in average pore size while maintaining excellent chemical stability towards water and acidic species.

In chapter 5, a simple solvothermal procedure was used to synthesize nickel-based, pillared DABCO-MOFs (DMOFs) of similar topologies $[Ni(L)(DABCO)_{0.5}]$, where L is the functionalized BDC (1,4-benzenedicarboxylic acid) linker and DABCO is 1,4-diazabicyclo[2.2.2]-octane. The stability of Ni-DMOF-ADC ([Ni(9,10-

anthracenedicarboxylic acid)$(DABCO)_{0.5}$]) and Ni-DMOF-TM ([Ni(2,3,5,6-tetramethyl-1,4-benzenedicarboxylic acid)$(DABCO)_{0.5}$]) in a humid environment was confirmed by BET surface area analysis on the water-exposed samples. When used as electrode materials, these DMOF capacitors exhibited excellent electrochemical performance. For example, a Ni-DMOF-ADC electrode showed specific capacitances of 552 and 438 F/g at current densities of 1 and 20 A/g, respectively, while maintaining outstanding cycling stability (98% retention over 16,000 cycles at current density of 10 A/g) for MOF-derived materials based supercapacitors. The excellent electrochemical performance is attributed to the conversion of DMOFs to highly functionalized nickel hydroxide that inherited the high stability of Ni-DMOF-ADC and remained intact during charge-discharge process. Further, this work provides a general approach for the application of nickel-based pillared MOFs as relatively stable electrode in electrical energy storage.

Finally, in chapter 6, positive and negative electrode materials were derived from a single ADC-rGO composite by choosing appropriate treatments. The structural properties and chemical composition of the prepared electrode materials (ADC-rGO-OH and ADC-rGO-C) were characterized by PXRD, XPS, Raman and FTIR. Characterization results support that the as-prepared positive electrode material is a highly functionalized nickel hydroxide coupled with graphene, DABCO, and ADC groups, which is an attribute of the pillared MOFs-rGO composite-as-template synthesis strategy. When being tested in a three-electrode configuration, ADC-rGO-OH exhibits attractive capacitance (1594 F/g at 1 A/g), good rate capability (70% capacitance retention altering from 1 to 20 A/g) and exceptional cycling performance (95% retention after 10,000 cycles with a current density of 20 A/g). On the other hand, the resulting negative electrode material (ADC-rGO-C) is a

nitrogen-doped porous carbon with high capacitance (330 F/g at 1 A/g) and remarkable rate capability (81% capacitance retention varying from 1 to 20 A/g). When assembled in a hybrid supercapacitor with the help of nitrogen-rich negative electrodes which demonstrated a hierarchical porous nature, the device exhibited high energy and power density (59 Wh/kg and 15.5 kW/kg), good rate capability (19% capacitance loss from 1 to 20 A/g), and exceptional cycling stability (95% retention over 10,000 cycles at a current density of 20 A/g). These findings imply that pillared MOFs and their combination with rGO contribute significantly to improving the electrochemical performance of the resulting electrode materials. The MOF-rGO-as-template strategy demonstrated here is expected to facilitate the development of next-generation high performance energy storage devices.

7.2 Recommendations

7.2.1 Further Investigating the Chemical Stability of MM-MOFs

Chapter 3 focused on the changes in water stability of Mg-MOF-74 after partial substitution with Ni or Co ions. A significant water stability improvement was observed in Mg-Ni-MOF-74 with the introduction of as little as 16 mol% Ni into the structure. Recent work by Howe et al.[1] suggested that the increased water stability of Mg-Ni-MOF-74 is related to a M-O bond length distortion in MM-MOF-74. These findings suggest that length distortion introduced by the mixed-metal defects in the MOF structure can play an important role in increasing the chemical stability of MOFs. This behavior should be further investigated in other unstable MOFs such as Cu-BTC,[2] DMOFs,[2] and MOF-5.[3] Understanding the chemical stability of other mixed-metal MOFs would play a crucial role in determining whether this mixed-metal synthesis can be used as a general approach to

increasing the chemical stability. Furthermore, it is well know that water loading of adsorbents at high temperature will be lower than that at room temperature. Therefore, the water stability of MM-MOFs at low and high temperatures should be investigated in the future as these results would be useful to determine how much stability depends on the loading of water. Long-term stability is another important factor that needs to be considered before applying adsorbents in practical processes. Therefore, long-term water exposure experiments on MM-MOFs should also be conducted in the future. Although water is ubiquitous in industrial streams, acidic impurities such as CO_2, SO_x, NO_x, and H_2S are also commonly found in many gas separation and purification systems.[4] Therefore, future works should investigate the chemical stability of MM-MOFs under acidic environments. Acidic stability tests on MM-MOFs would provide insight into the role of mixed-metal effects in MOF chemical stability and could be used as the general evaluation during the development of next-generation stable MOFs.

7.2.2 Further Understanding Chemical Stability Mechanisms in Defective UiO-66

Defect engineering has emerged as a developing technique in the MOF community to tune the MOF porosity, construct hierarchically porous structures, and manipulate the physical and chemical properties of MOF crystals.[5-9] Modulated synthesis has been demonstrated as a powerful yet simple approach for the synthesis of MOFs with various defect numbers and types.[10, 11] The incorporation of crystal imperfections is expected to cause structural collapse in the defective MOFs under exposure to water or acidic molecules. However, in chapter 4, it was shown that defective UiO-66 exhibits an excellent chemical stability towards water and acidic molecules when the defect sites are compensated with trifluoroacetate groups. Surprisingly, when acetate served as the

compensating group, a partial loss of surface area was observed in the defective UiO-66 after humid SO_2 exposure, as evidenced by the N_2 isotherms shown in Figure 7.1. This conflicting stability behavior in defective UiO-66 is not expected and requires further efforts to elucidate the possible mechanism in the future.

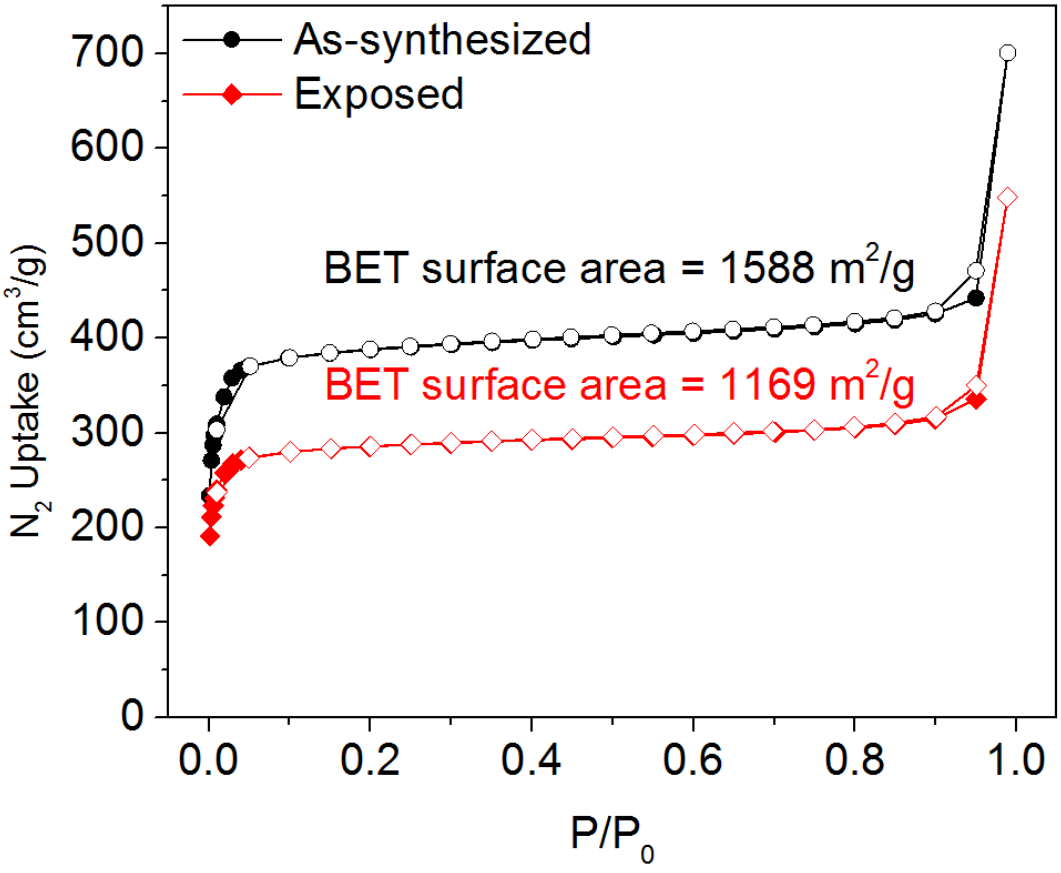

Figure 7.1: N_2 isotherms at 77 K for defective UiO-66 (acetic acid modulator) before and after exposure to 50 ppm SO_2 and 85% RH environment for 5 days (closed symbols - adsorption, open symbols - desorption).

One probable reason for this behavior would be the electronic effect introduced by the compensating group, which is recently proposed by Van de Voorde.[12] The pKa value of trifluoroacetic acid (pKa = 0.23) is much lower than that of acetic acid (pKa = 4.76). Thus, compared to acetic acid, the positively partial charge on metal center (Zr^{4+}) would

be significantly increased by the locally electronic withdraw from the coordinated trifluoroacetate group. A strong Zr-carboxylate bond would be introduced into the defective UiO-66, resulting in a chemically robust structure. Therefore, future studies could investigate the relationship between the pKa of acid modulator and chemical stability in the defective UiO-66. One strategy for further exploring this mechanism would be to synthesize defective UiO-66 variants using trifluoroacetic acid (pKa = 0.23), difluoroacetic acid (pKa = 1.24), fluoroacetic acid (pKa = 2.6), and acetic acid (pKa = 4.76) as the acid modulators.[13] Investigations of the changes in textural properties of the exposed structures would provide fundamental understandings on the relationship between the compensating groups introduced by acid modulators and chemical stability of defective UiO-66.

7.2.3 Further Utilizing MOF Templating Strategies for Electrical Energy Storage

Among the numerous electrode candidates, nickel hydroxide is one of the most promising electrode materials due to its relatively high specific capacitance.[14-16] However, its insufficient cycling performance greatly limits its applications. In chapter 6, it was demonstrated that the cycling stability of nickel hydroxide can be significantly improved by the incorporation of functional groups, which are likely derived from the MOF precursor during the MOF conversion. Beyond the incorporation of functional groups, there appears to be an additional method that can improve the cycling performance of nickel hydroxide in energy storage devices. The introduction of other transition metal ions into nickel hydroxide has become another effective method to optimize the cycling performance. For example, in a mixed-metal hydroxide containing binary metal ions (Co and Ni), an increased cycling stability relative to the pristine nickel hydroxide was reported.[17] The enhanced performance could be attributed to the unique porous disk-like architecture,

resulting from the introduction of Co ions. A similar trend was also observed in a ternary metal hydroxide. Li et al. synthesized a ternary metal hydroxide (Ni-Co-Fe) electrode material through an electrochemical method.[18] Compared to nickel hydroxide, this ternary metal hydroxide only dropped 6% of its capacity after 20,000 cycles. This method is similar to the mixed-metal strategy which was explored in chapter 3. As demonstrated in chapter 3, the metal composition in the MM-MOFs can be manipulated by the starting ratio of metal salts and reaction temperature. Combining the techniques developed in chapters 3 and 6, binary, ternary, even quaternary metal hydroxide compounds can be prepared by using MM-MOF-74 as the precursor. This proposed strategy of MM-MOF template synthesis is promising to synthesize a hydroxide composite possessing multiple metal ions, as well as function groups that are derived from the MOF precursor. Electrochemical experiments such as cyclic voltammograms, galvanostatic charge-discharge, and cycling stability measurements should be conducted on the resulting electrode materials. Such a study would provide a new method of developing advanced electrode materials for high performance energy storage applications.

7.3 References

1. Howe, J. D.; Morelock, C. R.; Jiao, Y.; Chapman, K. W.; Walton, K. S.; Sholl, D. S., *J. Phys. Chem. C* **2017**, *121* (1), 627-635.

2. DeCoste, J. B.; Peterson, G. W.; Jasuja, H.; Glover, T. G.; Huang, Y. G.; Walton, K. S., *J. Mater. Chem. A* **2013**, *1* (18), 5642-5650.

3. Ming, Y.; Purewal, J.; Yang, J.; Xu, C. C.; Soltis, R.; Warner, J.; Veenstra, M.; Gaab, M.; Muller, U.; Siegel, D. J., *Langmuir* **2015**, *31* (17), 4988-4995.

4. Rezaei, F.; Rownaghi, A. A.; Monjezi, S.; Lively, R. P.; Jones, C. W., *Energy Fuels* **2015**, *29* (9), 5467-5486.

5. Sholl, D. S.; Lively, R. P., *J. Phys. Chem. Lett.* **2015**, *6* (17), 3437-3444.

6. Fang, Z. L.; Bueken, B.; De Vos, D. E.; Fischer, R. A., *Angew. Chem. Int. Ed.* **2015**, *54* (25), 7234-7254.

7. Cheetham, A. K.; Bennett, T. D.; Coudert, F. X.; Goodwin, A. L., *Dalton Trans.* **2016**, *45* (10), 4113-4126.

8. Yuan, S.; Zou, L.; Qin, J. S.; Li, J.; Huang, L.; Feng, L.; Wang, X.; Bosch, M.; Alsalme, A.; Cagin, T.; Zhou, H. C., *Nat. Commun.* **2017**, *8*, 15356.

9. Taddei, M., *Coord. Chem. Rev.* **2017**, *343*, 1-24.

10. Gutov, O. V.; Molina, S.; Escudero-Adan, E. C.; Shafir, A., *Chem. Eur. J.* **2016**, *22* (38), 13582-13587.

11. Atzori, C.; Shearer, G. C.; Maschio, L.; Civaller, B.; Bonino, F.; Lamberti, C.; Svelle, S.; Lillerud, K. P.; Bordiga, S., *J. Phys. Chem. C* **2017**, *121* (17), 9312-9324.

12. Van de Voorde, B.; Stassen, I.; Bueken, B.; Vermoortele, F.; De Vos, D.; Ameloot, R.; Tan, J. C.; Bennett, T. D., *J. Mater. Chem. A* **2015**, *3* (4), 1737-1742.

13. Shearer, G. C.; Chavan, S.; Bordiga, S.; Svelle, S.; Olsbye, U.; Lillerud, K. P., *Chem. Mater.* **2016**, *28* (11), 3749-3761.

14. Li, H. B.; Yu, M. H.; Wang, F. X.; Liu, P.; Liang, Y.; Xiao, J.; Wang, C. X.; Tong, Y. X.; Yang, G. W., *Nat. Commun.* **2013**, *4*, 1894.

15. Zhu, Y. Q.; Cao, C. B.; Tao, S.; Chu, W. S.; Wu, Z. Y.; Li, Y. D., *Sci. Rep.* **2014**, *4*, 5787.

16. Jiang, W. C.; Yu, D. S.; Zhang, Q.; Goh, K. L.; Wei, L.; Yong, Y. L.; Jiang, R. R.; Wei, J.; Chen, Y., *Adv. Funct. Mater.* **2015**, *25* (7), 1063-1073.

17. Zhao, B.; Chen, D.; Xiong, X.; Song, B.; Hu, R.; Zhang, Q.; Rainwater, B. H.; Waller, G. H.; Zhen, D.; Ding, Y.; Chen, Y.; Qu, C.; Dang, D.; Wong, C.-P.; Liu, M., *Energy Storage Mater.* **2017**, *7*, 32-39.

18. Li, H. B.; Gao, Y. Q.; Wang, C. X.; Yang, G. W., *Adv. Energy Mater.* **2015**, *5* (6), 1401767.

APPENDIX A. CHAPTER 3 SUPPORTING INFORMATION

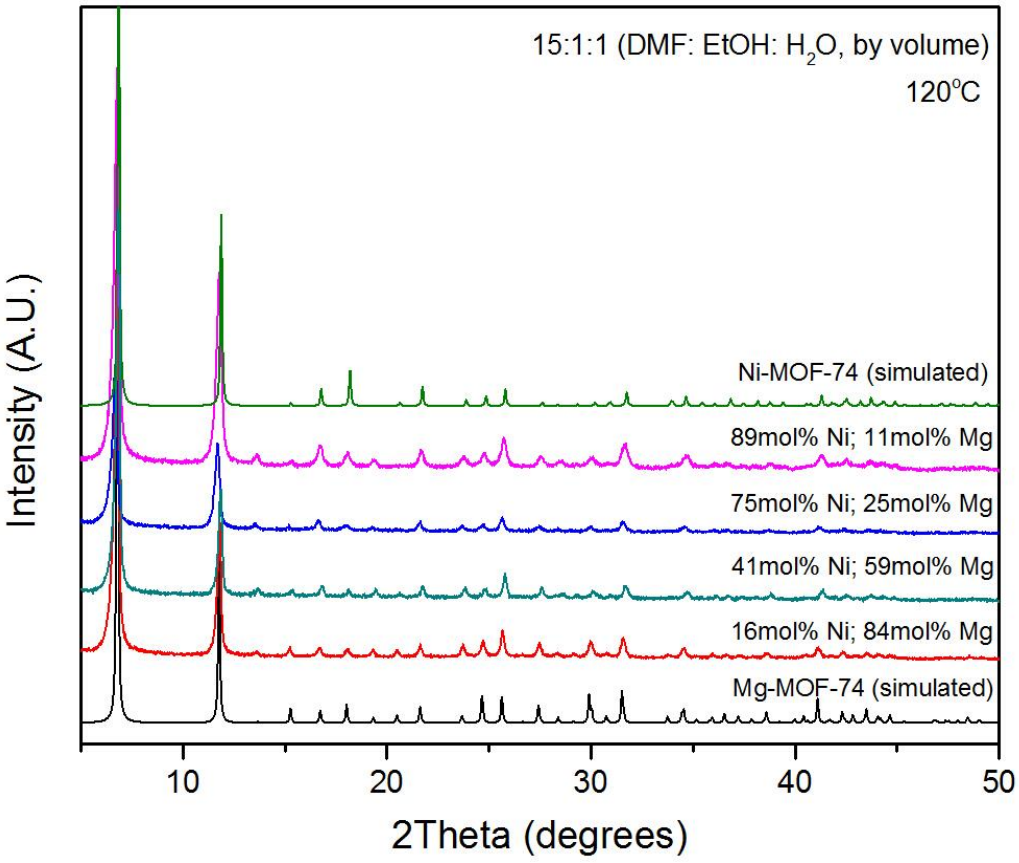

Figure A.1: Comparison of experimental PXRD patterns for as-synthesized Mg-Ni-MM-MOF-74 with various metal concentration levels (prepared at 120 °C and 15:1:1 DMF: EtOH: H_2O, v/v) and simulated patterns for the parent MOF-74 structure (Mg and Ni).[1,2]

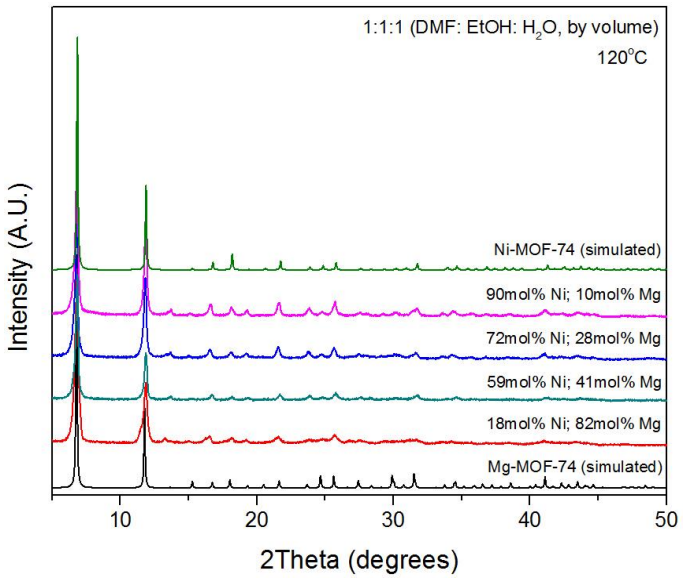

Figure A.2: Comparison of experimental PXRD patterns for as-synthesized Mg-Ni-MM-MOF-74 with various metal concentration levels (prepared at 120 °C and 1:1:1 DMF: EtOH: H_2O, v/v) and simulated patterns for the parent MOF-74 structure (Mg and Ni).

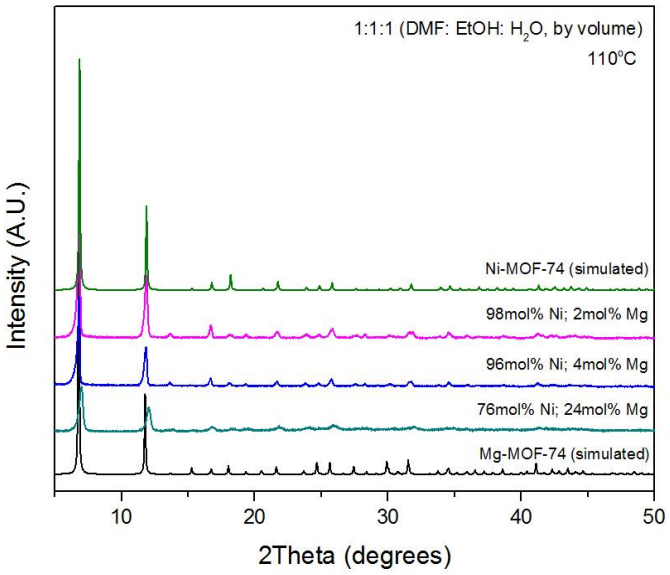

Figure A.3: Comparison of experimental PXRD patterns for as-synthesized Mg-Ni-MM-MOF-74 with various metal concentration levels (prepared at 110 °C and 1:1:1 DMF: EtOH: H_2O, v/v) and simulated patterns for the parent MOF-74 structure (Mg and Ni).

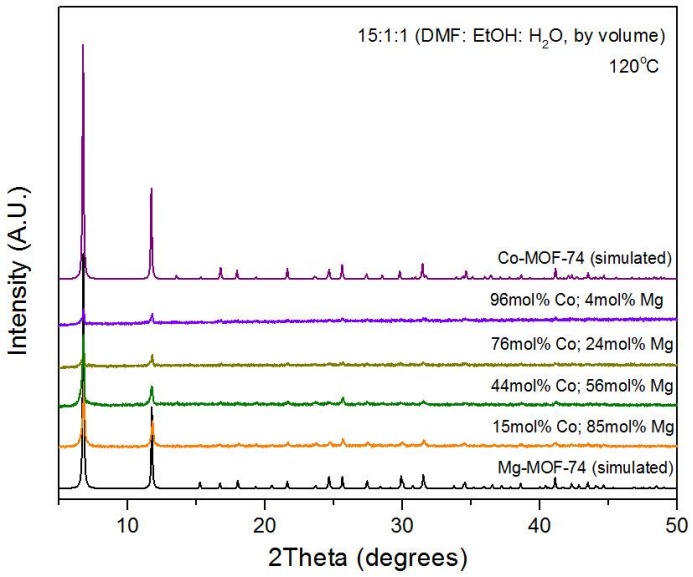

Figure A.4: Comparison of experimental PXRD patterns for as-synthesized Mg-Co-MM-MOF-74 with various metal concentration levels (prepared at 120 °C and 15:1:1 DMF: EtOH: H_2O, v/v) and simulated patterns for the parent MOF-74 structure (Mg and Co).

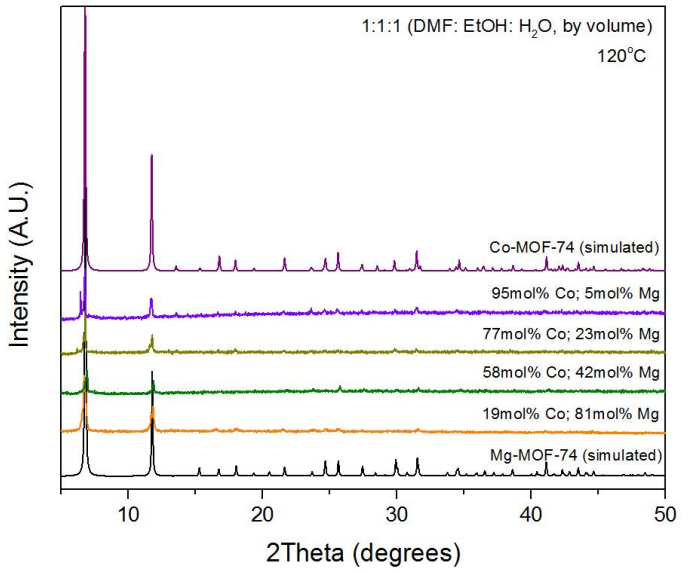

Figure A.5: Comparison of experimental PXRD patterns for as-synthesized Mg-Co-MM-MOF-74 with various metal concentration levels (prepared at 120 °C and 1:1:1 DMF: EtOH: H_2O, v/v) and simulated patterns for the parent MOF-74 structure (Mg and Co).[1,3]

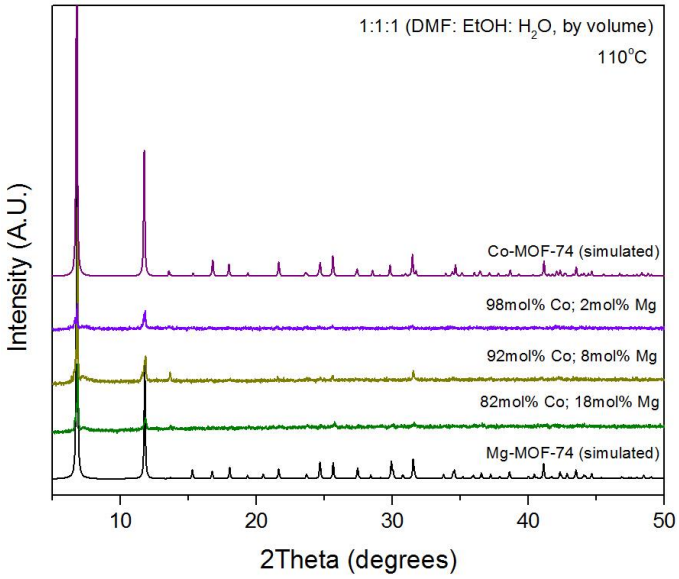

Figure A.6: Comparison of experimental PXRD patterns for as-synthesized Mg-Co-MM-MOF-74 with various metal concentration levels (prepared at 110 °C and 1:1:1 DMF: EtOH: H_2O, v/v) and simulated patterns for the parent MOF-74 structure (Mg and Co).

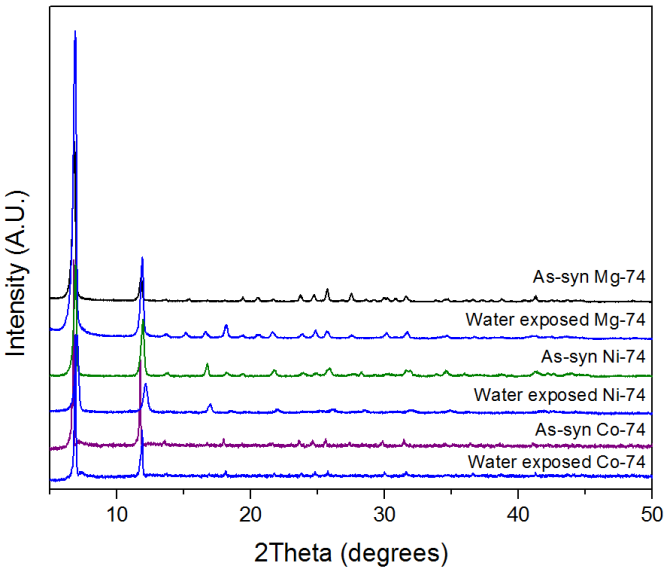

Figure A.7: Comparison of experimental PXRD patterns for as-synthesized M-MOF-74 (M= Mg, Ni, Co) and samples reactivated after water exposure.

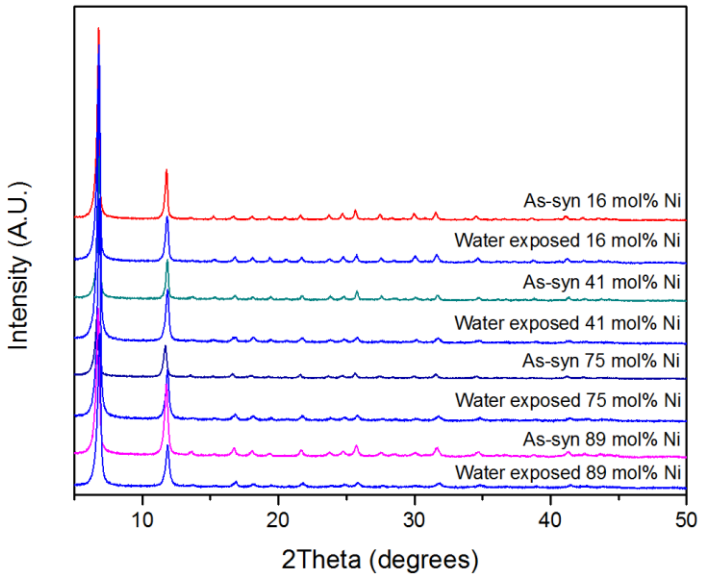

Figure A.8: Comparison of experimental PXRD patterns for as-synthesized Mg-Ni-MM-MOF-74 with various metal concentration levels (prepared at 120 °C and 15:1:1 DMF: EtOH: H_2O, v/v) and samples reactivated after water exposure.

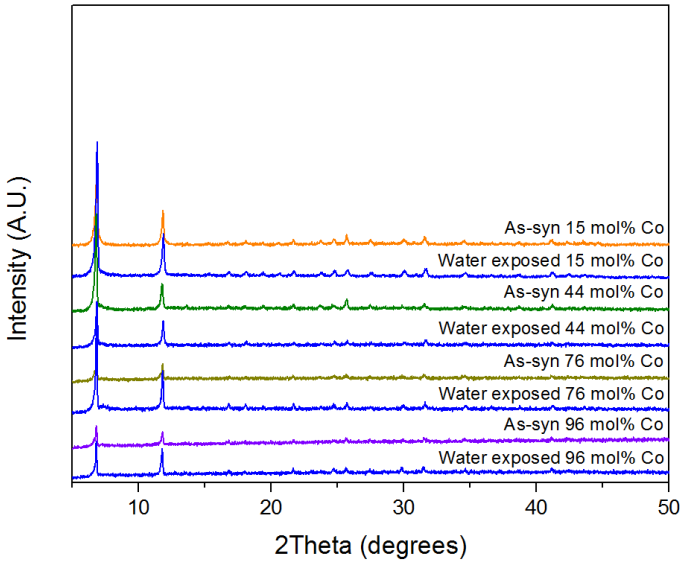

Figure A.9: Comparison of experimental PXRD patterns for as-synthesized Mg-Co-MM-MOF-74 with various metal concentration levels (prepared at 120 °C and 15:1:1 DMF: EtOH: H_2O, v/v) and samples reactivated after water exposure.

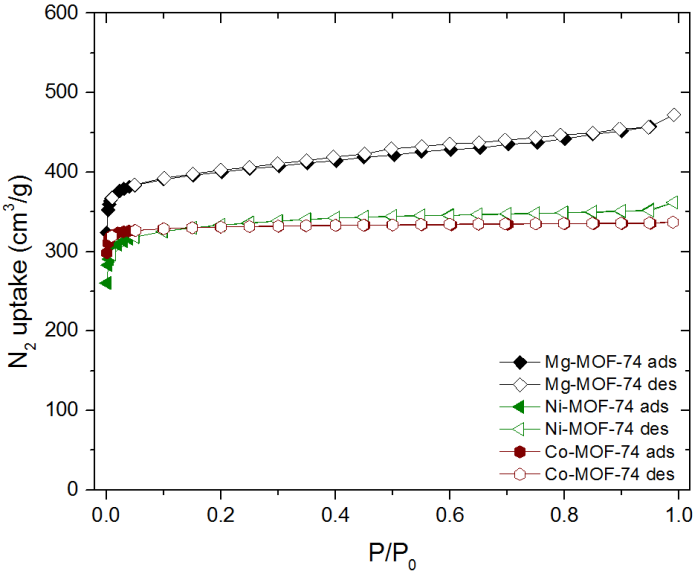

Figure A.10: N_2 isotherms of activated M-MOF-74 (M= Mg, Ni, Co) at 77 K (closed symbols – adsorption, open symbols – desorption).

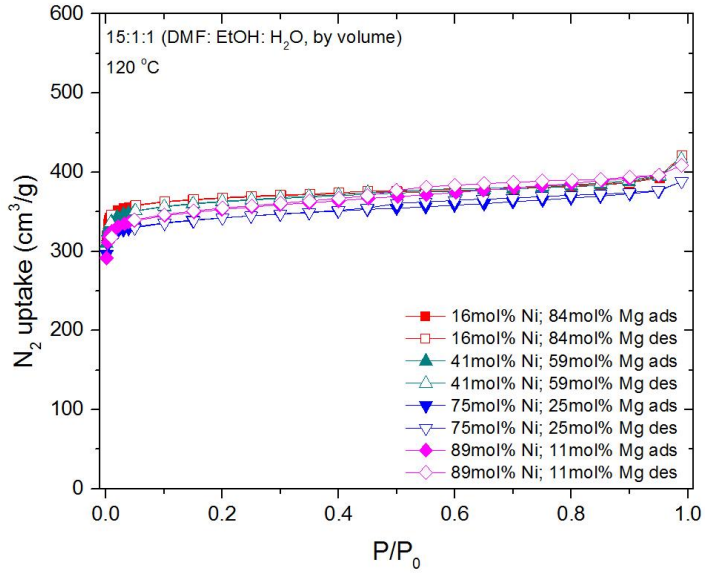

Figure A.11: N_2 isotherms of activated Mg-Ni-MM-MOF-74 with various metal concentration levels (prepared at 120 °C and 15:1:1 DMF: EtOH: H_2O, v/v) at 77 K (closed symbols – adsorption, open symbols – desorption).

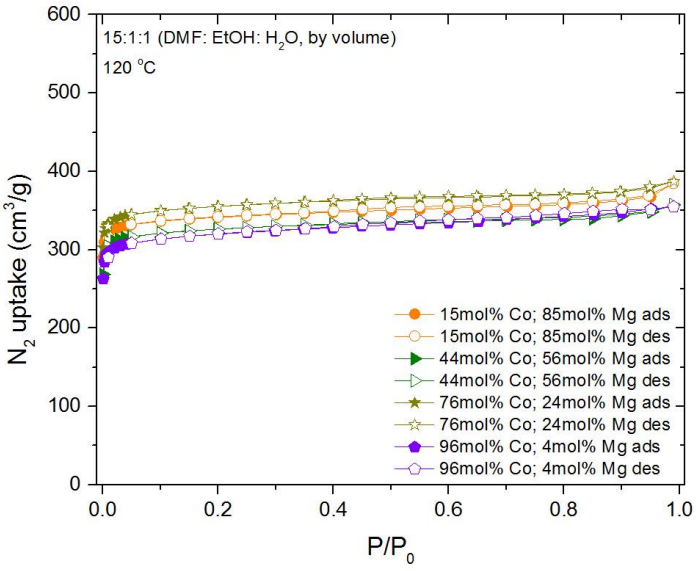

Figure A.12: N_2 isotherms of activated Mg-Co-MM-MOF-74 with various metal concentration levels (prepared at 120 °C and 15:1:1 DMF: EtOH: H_2O, v/v) at 77 K (closed symbols – adsorption, open symbols – desorption).

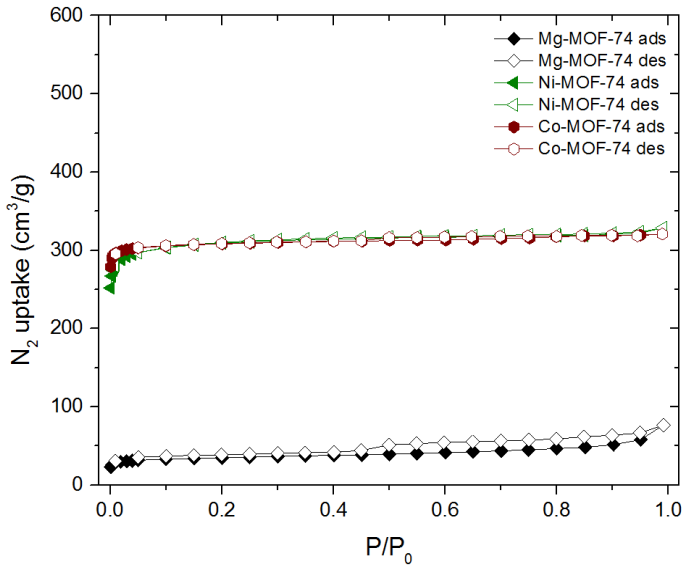

Figure A.13: N_2 isotherms of water exposed M-MOF-74 (M= Mg, Ni, Co) at 77 K (closed symbols – adsorption, open symbols – desorption).

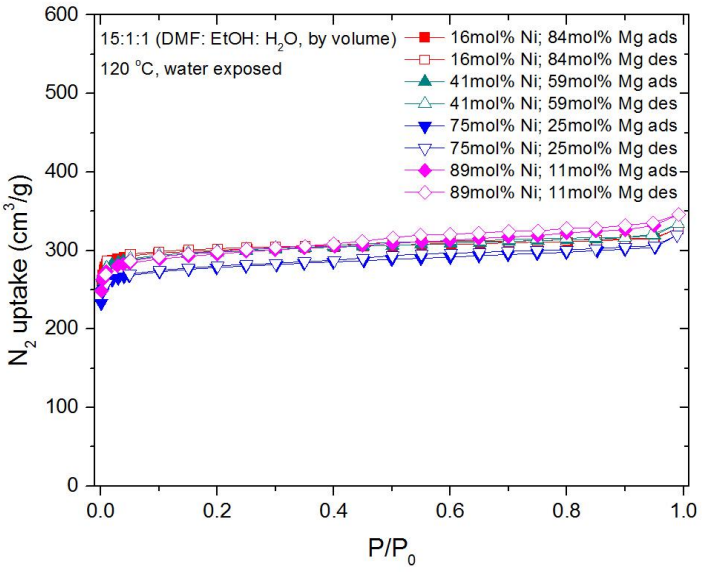

Figure A.14: N_2 isotherms of water exposed Mg-Ni-MM-MOF-74 with various metal concentration levels (prepared at 120 °C and 15:1:1 DMF: EtOH: H_2O, v/v) at 77 K (closed symbols – adsorption, open symbols – desorption).

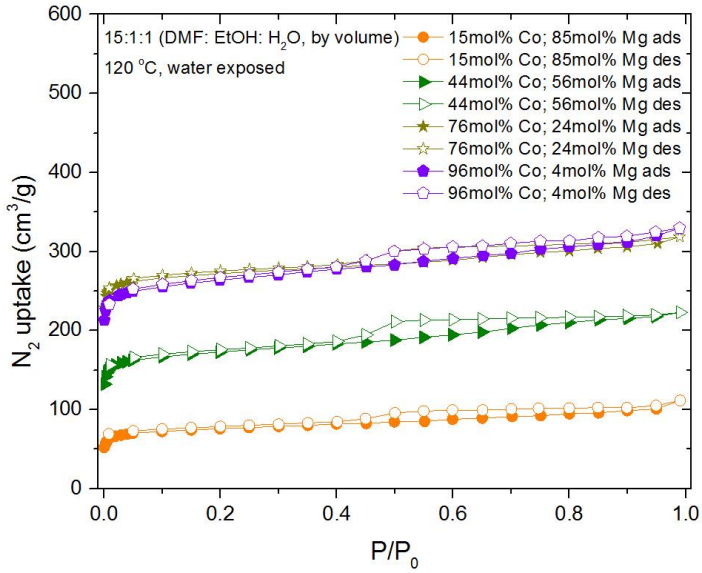

Figure A.15: N_2 isotherms of water exposed Mg-Co-MM-MOF-74 with various metal concentration levels (prepared at 120 °C and 15:1:1 DMF: EtOH: H_2O, v/v) at 77 K (closed symbols – adsorption, open symbols – desorption).

Table A.1: Brunauer-Emmett-Teller (BET) surface areas for parent MOF-74 and MM-MOF-74 compounds prepared at 120 ˚C and a 15:1:1 cosolvent volume ratio (DMF: EtOH: H_2O, v/v) before and after water exposure.

Material	BET surface area (m^2/g)	
	Before water exposure	After water exposure
Mg-MOF-74	1607	131
Ni-MOF-74	1337	1245
Co-MOF-74	1372	1272
16 mol% Ni; 84 mol% Mg	1502	1233
41 mol% Ni; 59 mol% Mg	1473	1209
75 mol% Ni; 25 mol% Mg	1387	1125
89 mol% Ni; 11 mol% Mg	1419	1191
15 mol% Co; 85 mol% Mg	1394	292
44 mol% Co; 56 mol% Mg	1331	679
76 mol% Co; 24 mol% Mg	1447	1100
96 mol% Co; 4 mol% Mg	1294	1045

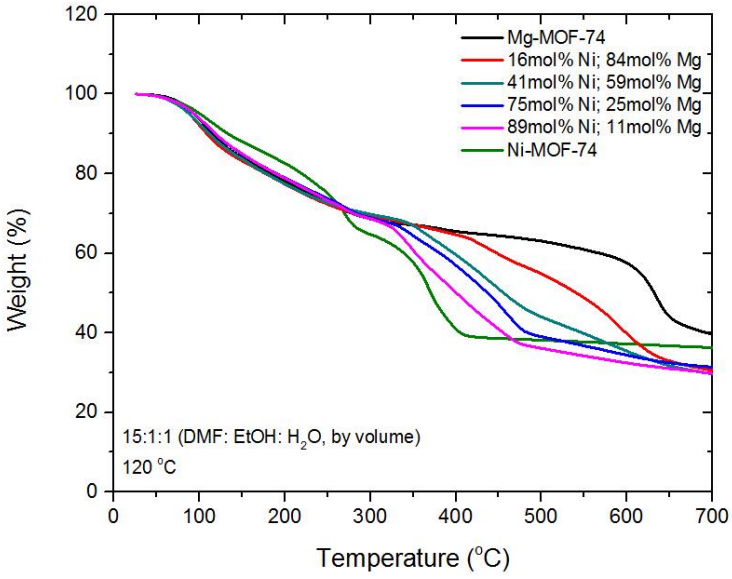

Figure A.16: TGA curves of as-synthesized Mg-Ni-MM-MOF-74 with various metal concentration levels (prepared at 120 °C and 15:1:1 DMF: EtOH: H_2O, v/v) and parent MOF-74 measured in helium flux.

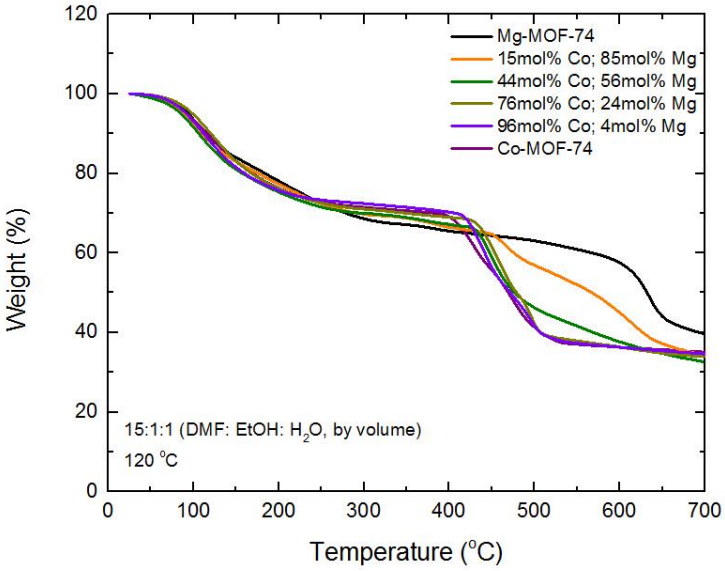

Figure A.17: TGA curves of as-synthesized Mg-Co-MM-MOF-74 with various metal concentration levels (prepared at 120 °C and 15:1:1 DMF: EtOH: H_2O, v/v) and parent MOF-74 measured in helium flux.

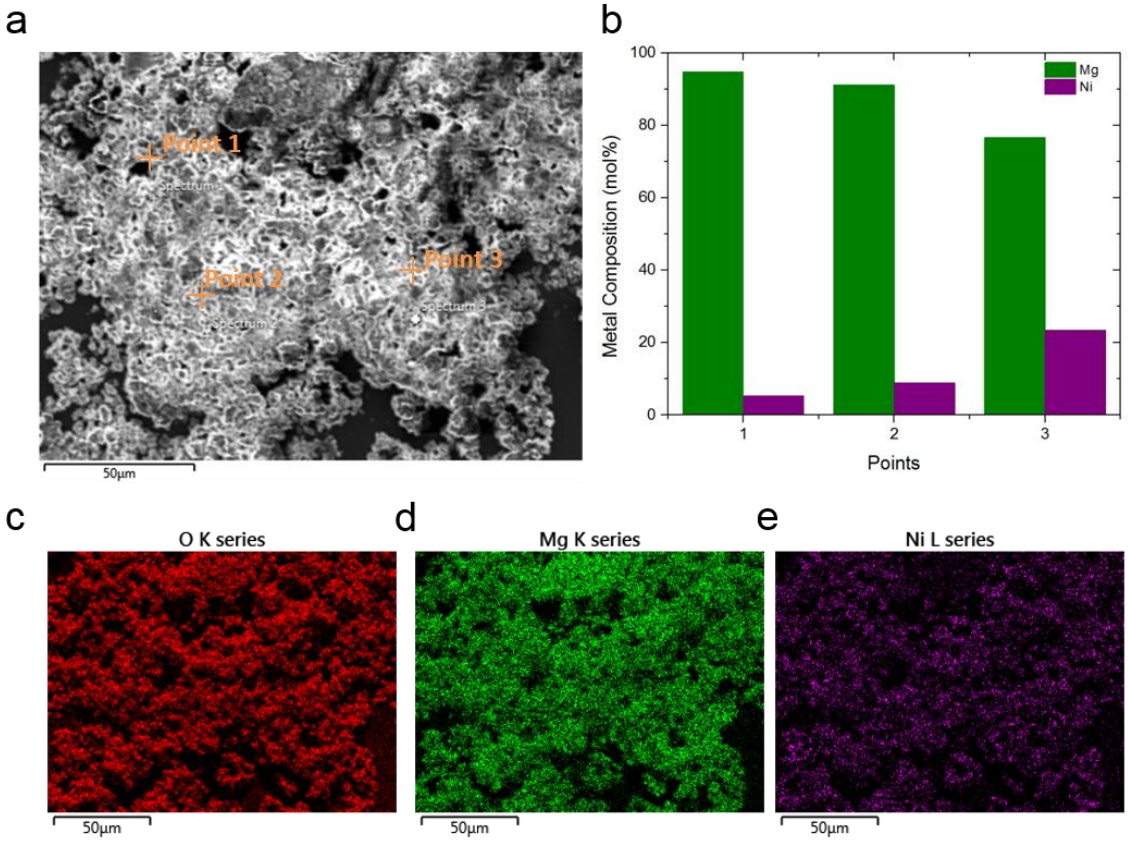

Figure A.18: SEM image and EDS results of 16 mol% Ni-Mg-MM-MOF-74 (120 °C, 15:1:1). (a) SEM image with specific EDS points, (b) EDS point mode graph, (c) O K EDS map, (d) Mg K EDS map, (e) Ni L EDS map.

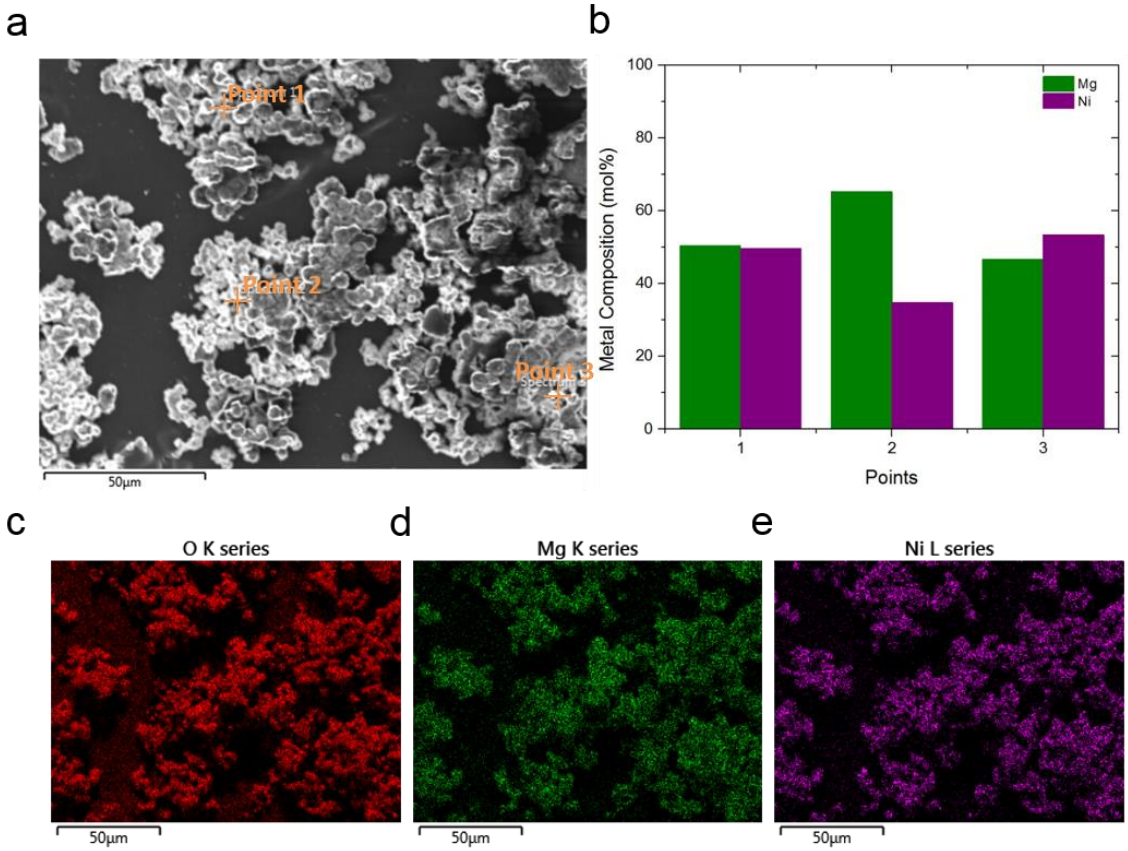

Figure A.19: SEM image and EDS results of 41 mol% Ni-Mg-MM-MOF-74 (120 °C, 15:1:1). (a) SEM image with specific EDS points, (b) EDS point mode graph, (c) O K EDS map, (d) Mg K EDS map, (e) Ni L EDS map.

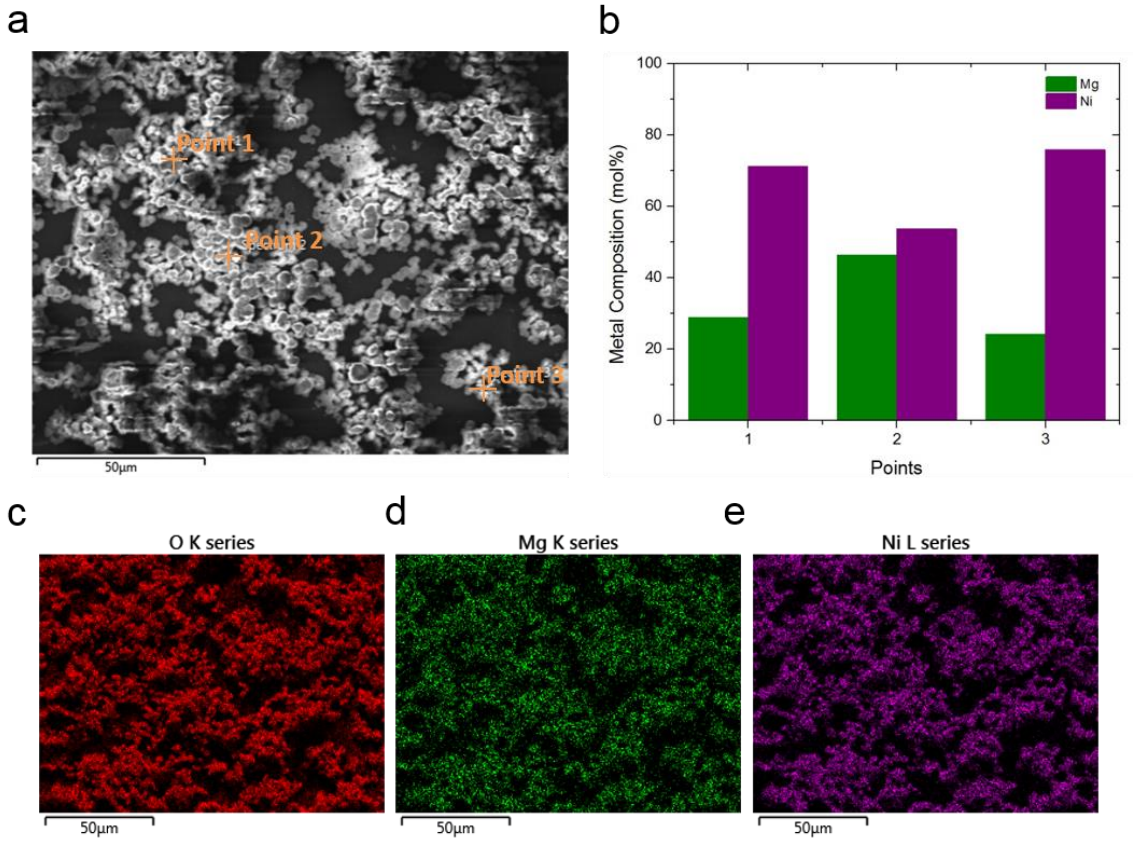

Figure A.20: SEM image and EDS results of 75 mol% Ni-Mg-MM-MOF-74 (120 °C, 15:1:1). (a) SEM image with specific EDS points, (b) EDS point mode graph, (c) O K EDS map, (d) Mg K EDS map, (e) Ni L EDS map.

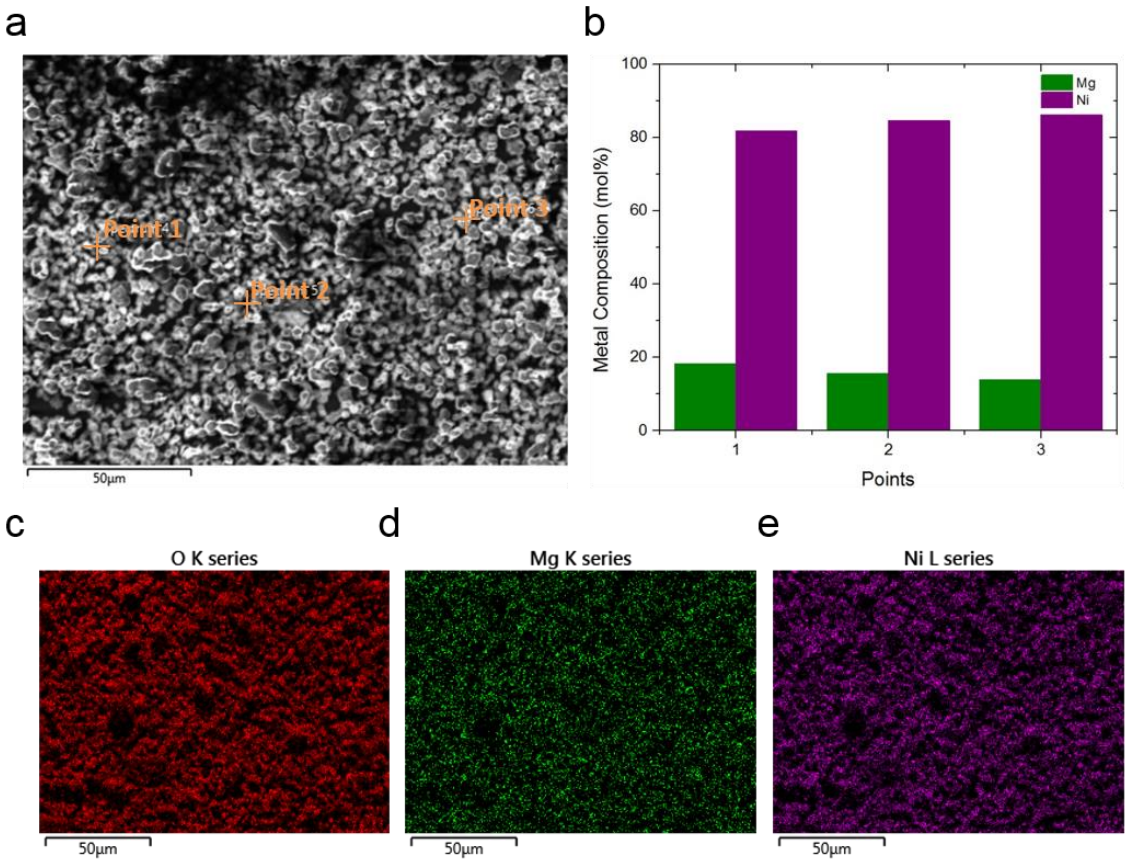

Figure A.21: SEM image and EDS results of 89 mol% Ni-Mg-MM-MOF-74 (120 °C, 15:1:1). (a) SEM image with specific EDS points, (b) EDS point mode graph, (c) O K EDS map, (d) Mg K EDS map, (e) Ni L EDS map.

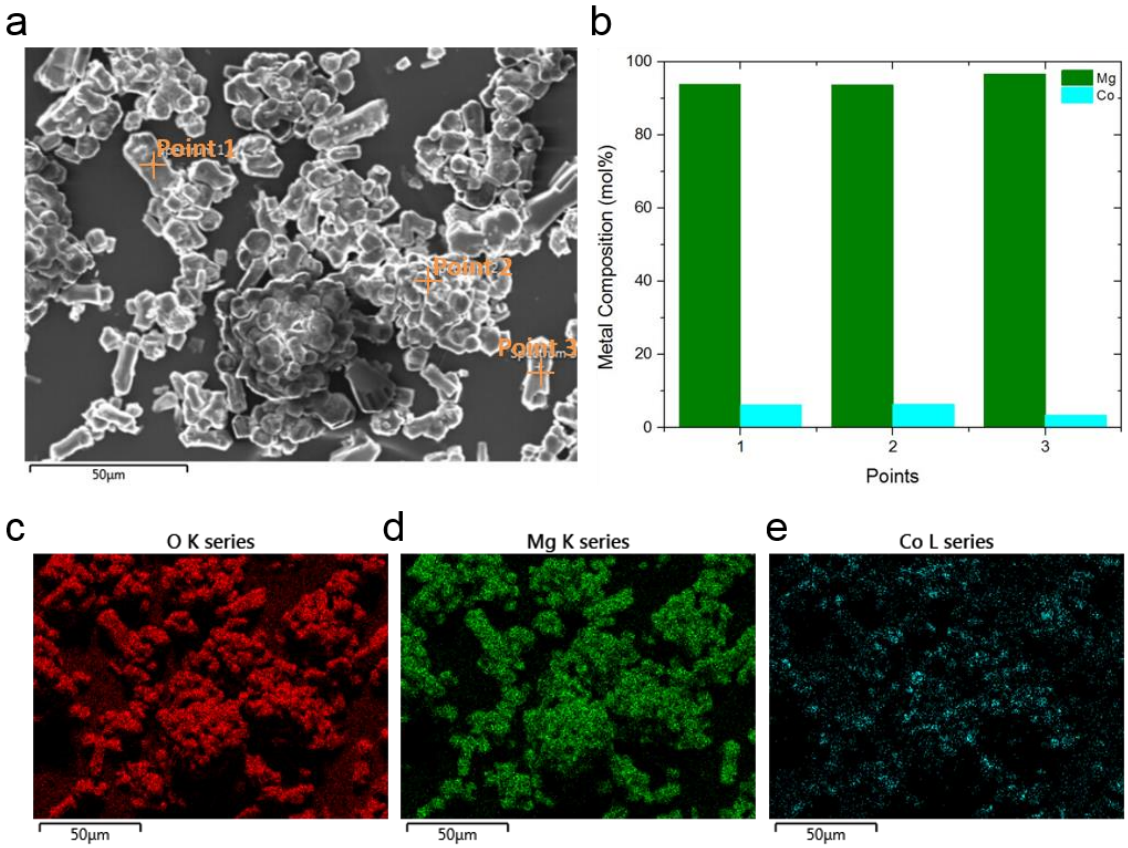

Figure A.22: SEM image and EDS results of 15 mol% Co-Mg-MM-MOF-74 (120 °C, 15:1:1). (a) SEM image with specific EDS points, (b) EDS point mode graph, (c) O K EDS map, (d) Mg K EDS map, (e) Co L EDS map.

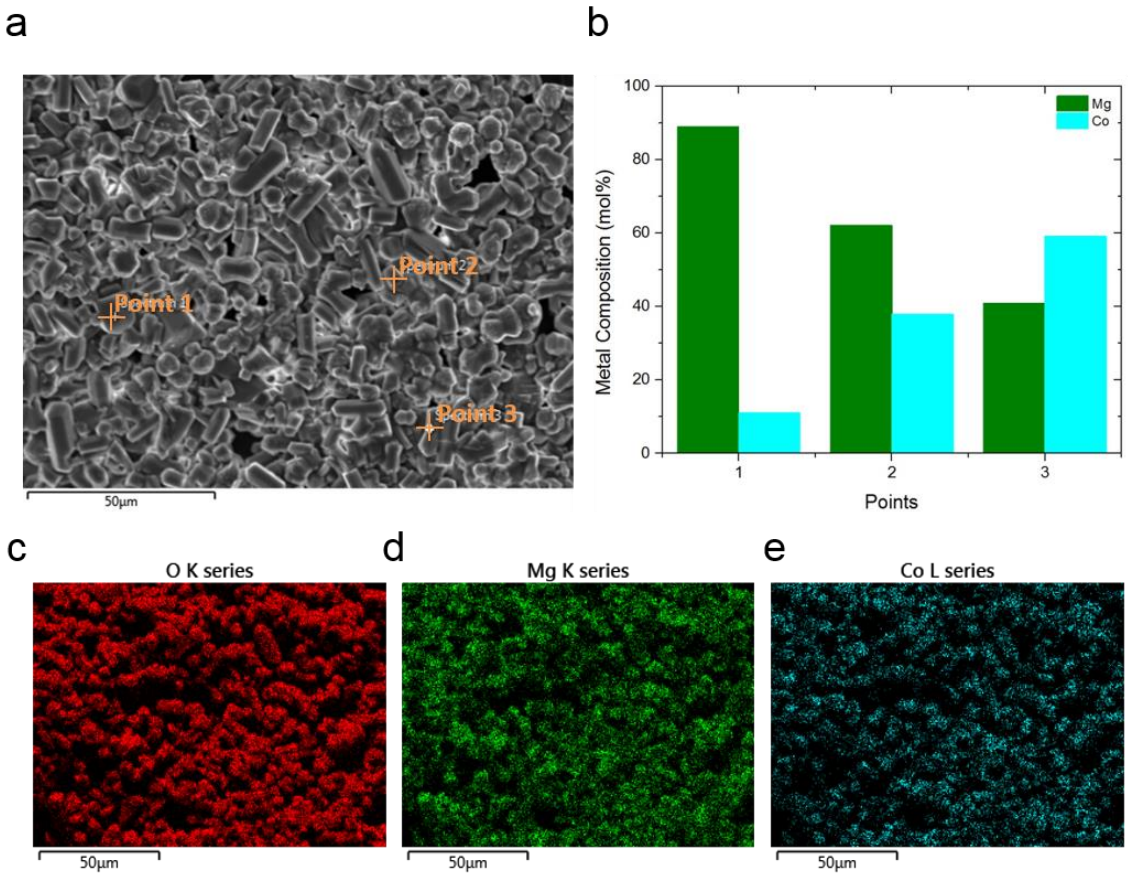

Figure A.23: SEM image and EDS results of 44 mol% Co-Mg-MM-MOF-74 (120 °C, 15:1:1). (a) SEM image with specific EDS points, (b) EDS point mode graph, (c) O K EDS map, (d) Mg K EDS map, (e) Co L EDS map.

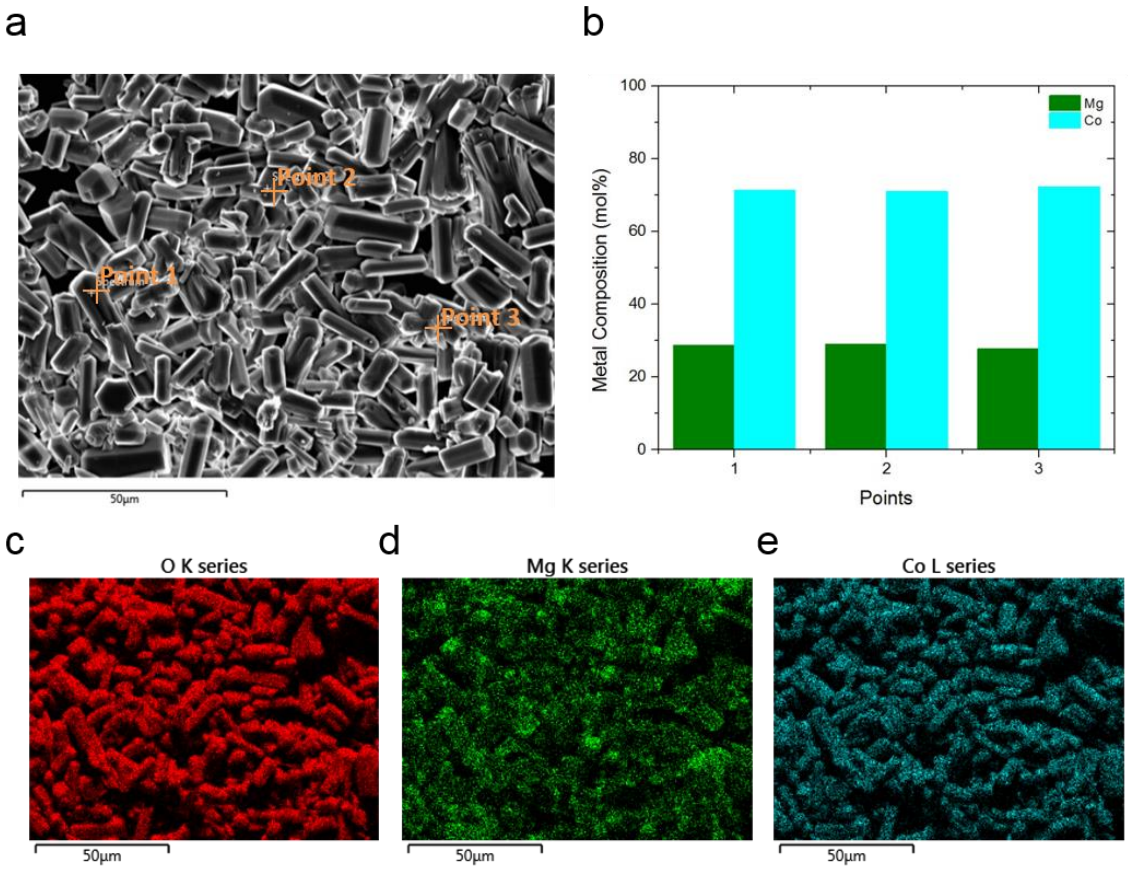

Figure A.24: SEM image and EDS results of 76 mol% Co-Mg-MM-MOF-74 (120 °C, 15:1:1). (a) SEM image with specific EDS points, (b) EDS point mode graph, (c) O K EDS map, (d) Mg K EDS map, (e) Co L EDS map.

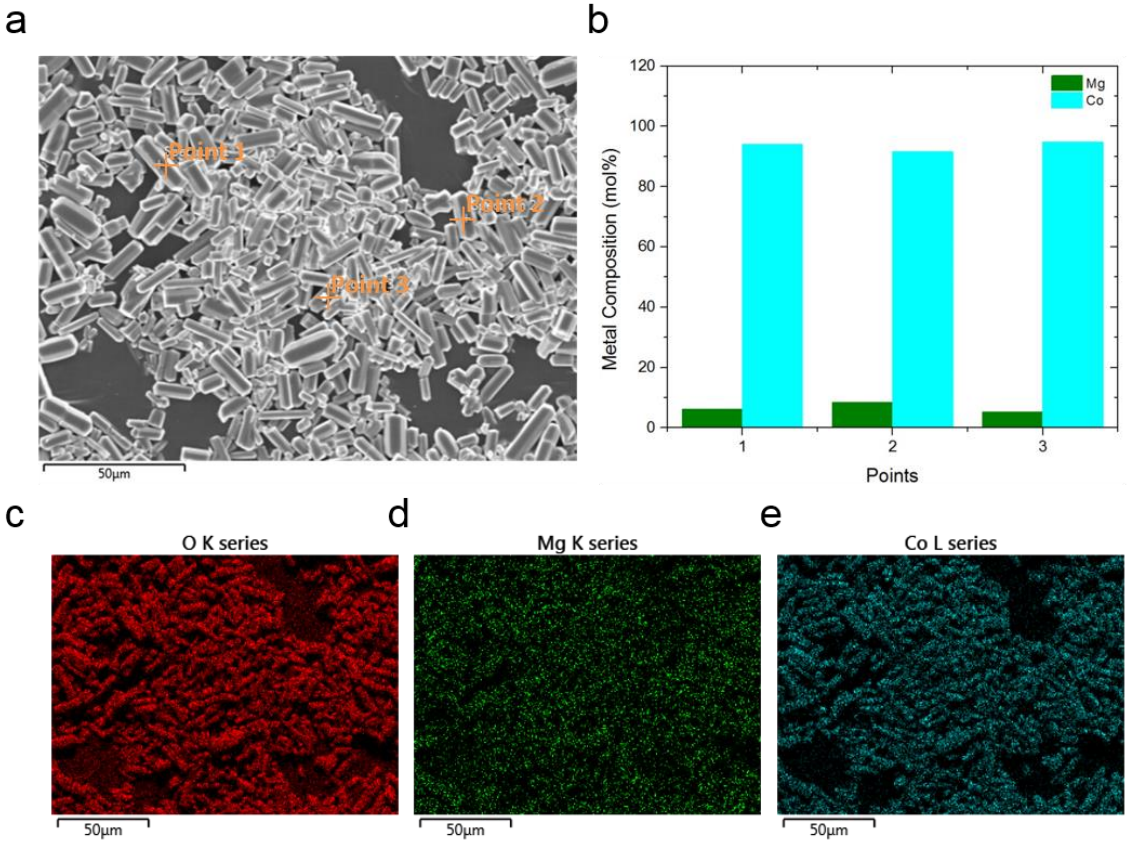

Figure A.25: SEM image and EDS results of 96 mol% Co-Mg-MM-MOF-74 (120 °C, 15:1:1). (a) SEM image with specific EDS points, (b) EDS point mode graph, (c) O K EDS map, (d) Mg K EDS map, (e) Co L EDS map.

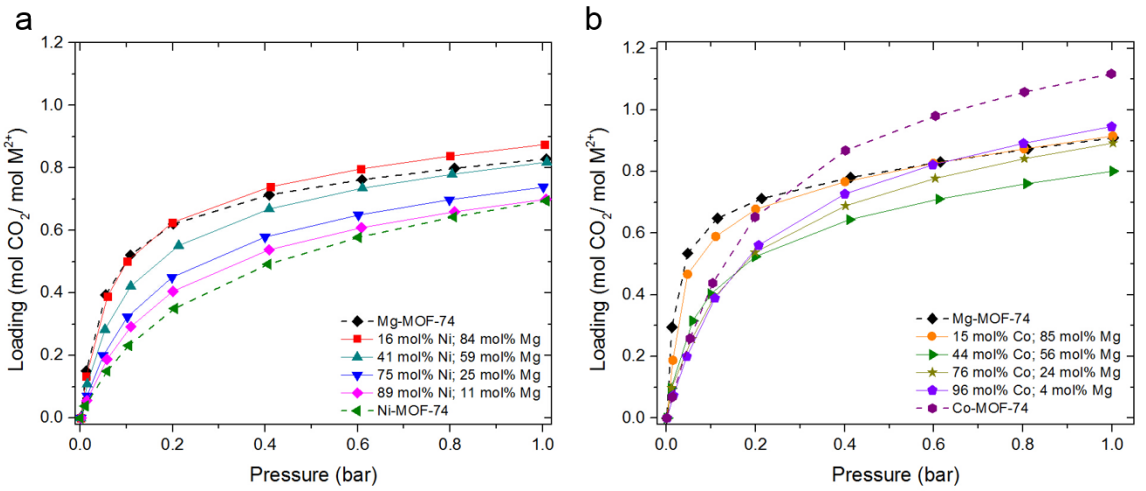

Figure A.26: Gravimetric CO_2 adsorption isotherms at 45 °C in the 0-1 bar region for Mg-*M*-MM-MOF-74 (a: M = Ni, b: M = Co) prepared at 120 °C and a 15:1:1 cosolvent volume ratio (DMF: EtOH: H_2O, v/v).

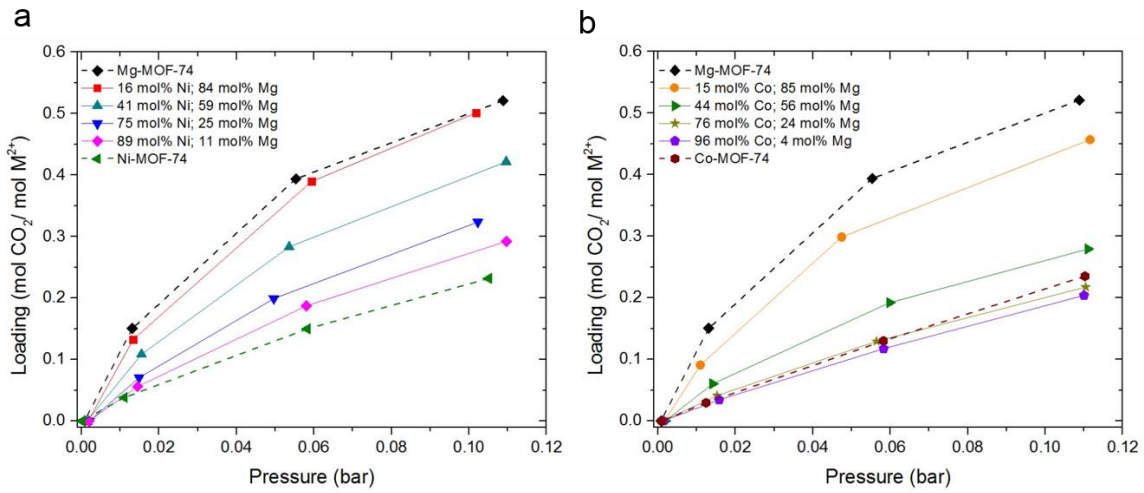

Figure A.27: Gravimetric CO_2 adsorption isotherms at 45 °C in the low-pressure region (below 0.1 bar) for Mg-*M*-MM-MOF-74 (a: M = Ni, b: M = Co).

The CO_2 adsorption isotherms for MM-MOF-74 (120 °C, 15:1:1) collected at 5 °C, 25 °C and 45 °C were fit with the Toth model (Equation A.1), where P is the pressure, q is the amount of adsorbed CO_2, q^{sat} is the saturation CO_2 capacity, b is the adsorbent affinity and t is the heterogeneity of the adsorbent surface. The fitting isotherms can be found in Figure A.28 and Figure A.29, and the Toth model fitting parameters are tabulated in Table A.2 and Table A.3. The isosteric heats of adsorption at specific CO_2 loadings were calculated from the Toth model fitting parameters using the Clausius-Clapeyron equation (Equation A.2), where q_{ST} is the isosteric heat of adsorption, R is the universal gas constant, T is the temperature, P is the pressure, and q is the amount of adsorbed CO_2.

$$q = \frac{q^{sat} bP}{(1+(bp)^t)^{1/t}} \tag{A.1}$$

$$\frac{q_{ST}}{RT^2} = -\left(\frac{\partial \ln P}{\partial T}\right)_q \tag{A.2}$$

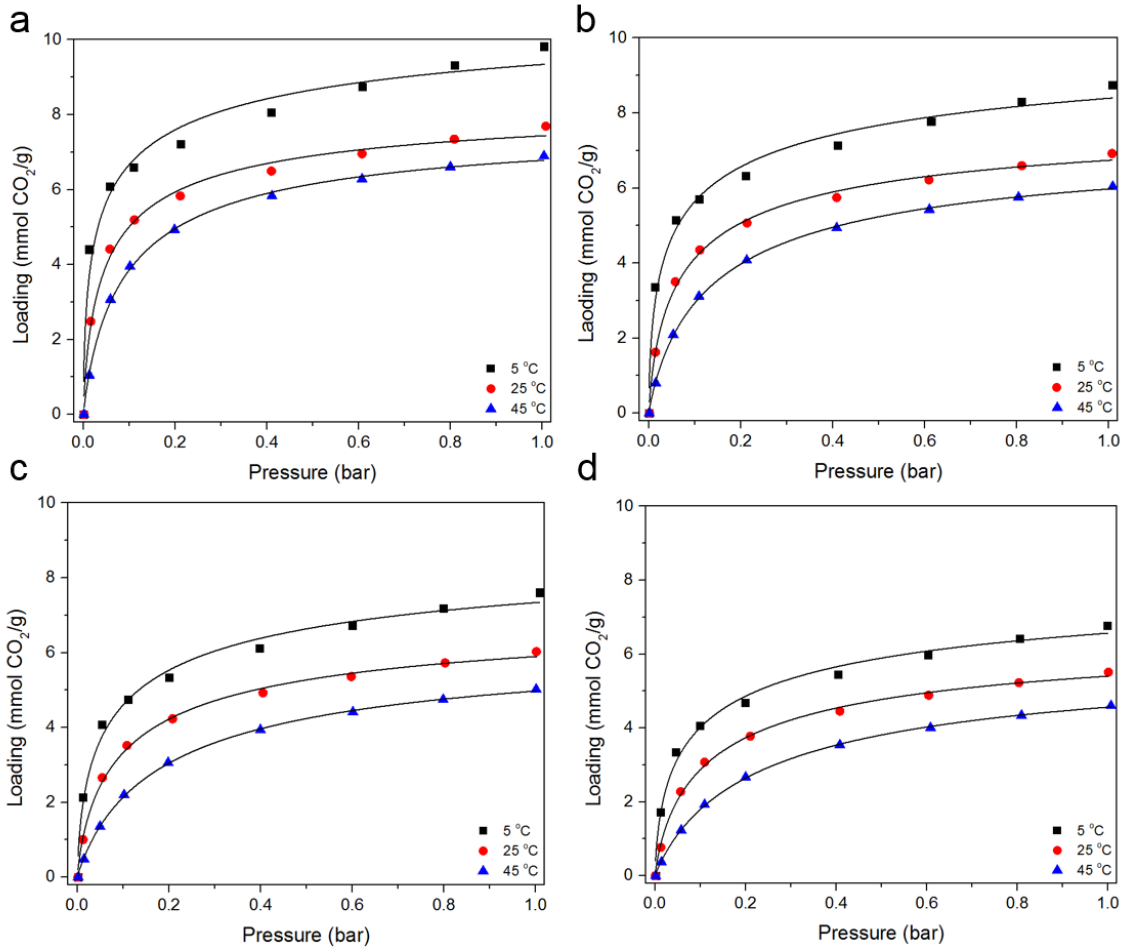

Figure A.28: Toth model fits for CO_2 adsorption in Mg-Ni-MM-MOF-74 with various metal concentration levels (a: 16 mol% Ni, b: 41 mol% Ni, c: 75 mol% Ni, d: 89 mol% Ni; 120 °C, 15:1:1) at 5, 25 and 45 °C.

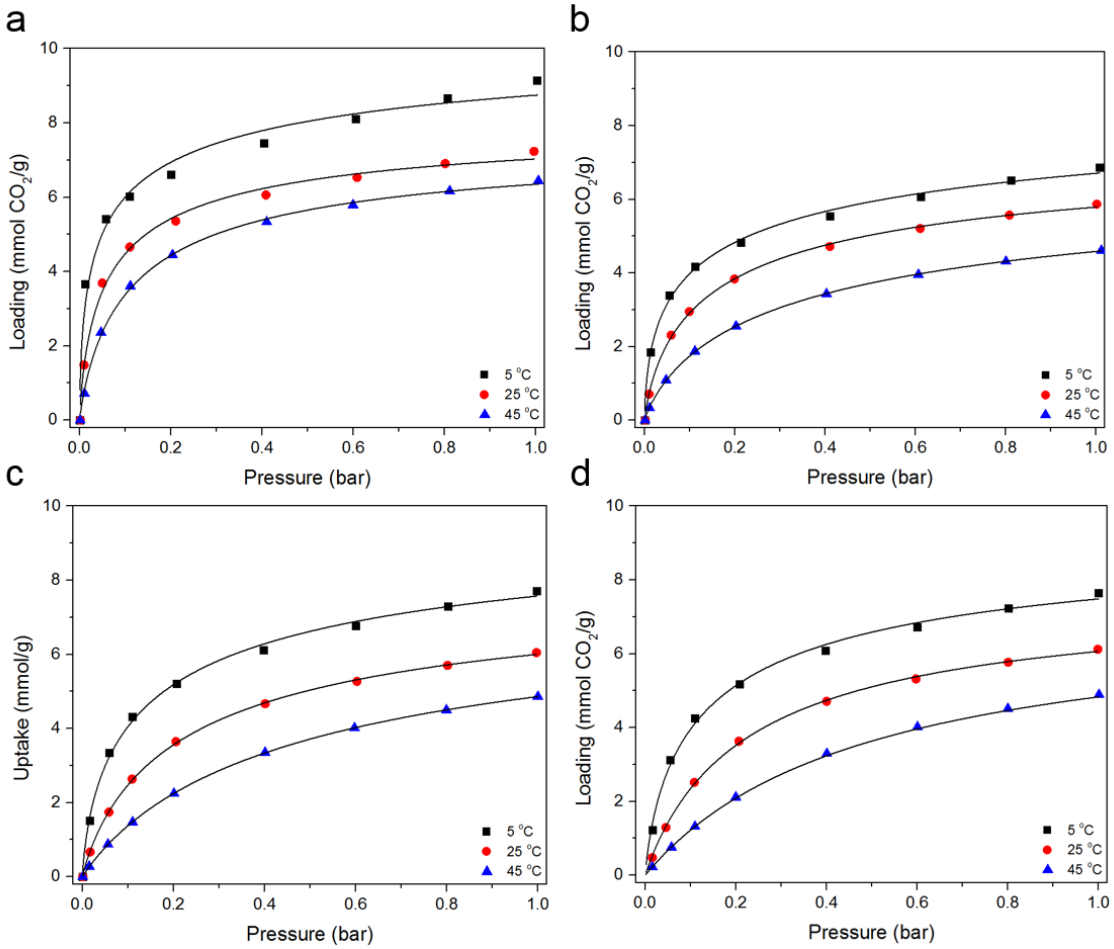

Figure A.29: Toth model fits for CO_2 adsorption in Mg-Co-MM-MOF-74 with various metal concentration levels (a: 15 mol% Co, b: 44 mol% Co, c: 76 mol% Co, d: 96 mol% Co; 120 °C, 15:1:1) at 5, 25 and 45 °C.

Table A.2: Toth model fitting parameters for CO_2 adsorption in Mg-Ni-MM-MOF-74 with various metal concentration levels at 5, 25 and 45 °C.

16 mol% Ni-Mg	5 °C	25 °C	45 °C	75 mol% Ni-Mg	5 °C	25 °C	45 °C
q^{sat}	11.96	8.62	7.88	q^{sat}	9.76	7.41	6.44
b	261.90	43.51	14.51	b	61.58	19.70	6.57
t	0.404	0.62	0.78	t	0.47	0.63	0.79
41 mol% Ni-Mg	5 °C	25 °C	45 °C	89 mol% Ni-Mg	5 °C	25 °C	45 °C
q^{sat}	11.38	8.21	7.46	q^{sat}	9.09	6.94	6.12
b	169.76	29.02	9.88	b	60.27	15.32	5.26
t	0.40	0.61	0.75	t	0.45	0.64	0.80

Table A.3: Toth model fitting parameters for CO_2 adsorption in Mg-Co-MM-MOF-74 with various metal concentration levels at 5, 25 and 45 °C.

15 mol% Co-Mg	5 °C	25 °C	45 °C	75 mol% Co-Mg	5 °C	25 °C	45 °C
q^{sat}	11.53	8.37	7.74	q^{sat}	10.80	8.22	7.76
b	182.02	33.36	12.86	b	22.42	6.19	2.46
t	0.41	0.62	0.73	t	0.52	0.74	0.83
44 mol% Co-Mg	5 °C	25 °C	45 °C	96 mol% Co-Mg	5 °C	25 °C	45 °C
q^{sat}	10.73	7.93	7.28	q^{sat}	9.84	7.68	7.20
b	91.50	13.95	5.34	b	15.98	4.82	2.04
t	0.369	0.60	0.64	t	0.61	0.91	1.00

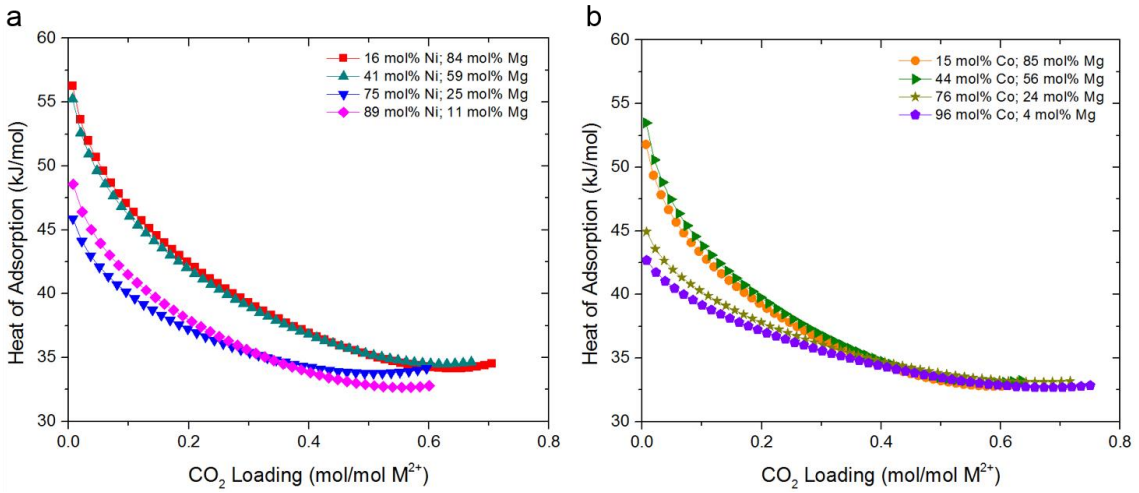

Figure A.30: Isosteric heats of CO_2 adsorption for Mg-*M*-MM-MOF-74 (a: M = Ni^{2+}, b: M = Co^{2+}) prepared at 120 °C and a 15:1:1 cosolvent volume ratio (DMF: EtOH: H_2O, v/v).

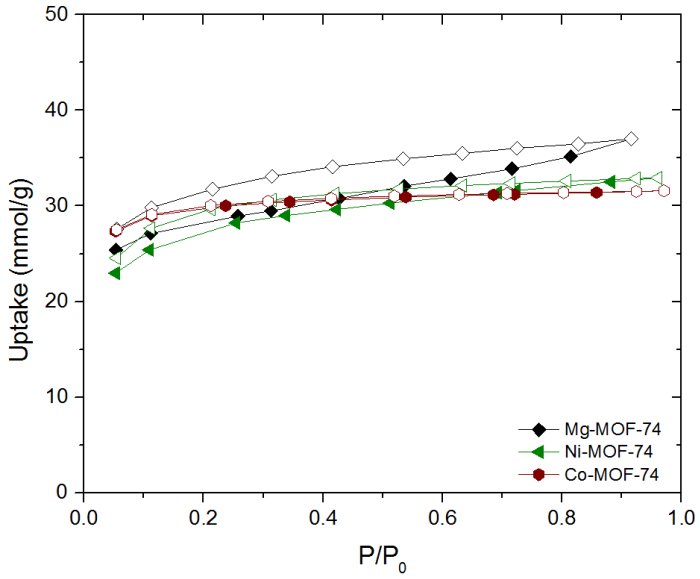

Figure A.31: Water vapor isotherms in parent M-MOF-74 (M = Mg, Ni, Co) at 22 °C (closed symbols – adsorption, open symbols – desorption).

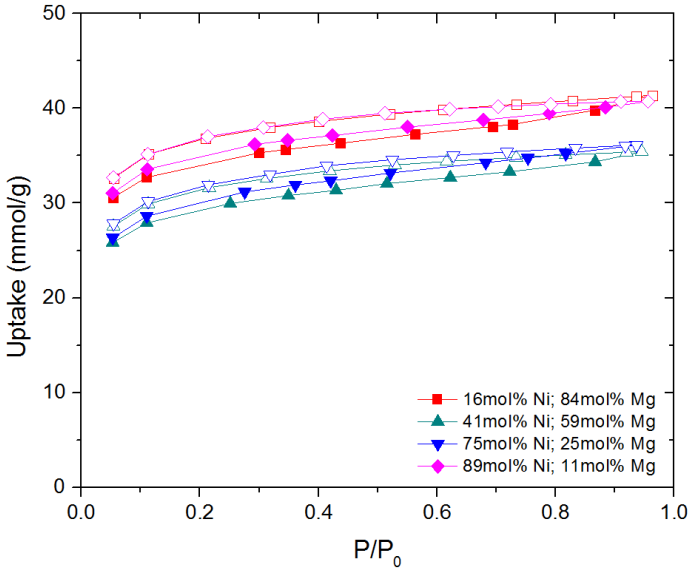

Figure A.32: Water vapor isotherms in activated Mg-Ni-MM-MOF-74 with various metal concentration levels (prepared at 120 °C and 15:1:1 DMF: EtOH: H_2O, v/v) at 22 °C (closed symbols – adsorption, open symbols – desorption).

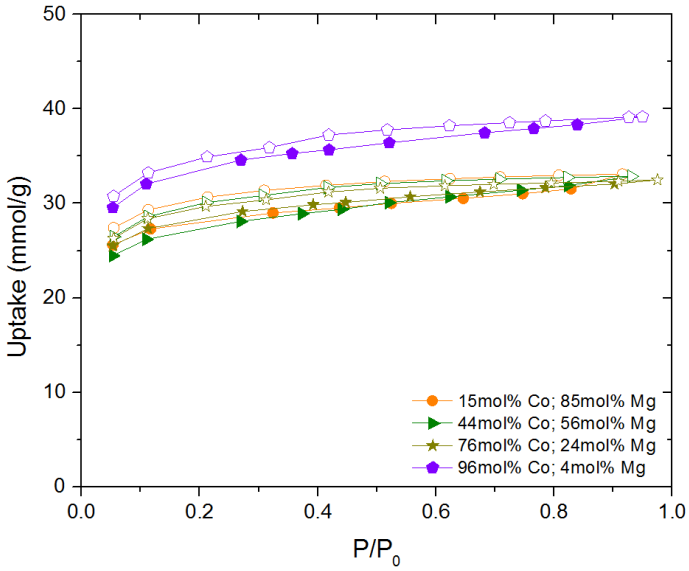

Figure A.33: Water vapor isotherms in activated Mg-Co-MM-MOF-74 with various metal concentration levels (prepared at 120 °C and 15:1:1 DMF: EtOH: H_2O, v/v) at 22 °C (closed symbols – adsorption, open symbols – desorption).

A.1 References

1. Dietzel, P. D. C.; Blom, R.; Fjellvag, H., *Eur. J. Inorg. Chem.* **2008**, (23), 3624-3632.

2. Dietzel, P. D. C.; Panella, B.; Hirscher, M.; Blom, R.; Fjellvag, H., *Chem. Commun.* **2006**, (9), 959-961.

3. Dietzel, P. D. C.; Morita, Y.; Blom, R.; Fjellvag, H., *Angew. Chem. Int. Ed.* **2005**, *44* (39), 6354-6358.

APPENDIX B. CHAPTER 4 SUPPORTING INFORMATION

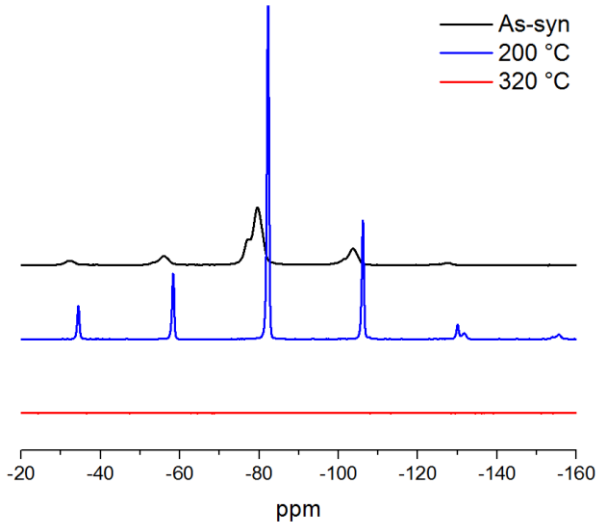

Figure B.1: Mass-normalized ^{19}F solid-state NMR spectra of as-synthesized (black), 200 °C (blue), and 320 °C (red) defective UiO-66 with 20X addition of TFA during the synthesis.

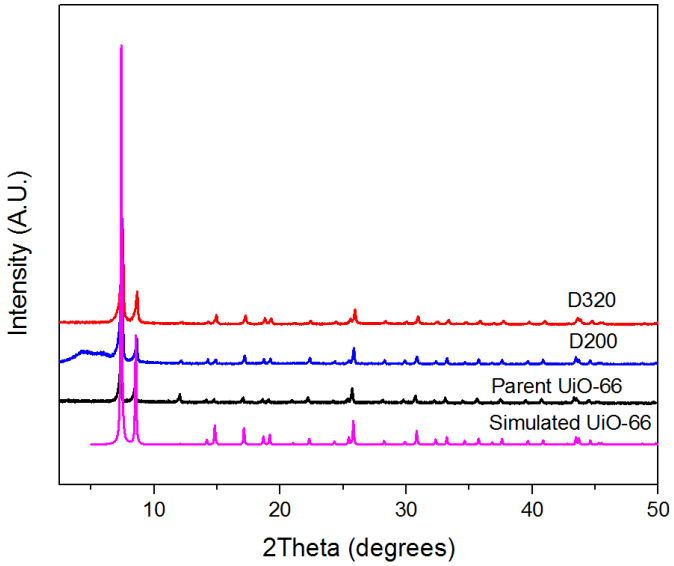

Figure B.2: PXRD patterns for as-synthesized parent UiO-66, D200 and D320.

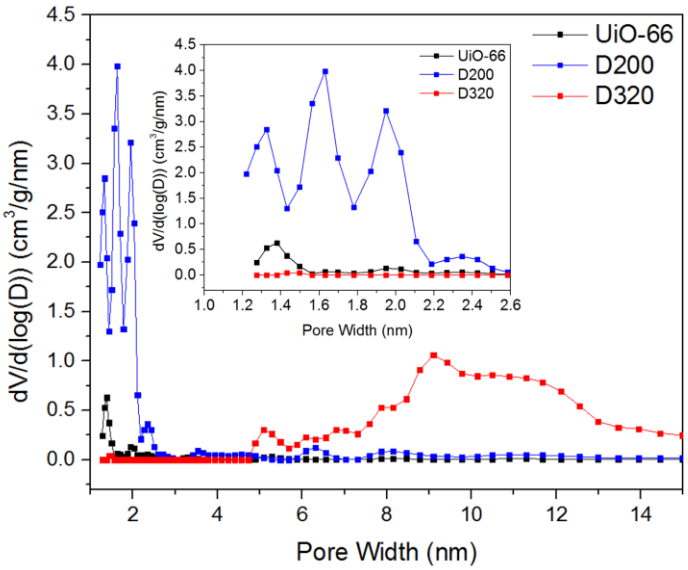

Figure B.3: Pore size distributions of parent UiO-66, D200, and D320 according to non-local density functional theory.

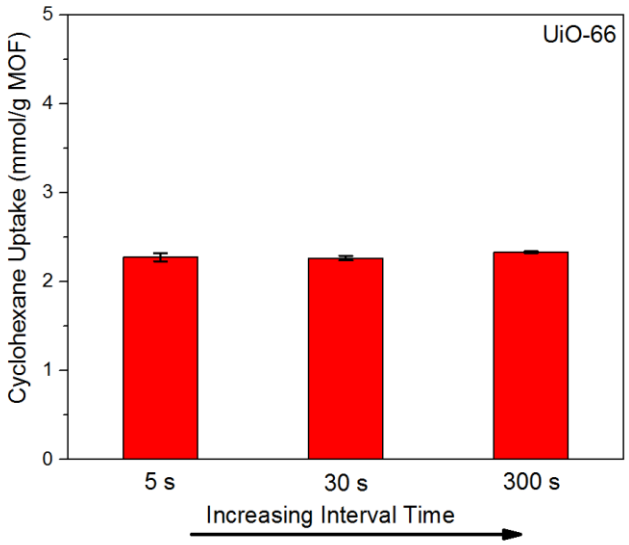

Figure B.4: Cyclohexane uptake of parent UiO-66 at 25 °C with interval times of 5 s, 30 s, and 300 s.

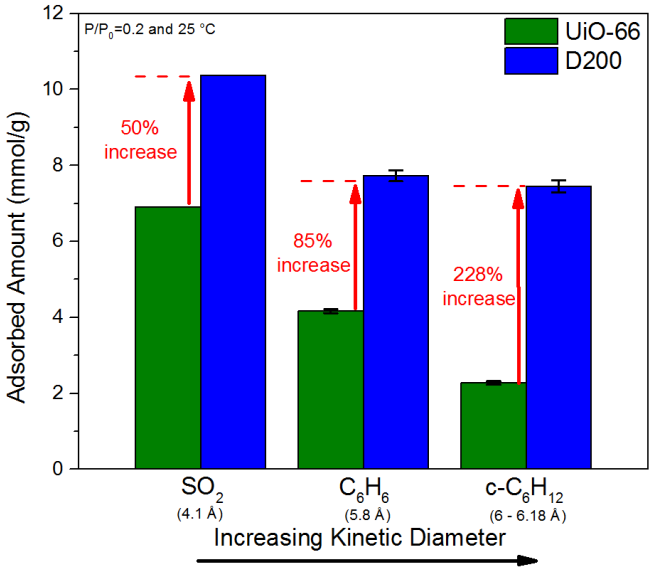

Figure B.5: Adsorption capacities (mmol/g, at P/P_0 = 0.2 and T = 25 °C) of SO_2, benzene (C_6H_6), and cyclohexane (c-C_6H_{12}) for parent UiO-66 and D200.

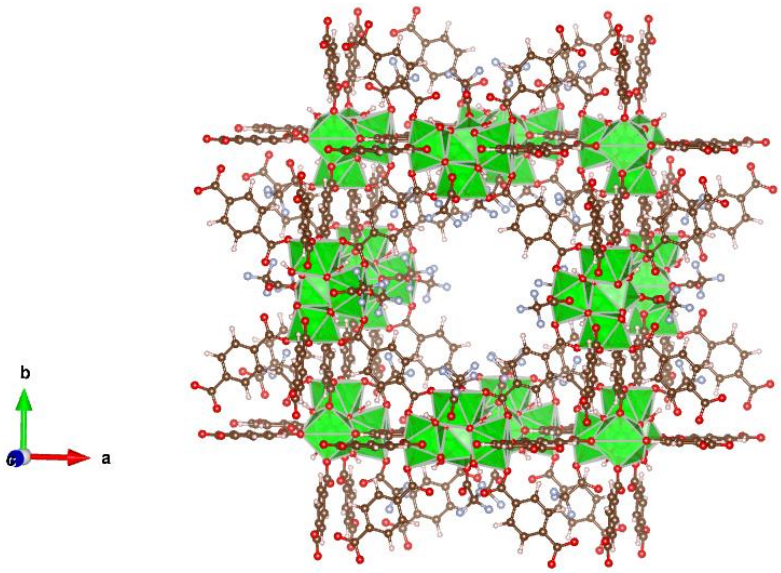

Figure B.6: **Reo** defective UiO-66 structure (D200) with trifluoroacetate ligands compensating Zr_6 clusters. Zr atoms are shown in green, O atoms are shown in red, C atoms are shown in gray, H atoms are shown in white, and F atoms are shown in blue.

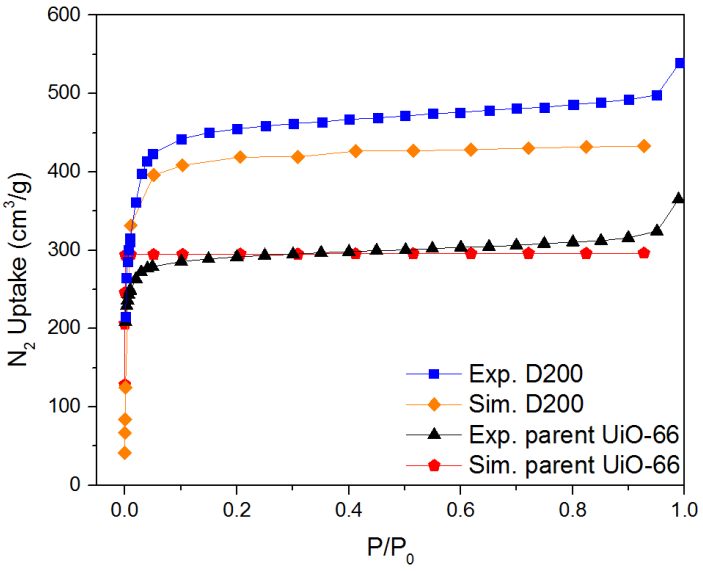

Figure B.7: Experimental and computational N_2 adsorption isotherms at 77 K for parent UiO-66 and D200.

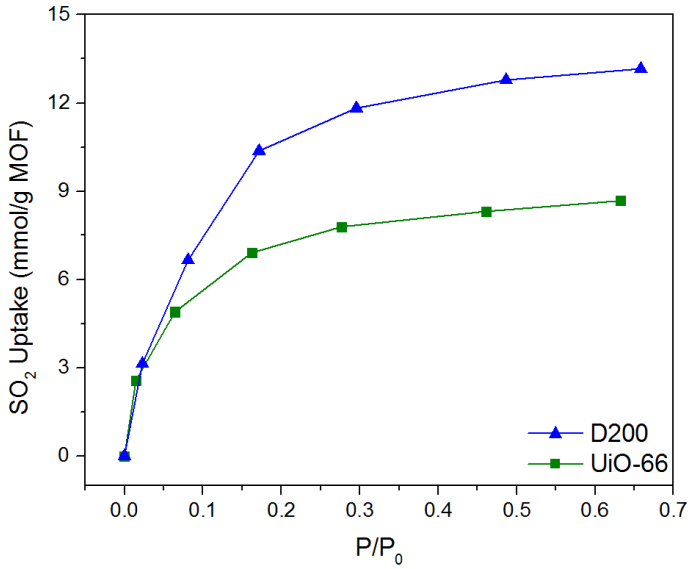

Figure B.8: SO_2 adsorption isotherms at 25 °C for parent UiO-66 and D200.

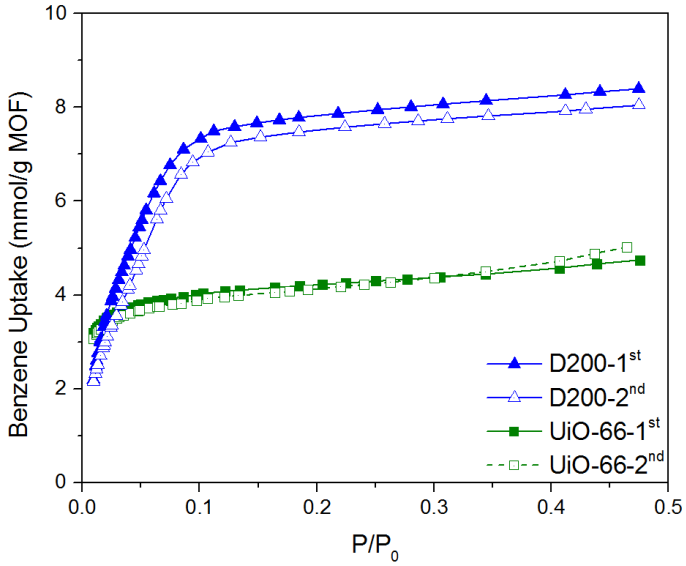

Figure B.9: Benzene adsorption isotherms at 25 °C in the low-pressure region for parent UiO-66 and D200 (two separate runs).

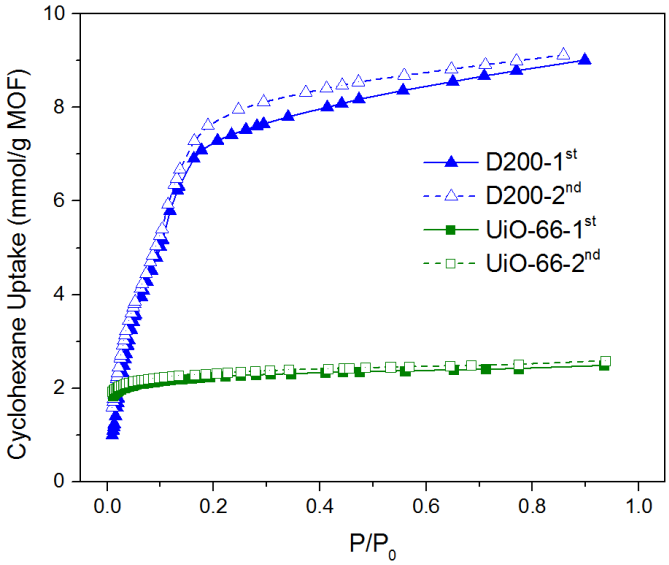

Figure B.10: Cyclohexane isotherms at 25 °C for parent UiO-66 and D200 (two separate runs).

To determine the number of defect sites per Zr_6 introduced by TFA modulator, ICP-OES elemental analysis was performed on the defective UiO-66 with various concentrations of TFA modulator. Weight and molar percentages of F and Zr species within the tested samples were summarized in Table B.1. The number of defect sites per Zr_6 cluster within each sample was equal to the ratio of molar percentage of CF_3 group over molar percentage of Zr_6 cluster, which was included in the last column in Table B.1.

Table B.1: The number of defect sites per Zr_6 in defective UiO-66 using TFA modulator at various concentrations.

Sample type	F wt%	Zr wt%	CF_3 group mol%	Zr_6 cluster mol%	Number of defect sites/Zr_6 cluster
2.5X	3.07	33.38	0.054	0.061	0.89
5X	4.04	31.83	0.071	0.058	1.22
10X	6.00	36.31	0.10	0.066	1.58
20X	9.17	38.36	0.16	0.070	2.30

Table B.2: BET surface area in m^2/g for as-synthesized, water (120 h), dry SO_2, humid SO_2 (6000 ppm-h, 85% RH), and aqueous SO_2 (6000 ppm-h) exposed parent and defective UiO-66. The exposure experiments were conducted on fresh samples for two separate times.

Sample Type	As-synthesized	Aqueous H_2O	Dry SO_2	Humid SO_2	Aqueous SO_2
UiO-66 200°C	1136	1100/1134	1146/1094	1139/1111	1119/1190
D200-2.5X	1361	1497/1351	1271/1394	1372/1364	1425/1336
D200-5X	1422	1495/1477	1394/1390	1414/1395	1274/1375
D200-10X	1641	1676/1558	1601/1638	1553/1604	1503/1515
D200-20X	1808	1735/1558	1801/1811	1830/1740	1606/1473
UiO-66 320°C	1131	1085/1110	1129/1148	1067/1042	1086/1040
D320-2.5X	1110	951/1069	1058/1170	803/845	1083/1049
D320-5X	969	876/799	1086/966	650/635	858/776
D320-10X	1003	698/771	1089/1005	677/595	701/644
D320-20X	854	466/432	815/845	404/363	397/434

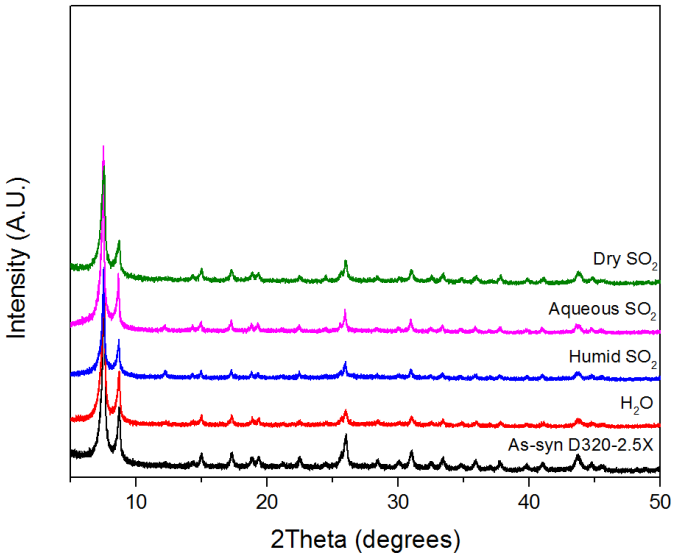

Figure B.11: PXRD patterns for as-synthesized and exposed defective UiO-66 (D320-2.5X).

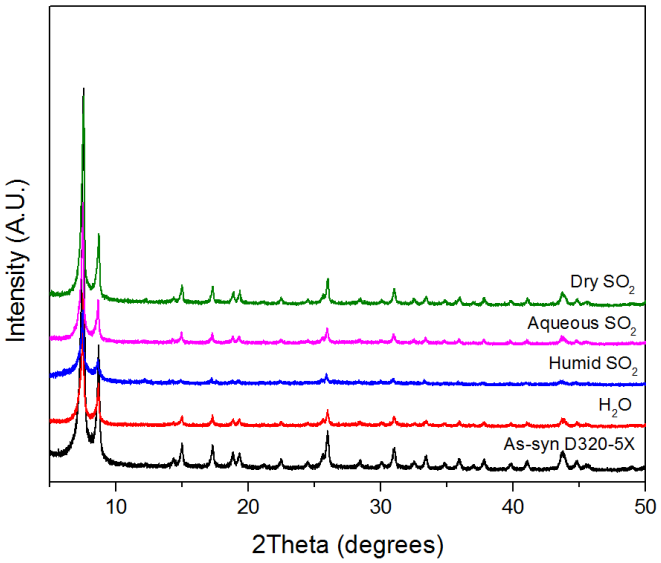

Figure B.12: PXRD patterns for as-synthesized and exposed defective UiO-66 (D320-5X).

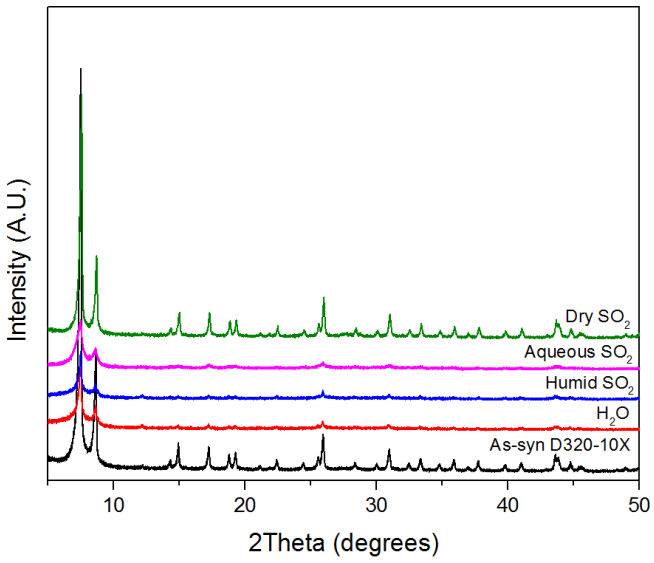

Figure B.13: PXRD patterns for as-synthesized and exposed defective UiO-66 (D320-10X).

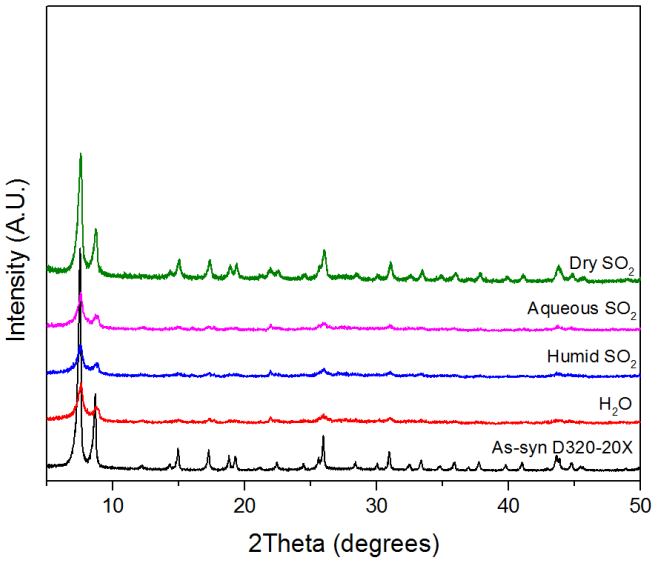

Figure B.14: PXRD patterns for as-synthesized and exposed defective UiO-66 (D320-20X).

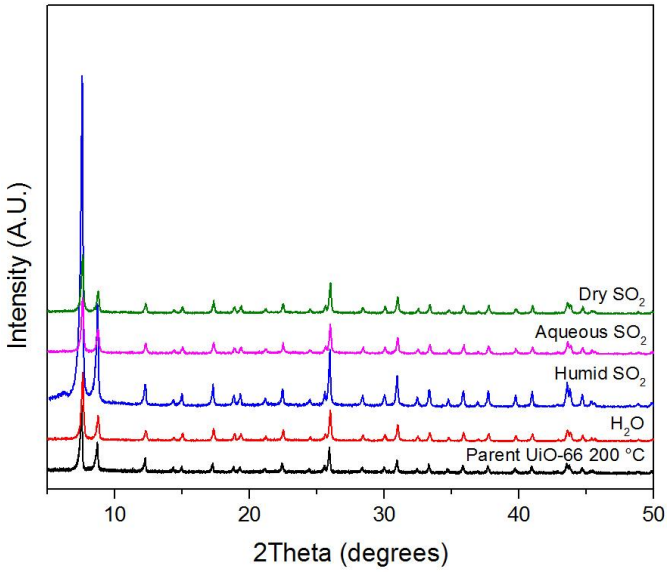

Figure B.15: PXRD patterns for as-synthesized and exposed parent UiO-66 (200 °C).

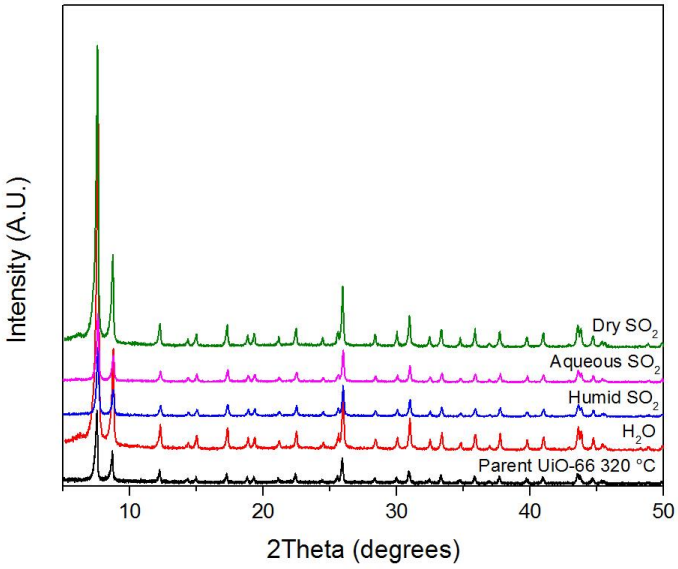

Figure B.16: PXRD patterns for as-synthesized and exposed parent UiO-66 (320 °C).

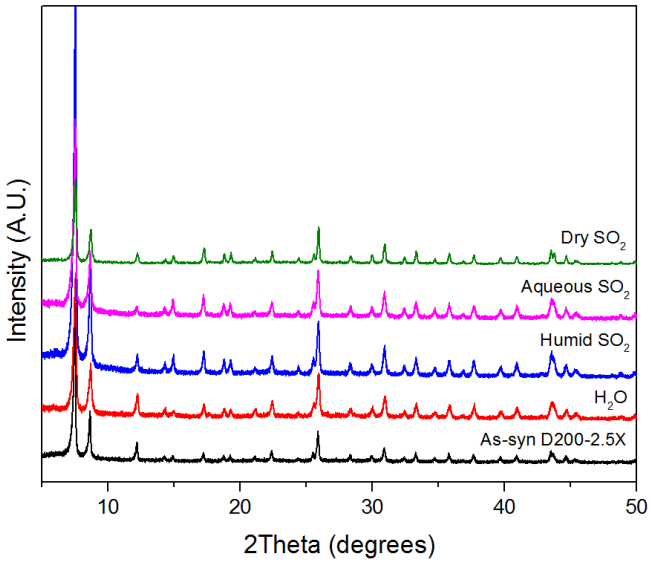

Figure B.17: PXRD patterns for as-synthesized and exposed defective UiO-66 (D200-2.5X).

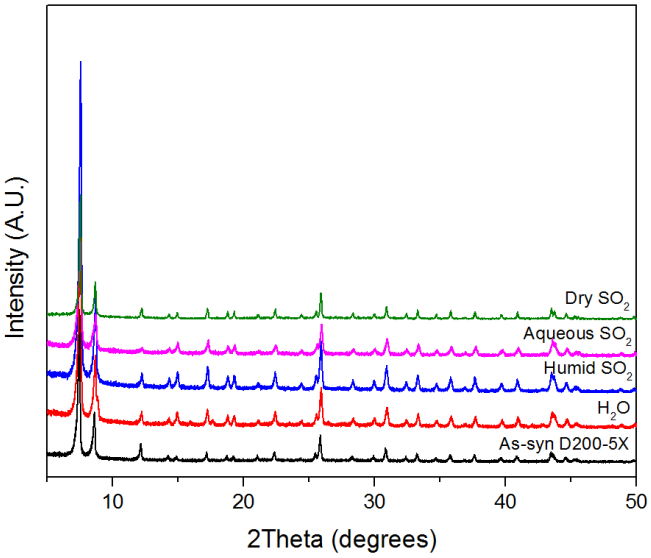

Figure B.18: PXRD patterns for as-synthesized and exposed defective UiO-66 (D200-5X).

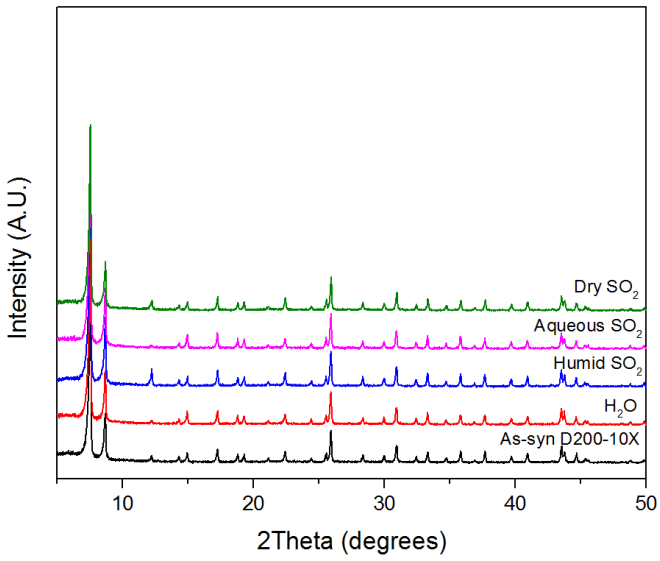

Figure B.19: PXRD patterns for as-synthesized and exposed defective UiO-66 (D200-10X).

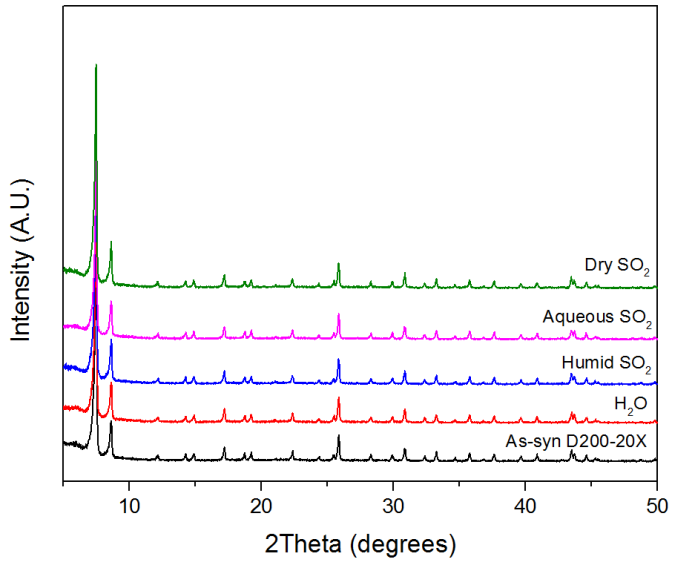

Figure B.20: PXRD patterns for as-synthesized and exposed defective UiO-66 (D200-20X).

APPENDIX C. CHAPTER 5 SUPPORTING INFORMATION

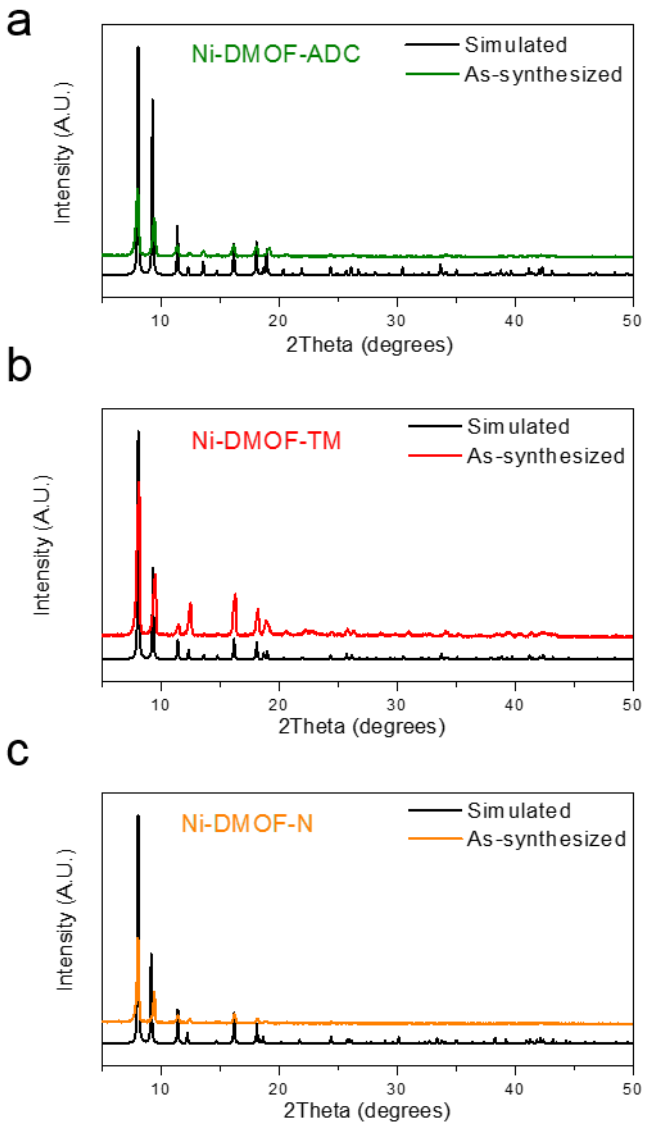

Figure C.1: PXRD patterns of as-synthesized and simulated (a) DMOF-ADC,[1] (b) DMOF-TM,[2] and (c) DMOF-NDC.[2]

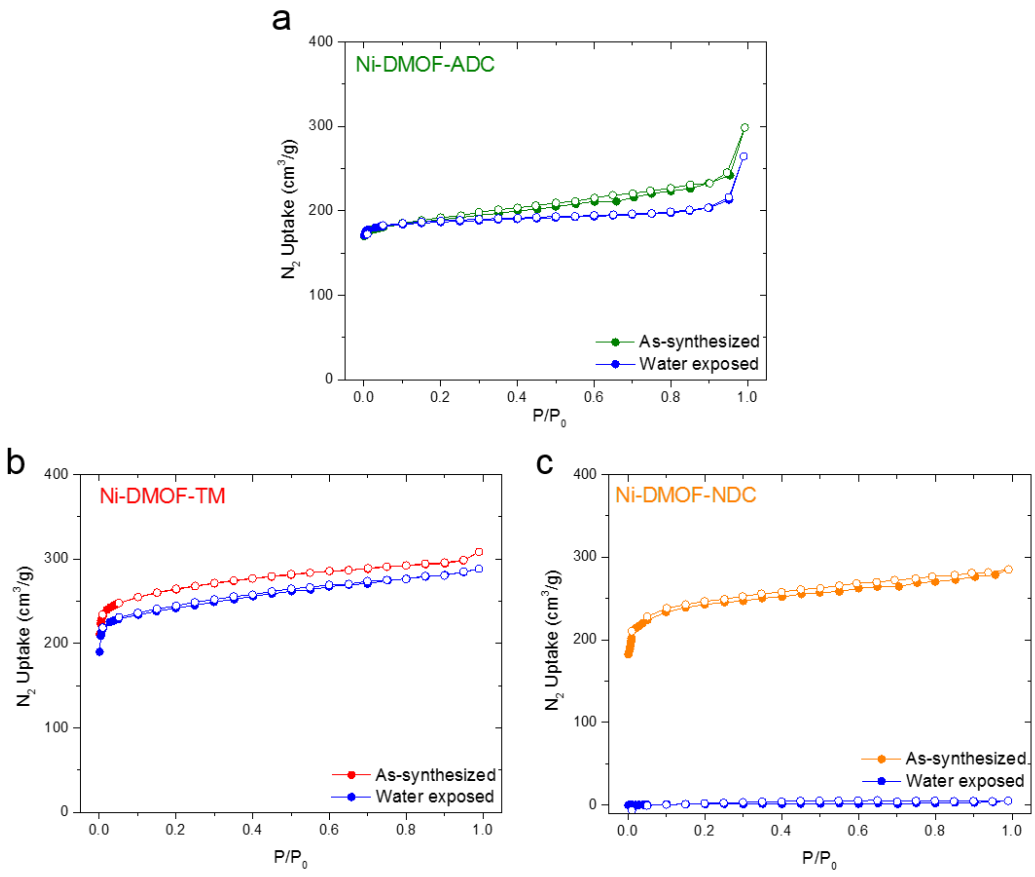

Figure C.2: N_2 adsorption-desorption curves at 77 K on the activated MOF samples (closed symbols – adsorption, open symbols – desorption).

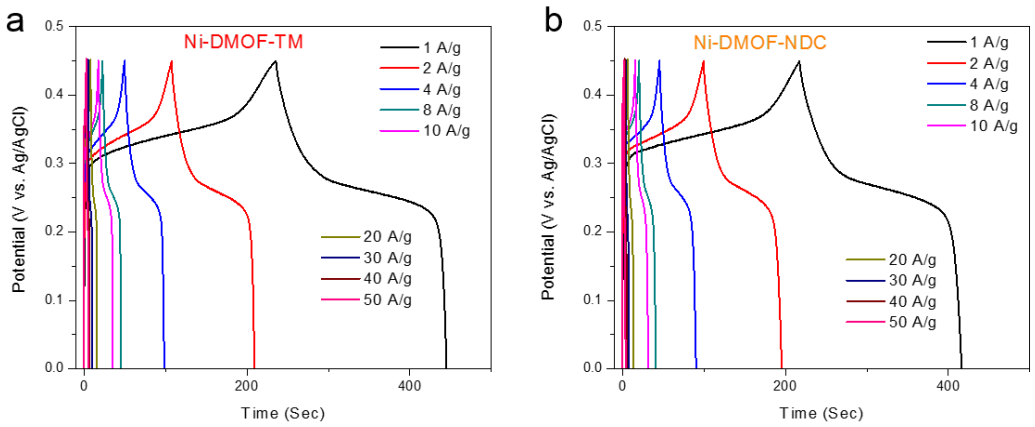

Figure C.3: GCD curves of (a) Ni-DMOF-TM and (b) Ni-DMOF-NDC at different constant current densities.

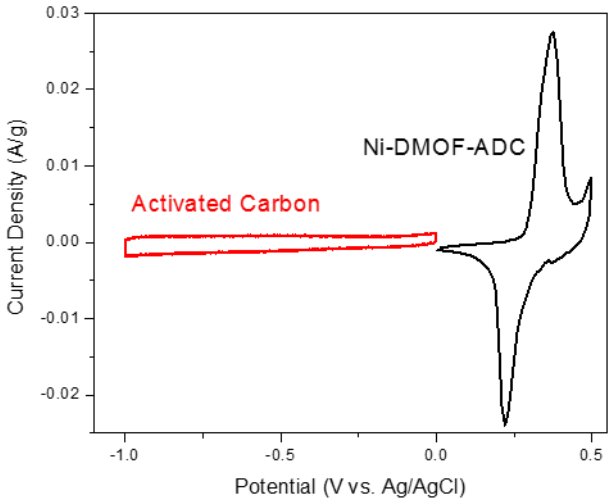

Figure C.4: CV curves for AC electrode and Ni-DMOF-ADC electrode.

Figure C.5a shows the CV curves of optimized Ni-DMOF-ADC, Ni-DMOF-TM, and Ni-DMOF-NDC asymmetric supercapacitor at 10 mV/s between 0 and 1.5 V in 2 M KOH aqueous electrolyte. Two pairs of broad redox peaks can be found on these curves, which is consistent with the pseudocapacitance behavior of the fabricated asymmetric supercapacitor. The specific capacitances are correlated to the average area of a CV curve which follow the order of Ni-DMOF-ADC > Ni-DMOF-TM > Ni-DMOF-NDC. Figure C.5b shows the CV response of Ni-DMOF-ADC asymmetric supercapacitor at different scan rates of 5, 10, and 20 mV/s between 0 and 1.5 V. With the increase of scan rates, the current response increased accordingly. GCD curves were obtained for Ni-DMOF-ADC in the potential range of 0-1.45 V Figure C.5c. The charge-discharge curves further indicate the pseudocapacitive behavior of the asymmetric supercapacitor as both curves were slightly nonlinear with the potential.

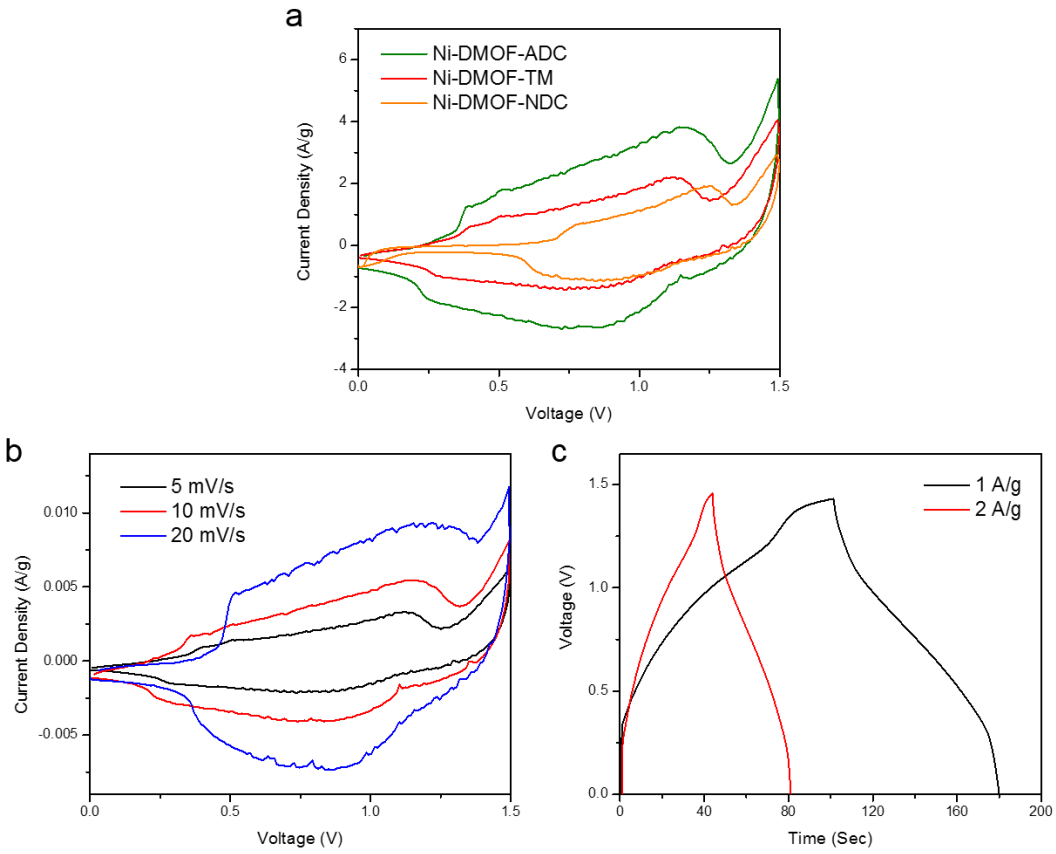

Figure C.5: Electrochemical characterization of the Ni-DMOF-based asymmetric supercapacitor. (a) CV curves of MOF samples at a scan rate of 10 mV/s in 2M KOH. (b) CV curves of Ni-DMOF-A at scan rates of 5, 10, and 20 mV/s. (c) GCD curves of Ni-DMOF-ADC at different current densities.

In recent years, Raman spectroscopy has been proven to be very useful to unravel the nature of MOF structure.[3-5] For the Raman spectrum of as-prepared MOF material, distinctive sharp Raman bands are observed indicating well-organized bonding within the MOF structure. To be specific, for the aromatic ring ligand, the sharp Raman band near 3070 cm^{-1} correspond to the aromatic C-H stretch vibration within anthracene rings. The strong bands at 1617, 1565, and 1396 cm^{-1} are from the stretching modes of C-C bond of Aromatic rings.[6] The weak shoulder band at 1372 cm^{-1} corresponds to the stretching vibration of COO group bonded to anthracene ring. For the DABCO ligand, the weak band

near 2970 cm^{-1} corresponds to the stretching vibration sp^3 C-H bond within in DABCO ligand. The strong bands at 1014 cm^{-1} and 793 cm^{-1} are assigned to asymmetric and symmetric N-C_3 vibration within DABCO ligand, respectively.[7] For the bonding between Ni and C(O)O group, the Raman band at 416 cm^{-1} is most likely to be caused by Ni-O bond stretching vibration.

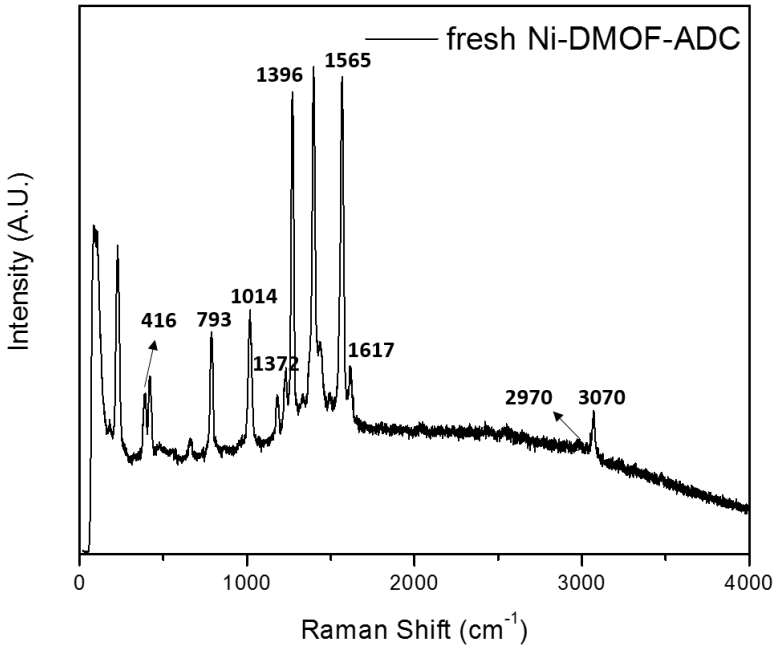

Figure C.6: Raman spectrum of fresh Ni-DMOF-ADC electrode.

In order to further illustrate the problem, we have also measured the N_2 isotherms of the converted structure and applied the BET model to determine specific surface areas. The BET analysis is performed over the range $0.05 < P/P_0 < 0.3$ according to previously reported method.[8] The converted layered structure has a 3-D nanostructure inherited from MOFs, which provided larger surface areas compared to other nickel hydroxides, thus

increasing the electrode-electrolyte contact area and decreasing the polarization of the electrode in charge-discharge cycles.

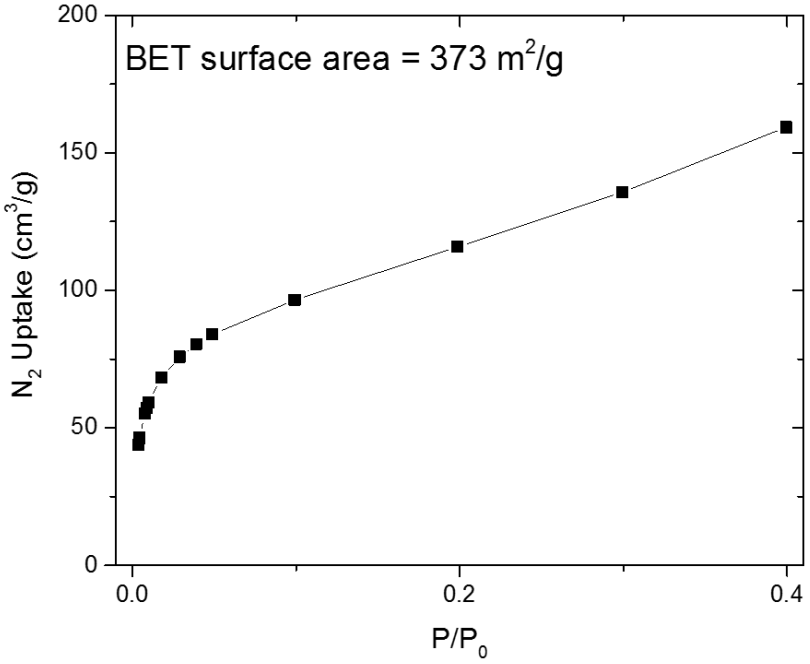

Figure C.7: N_2 adsorption isotherm at 77 K on the DMOF-ADC derived material.

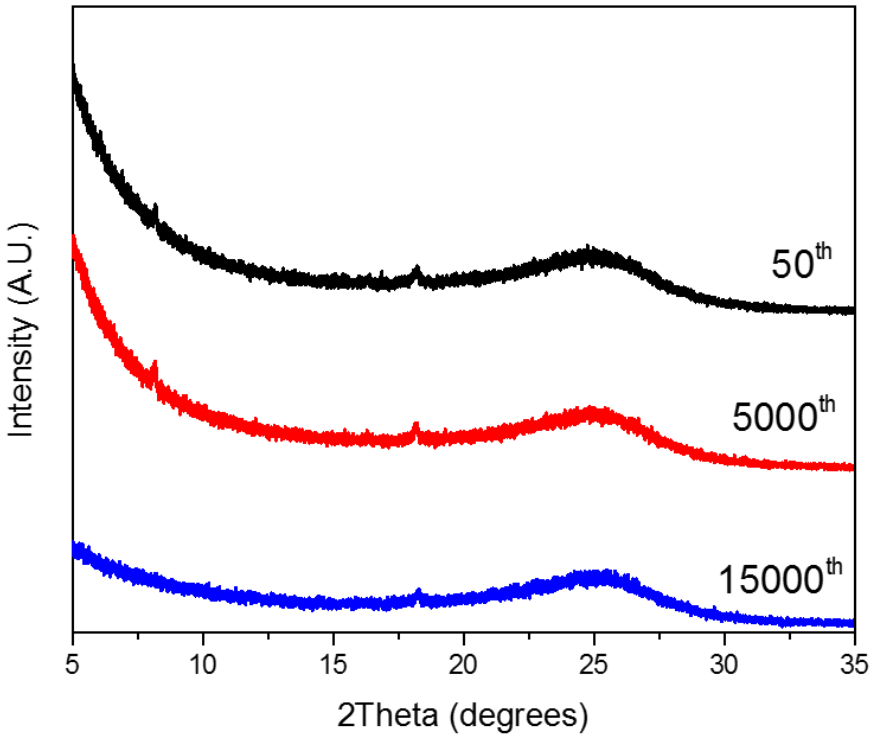

Figure C.8: PXRD patterns of Ni-DMOF-ADC electrodes from 50th, 5000th, 15000th cycles (after each specific cycle, the electrode film attached with a piece of carbon fiber paper was taken from the asymmetric cell and washed with deionized water for five times and then dried before PXRD measurements).

Compared with similar materials in the literature, we find that the cycling stability of Ni-DMOF-ADC derived nickel hydroxide is superior to the others (Table C.1).

Table C.1: Cycling stability comparison of similar materials.

Material	Cycles	Capacitance retention (%)
This work	**16000**	**98**
NiOOH/graphene (Gr) hydrogels[9]	8000	85.3
$Ni(OH)_2$/Gr[10]	3000	94.7
$Ni(OH)_2$-carbon nanotube-conducting polymer[11]	30000	86
Ni-MOF/carbon nanotube[12]	5000	95
Amorphous $Ni(OH)_2$ nanospheres[13]	5000	97
3-D interconnected $Ni(OH)_2$/ultrathin-graphite foam[14]	10000	63.2

C.1 References

1. Tanaka, D.; Horike, S.; Kitagawa, S.; Ohba, M.; Hasegawa, M.; Ozawa, Y.; Toriumi, K., *Chem. Commun.* **2007**, (30), 3142-3144.

2. Chun, H.; Dybtsev, D. N.; Kim, H.; Kim, K., *Chem. Eur. J.* **2005**, *11* (12), 3521-3529.

3. Nagai, A.; Guo, Z. Q.; Feng, X.; Jin, S. B.; Chen, X.; Ding, X. S.; Jiang, D. L., *Nat. Commun.* **2011**, *2*, 536.

4. Talin, A. A.; Centrone, A.; Ford, A. C.; Foster, M. E.; Stavila, V.; Haney, P.; Kinney, R. A.; Szalai, V.; El Gabaly, F.; Yoon, H. P.; Leonard, F.; Allendorf, M. D., *Science* **2014**, *343* (6166), 66-69.

5. Tan, K.; Nijem, N.; Gao, Y. Z.; Zuluaga, S.; Li, J.; Thonhauser, T.; Chabal, Y. J., *Crystengcomm* **2015**, *17* (2), 247-260.

6. Xie, Y. F.; Wang, X.; Han, X. X.; Xue, X. X.; Ji, W.; Qi, Z. H.; Liu, J. Q.; Zhao, B.; Ozaki, Y., *Analyst* **2010**, *135* (6), 1389-1394.

7. Guzonas, D. A.; Irish, D. E., *Can. J. Chem.* **1988**, *66* (5), 1249-1257.

8. Walton, K. S.; Snurr, R. Q., *J. Am. Chem. Soc.* **2007**, *129* (27), 8552-8556.

9. Wang, R. H.; Xu, C. H.; Lee, J. M., *Nano Energy* **2016**, *19*, 210-221.

10. Yan, J.; Fan, Z. J.; Sun, W.; Ning, G. Q.; Wei, T.; Zhang, Q.; Zhang, R. F.; Zhi, L. J.; Wei, F., *Adv. Funct. Mater.* **2012**, *22* (12), 2632-2641.

11. Jiang, W. C.; Yu, D. S.; Zhang, Q.; Goh, K. L.; Wei, L.; Yong, Y. L.; Jiang, R. R.; Wei, J.; Chen, Y., *Adv. Funct. Mater.* **2015**, *25* (7), 1063-1073.

12. Wen, P.; Gong, P. W.; Sun, J. F.; Wang, J. Q.; Yang, S. R., *J. Mater. Chem. A* **2015**, *3* (26), 13874-13883.

13. Li, H. B.; Yu, M. H.; Wang, F. X.; Liu, P.; Liang, Y.; Xiao, J.; Wang, C. X.; Tong, Y. X.; Yang, G. W., *Nat. Commun.* **2013**, *4*, 1894.

14. Ji, J. Y.; Zhang, L. L.; Ji, H. X.; Li, Y.; Zhao, X.; Bai, X.; Fan, X. B.; Zhang, F. B.; Ruoff, R. S., *ACS Nano* **2013**, *7* (7), 6237-6243.

APPENDIX D. CHAPTER 6 SUPPORTING INFORMATION

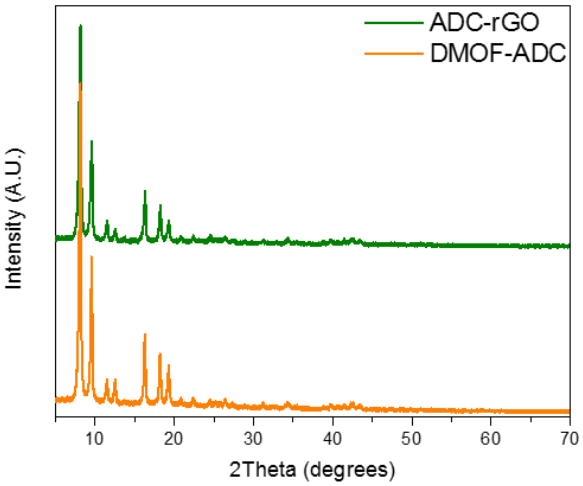

Figure D.1: PXRD patterns for as-synthesized DMOF-ADC and ADC-rGO.

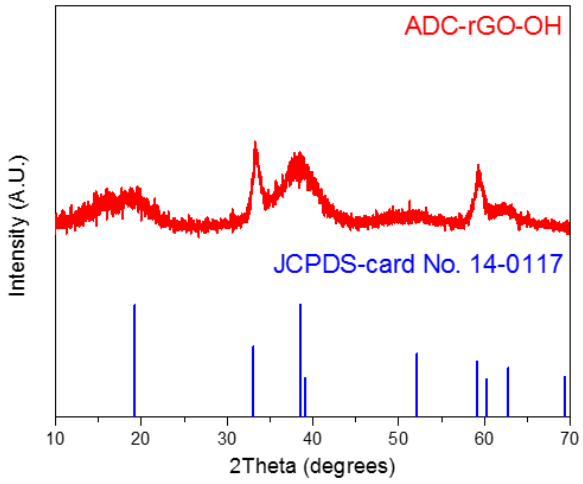

Figure D.2: PXRD patterns for ADC-rGO-OH and JCPDS-card (14-0117) for β-$Ni(OH)_2$.

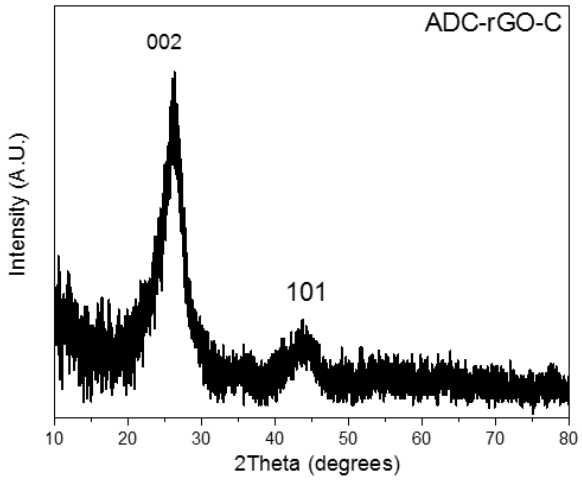

Figure D.3: PXRD patterns for ADC-rGO-C.

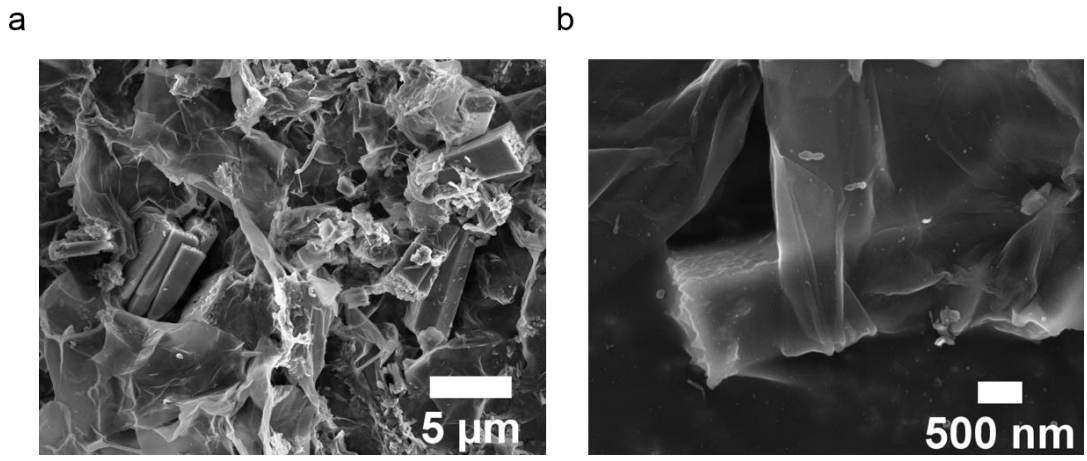

Figure D.4: SEM images for ADC-rGO at (a) low and (b) high magnification levels.

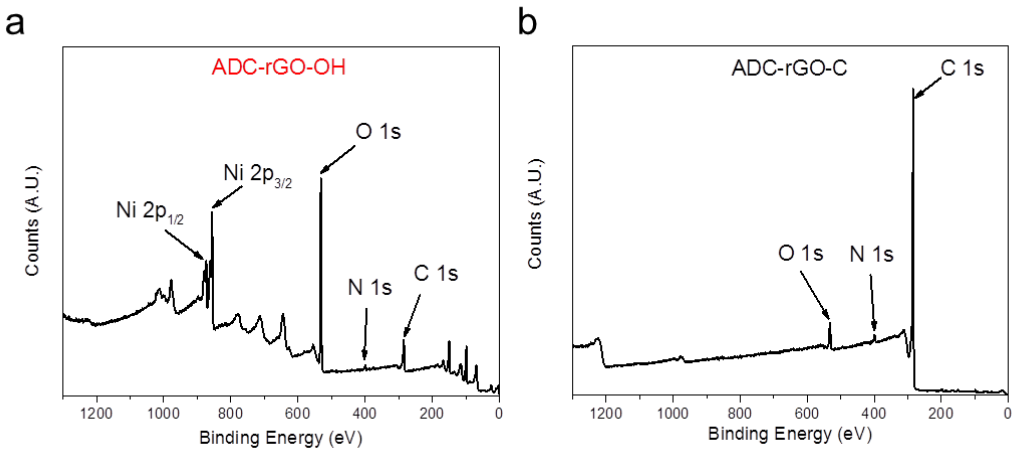

Figure D.5: XPS survey spectra for (a) ADC-rGO-OH and (b) ADC-rGO-C.

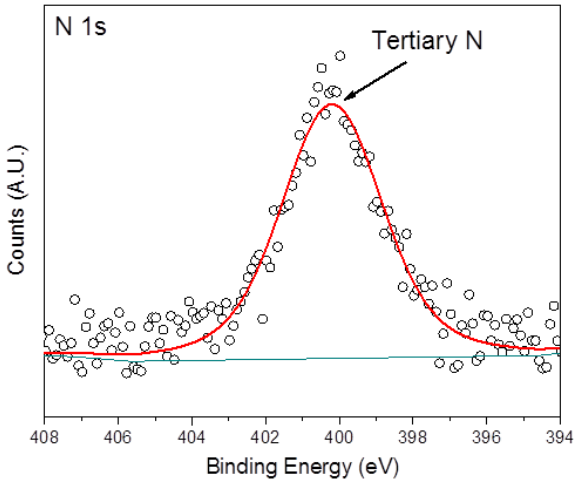

Figure D.6: High-resolution N 1s spectrum for ADC-rGO-OH.

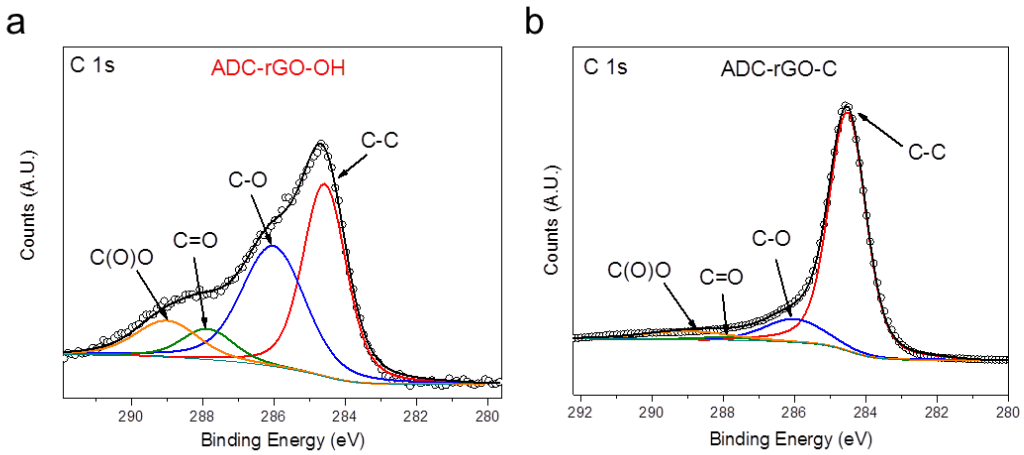

Figure D.7: High-resolution C 1s XPS spectrum for (a) ADC-rGO-OH and (b) ADC-rGO-C.

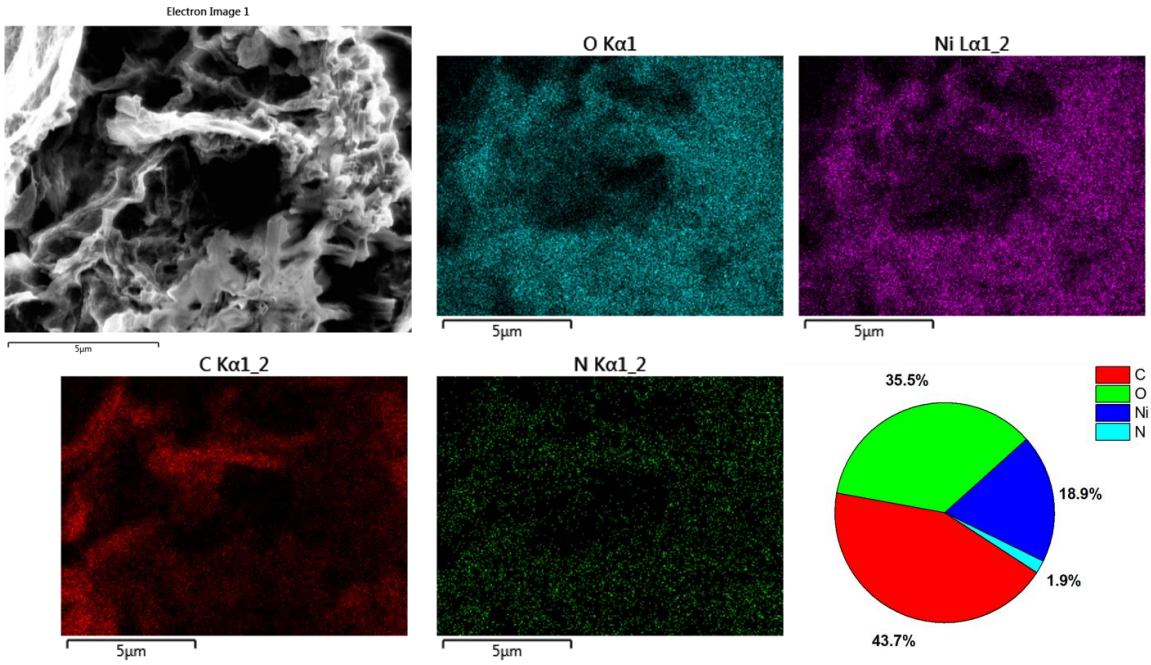

Figure D.8: Energy dispersive X-ray spectroscopy (EDS) elemental mapping of ADC-rGO-OH.

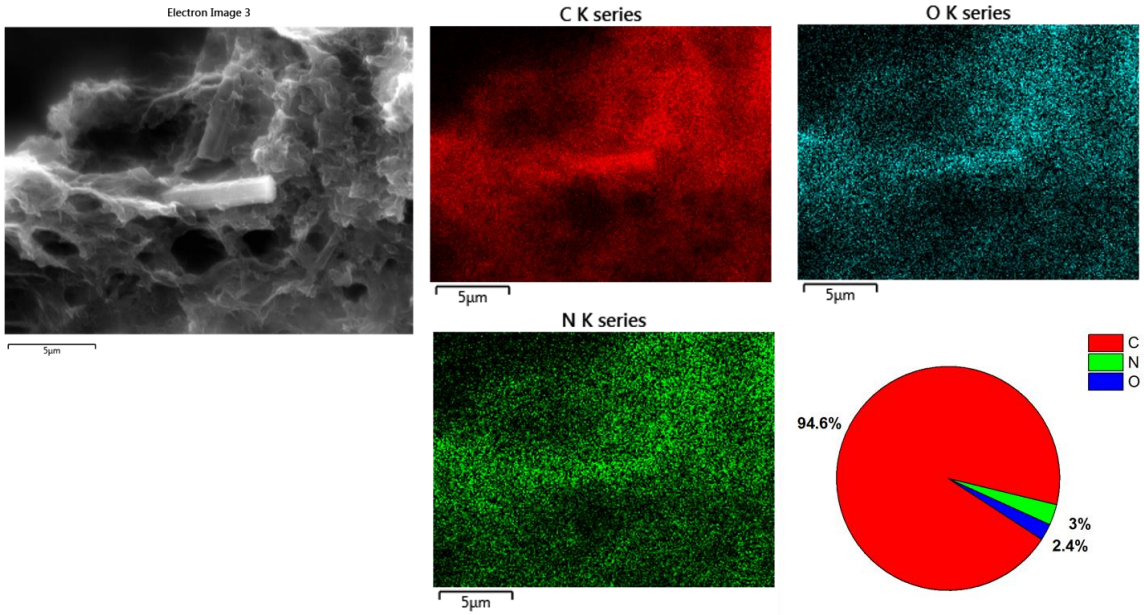

Figure D.9: EDS elemental mapping of ADC-rGO-C.

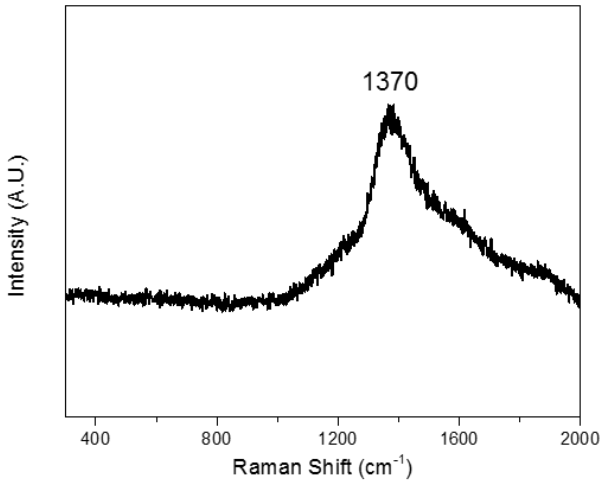

Figure D.10: Raman spectrum of glass substrate.

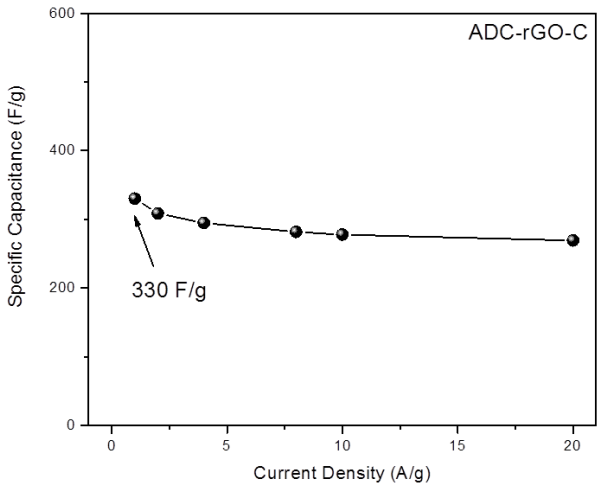

Figure D.11: Rate performance of ADC-rGO-C.

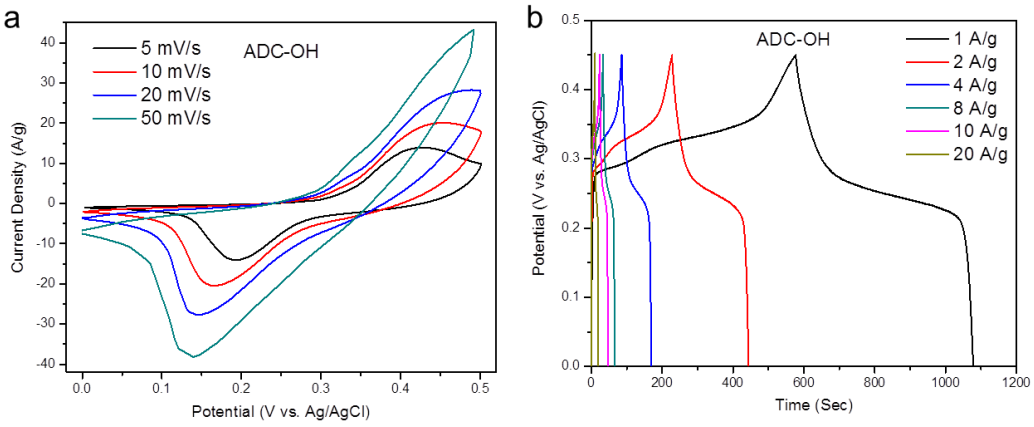

Figure D.12: (a) CV curves of ADC-OH at different scan rates. (b) GCD curves of ADC-OH at various current densities.

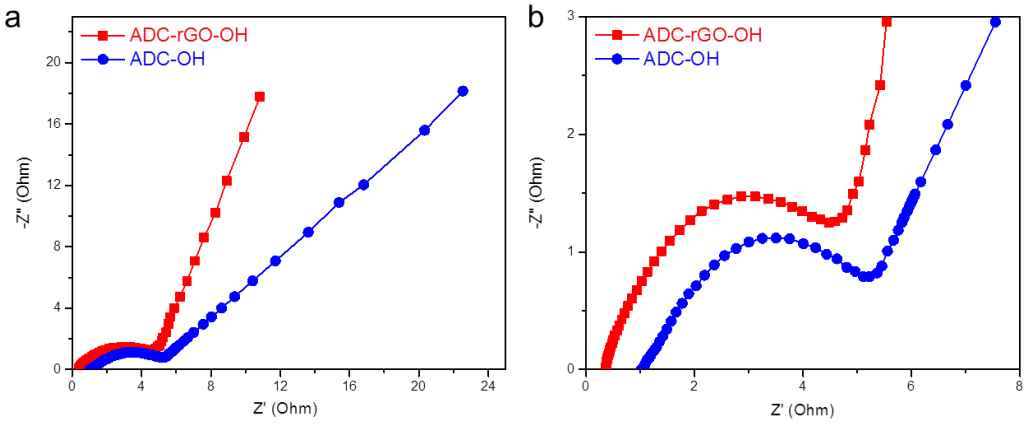

Figure D.13: (a) Nyquist plots of ADC-OH and ADC-rGO-OH collected in the three-electrode configuration. (b) The enlarged plots of the indicated region.

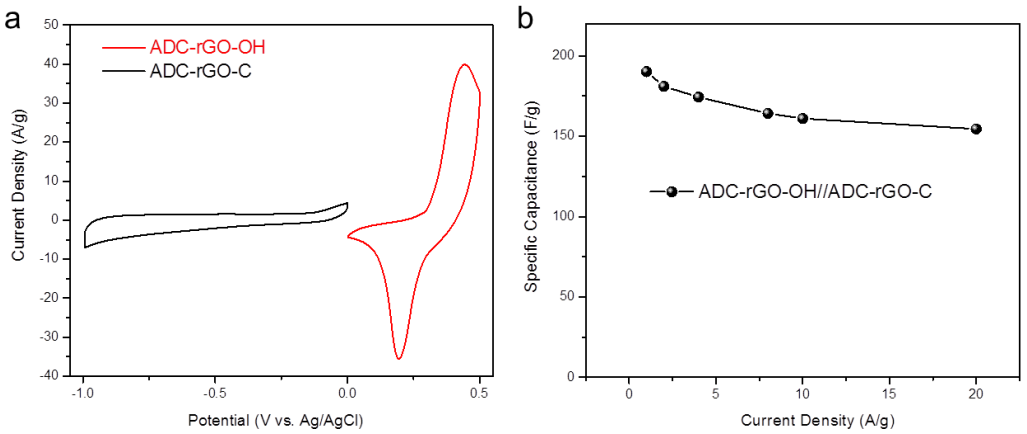

Figure D.14: (a) CV curves comparison between ADC-rGO-OH and ADC-rGO-C at 10 mV/s. (b) The specific capacitance of hybrid device at various current densities.

Table D.1: Comparison of the cycling performance of the hybrid supercapacitor device using ADC-rGO-OH and ADC-rGO-C as positive and negative electrodes with those of advanced hybrid/asymmetric supercapacitors.

Electrode materials of hybrid/asymmetric supercapacitor device	Cycling performance	Reference
ADC-rGO-OH//ADC-rGO-C	**~95% after 10,000 cycles at 20 A/g**	**This work**
Metaborate Ni/$Co(OH)_2$/graphene (Gr)//activated carbon (AC)	83% after 10,000 cycles at 5 A/g	*Nano. Lett* **2017**, *17*, 429 (Ref. 30)
MOF-derived hydroxides//N-doped carbon	91.3% after 10,000 cycles at 13.5 A/g	*ACS Energy Lett.* **2017**, *2*, 1263 (Ref. 37)
MOF-derived Ni-Co oxide//Gr/multishelled mesoporous carbon sphere	91.3% after 10,000 cycles at 10 A/g	*Adv. Mater.* **2017**, *29*, 4085 (Ref. 70)
N-doped AC//Si/carbon	76.3% after 8,000 cycles at 1.6 A/g	*Energy Environ. Sci.* **2016**, *9*, 102 (Ref. 76)
$MnCo_2O_4$@$Ni(OH)_2$//AC film	90% after 2,500 cycles at 6 A/g	*Adv. Funct. Mater.* **2016**, *26*, 4085 (Ref. 77)
3-D-G@MnO_2//3-D nanoporous Gr film	92% after 5,000 cycles at 2 mA/cm^2	*Adv. Energy. Mater.* **2016**, *6*, 1600755 (Ref. 78)
NiO-hollow sphere carbon//N-doped Gr	86.4% after 10,000 cycles at 6.7 A/g	*Energy Environ. Sci.*, **2015**, *8*, 188 (Ref. 74)
Ni-Co-Fe hydroxide//AC	94% after 20,000 cycles at 6 A/g	*Adv. Energy Mater.* **2015**, *5*, 1401767 (Ref. 29)